Numerical methods for the prediction of gravitational lensing signal as a probe of the mass content on the Universe

Céline Gouin

École Doctorale d'Astronomie et Astrophysique d'Ile-de-France

Doctoral Thesis

Numerical Methods for the prediction of Gravitational Lensing Signal as a probe of the mass content of the Universe

Author:
Céline Gouin

Directors:
Raphaël Gavazzi and Christophe Pichon

prepared at Institut d'Astrophysique de Paris, CNRS (UMR 7095), Sorbonnes Universités Sciences (Paris VI)

Composition of the jury

Reviewers:	Oliver Hahn	-	Observatoire de Côte d'Azur, France
	Geneviève Soucail	-	IRAP, Toulouse, France
Advisors:	Raphaël Gavazzi	-	Institut d'Astrophysique de Paris, France
	Christophe Pichon	-	Institut d'Astrophysique de Paris, France
President:	Michael Joyce	-	LPNHE, Paris, France
Examinators:	Massimo Meneghetti	-	Université de Bologne, Italie
	Dominique Aubert	-	Observatoire de Strasbourg, France

SORBONNE UNIVERSITÉ
CRÉATEURS DE FUTURS DEPUIS 1257

July 22, 2019

IAP

Contents

Acknowledgements **v**

Abstract **vii**

Résumé **ix**

Introduction **xi**

1 The concordance model of cosmology **1**
1.1 A homogeneous and isotropic Universe 1
1.2 Cosmological structure formation 6
1.3 The observational foundations of the ΛCDM model 25
1.4 Numerical simulations 34

2 Gravitational lensing **45**
2.1 The gravitational lensing formalism 46
2.2 The variety of weak lensing observables 50
2.3 Numerical methods to predict the lensing signal 58
2.4 Conclusion 66

3 Multipolar moments of weak lensing signal around clusters (article) **67**
3.1 Context 67
3.2 Paper presentation 68
3.3 Details on the preliminary numerical work 69
3.4 Overview of my different contribution 72
3.5 Perspectives 72

4 Gravitational lensing in the Horizon-AGN simulation light-cone **91**
4.1 Weak lensing in the Horizon-AGN simulation light-cone: Small scale baryonic effects 91
4.2 Production of lensed mock images 108

5 Conclusion **117**
5.1 Context 117
5.2 Summary and immediate objectives 119
5.3 Perspectives 120

A Complements to chapter 1 **123**
A.1 Additional cosmological definitions 123
A.2 The spherical collapse for an Einstein-de-Sitter Universe 124
A.3 Numerical simulation - The smoothing scheme 124

B Lagrangian theory of harmonic power spectra (article) **125**

Bibliography **139**

Acknowledgements

Je tiens à remercier mes directeurs de thèse Raphaël Gavazzi et Christophe Pichon pour l'aide précieuse qu'ils m'ont apportées tout au long de cette thèse. Je remercie tout particulièrement Raphaël Gavazzi, pour sa pédagogie, sa patience et ces encouragements. J'adresse aussi ma gratitude à Christophe Pichon, pour l'aide et les conseils qu'il m'a prodigué.

Je tiens également à remercier l'équipe avec laquelle j'ai intéragi, et qui m'ont aidé dans la réalisation de ce travail de thèse. Plus particulièrement, un grand merci à Yohan Dubois, Sandrine Codis, Sébastien Peirani, Emmanuel Bertin et Clotilde Laigle, pour leur collaboration et l'aide continue qu'il m'ont apportées dans ces travaux.

Je remercie les doctorants de l'IAP, pour leur accueil et leur amitié.

J'adresse tous mes remerciements à Geneviève Soucail et Oliver Hahn, de l'honneur qu'ils m'ont fait en acceptant d'être rapporteurs de cette thèse. De plus, je remercie Michael Joyce, Massimo Meneghetti et Dominique Aubert, d'avoir accepté d'être membre de mon jury de thèse.

Finalement, je dédie cette thèse à ma famille.

Abstract

Upcoming weak lensing surveys such as Euclid, LSST and WFIRST will provide an unprecedented opportunity to investigate the dark Universe from the entire extragalactic sky down to very small scales. Through these large scale surveys, gravitational lensing is an indispensable cosmological probe to investigate the dark energy and the dark matter. Indeed, one can use it to reconstruct the matter distribution by measuring the distortions of background galaxies induced by mass inhomogeneities along the line-of-sight. It thus constitutes an unbiased tracer the matter distribution in the Universe. Due to the new level of accuracy in observations, we must perform cosmological predictions in state-of-art simulations, and to precisely quantify its variances, noises, potential biases and potential degeneracies coming from the late non-linear evolution and baryonic physics. In this context, my thesis focuses on the construction of accurate lensing observables.

The first part of my PhD work characterises the geometry of large-scale structure through weak lensing (Gouin et al. 2017). I relied on multipolar decomposition of weak lensing signal to quantify the azimuthal distribution of dark matter at different scales, centred on galaxy clusters. The statistical properties of these multipolar moments are estimated on a mock catalogue of clusters, extracted from a large N-body cosmological simulation. I built a novel statistical estimator, the multipolar power spectrum while stacking the modulus of aperture multipole moments. This method allowed me to quantify the angular distribution of matter in central and external regions of cosmic nodes. The harmonic distortions computed in the vicinity of clusters, appear to trace the non-linear sharpening of the filamentary structure. Larger number of filaments seem to be connected to high-mass clusters. The angular shape of cluster core is also investigated, and more massive DM halos appears more elliptical. The detection level of multipolar moment of WL with current and the upcoming Euclid lensing data sets is estimated. In a follow up paper, led by S. Codis, we derived the multipolar statistics of the field in a shell around a central peak from the linear and weakly non-linear regimes (Codis et al. 2017). It provides theoretical support for the results presented in the first paper.

In the last part of my thesis, I mock the weak gravitational lensing signal in the light-cone of the Horizon-AGN simulation (Dubois et al. 2014). To do so, I propagate light-rays along the light-cone in the multiple-lens-plane approximation. Two different algorithms are developed to construct the deflection field on each lens plane: the first one accurately integrates the acceleration along the path of light rays on each cell of the AMR simulation, while the second method adaptively smooths particles depending of the total local density. The latter allowed me to distinguish the lensing contribution of dark and baryonic matter. This numerically intensive work, is validated using various analysis software that I developed (ray tracing, extraction and interpretation of two-point statistics,...). The impact of baryons is significant in cosmic shear statistics for angular scales below a few arcmins. In addition, the galaxy-galaxy lensing signal is compared to current observational measurements (Leauthaud et al. 2017), and seems in good agreement. I also present my ongoing effort of producing mock observations fully derived from the Horizon-AGN simulation (light emission, lensing,..), with the underlying goal of mimicking a

complete end-to-end lensing pipeline, including all the relevant effects (magnification, photometric redshifts, intrinsic alignments,...). This could potentially help understanding systematic effects that may be play in a survey like Euclid.

Keywords: cosmology, large-scale structure of the Universe, dark matter halos, galaxy clusters, galaxy, weak gravitational lensing, Methods: statistical and numerical.

Résumé

Les relevés à venir comme Euclid, LSST et WFIRST vont nous ouvrir la perspective d'étudier l'univers profond, de l'ensemble de la voûte céleste extragalactique jusqu'aux toutes petites échelles. Pour ces grands relevés, l'astigmatisme cosmique correspond à une sonde indispensable pour étudier la nature de l'énergie noire et la matière noire. De fait, nous pouvons l'utiliser pour reconstruire la distribution de matière en mesurant les distorsions que subissent les galaxies d'arrière plan en raison des inhomogénéités de la distribution sur la ligne de visée. Cette méthode constitue donc un traceur non biaisé de la distribution de matière dans l'univers. Compte tenu de la précision des mesures dans les observations, nous devons faire des prédictions cosmiques en nous reposant sur des simulations correspondant à l'état de l'art afin de quantifier avec précision la variance, le bruit, les biais et les dégénérescences potentielles provenant de l'évolution non linéaire de la gravitation et les effets liés aux baryons. Dans ce contexte, ma thèse se focalise sur la construction d'estimateurs précis basés sur les observables de lentillage.

La première partie de ma thèse a pour objectif de caractériser la géométrie des grandes structures par astigmatisme cosmique (Gouin et al. 2017). Je me suis reposée sur une décomposition multipolaire du signal afin de quantifier la distribution azimutale de la matière noire à différentes échelles, centrée sur les amas de galaxies. Les propriétés statistiques de ces moments multipolaires sont estimées à partir de catalogues synthétiques d'amas, extraits d'une simulation cosmologique N-corps de grande taille. J'ai construit un nouvel estimateur statistique, le spectre de puissance multipolaire, qui consiste à empiler le module d'ouverture des moments multipolaires. Cette méthode m'a permis de quantifier la distribution angulaire de la matière dans la région centrale et périphérique des noeuds de la toile cosmique. Les distorsions harmoniques calculées dans le voisinage des amas semblent tracer le renforcement non linéaire de la structure filamentaire. Un plus grand nombre de filaments semblent connectés aux amas de forte masse. La géométrie angulaire des amas est aussi sondée et semble plus elliptique pour les amas les plus massifs. Je quantifie aussi le niveau de détection des moments multipolaires par astigmatisme par les relevés actuels et à venir (Euclid). Dans un second article, porté par S. Codis, nous avons estimé la statistique multipolaire dans le champ au voisinage d'un pic central dans le régime linéaire et faiblement non linéaire (Codis et al. 2017). Cette étude complémente théoriquement le premier article.

Dans la dernière partie de ma thèse, je synthétise le signal d'astigmatisme cosmique dans le cône de lumière de la simulation Horizon AGN (Dubois et al. 2014). Pour ce faire, je propage les rayons de lumière le long du cône dans l'approximation des plans de lentillage multiples. Deux algorithmes distincts sont utilisés pour quantifier la déflection de chaque plan: le premier estime avec précision l'accélération le long du chemin en utilisant les cellules de la simulation AMR, alors que le second algorithme lisse de manière adaptative les particules en fonction de la densité locale totale. Cette seconde méthode m'a permis de distinguer la construction du lentillage de la matière noire et de la matière baryonique respectivement. Ce travail numérique intensif est validé sur différents outils d'analyse que j'ai développés (tracé de rayon, extraction et interprétation de statistiques à deux points, etc). L'effet des baryons est significatif dans la statistique du

cisaillement aux échelles angulaires inférieures à l'arc-minute. Le signal de cisaillement galaxie -galaxie est comparée aux observations récentes de Leauthaud et al. (2017), et semble être en bon accord. Je présente enfin mes travaux récents pour produire des observations synthétiques déduites entièrement de la simulation (émission et lentillage) avec pour objectif de modéliser la synthèse d'image 'end-to-end' en prenant en compte tous les effets (magnification, redshift photométrique, alignements intrinsèques). Ces travaux permettront de mieux comprendre les effets systématiques auxquels un relevé comme Euclid sera confronté.

Introduction

Even if the current cosmological model largely explains the history and structure of the Universe, dark energy and dark matter, two key components remain a mystery. In this context, the gravitational lensing signal is a promising way to investigate both of these components. Indeed, regardless of its nature or dynamical state, the matter along the light-of-sight can be probed with the distortions of background galaxies via gravitational lensing. As light deflection is directly induced by the gravitational potential, one can reconstruct the projected density of the lens by measuring the deformation of background galaxies. The lensing signal can thus be used as an unbiased tracer to map the total mass content on the Universe. Characterising the distribution of matter on large scale is a unique cosmological probe of the concordance model of cosmology. Gravitational lensing can also potentially shed some light on the behaviour of dark matter on galactic scales, which is the locus of a complex dynamical interplay between dark matter and baryons.

Upcoming cosmological experiments, like the *Euclid* mission, intend to measure the gravitational lensing signals (both weak and strong) with unprecedented sensitivity on a broad range of scales. In order to maximise the scientific returns from these future data sets, we require accurate theoretical predictions of cosmological observables such as the lensing signal. A new generation of numerical simulations was developed in the recent years to fulfil this requirement. Numerical simulations are a powerful tool to investigate the evolution of the cosmic density field predicted for the ΛCDM model. Indeed, they are the only way to accurately describe non-linear matter clustering at all times and on a large range of scales (going from conventional large scales to the less-known smaller scales via hydrodynamical simulation).

With the advent of high performance computing, cosmological simulations can provide a precise description of the matter distribution on both large and small scales. By focusing on the impact of baryons on the total matter density field, hydrodynamical simulations provide a way to investigate galaxy formation and evolution, and the key processes involved. By performing post-processing analyses of such cosmological simulations, we can construct estimators of cosmological observables in order to guide our interpretations of observational results. The output of a simulation can be used to test the validity of observational pipelines (e.g. source detection pipelines).

In this framework, my doctoral thesis work is focused on the construction of accurate estimators of the lensing signal via numerical simulations (both N-body and hydrodynamical simulations). For this purpose, I have developed numerical methods to post-process cosmological simulations, and build realistic mock lensing observables. In particular, I focused on the characterisation of the dark matter filamentary structure on large scales, and on the impact of baryons on lensing statistics on small scales. This doctoral thesis is organized as follows:

- I begin with an overview of the cosmological concordance model in Chapter 1. I describe

both its success in explaining the large scale structure observed in the Universe and its shortcomings on intermediate and smaller scales. I also give a brief theoretical outline of the theory of structure formation from the linear to the non-linear regime. I will show that numerical simulations are required to probe the non-linear evolution of the density field. As a result, I also give an overview of the basics of numerical methods. Finally, I discuss the impact of baryonic matter on the underlying density field as investigated with hydrodynamical simulations.

- I follow with a review of gravitational lensing theory in Chapter 2. Standard lensing observables are also reviewed in the weak regime. Numerical methods to predict the lensing signal from both N-body and hydrodynamical simulations, are finally presented.

- In Chapter 3, I present a first attempt to characterise the statistics of dark matter filaments at the outskirts of galaxy clusters with lensing shear signal (Gouin et al. 2017). As the filamentary structures have a low density contrast compared to massive clusters, detecting dark filaments via weak lensing is challenging (it is currently limited massive bridge of matter between two galaxy clusters). In this study I develop a statistical estimator, based on the multipolar decomposition of the projected density, and use it to probe the azimuthal shape of galaxy clusters in both internal and external regions. By using a pure dark matter N-body simulation, I calculate and average multipolar moments over a large number of mock galaxy clusters as a function of mass and redshift bins. This numerical result is compared to theoretical predictions performed in a companion paper (Codis et al. 2017). Finally, the prospects of measuring this signal are estimated for current and future lensing data sets.

- Chapter 4 is devoted to the prediction of weak lensing statistics extracted from the Horizon-AGN hydrodynamical cosmological simulation (Gouin et al, 2018, in preparation). I present the ray-tracing algorithm, the construction of the deflection field, and the resulting mock lensing observables. Standard weak lensing statistics such as the convergence power spectrum, the two-point shear correlation and the galaxy-galaxy lensing are predicted up to highly non-linear scales (few arcsec).These lensing signal predictions have the advantage of taking into account the full baryonic physics, all the matter along the line of sight, and the coupling of lens planes into account. Common lensing assumptions, such as Born approximation and reduced shear, are also investigated.

- The thesis concludes with a summary and an outlook

Chapter 1

The concordance model of cosmology

In the past decade, major observational discoveries and theoretical advances have led the community to converge towards a common model to describe our Universe: the "concordance" model. One of the most important observational evidence is the measurement of the cosmic microwave background, the oldest observed light emission of our Universe, i.e. an imprint of its primordial stage. This observation is a strong argument in favour of an isotropic and homogeneous Universe which is expanding and evolving with cosmic time. Complementary, the formalism of General Relativity provides a coherent description of Universe evolution, i.e. its thermal history and the growth of primordial density anisotropies. Nevertheless, the ΛCDM model relies on two components as yet undetected directly: non-baryonic matter (which only interacts gravitationally) and an supposed energy component which is responsible of the acceleration of the expansion of the Universe. The main cosmological challenge of the 21th century is therefore to improve our knowledge of these two "dark ingredients".

In section 1.1, I review the cosmological model in order to set the scene of this PhD work. In particular, as this thesis focuses on the characterisation of the density field at non-linear scales, we resume theoretical models of structure formation for both linear and non-linear regimes in section 1.2. Section 1.3 presents the observational evidence in support of the ΛCDM model on large scale, and lists some points of contention on smaller scales. Finally, I present in section 1.4 an overview of numerical simulations and the associated numerical methods as a powerful tool to study the structure formation in the fully non-linear case. I then discuss when simulations are necessary to improve our understanding of structure formation and to constrain cosmological observables.

1.1 A homogeneous and isotropic Universe

The concordance cosmological model is based on two fundamental principles: isotropy and homogeneity of the Universe. In other word, it supposes that there are no special directions or places in the Universe. While the initial motivation for these assumptions was purely philosophical, we show in section 1.3 that the detection of the Cosmic Microwave Background in 1992 by COBE has provided empirical support for these cosmological principles (Smoot et al. 1992).

1.1.1 The General Relativity

Proposed by Einstein (1905), the Special Relativity is based on two postulates: the principle of relativity[1] and the invariance of the speed of light.

[1] The laws of physics are identical in all inertial frames of reference

With these assumptions, the concept of a four-dimensional description of the Universe (three of space and one of time) relative to a reference frame has emerged and led to the notion of space-time. In addition, Special relativity induces a large number of consequences like length contraction, time dilation, and mass–energy equivalence.

The general theory of relativity, developed by Einstein (1916), extends the relativity principle to all frames of reference. The equivalence principle of gravitational and inertial mass follows. Therefore, General Relativity offers a rigorous mathematical formalism to describe the gravity as a geometrical phenomenon: space-time is locally curved by the presence of matter and energy.

One can link the mass-energy content to the geometrical properties of the space-time from the Einstein's field equations:

$$G_{\mu\nu} + \Lambda g_{\mu\nu} = \frac{8\pi G}{c^4} T_{\mu\nu} \,, \tag{1.1}$$

where $T_{\mu\nu}$ is the energy-momentum tensor which describes the mass and energy contained in the Universe. This is the compact form of a tensor equation which connects a set of symmetric 4×4 tensors. The Einstein tensor $G_{\mu\nu}$ is related to the symmetric metric tensor $g_{\mu\nu}$ which accounts for the geometrical properties of the space-time. Finally, the cosmological constant Λ was first introduced by Einstein to allow a stationary Universe. After being suppressed by the evidence of an expanding Universe, it has been added back to permit an accelerated expansion in order to agree with the observations (see section 1.3). According to General Relativity, energy and momentum are conserved. In addition, in the weak-field approximation, Einstein's theory can be reduced to Newtonian mechanics.

1.1.2 Friedmann equations

The cosmological principle supposes a high level of symmetry in the geometry of space-time. Therefore, considering an homogeneous and isotropic Universe in expansion, the Einstein field equations can be solved by an exact solution of the metric tensor: the Friedmann-Lemaitre-Robertson-Walker (FLRW) metric. Historically, this solution is first introduced by Friedmann (1922, 1924), as a cosmological model assuming the cosmological principles. Then, Lemaître (1931) extended this model to an expending Universe, with its observational evidence provided by Hubble (1929). Finally, Robertson and Walker independently proved that this solution is the only metric consistent with the assumption of homogeneity and isotropy of space (Robertson 1935; Walker 1937). Following this metric, the line element ds, *i.e.* the space-time interval between events, can be expressed as:

$$ds^2 = c^2 dt^2 - a(t) \left(\frac{dr^2}{1 - kr^2} + r^2 d\Omega^2 \right) , \tag{1.2}$$

where (r, θ, ϕ) denote the polar spatial coordinates, t is the time coordinate (called the cosmic time), and the solid angle element $d\Omega^2 = d\theta^2 + \sin^2\theta d\phi^2$. The constant k characterises the curvature of space, and can take three different values, such as $k = 0, \pm 1$. These correspond to a flat, spherical or hyperbolic curvature, respectively. The function $a(t)$ is called the scale factor: it describes the dilation or contraction of space scales over the evolution of cosmic time.

Taking the scale reference at the current time, we define $a(t_0) = 1$. From the field equation 1.1 and the metric 1.2, one can assume $T_{\mu\nu}$ has the form of a stress tensor for a prefect fluid[2]. In

[2]It has be demonstrated by Weinberg (1972) that isotropy and homogeneity involve a tensor with a perfect fluid form, such as $T^{00} = \rho c^2$, $T^{\nu\nu} = -p$, where ρ is the density and p is the pressure.

so doing, we can infer the Friedmann equations:

$$\left(\frac{\dot{a}}{a}\right)^2 = \frac{8\pi G\rho}{3} - \frac{Kc^2}{a^2} + \frac{\Lambda c^2}{3}\,, \tag{1.3}$$

$$\frac{\ddot{a}}{a} = -\frac{4\pi G}{3}\left(\rho + \frac{3p}{c^2}\right) + \frac{\Lambda c^2}{3}\,. \tag{1.4}$$

These two independent equations imply that the evolution of the scale factor $a(t)$ depends on the density $\rho(t)$ and the pressure $p(t)$ of the matter contained in the universe. It is useful to introduce, at this juncture, the Hubble parameter which describes the rate of cosmic expansion: $H(t) = \dot{a}(t)/a(t)$.

These equations can be solved by taking an equation of state for the matter component of the form $p = \omega\rho\, c^2$ with constant parameter ω. We obtain an expression for the density as a function of the scale factor a:

$$\rho(a) = \rho_0 a^{-3(\omega+1)}\,. \tag{1.5}$$

Here, let us take a moment to distinguish the various components of matter. Specifically, we have radiation, with $\omega = 1/3$ (relativistic particles), and non-relativistic matter, with $\omega = 0$ (dust matter). In fact, dust can be described like an ideal gas, so that the parameter of state equation can be approximated as $\omega_m \approx \overline{v^2}/3c^2 \approx 0$, with v the velocity of matter particle[3]. It follows that matter is diluted in an expending Universe as $\rho_m \propto a^{-3}$. Considering ultra-relativistic matter, one can demonstrate that the pressure exerted by electromagnetic radiation is equal to one third of the average energy density[4]. By considering the expression of effective mass of radiation as $m = E/c^2$ (Einstein 1907), it follows that $p = \rho c^2/3$. Therefore the density of relativistic particles decreases more rapidly than the volume expansion, such as $\rho \propto a^{-4}$.

The cosmological constant Λ can be identified as a perfect fluid in the first Friedmann equation[5] with a density $\rho_\Lambda = \Lambda c^2/(8\pi G)$. Following this density formulation, the second Friedmann equation[6] leads to $\omega_\Lambda = -1$.

Similarly, the curvature can be expressed as a fluid with a density $\rho_K = 3Kc^2/(8\pi G a^2)$ (from the first Friedmann equation), and it leads to an equation of state such as $\omega_K = -1/3$ (from the second Friedmann equation). The density of this hypothetical fluid decreases with the expansion of the Universe like $\rho_K \propto a^{-2}$. Applying all the above simplifications, we can then re-write the Friedmann equations as a direct sum of the i components:

$$H^2(t) = \left(\frac{\dot{a}}{a}\right)^2 = \frac{8\pi G}{3}\sum_i \rho_i\,, \tag{1.6}$$

$$\frac{\ddot{a}}{a} = -\frac{4\pi G}{3}\sum_i \left(\rho_i + \frac{3p_i}{c^2}\right)\,. \tag{1.7}$$

Therefore it becomes natural to define the total density of Universe - the "critical density" - as function of the cosmic time:

$$\rho_c(t) = \frac{3H^2(t)}{8\pi G}\,. \tag{1.8}$$

[3]Following ideal gas law, the pressure is $p = k_b T\rho/\mu$, where μ is the mean particle mass, T is the temperature of the gas, and k_b is the Boltzmann constant. According to the kinetic theory of gases, one can find that $k_b T = \mu\overline{v^2}/3$. It leads to $p = \rho \times \overline{v^2}/3c^2$.

[4]For an isotropic radiation, the pressure is averaged over all solid angles, and leads to $p = \epsilon/3$, with ϵ the energy per unit volume (Boltzmann 1884).

[5]we solve the equation: $\frac{8\pi G\rho_\Lambda}{3} = \frac{\Lambda c^2}{3}$

[6]we solve the equation: $\frac{4\pi G}{3}\left(\rho_\Lambda + \frac{3p_\Lambda}{c^2}\right) = \frac{\Lambda c^2}{3}$, with $P_\Lambda = \omega_\Lambda \rho_\Lambda c^2$

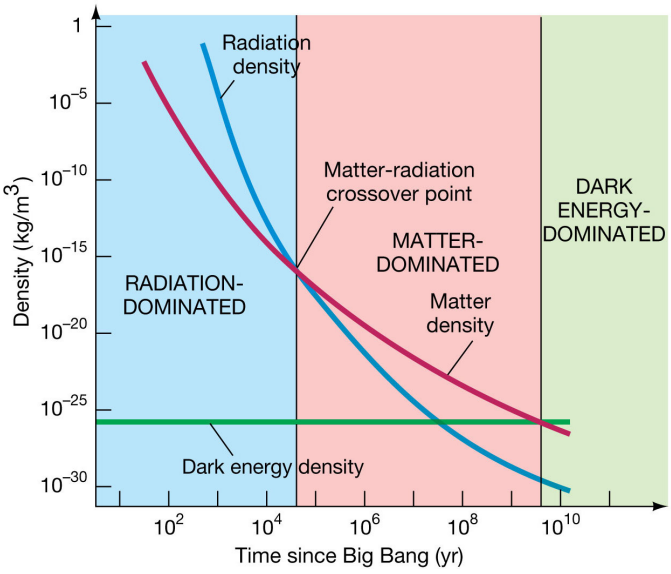

Figure 1.1 – The density evolution of the different components: radiation, matter and dark energy. Image credit: Pearson Education.

It is usual to rewrite the density of each species i as function of this reference density ρ_c, by considering the density parameters:

$$\Omega_i(t) = \frac{\rho_i(t)}{\rho_{\rm crit}(t)} \,. \tag{1.9}$$

The first Friedmann equation becomes $\Omega_r + \Omega_m + \Omega_\Lambda + \Omega_K = 1$, thus it supposes a conservation of the matter-energy content in an expending Universe. The Universe should be denser in the past, and its content should be dilluted with space-time expansion. One can finally rewrite the Friedmann equation in terms of the density parameters at the present time t_0:

$$\left(\frac{H(t)}{H_0}\right)^2 = \frac{\Omega_{r,0}}{a(t)^4} + \frac{\Omega_{m,0}}{a(t)^3} + \frac{\Omega_{K,0}}{a(t)^2} + \Omega_{\Lambda,0} \,, \tag{1.10}$$

where $H_0 \equiv H(t_0)$ and $\Omega_{i,0} = \rho_i(t_0)/\rho_{\rm crit}(t_0)$ are respectively the Hubble parameter and the density parameters at current time. Following this formulation, it becomes easy to describe the density evolution of the different components over the cosmic time, as it is illustrated in figure 1.1. Additional definitions, such as the notion of redshift, the various cosmological distances and the horizon concept, are provided in Appendix A.

1.1.3 Overview of the different epochs

First, we note that this model requires a singularity at the initial time $t = 0$ with $a(0) = 0$ - this corresponds to the Big Bang[7]. Shortly after the Big Bang, the Universe has exponentially expended - via the so-called inflation phase (detailed in section 1.2.1). From the equation 1.10, one can fully describe the expansion of the Universe as a function of the dominant matter component for a given era.

For a flat Universe ($k = 0$), the scale factor can be expressed as a function of the time:

$$a(t) = a_0 t^{\frac{2}{3(\omega+1)}} \,. \tag{1.11}$$

In the early stage of the Universe, after inflation, radiation is expected to dominate over other components, and as we saw, it density decreases with Universe expansion in a^{-4} (see figure

[7]There is no currently available physical theory to describe the Universe for times smaller than the Planck time ($t \sim 10^{-43}$ seconds).

1.1). When radiation dominated, the typical scale factor evolution is thus $a(t) \propto t^{1/2}$. At this epoch, baryonic matter and radiation are coupled and form a hot plasma of photons, electrons, and protons. As cosmic time evolves, space slowly expands, leading to a decline in the radiation density.

Eventually, the radiation and matter components are expected to be found in the same proportions. This occurs when the scale factor is equal to $a(t_{\rm eq}) = \Omega_r/\Omega_m$.

At this time, photons become free to travel across the Universe, and baryons start to form the first primordial neutral elements: this is the beginning of the matter-dominated epoch. Assuming an Einstein-de-Sitter (EdS) model with $\Omega_m = 1$ and $\Omega_k = \Omega_\Lambda = 0$, the Universe expands as $a(t) \propto t^{2/3}$.

Finally, at present time, we enter an epoch dominated by dark energy, i.e. the cosmological constant Λ. Assuming $\Omega_\Lambda = 1$, the expansion of the Universe grows exponentially as $a(t) \propto {\rm e}^{Ht}$.

1.1.4 Overview of the matter-energy components

Considering the concordance model of cosmology briefly described above, we have seen that the Universe is composed of radiation, non-relativistic matter, and dark energy. Their relative proportion has evolved with cosmic time until the present values (as detailed in section 1.3). Let me introduce in more detail the different components:

- Radiation gathers light and relativistic particles ($v \sim c$), principally photons and neutrinos, which interact via electromagnetism. Its energy density is now extremely low $\Omega_{r,0} < 10^{-4}$.
- The matter component has a significant proportion in the energy-mass budget of the Universe today, with $\Omega_{m,0} \sim 0.3$. One can distinguish two different types of matter:
  - The "baryonic" matter ($\Omega_{b,0} \sim 4\%$) which is the well-known constituent of ordinary matter (baryons and electrons included). This is the only component which participates in the four fundamental interactions: weak (leptons), strong (hadrons), electromagnetic, and gravitation. Baryonic matter is mainly in the form of gas and stars, and can be directly observed through their emission/absorption of electromagnetic radiations.
  - The dark matter (DM) is dominant compared to the baryons ($\Omega_{DM,0} \sim 27\%$). This unknown type of matter is required to explain the invisible mass content in the Universe (as detailed in sub-sections 1.3.1.5 afterwards). One can separate dark matter model into three different categories depending on the free streaming length of dark matter particles: cold (non-relativistic speed), warm, and hot (relativistic speed). Observational results are strongly in favour of cold collisionless dark matter particles[8]. The weakly interacting massive particles (WIMPs), are hypothetical particles which are the leading DM candidates for the non-baryonic dark matter[9] (Spergel & Steinhardt 2000a). Such particles are supposed to interact by gravitation and possibly by weak forces, and are thus difficult to detect (for more details see the recent review of Roszkowski et al. 2018).
- Finally the dark energy is an unknown form of energy which dominates today other Universe components, with $\Omega_{\rm DE,0} \sim 69\%$. This mysterious energy is characterised by a

[8]Large scale structure of the Universe, such as galaxy clusters, can be used to constrain the possible self-interaction of dark matter particles (Randall et al. 2008). Recently, the upper limit of the self-interaction cross section of dark matter is estimated to be $\sigma_{\rm DM}/m < 3.7{\rm h}^{-1}{\rm cm}^2{\rm g}^{-1}$ (Ueda et al. 2018).

[9]Baryonic dark matter is also considered, named MAssive Compact Halo Objects (MACHOs). They constitute massive baryonic objects which we cannot directly observed due to their lower level luminosity such as neutron stars, black holes, and white dwarfs. it is now admitted that MACHOs can not account for all the missing matter (Brandt 2016).

negative pressure: $\omega_{\rm DE} < -1/3$ (repulsive action), necessary to initiate cosmic acceleration (as detailed in sub-sections 1.3.1.3 .and 1.3.1.4 afterwards). The cosmological constant introduced into the field equations of General Relativity is the leading dark energy model, which mimics a homogeneous fluid with a fixed energy density over the cosmic time such as $p_\Lambda = -\rho_\Lambda$. Other alternative theories of dark energy have been proposed, including a cosmic field associated with inflation and quintessence models, with a low-energy scalar field. In fact, there is no reason to expect ω_Λ is constant and precisely equal to -1. For a review of the different dark energy cosmologies, see for example Bamba et al. (2012).

1.2 Cosmological structure formation

In the formalism developed above, we have made the approximation that the Universe is homogeneous. This is only valid for extremely large scales, i.e. $> 100\,$Mpc. For smaller scales, observations show a non-homogeneous matter distribution, as highlighted by mapping galaxies in the local Universe (see Figure 1.15). Galaxies are clearly not distributed uniformly in space, but rather spread in networks composed of voids, filaments and nodes. This raises the question: what cosmological model can explain the cosmic web observed today? In an attempt to answer this question, I will first explain where these primordial density fluctuations come from. Then, I will describe how the standard model of structure formation accounts for the growth of inhomogeneities. I will focus specifically on the growth of dark matter density fluctuations. This section is based on the lecture by Bernardeau (1998).

1.2.1 The origin of anisotropy in the density field - An inflationary scenario

The small anisotropies in the density field are expected to be generated during a phase of exponential expansion before the radiation dominated epoch, known as the Inflation (for more details see the review of Linde 2014). The inflationary scenario suggests that, shortly after the Big Bang, the Universe underwent an exponential expansion as supposed to be governed by a hypothetical scalar field. The inflation phase should lead to wash out any inhomogeneities. Indeed, it is a possible explanation of the cosmological principles, because all inhomogeneities were exponentially stretched during inflation. The apparent flatness of the Universe could also be explained with this scenario.

Only quantum fluctuations in the inflaton field would have survived to the Inflation. A visualisation of these primordial quantum anisotropies is available thanks to CMB observations, cf. figure 1.14. We will proceed to explain how these initial inflationary perturbations could have grown under the effect of gravity, leading to the large scale structure observed today.

1.2.2 The growth of inhomogeneities in the linear theory

First, let us start by explaining the growth of density inhomogeneity in the linear theory. The Newtonian approximation of a single flow is sufficient to describe the behaviour of structure formation, to the first order. This approximation only remains valid at the first stage of matter evolution, caused by gravitational instability. Over time, several flows with different velocities emerge and begin to mix ("shell crossing"): this occurs during the formation of non-linear structures. For a single flow, the time evolution following in a Newtonian approach is simply governed by fluid's dynamics equations:

$$\begin{cases} \text{Mass conservation} & \dfrac{\partial \rho}{\partial t} + \vec{\nabla}\,(\rho\ \vec{v}) = 0\,, \\ \text{Euler's equation} & \dfrac{\partial \vec{v}}{\partial t} + (\vec{v}.\vec{\nabla})\vec{v} = -\vec{\nabla}\phi\,, \\ \text{Poisson's equation} & \Delta\phi = 4\pi G\rho\,. \end{cases} \tag{1.12}$$

1.2.2.1 Linear perturbation theory

We now perturb this system of equations by a small density fluctuation δ, such that $\rho = \rho_0(1+\delta)$ where $\delta \ll 1$. The matter flow must be described in term of comoving quantities, such that our considered fluctuations evolve through an expanding Universe. We defined both its comoving coordinates $\vec{x}(t) = \vec{r}(t)/a(t)$ and its peculiar comoving velocity $\mathbf{u}(\mathbf{x}, t)$; the latter is the difference between the total velocity and the Hubble flow (the global expanding flow of the Universe). The fluid's dynamics equations then become:

$$\begin{cases} \dfrac{\partial \delta}{\partial t} + \dfrac{1}{a}\vec{\nabla}\left((1+\delta)\ \vec{u}\right) = 0\,, \\ \dfrac{\partial \vec{u}}{\partial t} + \dfrac{\dot{a}}{a}\vec{u} + \dfrac{1}{a}(\vec{u}.\vec{\nabla})\vec{u} = -\dfrac{1}{a}\vec{\nabla}\phi\,, \\ \Delta\phi = 4\pi G\rho_0 a^2\delta\,, \end{cases} \tag{1.13}$$

where ρ_0 is the mean matter density, defined such that $\rho_0 = \Omega_m\rho_{\text{crit}}$. By conserving only first order terms on this perturbative system, we obtain:

$$\begin{cases} \dot{\delta} + \dfrac{1}{a}\ \vec{\nabla}.\vec{u} = 0\,, \\ \ddot{\delta} + 2\dfrac{\dot{a}}{a}\dot{\delta}\ = 4\pi G\rho_0\delta\,. \end{cases} \tag{1.14}$$

The second equation, which describes the evolution of the density contrast, can be re-written as a function of the Hubble parameter:

$$\ddot{\delta} + 2H\dot{\delta} - \frac{3}{2}H^2\Omega_m(t)\delta = 0\,. \tag{1.15}$$

The solutions of this differential equation can be decomposed into two independent modes: one growing and one decreasing. The general solution is the sum of these modes:

$$\delta(\vec{x}, t) = D_+(t)\delta_+(\vec{x}, 0) + D_-(t)\delta_-(\vec{x}, 0)\,. \tag{1.16}$$

I will focus on the D_+ solution, as any perturbations on decaying mode tend to vanish and are therefore irrelevant to structure formation The space and time dependence can be separated here. Because $D_\pm$ is only time-dependant, the shape of perturbations does not change: only the amplitude of the density contrast changes. Therefore, in the linear regime of structure formation, density perturbations grow homogeneously. The evolution equation of density fluctuations 1.15, can be solved for any cosmological model, as the time evolution is governed by cosmological parameters and the scale factor. As demonstrated in Peebles (1980), the two modes can be expressed as depending on the Hubble parameter and the scale factor:

$$D_+(a) = H(a)\int_0^a \frac{da'}{(a'H(a'))^3}\,, \qquad D_-(t) = H(a)\,. \tag{1.17}$$

The structure growth factor D_+ can thus approximately be determined at each different epoch of the Universe:

- Radiation dominated epoch
  Before the equivalence between matter and radiation, one might distinguish two types of fluctuations which can be larger or smaller scales than the horizon size at the radiation dominated epoch, in which the horizon size grows as $D_h \propto a$. When perturbations enter the horizon, their wavelength is $\lambda \sim D_h(a_{\rm enter})$. For $\lambda > D_h(a_{\rm eq})$, the fluctuations do not enter into the horizon before the matter-radiation equivalence, and therefore grow continuously during this period. In contrast, smaller fluctuations which enter the horizon before the recombination have to be frozen until the matter dominated epoch. Indeed, it can be inferred from equation 1.17, that sub-horizon dark matter density fluctuations grow like $D_+ \propto a/a_{\rm eq}$.

- Matter dominated epoch
  This epoch can be approximated by considering as an Einstein-de-Sitter Universe in which the density fluctuations grow as $D_+ \propto a \propto t^{3/2}$.

1.2.2.2 Validity of the linear theory

The linear perturbation theory is valid to describe the structure formation on scales larger than a few Mpc. For structure below this scale, a non-linear description of fluid evolution is required. In addition, only perturbations smaller than the horizon size can be described in Newtonian approximation. For perturbations with super-horizon scales, the perturbative theory must be carried out in a fully-relativistic framework.

In the above mathematical development, we did not assume a pressure term in Euler's equation. Taking this additional term into account allows us to define the Jeans length, *i.e.* the minimal scale for perturbation where gravitation dominates over radiative pressure, and thus lead to gravitational instability. From these new considerations, one can show that prior to the decoupling between photons and baryons, the radiative pressure drives the evolution of the photon-baryons fluid. Thus, baryonic matter has to wait until recombination to collapse.

1.2.3 The growth of inhomogeneities in the non-linear theory

We now move on to density fluctuation with an higher amplitude $\delta \sim 1$, for which the linearisation of fluid dynamics equations no longer holds. To understand the global behaviour of the density field beyond the linear regime, the gravitational dynamics can be studied with different approaches - we now aim to review them.

1.2.3.1 The Zel'dovich approximation

An approximation of the non-linear growth of density fluctuations has been developed by Y. Zel'dovich (1970) (see also Shandarin & Zeldovich 1989). Let us begin by describing the dark matter fluid with a Lagrangian approach. The position of a particle at time t (Eulerian coordinates $\vec{x}$) can be given as a function of its initial positions (Lagrangian coordinates $\vec{q}$) and the displacement field $\vec{\psi}$:

$$\vec{x}(t) = \vec{q} + \vec{\psi}(\vec{q}, t)\,. \tag{1.18}$$

The Jacobian of this transformation is given as

$$J = \left|\frac{d\vec{x}}{d\vec{q}}\right| = \left|\delta_{ij} + \frac{\partial \psi_i}{\partial q_j}\right|, \tag{1.19}$$

and can be approximated to the first linear order as $J(\vec{q}, t) \sim 1 + \vec{\nabla}_q.\vec{\psi}(\vec{q}, t)$. By applying conservation of mass, one can relate the evolution of an infinitesimal volume element $d\vec{q}$ with a

density $\overline{\rho}$, to its evolved values $d\vec{x}$ and ρ:

$$\left|\frac{d\vec{x}}{d\vec{q}}\right| = \frac{\overline{\rho}}{\rho} \quad \Rightarrow \quad 1+\delta(\vec{q},t) = \left|\frac{d\vec{x}}{d\vec{q}}\right|^{-1} . \tag{1.20}$$

The Zel'dovich approximation assumes that the particle's motion is imposed by the initial acceleration field. Thus, particle trajectories are linear, and follow the direction of the initial force field. By re-writing the fluid's equation in terms of $\vec{\psi}$, we find that the displacement field in Zel'dovich approximation is:

$$\psi_{ZA}(\vec{q},t) = D_+(t)\psi_+(\vec{q}) \quad \Rightarrow \quad J = \left|\delta_{ij} + D_+ \frac{\partial \psi_i}{\partial q_j}\right| , \tag{1.21}$$

where $D_+(t)$ is the linear growth factor as described in the linear regime. One can express $\partial\psi_i^+/\partial q_j$ as a diagonal matrix with eigenvalues as $\lambda_1 > \lambda_2 > \lambda_3$. Therefore, the density contrast should evolve as:

$$1+\delta = ((1-\lambda_1 D_+)(1-\lambda_2 D_+)(1-\lambda_3 D_+))^{-1} . \tag{1.22}$$

It appears that the growth of the density contrast follows preferential directions (assuming $\lambda_1, \lambda_2, \lambda_3 > 0$). As D_+ increase with the cosmic time, we have $\lambda_1 D_+ \to 1$ meaning that the collapse is faster along one direction. Critical lines will form, and this first dense structure (walls), is known as the *Zel'dovich pancake*. The density contrast then starts to increase along the second preferential direction, characterised by λ_2. This two-dimensional contraction leads to the formation of filaments. Finally, as $\lambda_3 D_+ \to 1$, we end up with the formation of 3-D density peaks, the nodes of the cosmic web. As such, that the Zel'dovich approximation can roughly explain the filamentary structure observed in the Universe. The main limitation appears in these denser regions when shell crossing starts to occur, because the Zel'dovich approximation assumes non-interacting matter. Extensions of the Zel'dovich dynamics have been proposed, for example, by adding an artificial viscosity. We reach the so-called adhesion model (Gurbatov et al. 1989; Kofman et al. 1992; Bernardeau & Valageas 2010; Gurbatov et al. 2012).

1.2.3.2 The spherical collapse

Considering a unique, spherically-symmetric density excess allows some exact solutions of perturbation growth in the non-linear regime. This approximation constitutes a first description of the global behaviour of hierarchical structure formation, and describes the virialisation of massive objects (galaxies and galaxy clusters).

Let us consider a local spherical region with a physical radius $r(t)$, a density ρ and the mass contained in the sphere of radius r is $M(<r)$. The physical equation of motion is then simply:

$$\frac{d^2 r}{dt^2} = -\frac{GM(<r)}{r^2} . \tag{1.23}$$

In a closed Universe, this differential equation can be solved by the following parametric equations:

$$\frac{r}{r_{\rm ta}} = \frac{1}{2}(1-\cos\theta) , \qquad \frac{t}{t_{\rm ta}} = \frac{1}{\pi}(\theta - \sin\theta) . \tag{1.24}$$

As this perturbation is over-dense, it will expand until some maximum physical radius $r_{\rm ta}$ reached at time $t_{\rm ta}$, and then turn-around, by collapsing due to its self-gravity. The total energy of the system is conserved and can be written as:

$$E = \frac{1}{2}\left(\frac{dr}{dt}\right)^2 - \frac{GM}{r} . \tag{1.25}$$

When the kinetic energy becomes zero, the over-density starts to collapse at $r = r_{\rm ta}$ and $t = t_{\rm ta}$:

$$\theta = \pi\,, \qquad r_{\rm ta} = \frac{GM}{E}\,, \qquad t_{\rm ta} = \frac{\pi GM}{(-2E)^{3/2}}\,. \tag{1.26}$$

Following the evolution of this system, we find that the sphere collapses into a singularity at $r = 0$. In practice, the dark matter perturbation relaxes into a state of virial equilibrium when the total energy equals half the potential energy. In this case, r and t become:

$$\theta = 2\pi\,, \qquad r_{\rm vir} = \frac{r_{\rm ta}}{2}\,, \qquad t_{\rm vir} = 2t_{\rm ta}\,. \tag{1.27}$$

This collapsed object is in fact what we refer to as a dark matter halo.

For $\theta \ll 1$, the mean density inside the radius r can be Taylor-expanded:

$$\overline{\rho}(<r,t) = \frac{M(<r)}{4/3\pi r^3} \sim \frac{1}{6\pi G t^2}\left(1 + \frac{3}{20}\left(\frac{6\pi t}{t_{\rm ta}}\right)^{2/3} + ...\right)\,. \tag{1.28}$$

Thus, it can be compared to the linear density perturbation in an Einstein-de-Sitter universe (EdS) as $\rho = \rho_0(1+\delta)$. By identification we find that:

$$\delta_{\rm lin} \equiv \delta(t_{\rm vir}) = \frac{3}{20}(12\pi)^{2/3} = 1.686\,. \tag{1.29}$$

This means that an overdense sphere is considered collapsed when, in the linear theory, the density contrast δ reaches the value of 1.686. Therefore, when the density contrast of a fluctuation become higher than this limit, one should describe its evolution in the non-linear regime.

One can also define Δ as the density ratio between the mean density inside a specific region and the background density, both at a given time. An over-density is then virialised when $\rho(t) > \Delta_{\rm vir}\overline{\rho}(t)$:

$$\Delta_{\rm vir} = \frac{\overline{\rho}(<r_{\rm vir}, t_{\rm vir})}{\overline{\rho}_(t_{\rm vir})} = 18\pi^2 \sim 178\,. \tag{1.30}$$

This is a good criterion to characterise collapsed objects. Even if these conclusions suppose an EdS Universe, these values do not change drastically for other cosmological parameters. The exact solution of the spherical collapse, given the density contrast as a function of time is developed in Appendix A.2 for the EdS model. It shows that the evolution of a perturbation is governed by the initial overdensity.

1.2.3.3 The Press-Schechter mass function

Having defined haloes as collapsed spherical objects, we now determine the abundance of dark matter haloes in our Universe. To do so, we present a simple approach known as the Press-Schechter formalism (Press & Schechter 1974). It is a combination of the spherical collapse model and the linear theory of structure formation. First, let us assign a length scale to a mass scale in spherical approximation, as:

$$R(M) = \left(\frac{3M}{4\pi\rho_0}\right)^{1/3}\,. \tag{1.31}$$

We can consider a smoothed density contrast δ_R at some mass or length scale by filtering density fluctuations with a window function W_R, such that:

$$\delta_R(\vec{x}) = \int \delta(\vec{x'}) W_R(|\vec{x} - \vec{x'}|)\; d\vec{x'}\,. \tag{1.32}$$

Assuming that the smoothed density field is a Gaussian random field, its probability distribution function can be written as:

$$p\left(\delta_R\right) = \frac{1}{\sqrt{2\pi\sigma_R^2}} \exp\left[\frac{{\delta_R}^2}{2\sigma_R^2}\right], \tag{1.33}$$

where $\sigma_R \equiv \sigma_M$ is the variance of the smoothed field. Previously, we have seen that a region collapses if its density contrast is $\delta_{\rm lin} > \delta_c$. We therefore assume that the fraction of objects which have a mass larger than M is equal to the probability of having a point with a density larger than the linear critical density. The fraction of mass in objects larger than M is then:

$$f(>M) = \int_{\delta_c}^{\infty} p\left(\delta_R\right) d\delta\,, \tag{1.34}$$

$$= \frac{1}{2} - \frac{1}{2}\mathrm{erf}\left(\frac{\delta_c}{\sigma_R\sqrt{2}}\right). \tag{1.35}$$

We can finally derive the number density of objects of a given mass M as:

$$\frac{d^2n}{dMdV} = \frac{2\rho_0}{M}\left|\frac{\partial f}{\partial M}\right|, \tag{1.36}$$

$$= \sqrt{\frac{2}{\pi}}\frac{\delta_c\rho_0}{M}\left|\frac{d\ln\sigma_M}{dM}\right|\exp\left(-\frac{\delta_c^2}{2\sigma_M^2}\right). \tag{1.37}$$

This is the Press-Schechter mass function, an estimation of the number of collapsed dark matter haloes per unit of mass and comoving volume. Note that we have added an *ad hoc* factor of 2 to obtain the correct normalisation. It is due to a failure of Press-Schechter formalism: only half of the mass is accounted for (Mo & White 2002).

What of the evolution of the halo mass function over the cosmic time? The answer is not trivial because the time dependance is hidden in σ_R and δ_c. Nevertheless,using the linear perturbation theory, one can assume that the variance of the density contrast evolves as $\sigma_R(z) \propto \sigma_R(z = 0)D_+(z)$. Following this assumption, the mass function evolves as a power law $dn/dM \propto M^{-2}$ for low mass objects. It is congruent with a hierarchical structure formation scenario, as low-mass haloes tend to merge in higher massive object. Finally, an more realistic formulation of the halo mass function is provided by Sheth & Tormen (2002), who consider an ellipsoidal collapse. Figure 1.2 shows the typical behaviour of the halo mass function, and compares results from the Press-Schechter and the Sheth-Tormen formulations, with N-body simulations (*cf* section 1.4).

1.2.3.4 The highly non-linear regime

At later times, for density perturbations with $\delta > 1$, two paths can be considered to model structure formation. The first, fully analytical, uses cosmological perturbation theory in order to go beyond linear approximation and explain mode couplings. This approach succeeds at describing the density field statistics (Bernardeau et al. 2002; Bernardeau 2013). The second method to compute the non-linear gravitational dynamics is to use numerical simulations. As explained in detail in section 1.4, N-body codes discretise the density field into a large number of particles. By this method, they can reproduce structure formation from initial conditions to the present time, and provide robust predictions which can in turn to be compared with observational results.

1.2.4 The structure of dark matter haloes

Dark matter haloes can be defined as highly non-linear self-gravitating systems formed by the collapse of primordial density fluctuations. Nevertheless, the properties of such objects are still

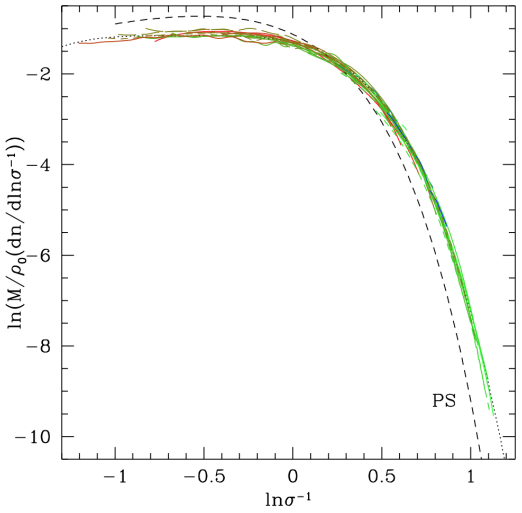

Figure 1.2 – The halo mass function in numerical simulations of the Virgo collaboration. The Press-Schechter halo mass function (dashed line) is compared to a fitting formula similar to Sheth-Tormen (dotted line). This figure is from Jenkins et al. (2001).

not well understood in detail. As the nature of dark matter remains unknown, we lack information to correctly describe in detail dark haloes. I will present here a few broadly admitted features of dark haloes in accordance with the ΛCDM model. Their properties are mainly predicted and/or validated via N-body simulations (as described section 1.4), and might change by changing the nature of the dark matter.

1.2.4.1 Halo density profile

The properties of dark matter haloes have been extensively explored and calibrated with high-resolution N-body simulations. One of the main feature is their radial density profile. Because the spherically-averaged density profile present a strong similar shape for all the haloes, independently of their mass and the redshift, one can talk about a universal profile.

One of the most famous radial density models is the Navarro-Frenk-White (NFW) profile Navarro et al. (1996b, 1997):

$$\frac{\rho(r)}{\rho_{\rm crit}} = \frac{\delta_c}{(r/r_s)(1+r/r_s)^2}\,. \tag{1.38}$$

There are two free parameters in the function above: the first one is the characteristic dimensionless density δ_c and the second is the characteristic radius r_s. Here, $\rho_{\rm crit}$ is the critical density of the Universe.

In the NFW profile, the scale radius r_s delimits the slope change: the central part of the halo ($r \ll r_s$) appears peaked with $\rho(r) \propto r^{-1}$, whereas the density profile in external regions ($r \gg r_s$) decreases as $\rho(r) \propto r^{-3}$. Because the observational evidence of dark matter haloes is revealed by the dynamics of satellites or stars (cf section 1.3), it is common to relate the radial density profile to it circular velocity:

$$v_{\rm rot} = \left(\frac{GM(<r)}{r}\right)^{1/2} \Rightarrow \begin{cases} \rho(r) \propto r^{-1} & v_{\rm rot} \propto r^{1/2} \qquad \text{Cusp profile}\,, \\ \rho(r) \propto r^{-2} & v_{\rm rot} \propto ct \qquad \text{Isothermal profile}\,. \end{cases} \tag{1.39}$$

These two different mean velocity profiles are shown in figure 1.20 and compared to observational measurements. We introduce here a simplest model: the isothermal profile[10]. We see that the different slopes of the density profile strongly affect the velocity profile in the central regions.

[10]The density distribution for a singular isothermal sphere profile (SIS) is $\rho(r) = \frac{\sigma_V^2}{2\pi G r^2}$, where σ_V is the velocity dispersion

Let us now introduce the notion of virial radius, which serves as the demarcation line between a halo's interior (where it is roughly in dynamical equilibrium) and regions external to it, where accretion occurs. Mathematically, one can define the virial radius as the radius of a sphere centred on the halo, where the spherical density inside equals $\Delta_{\rm vir}\rho_{\rm crit}$:

$$\Delta_{\rm vir}\rho_{\rm crit} = \frac{M(< r_{\rm vir})}{4/3\pi r_{\rm vir}^3}\,. \tag{1.40}$$

As explained in section 1.2.3.2, for a spherical collapse, $\Delta_{\rm vir} = 178$ is the theoretical value for an Einstein-de-Sitter model. An exact formulation of $\Delta_{\rm vir}$, expressed as a function of the cosmological parameters, is presented by Bryan & Norman (1998). Note that, the overdensity parameter $\Delta_{\rm vir}$ is typically approximated at the value 200, under which approximation the halo mass and virial radius become M_{200}, r_{200}.

Plotting the density profiles of a large sample of simulated haloes highlights the fact that low-mass haloes tend to be more peaked in central region compared to massive haloes. It is for this reason that scale parameter r_s is compared to the virial radius to characterise the concentration of the halo: $c = r_{\rm vir}/r_s$. Finally, one can link the characteristic density δ_c to the concentration c by examining $\rho/\rho_{\rm crit}$ as a function of $r/r_{\rm vir}$. In so doing, we see that the halo mass density profile can be described with a single free parameter c, which depends on the halo mass. The halo concentration distributions are well-known through N-body simulations (Bullock et al. 2001; Neto et al. 2007; Duffy et al. 2008; Giocoli et al. 2012; Ludlow et al. 2013; Klypin et al. 2016). With such simulations, an anti-correlation between c and M was found: this is an expected result in the hierarchical clustering scenario. As illustrated figure 1.3, this relation is quite well-described by a power law: $c \propto M^{-0.1}$ (Neto et al. 2007). Comparing this prediction and observational results is crucial if we are to improve our understanding of the hierarchical build-up of virialised dark matter structures.

In addition to the NFW profile, other models of the radial density profile have been proposed in the literature (Hernquist 1990; Cole & Lacey 1996; Moore 1999; Jing & Suto 2002; Merritt et al. 2006). Considering the logarithmic slope of the density profile $\gamma = d\ln\rho/dr$ one can write the Einasto profile (Einasto 1965; Einasto et al. 1984) as a radial power law: $\gamma \propto r^{\alpha}$. Indeed, with advances in high-resolution simulations, the internal slope and its dependence to the halo mass are still debated (Jing & Suto 2000; Ricotti 2003; Navarro et al. 2004; Diemand et al. 2005; Graham et al. 2006). As for the external regions, the outer density profiles seems to be strongly influenced by the accretion history of haloes and their environment (Diemer & Kravtsov 2014).

Finally, alternative models of dark matter, such as the warm dark matter (Bode et al. 2001) or the self-interacting dark matter (Spergel & Steinhardt 2000b), tend to predict a shallower slope of the density profile in the halo's center, and even produce a constant density core, whose size might depend on the self interaction cross-section or temperature, for instance. For example, figure 1.4 shows the impact of warm dark matter (WDM) on the density profile (and thus on concentration parameter) for low mass DM haloes (Bose et al. 2016; Ludlow et al. 2016). The WDM haloes present lower central densities than their CDM counterparts, and it difference increases as halo mass decreases.

1.2.4.2 Halo Shape

An other important feature of dark matter haloes is their 3-dimensional shape, which ought to be triaxial according to the CDM model (Frenk et al. 1988). Indeed, the hierarchical formation scenario supposes that low-mass haloes were first formed by anisotropic collapse, and have since grown by accreting the surrounding matter in preferential directions and via halo mergers (Kauffmann & White 1993).

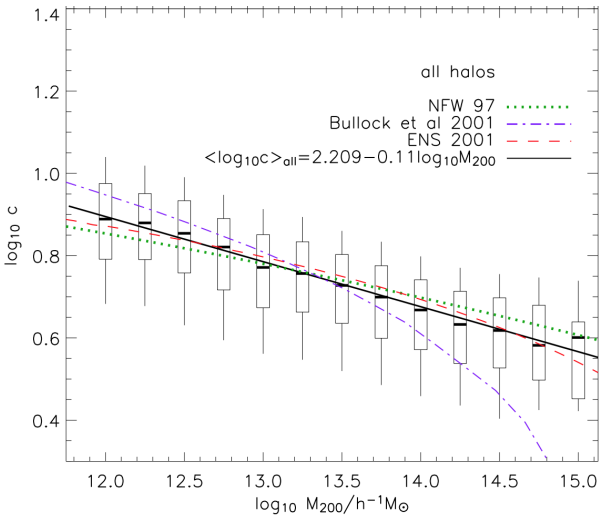

Figure 1.3 – Typical numerical prediction for the mass-concentration relation for DM haloes at $z = 0$ (Neto et al. 2007). The statistics of halo concentrations is computed from the Millennium Simulation. The average halo concentration apprears to decrease monotonically with mass such as it is well fitted by a power law. The DM halo model from Bullock et al. (2001) is in disagreement with the simulation results presented here, which agree better with NFW predictions.

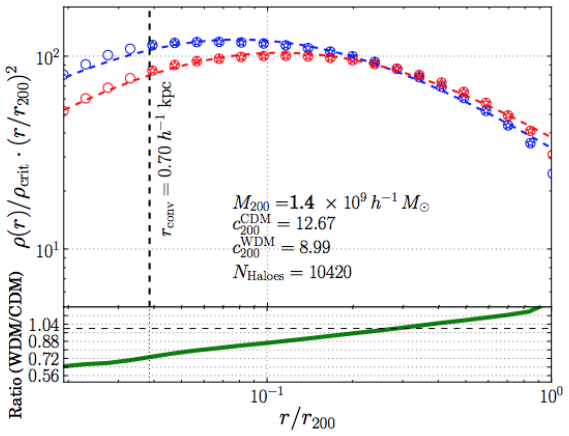

Figure 1.4 – Stacked spherically-averaged density profiles for simulated CDM (blue) and WDM (red) haloes (Bose et al. 2016). The concentrations of WDM haloes are lower than those of CDM haloes for a same halo mass bin.

The triaxiality of haloes have been characterised using N-body simulations, and its evolution as a function of other halo properties such as the halo mass, redshift, and the time of formation (Dubinski & Carlberg 1991; Warren et al. 1992; Jing & Suto 2002; Allgood et al. 2006; Hayashi et al. 2007; Faltenbacher & White 2010; Schneider et al. 2012; Despali et al. 2014) has been explored.

To do so, we model the halo's inertia tensor and the triaxial halo axis lengths $a \leq b \leq c$. The ellipsoidal shape can be characterised by different parameters: by the ratio of the minor to the major axis $s \equiv a/c$ and the ratio of the intermediate to the major $q \equiv b/c$, by the triaxiality parameter $T \equiv (a^2 - b^2)/(a^2 - c^2)$, or either by the ellipticity e and the prolateness p. Studying the distribution of these shape parameters highlights the averaged triaxial shape of haloes. They appear to be correlated with the halo mass (at a given redshift), such that massive haloes are less spherical than smaller ones. As well, considering the same halo mass range over the cosmic time, halo shape tends to be more elliptical at higher redshift.

To correctly quantify the evolution of halo properties, we must consider the merger history of haloes. In other words, comparing haloes at different times without considering the evolution of our halo sample can induce what is known as progenitor bias (e.g. Croton et al. 2007). Since haloes grow by successive mergers, it is possible to reconstruct their merger history (merger tree) and examine the main progenitor of a final system at a given time - this main progenitor is the halo which provides the largest mass contribution.

Morphological evolution is explored by calibrating the relation between halo shape and the halo formation time. Despali et al. (2014) found that older collapsed systems are more spherical than the ones who collapsed more recently. Indeed, massive systems formed at later times - usually through major mergers of smaller systems - still grow via anisotropic matter accretion along the filamentary structure. Their residual shapes are thus elongated and influenced by their initial environment. In contrast, small haloes, formed at earlier times, have relaxed, and thus appear rounder and more concentrated. This phenomenon is illustrated in figure 1.5.

The characterisation of asymmetries in the mass distribution, is also important to investigate the dark matter nature and to refine our understanding on the growth of the dark structures embedded in the cosmic web. Indeed, its nature influences the shape of dark haloes: weakly self-interacting dark matter tend to provide rounder shape (Yoshida et al. 2000; Peter et al. 2013). As shown figure 1.6, we observe that self-interacting dark matter haloes are rounder than CDM haloes (Vogelsberger et al. 2012).

1.2.4.3 Halo substructure

Zooming into N-body simulation reveals a large amount of dark matter substructure within dark matter haloes. This is shown in figure 1.6. These structures, which lie within the virial radius of the parent halo, are sub-haloes.

In theoretical terms, these small-scale structures are understood as small clumps of dark matter which have been accreted into a larger one. Thus, they became small structures orbiting within the potential well of their host. Tidal forces from the larger halo and dynamical friction, can destroy these self-bound entities over time: they do so by dissipating their mass, their energy and their angular momentum.

In order to improve our understanding of subhalo populations and validate a more global picture, their properties have been modeled into dark matter simulations (Tormen et al. 1998; Moore et al. 1999a; Klypin et al. 1999; Ghigna et al. 2000; Stoehr et al. 2002; Hayashi et al. 2003; Gao et al. 2004; Zentner et al. 2005; Diemand et al. 2008; Springel et al. 2008a; Giocoli et al. 2010; Klypin et al. 2011; Gao et al. 2011). Such studies require a very high level of resolution to properly distinguish and model sub-structures in dark matter haloes. However, numerical predictions of sub-halo properties are still under debate (e.g. possibility of bias introduced by

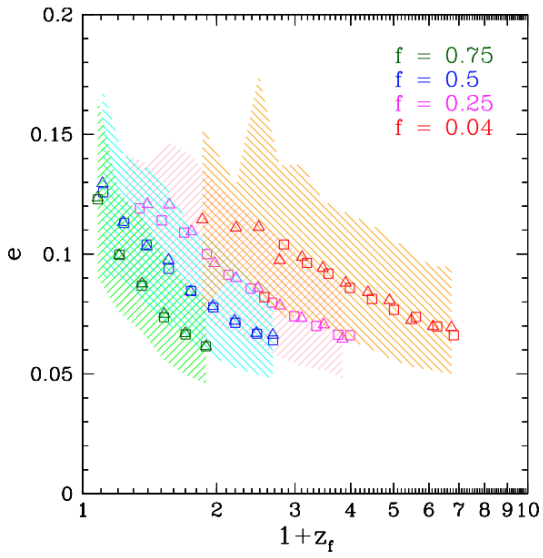

Figure 1.5 – Relation between the ellipticity of haloes at $z = 0$, and the formation redshift $z_{\rm f}$. One can define the formation redshift such as the redshift where the main halo progenitor assembles a fraction f of its mass. It apprears that haloes formed at earlier cosmic time (or with a larger $z_{\rm f}$) are now less elliptical, than haloes formed at later time. Credit to Despali et al. (2014).

numerical artefacts van den Bosch et al. 2018). A list of structures obtained from numerical simulations which are generally agreed upon to be sub-halo features is listed below:

- The dark matter clumps appear to constitute about $5\% - 15\%$ of the total mass of the host halo.
- The subhalo mass function for an individual halo converges quite well to a power-law, $dn_{sub}/dm_{sub} \propto m_{sub}^{-\alpha}$ with $\alpha \sim 1.8$, independent of the host halo's mass or redshift.
- The concentration of haloes is anti-correlated with it fraction of substructures, meaning that for a given mass, denser haloes have lesser substructures.
- Subhaloes with masses greater than a few percent relative to the host halo's mass tend to merge rapidly, as opposed to low-mass satellites which tend to survive longer. This is a consequence of dynamical friction.
- The sub-structure density profiles appear to have softer cores than both their host and independent haloes with the same mass.
- The radial distribution of sub-haloes within the parent halo roughly follows the radial density profile of the host halo, but is significantly less concentrated at the center.

Note that warm dark matter drastically reduces the abundance of low-mass sub-haloes (Lovell et al. 2014). As for self-interacting dark matter, it tends to produce less sub-haloes and with a constant density cores (Burkert 2000; Vogelsberger et al. 2012; Rocha et al. 2013). As shown in figure1.6, the self-interacting dark matter significantly affect the structure and abundance of subhaloes.

Because sub-haloes can be the host of galactic systems embedded in large structures (such as a galaxy cluster), the properties of its dark satellites are essential for the field of galaxy formation and evolution. Indeed, the evolution of a satellite galaxy is directly influenced by their host dark matter sub-haloes (impact on parameters such as their orbit, velocity, mass, etc). The impact of galaxies on sub-halo structure formation and evolution is beyond the scope of this introduction, however, and will be discussed when relevant to hydrodynamical numerical simulations.

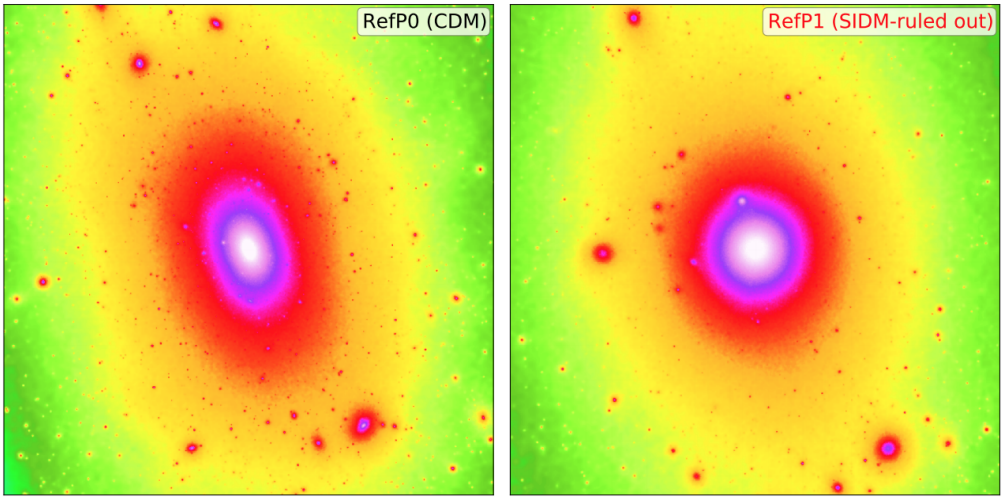

Figure 1.6 – The projected DM density around a massive system. On the left is the CDM model applied in numerical simulation; on the right, an alternative DM model (Self-Interacting Dark Matter). We observe that changing the dark matter nature can drastically influence the abundance of dark matter clumps and the halo shape. Image credit: Vogelsberger et al. (2012).

1.2.5 Galaxies within dark matter haloes

At the center on the density peaks, the dark matter has collapsed into non-linear objects (DM haloes), which enable galaxy formation. Baryons has sunk into gravitational potential wells of dark matter after the recombination, and cooled to form the first stars (White & Rees 1978). Therefore, the formation of galaxies has occurred through highly non-linear processes which include both hierachical clustering of the dark matter, and the dissipative physics of baryons (cooling and fragmentation of the gas). One can define a galaxy as a gravitationally bound system composed of stars, gas, dust and surrounded by a DM halo. Our understanding of structure formation and evolution at this scale remains incomplete, and poses significant challenges in the modern cosmology.

1.2.5.1 Galaxy formation and evolution: accretion flow and merger events

Observations of galaxies provide a wide variety of galaxies in terms of color, size and shape at all times in the Universe. One natural first approach is to classify them depending of their morphology: this is the so-called Hubble sequence (Hubble 1936), as illustrated in figure 1.7. It segregates morphological types from the ellipticals to spirals and irregular galaxies.

Spiral galaxies (with or without a bar) contained a central bulge, a stellar disk and an interstellar medium (gas and dust). In the ΛCDM paradigm, disc galaxies (*late-type* galaxies[11]) are supposed to be formed, and to growth by cosmic gas accretion. Anisotropic accretion of cosmic cold gas stream leads to build up gas disc structure at the center of DM haloes[12], which induced *in situ* star formation (see *e.g.*, Kereš et al. 2005; Dekel et al. 2009). In this rotation-dominated

[11]This nomenclature of "early-type" and "late-type" galaxies comes from the past wrong understanding of galaxy evolution on the Hubble sequence: from elliptical to spiral galaxies (Hubble 1936).

[12]The gas infalls along preferential direction form a gas disc (galactic spin) around the spheroidal galaxy previously created by monolithic collapse of merging gas clouds (Fall & Efstathiou 1980; Mo et al. 1998).

system, a small fraction (around 2%[13]) of the gas is converted into stars. Cosmic gas inflow forms a corona of hot gas in the halo (Birnboim & Dekel 2003), and as gas cooling, it supplies the cold gas reservoir of the galaxy. Young massive stars are thus formed on the spirals arms, which in result appear mainly blue.

In contrast, elliptical (*early-type*) galaxies have smooth ellipsoidal shape. They are supposed to be predominantly formed by hierarchical clustering, *i.e.* through repeated galaxy merging events (Toomre 1977; White & Frenk 1991; Cole et al. 2000; De Lucia et al. 2006). From violent major merger[14] (or repeated minor events), the discs of galaxies are destroyed[15] and form a spheroidal slowly-rotating remnant. During merging process, the star formation can first be triggered, and rapidly consume the gas reservoir(Mihos & Hernquist 1996; Hopkins et al. 2006). Finally, without inflowing materials (strangulation) or cooling of the gas, a reddening of the merged galaxy is induced by increasing the age and metallicity of stars (see., e.g. Faber et al. 1992; Ferreras et al. 1999). Note that the spheroidal remnant can re-build a disc if the merger is wet or more gas is acquired later (Baugh et al. 1996; Moster et al. 2010a).

Below, we draw the global picture of the bimodality observed in galaxy properties: from disc-dominated galaxies formed by cosmic gas accretion (predominantly blue and star-forming) to spheroid-dominated galaxies formed by merger events (largely red with old stellar populations) (e.g. (Baldry et al. 2004; Dekel & Birnboim 2006). This bimodality is shown in figure 1.8, in the color-mass diagram of observed galaxies, and by separating the early- and late- type galaxies Schawinski et al. (2014). This bimodality is not perfect: galaxies in transition phase from spirals to spheroids, from star-forming to passive, are identified in the "green valley". In fact, red spirals and blue ellipticals are present (in small minority) in the sky. Galaxy evolution is still debated through the crucial question: What physical mechanisms regulate star formation over the cosmic time? How well are galaxy formation models able to reproduce the observed galaxy properties[16] and scaling relations[17]?

1.2.5.2 Galaxy-halo connection

By comparing the mass function of dark matter halo and the galaxy stellar mass function, we observed that low- and high- massive haloes present a deficit in stellar mass (see *e.g.* Cole et al. 2001; Yang et al. 2003; Behroozi et al. 2010a; Moster et al. 2010b). This corresponds to an inefficient star formation at these two mass ranges, as illustrated figure 1.9. The regulation of star formation efficiency in galaxies is not fully understood, but can be explained by considering complex outflow processes.

The feedback of supernovae and strong stellar-driven winds seem to be the dominant processes for switching off the star formation in low-mass galaxies (Dekel & Silk 1986; Larson 1974). In fact, supernovae explosions heat the interstellar medium by incorporating thermal and kinetic energy, which reduce further the creation of stars. In addition, this mechanism tend to remove a

[13] the Schmidt-Kennicutt law establishes an empirical relation between gas surface density and star formation rate per unit surface such as the $\Sigma_{SFR} \propto (\Sigma_{gas})^n$ (Schmidt 1959). Focus on nearby spiral galaxies, Kennicutt (1998) estimated that $n = 1.4 \pm 0.15$.

[14] We distinguish major merger in which the two merger galaxies have similar size, to minor merger in which the smaller galaxy is accreted onto the larger one.

[15] Merger event is a natural dissipative phenomenon which transform a rotation-dominated to dispersion-dominated system.

[16] such as distribution function of the stellar mass, star formation rate of galaxies and the proportion of disk-dominated and spheroid-dominated galaxies.

[17] such as radial size, density, internal velocity,.. of galaxies

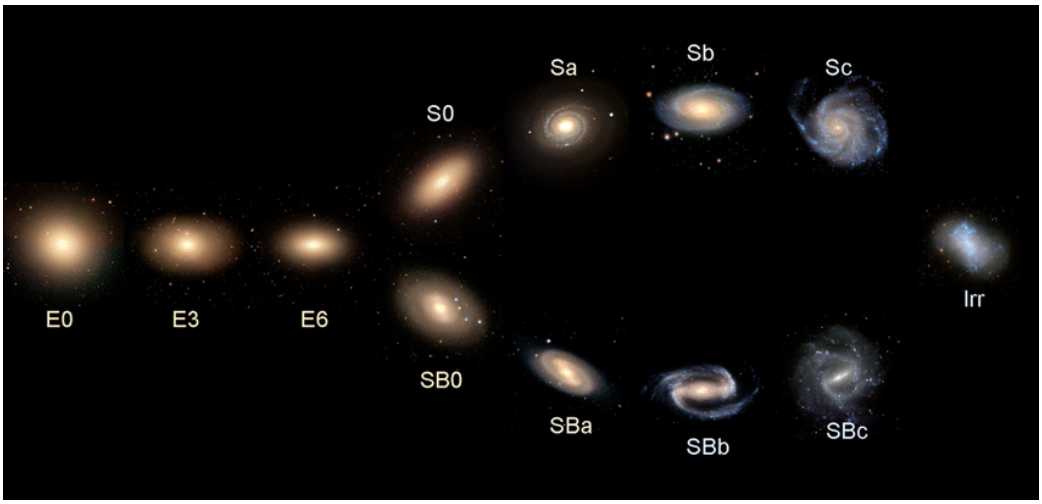

Figure 1.7 – The Hubble Sequence. Spiral galaxies are denoted S and spiral with a bar are indicated by SB. The second notation a, b, c refer respectively to tightly, less tightly, and loosely wound spiral arms. Denoted by the letter E, we have the elliptical galaxies. The following number represents the degree of ellipticity, such as $E6$ denotes a ellipsoidal galaxy with $e = 0.6$. Credit to Cui Y. et al (2016).

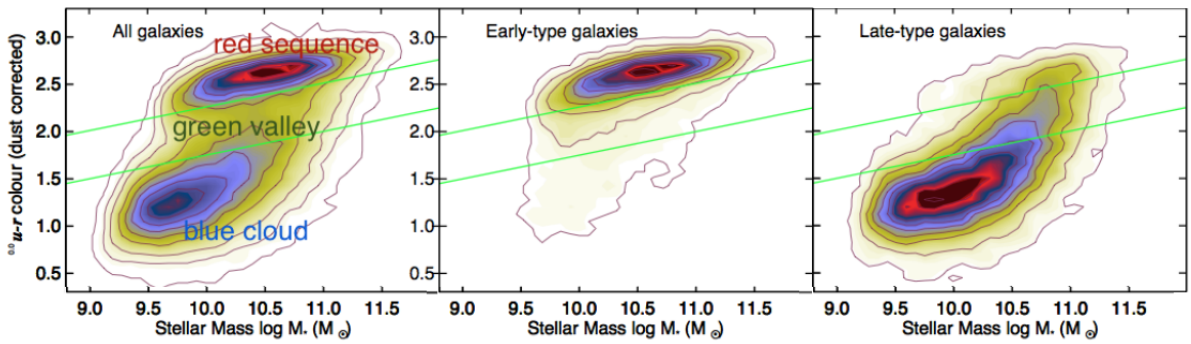

Figure 1.8 – The colour-mass diagram of galaxies, split by shape: on the right all the galaxies, at the middle the ellipticals (or early-types), and at the left the spirals (or late-types). Credit to Schawinski et al. (2014).

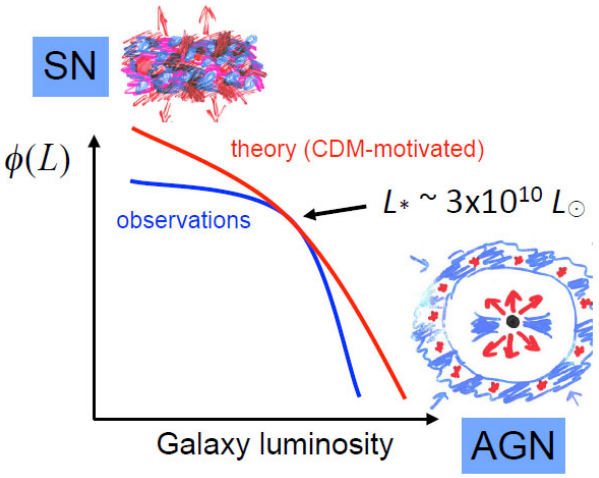

Figure 1.9 – Schematic view of the galaxy luminosity function (an histogram of the luminosity of galaxies), a proxy of the mass function. The dark matter halo mass function expect from the ΛCDM model is presented in blue, whereas observational results lead to the galaxy mass function shows in red. For low and high massive galaxies two different mechanisms (SN and AGN feedbacks) are proposed to explain this discrepancy between these two mass functions. Credit to (Silk & Mamon 2012).

consistent fraction of the gas, preferentially in small massive galaxies.

At high masses, the inefficient star formation in galaxies can be explained by considering the feedback from Active Galactic Nuclei (AGN) (Silk & Rees 1998; Croton et al. 2006a). Massive galaxies may contain a central supermassive black hole (for observational evidence, see *e.g.* Kormendy & Ho 2013), which may eject a gas fraction of the inter-stellar medium, and heat the halo gas (see Fabian 2012; Heckman & Best 2014, for recent reviews). The efficiency of AGN feedback in suppressing the *in situ* star formation in the galaxy remains nevertheless uncertain. To improve our understanding on the small-scale physical processes acting inside dark matter haloes, the physics of galaxy formation is now explored by using high resolution hydrodynamical cosmological simulations (as discussed in section 1.4).

Investigating on the galaxy-dark halo connection is fundamental to refine our understanding on the link between the luminous properties of galaxies and the dark matter haloes in which they reside. To explore this relation, two different parametric models are currently used: either sub-halo abundance matching (SHAM) models (Conroy et al. 2006; Behroozi et al. 2010b, 2013; Moster et al. 2010b, 2013, 2018), or Halo Occupation Distribution (HOD) models (Berlind & Weinberg 2002; Zheng et al. 2005; Leauthaud et al. 2011).

According to the ΛCDM model, all galaxies are assumed to be formed and to live in dark matter haloes and sub-haloes. The SHAM models connect galaxies to sub-haloes, by assuming that there is only one galaxy per dark matter halo. In fact, one halo can contain more than one galaxy: a central and few *satellites* (those hosted by sub-haloes). This distinction is considered by HOD models which assign at each halo the expected number of central and satellite galaxies. Therefore, it contains additional free parameters, and requires information on the galaxy clustering (Coupon et al. 2015).

Both techniques assume that the statistical properties of the galaxies (such as the luminosity or stellar mass function) are fully determined by the dark matter (sub)halo mass. Notice that it assumes that the above discussed physical processes are not modelled here.

As illustrated in figure 1.10, HOD and SHAM models are used to estimate the stellar-to-halo mass relationship (SHMR) and its evolution in redshift (see *e.g.* Behroozi et al. 2010a; Leauthaud et al. 2012). These phenomenological models provide a powerful tool to inform galaxy evolution models, by determining, for example, the characteristic halo mass where the star formation is the most efficient (*i.e.* where M_*/M_h is maximized).

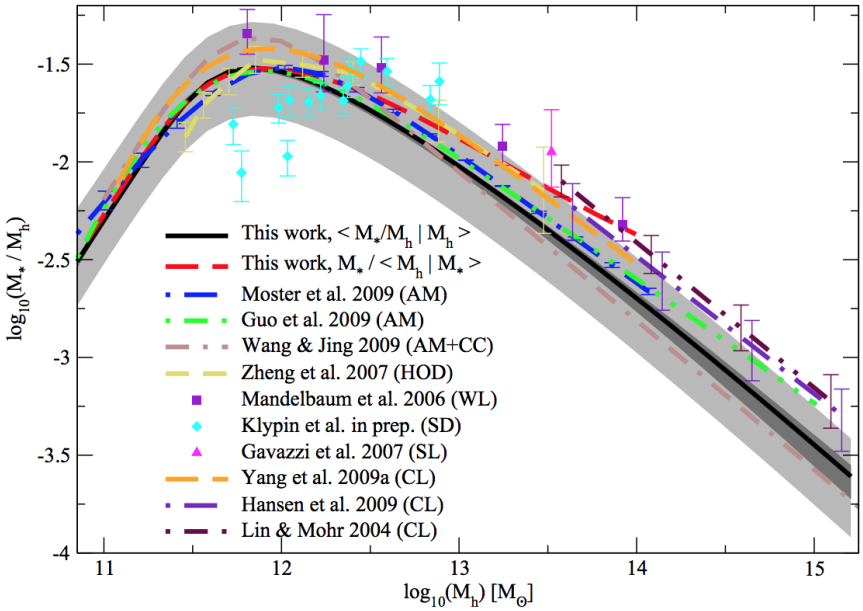

Figure 1.10 – The figure comes from Behroozi et al. (2010a). The ratio between stellar mass and halo mass M_*/M_h is presented as a function of the halo mass. Observational results and different semi-analytical models are represented.

1.2.5.3 Large scale environment and galaxy clusters

In addition, as galaxies form and evolve in the cosmic web, one might ask if their properties are shaped by their host halo's environment (*i.e.* their location in the cosmic web). This relation between large scale environment and galaxy properties is currently being extensively investigated through hydrodynamical cosmological simulations, theoretical models and galaxy surveys.

I will begin with a brief overview of galaxy clusters, which are massive gravitationally-bound structures with a typical size of few Mpc and a mass range of $\sim 10^{14} - 10^{15} M_\odot$. Galaxy clusters are located at the nodes of the cosmic web, and grow by accreting matter along cosmic filaments. They gather from hundreds to thousands of galaxies, and contain hot diffuse gas and large amounts of dark matter. The hot, nearly fully-ionized plasma is in fact the main baryonic material in galaxy clusters. It is called the Intra-Cluster Medium (ICM) and emits in X-ray band via thermal Bremsstrahlung (typically $T \sim 10^7 - 10^8$ K[18]). For a review on X-ray emission of galaxy clusters see *e.g.* Peterson & Fabian (2006).

Early observations show that cluster galaxies evolve differently from isolated galaxies (Gunn & Gott 1972; Oemler 1974; Dressler 1980). Blue galaxies are relatively dominant in low density environments, whereas dense environments are mostly populated with red galaxies(Hogg et al. 2003; Baldry et al. 2006; Peng et al. 2010; Tomczak et al. 2017). Different physical processes exist in the literature to explain the quenching of star-forming galaxies inside cluster's dense environment, and this is a topic still under debate: Ram pressure stripping by the intra-cluster medium (Gunn & Gott 1972; Abadi et al. 1999), tidal stripping by the main cluster potential (Byrd & Valtonen 1990), galaxy harassment (Moore et al. 1996)... Finally, one can ask if the proportion of passive galaxies already dominates the infalling material accretion? What is the fraction of red galaxies depending of the cluster distance?

Currently, the question of the environment's impact has been extended to the LSS by studying

[18]The high temperature is created by the deep dark matter gravitational potential.

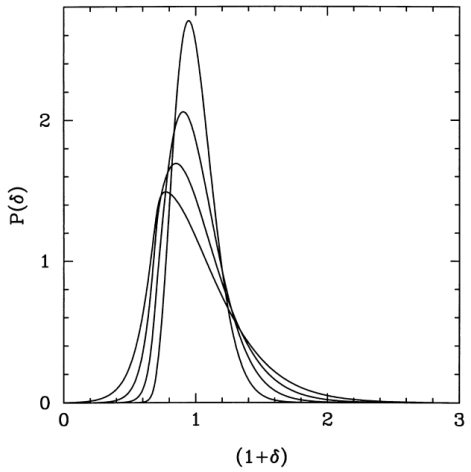

Figure 1.11 – The evolution of the one-point distribution function, $P(\delta)$, calculated from second-order perturbation theory. Image credit: Taylor & Watts (2000).

the variations of galaxy properties (color, mass, and type) as a function of their distance to filaments and to cosmic nodes. From observations and hydrodynamical simulations, it appears that massive (and/or passive) galaxies are on average located closer to cosmic filaments and walls, compare to the less massive (and/or star-forming) ones (see *e.g.* Laigle et al. 2018; Kraljic et al. 2018a). It can be explained by considering the anisotropic tides of the cosmic web which influence the assembly history of galaxies, and hence, their properties (Codis et al. 2012a; Kraljic et al. 2018b). It appears that galaxies keep a memory of the cosmic flows from which they are formed and evolved. Nevertheless, the relative importance of major/minor mergers, large-scale environment, and baryonic physics in galaxy evolution over the cosmic time remain still debated.

1.2.6 The statistics of the density field

Statistics of the density field have been a fertile area of study over the last decades, because they encode crucial information about initial conditions and their dynamical evolution. We now show how non-linear structure formation affects the statistics of the density field.

1.2.6.1 The probability distribution of the density contrast

The one-point statistics of the density field are fully encoded in its probability distribution function by definition. According to the ΛCDM model, the primordial density contrast is expected to be a Gaussian random field. As cosmic time increases, the probability distribution function of the density will be affected by the emergence of non-linear structures. Indeed, in the linear regime of structure formation, we expect an homogeneous growth of the structure as: $\delta(\vec{x}, a) = D_+(a)\delta_i(\vec{x})$. As well, the decoupling between time and space is also verified in the Fourier space $\widehat{\delta}(\vec{k}, a) = D_+(a)\widehat{\delta}_i(\vec{k})$. Following these homogeneous and linear properties, gaussianity is conserved in the linear regime. Nevertheless, the separation fails in non-linear structure formation, because the growth of density fluctuation becomes scale-dependant. Thus, a coupling of k-modes is expected in Fourier space, *i.e.* $\widehat{\delta}(\vec{k}, a) = D_+(a, \vec{k})\widehat{\delta}_i(\vec{k})$. As modes are not longer independent, they can be superposed: the statistics of the density contrast thus become non-Gaussian (Bernardeau & Kofman 1995; Scoccimarro & Frieman 1996; Bernardeau et al. 2002, 2014). This effect is illustrated in figure 1.11, where the initial density contrast is Gaussian, but by making it evolve in the non-linear regime the non-Gaussianities increase with time. These results are analytical (Taylor & Watts 2000), and the same behaviour can be observed with N-body simulations. As cosmic time evolves, the probability distribution function becomes asymmetric, reflecting the voids expanding and peaks contracting.

1.2.6.2 The two-point statistics

The non-linear evolution of the density field is not only encoded in the one-point statistic but also in higher order correlation functions. Since density fluctuations have a zero mean, it may be more interesting to study the two-point correlation function of the density contrast $\xi(\vec{r})$, or its Fourier counterpart, the power spectrum $P_\delta(\vec{k})$, which are defined by:

$$\xi(\vec{r}) = \langle \delta(\vec{x})\delta(\vec{x}+\vec{r})\rangle \,, \qquad \langle \tilde{\delta}(\vec{k})\tilde{\delta}^*(\vec{k'})\rangle = (2\pi)^3\delta_D(\vec{k}+\vec{k'})P_\delta(|\vec{k}|)\,. \tag{1.41}$$

In the ΛCDM model, the initial power spectrum is assumed to be a simple power law as $P_\delta(k,t_i) \propto k^{n_s}$. Furthermore, according to the inflationary scenario, the primordial scale-invariant power spectrum should be defined with a spectral index at $n_s \sim 1$. As the power spectrum is supposed to grow like $D_+^2(t)$ in the linear theory, one can approximate the evolution of the spectrum as:

$$P_\delta(k,t) \propto T^2(k)\left(\frac{D_+(t)}{D_+(t_i)}\right)^2 k^{n_s}\,. \tag{1.42}$$

The transfer function $T(k)$ encodes the scale-dependent effects due to the micro-physics at the epoch of matter-radiation equivalence. To fully understand the behaviour of the linear matter power spectrum, one can strongly simplify the transfer function. We have seen that prior to the matter-radiation equivalence, one can distinguish sub- and super- horizon dark matter density perturbations, which have evolved differently at the radiation epoch. The smaller modes ($k \ll k_{\rm eq}$) have been suppressed relatively to the larger modes ($k \gg k_{\rm eq}$) by a factor $(a/a_{\rm eq})^2$. We can thus write a rough estimate of the transfer function and the matter power spectrum for $n_s \sim 1$:

$$T(k) \propto \begin{cases} 1 & (k \ll k_{\rm eq}) \\ k^{-2} & (k \gg k_{\rm eq}) \end{cases} \qquad P_\delta(k) \propto \begin{cases} k & (k \ll k_{\rm eq}) \\ k^{-3} & (k \gg k_{\rm eq}) \end{cases}\,. \tag{1.43}$$

Accurate expressions of the transfer function exist in the literature (Bardeen et al. 1986; Eisenstein & Hu 1998). As illustrated in figure 1.12, one can distinguish between the different behaviours of linear and non-linear matter power spectra. We see that the non-linear structure formation increases the spectral amplitude at small scales. The theoretical predictions presented here are computed with Cosmic Linear Anisotropy Solving System code (Blas et al. 2011; Lesgourgues 2011). This is a Boltzmann code which numerically perturbs and solves the fluid equations for given initial conditions to provide theoretical predictions of cosmological observables (see also CAMB code, Seljak & Zaldarriaga 1996). In practice, it numerically integrates the linear theory of cosmological perturbations, from the radiation dominated epoch until the present time. In addition, non-linear evolution of the density field can also be considered by using HALOFIT, a fitting formula for the non-linear matter power spectrum, where fitting parameters are determined from accurate N-body simulations (Smith et al. 2003; Takahashi et al. 2012) (cf. section 1.2.6.4.).

1.2.6.3 The Halo and galaxy biases

The total density field can be well-described as a function of the dark matter halo distribution, as illustrated in figure 1.13. However, the statistics computed from halo distributions differ from the statistics extracted from the complete density field: this difference can be modelled as a bias parameter (Kaiser 1984; Bardeen et al. 1986; Bond et al. 1991). To understand this bias parameter, let us introduce the distribution of dark matter halo δ_H, which can be related to the "background" over-density δ as:

$$\delta_H(\vec{r}, M_H, z) = b_H\ \delta(\vec{r}, z)\,, \tag{1.44}$$

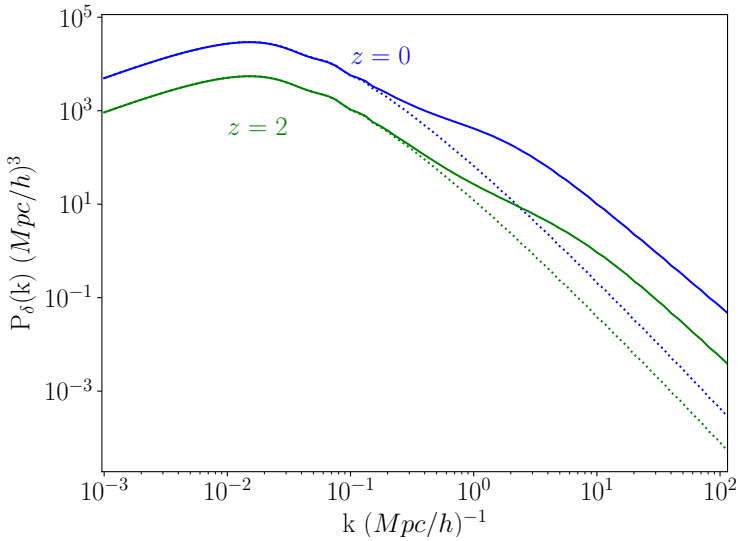

Figure 1.12 – The matter power spectra for z=0 and z=2, computed using the CLASS code (Blas et al. 2011). The dotted lines represent P_δ in linear perturbation theory, whereas solid lines show the non-linear power spectra.

where the halo bias is a function of the halo mass M_H, of the time z, the scale, and the environment, such that $b_H = f(\vec{r}, M_H, \delta, z)$. Theoretical demonstrations based on the halo mass function have led to models of the halo bias as a function of the halo mass: these models are scale-independent on large scales (Sheth & Tormen 1999; Kravtsov & Klypin 1999). More complex bias models have been proposed in the literature, e.g. stochastic (Matsubara 1999), non-linear (Mo & White 1996), or scale-dependant (Smith et al. 2007; Desjacques et al. 2010) bias models. These bias models attempt to preserve the non-linear evolution of matter density field. Complementary, studying the clustering of dark matter haloes in N-body simulations (Hamana et al. 2001; Cen et al. 2004; Tinker et al. 2010; Jose et al. 2016; Hoffmann et al. 2017), has led to calibrated halo bias in linear and non-linear approximations, as function of the smoothing scale of the density contrast and the halo peak height $\nu(M, z)$.

In practice, the large-scale structure are traced by the galaxy distribution. This encourages the study of the bias between galaxies and dark matter halo distribution (Scoccimarro et al. 2001; Peacock & Smith 2000; Croton et al. 2007). It appears that the galaxy-halo connection depends on the complex physics within galaxies (cf section 1.4). The galaxy bias may thus change based on the galaxy population under consideration (i.e. its distribution of magnitude, color, type,...).

The galaxy clustering is affected by the considered galaxy sample (Madgwick et al. 2003; Zehavi et al. 2005; Li et al. 2006a; Zehavi et al. 2011). Moreover, because the halo-galaxy mass relation is non-linear, the link between the galaxy distribution and the underlying total matter density is non-trivial and scale-dependent. The galaxy bias can be treated, to first order, as a linear constant b_1:

$$\delta_g = b_1 \delta_{dm} \,. \tag{1.45}$$

Note that this approximation seems to fail in regions of high density (Kaiser 1984): this would indicate that the bias is strongly influenced by the complexity of galaxy formation on smaller scales. Recently, time-dependent models of the galaxy bias have been calibrated into observations and simulations (Marinoni et al. 2005; Clerkin et al. 2015; Chang et al. 2016). Understanding bias tracers remain a crucial issue to properly extract cosmological information from galaxy clustering.

1.2.6.4 The two-point correlation function with the halo model

An approximate and effective description of matter clustering is the halo model (Seljak 2000; Berlind & Weinberg 2002; Cooray & Sheth 2002). This formalism assumes that all the matter in the Universe can be found in dark matter haloes, as illustrated figure in 1.13. It is also based

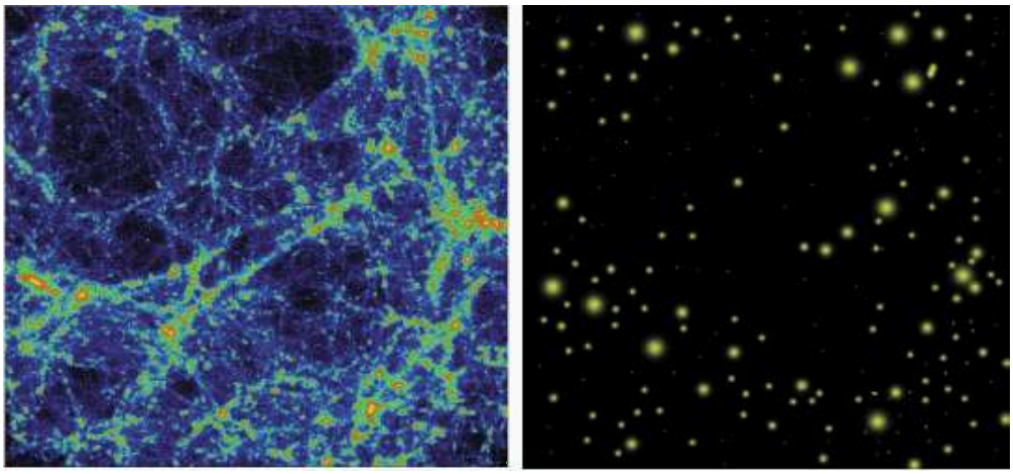

Figure 1.13 – This figure comes from Cooray & Sheth (2002). One the left is drawn the total matter density field as predicted from N-body simulation, one the right only dark matter virialised structures (haloes) are represented.

on a few previous mathematical developments: the NFW density profile, the halo mass function $n(M, z)$, the halo bias $b(M)$, and the linear power spectrum $P_{\rm lin}(k)$. Specifically, it distinguishes between the 1-halo term, which refers to the contributions at small scales (correlations within the same halo), and the 2-halo term, which encodes the contributions at large scales (correlations between the two separate haloes) such that $\xi_{DM}(\vec{r}) = \xi_{1h}(\vec{r}) + \xi_{2h}(\vec{r})$. Based on the halo model of structure formation, one can derive fitting formula of the matter power spectrum, the so-called Halofit model (Smith et al. 2003; Takahashi et al. 2012).

1.3 The observational foundations of the ΛCDM model

In this section, we will review the main observational evidences, acquired over of the last century, which have led to the construction of our current concordance model. As mentioned in 1.1 and 1.2, the ΛCDM model is based on a few assumptions:

- The Universe is expanding, flat ($k = 0$), homogeneous and isotropic at large scales.
- Inflationary scenarios predict adiabatic primordial anisotropies that can be described with a Gaussian random field with a power spectrum $P \propto k^{n_s}$, with $n_s \sim 1$.
- The mass-energy budget of the Universe is as follows: $\sim 5\%$ of ordinary matter (baryons), $\sim 26\%$ of dark matter (cold and collisonless), and $\sim 69\%$ of dark energy (with a state parameter $w \sim -1$).
- The Universe's history is as follows (after the inflation): a radiation-dominated era, a phase of radiation-matter equivalence, a recombination period in which matter decouples from the photons and starts to form the first elements, a matter-dominated epoch, and finally, an accelerated expansion phase driven by dark energy.

Let us describe the observational evidence for these widely admitted properties.

1.3.1 The success of the cosmological model on large scale

1.3.1.1 The cosmic microwave background

Perhaps the greatest piece of evidence in favour of the ΛCDM model is the direct observation of the oldest electromagnetic radiation in the Universe, the Cosmic Microwave Background (CMB). This emission constitutes the first light emission in the history of the Universe, emitted at the recombination epoch (known as *last scattering surface*). Indeed, in the radiation epoch, when baryons and photons were strongly coupled into a relativistic plasma in thermodynamic equilibrium, acoustic waves were generated by the balance between gravitational collapse and radiation pressure around over-dense regions. These acoustic oscillations propagated at the sound speed. When the matter became neutral during recombination, the sound speed and the radiative pressure drastically decreased (drag epoch). As light and matter decoupled, neutral atoms first formed and photons become free to travel through space (free-stream), the Universe became transparent at $z_{rec} \sim 1089$. Thus this emission supports the model of an no-static Universe, which is supposed to have experienced an initial hot plasma phase.

The first observation of the CMB in 1964 by radio astronomers was accidental (Penzias and Wilson). It was followed by space missions dedicated to provide an accurate characterisation of this signal, such as the COBE (Smoot et al. 1992), the Wilkinson Microwave Anisotropy Probe (Spergel et al. 2003), and Planck missions (Planck Collaboration et al. 2016a). It appears as a perfect black body emission with a mean temperature $\overline{T} \sim 2.73K$, because it has been redshifted to low temperature by the expension of the Universe.

This apparent isotropy is a strong argument in favour of cosmological principles, as tiny thermal inhomogeneities are only visible at the relative order $\Delta T/T \sim 10^{-5}$. Its residual temperature fluctuations support structures formation scenario based of the growth of primordial inflationary anisotropies by gravitational instability.

To extract further information, one might study the angular power spectrum of temperature fluctuations, as illustrated figure 1.14. Angular correlations in the CMB contain information on the curvature of the Universe and on the abundances of the different components (dark matter, baryons and dark energy) at the first stage of the Universe. In particular, one can demonstrate that the first peak at $l \sim 200$ (or $\theta \sim 1°$) indicate a (nearly) flat space-time Universe. Moreover, the relative peak heights between even and odd peak can constrain $\Omega_b h^2$. Constraints on Ω_m, Ω_Λ and σ_8 are also extracted from this crucial observation. Here, the parameter σ_8 characterises the amplitude of density contrast fluctuations. It is defined as the effective variance of density fluctuations within spheres of 8 h^{-1}Mpc.

1.3.1.2 Galaxy clustering

A global picture of the galaxy distribution on large scales was first drawn by the CfA catalogue (de Lapparent et al. 1986), and was later refined by large redshift surveys such as the 2-degree Field (Peacock et al. 2001) and the Sloan Digital Sky Survey (York et al. 2000). They emphasise the filamentary structure of matter distribution in the local Universe, as concentrated along filaments, walls, and nodes. As shown figure 1.15, the observed cosmic web confirms a non-linear evolution of density fluctuations.

Probing the statistics of the matter density field constitutes another important test of the ΛCDM model. The matter power spectrum is therefore measured via large galaxy surveys, and completed by other observables such as Lyman Alpha forest measurements and gravitational lensing, as illustrated in figure 1.16 (Tegmark et al. 2004).

As previously explained, the global slope change in the matter power spectrum is induced by the matter-radiation equivalence, i.e. dark matter fluctuations should not evolve similarly depending of their size relative to the horizon before the equivalence. The characterisation of the

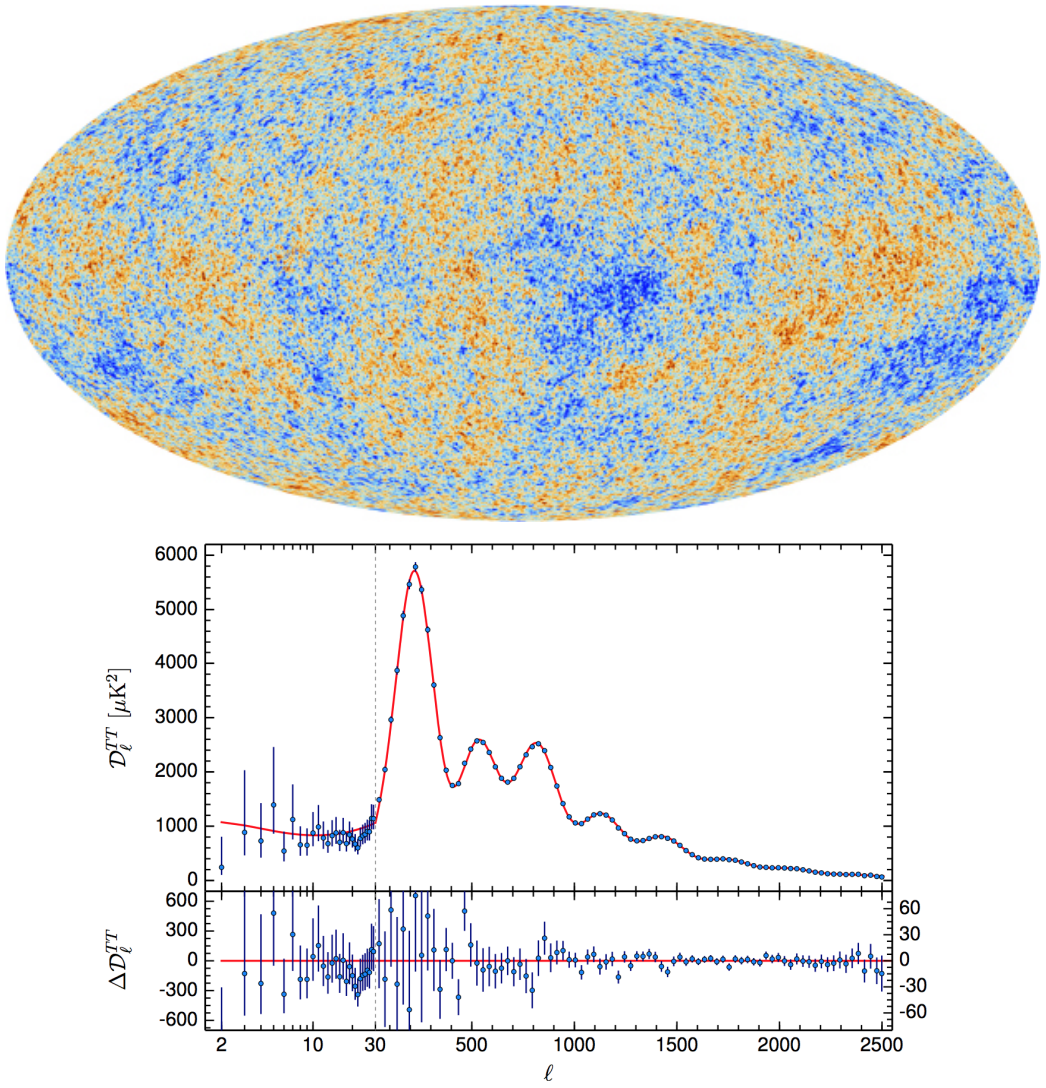

Figure 1.14 – Power spectrum of temperature fluctuations in the Cosmic Microwave Background, compared to the best fit ΛCDM model Planck Collaboration et al. (2016b). Right figure: The anisotropies of the Cosmic Microwave Background (CMB) as observed by Planck (Credit: ESA/Planck Collaboration)

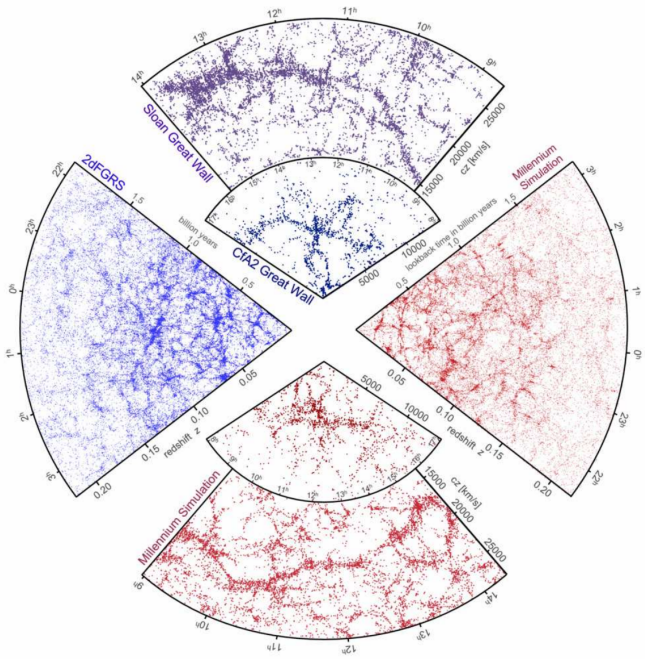

Figure 1.15 – Large scale structures as observed by the common large galaxy catalog CfA, 2dFGRS, and SDSS, and its comparision with mock simulated DM density field constructed from Millennium Simulation, a N-body simulation.
Credit to Springel et al. (2006).

scale $k_{\rm eq}$ can thus be directly related to the matter-radiation equality, and constitutes a constraint on the density parameter $\Omega_m h$ (Pope et al. 2004; Tegmark et al. 2006).

1.3.1.3 The evidence for dark energy - The Baryon Acoustic Oscillations

Large galaxy spectroscopic surveys reveal the expected peak of Baryonic Acoustic Oscillations (BAO) in the matter correlation function $\xi(\vec{r})$ (Eisenstein et al. 2005; Glazebrook & Blake 2005; Cole et al. 2005; Beutler et al. 2011; Anderson et al. 2014; Gil-Marín et al. 2016).

As illustrated in figure 1.16, the BAO peak was first detected with sufficient significance in the correlation function of the luminous red galaxy sample of the SDSS, by Eisenstein et al. (2005). It appears that baryons remains over-dense in a spherical shell with a comoving radius $100h^{-1}$ Mpc, as an imprint of the acoustic oscillation of the photon-baryon fluid at the epoch of equivalence. Note that the overall shape of the correlation function $\xi(\vec{r})$, is used to constrain the matter density $\Omega_m h^{-2}$.

Because the comoving position of the peak is unchanged from recombinaison to the present day, its measurement at any redshift is used to infer angular distances in the Universe. Thus, the BAO measurements provide an incredible improvement on the characterisation of dark energy by strongly constrain Ω_Λ (Blake & Glazebrook 2003; Nunes et al. 2016). Its measurement confirms a few features of the standard cosmological theory: the presence of dark matter, the gravitational clustering theory, the expansion of the Universe.

1.3.1.4 The evidence for dark energy - The SNe type Ia

Type Ia supernovae (SNe) are a powerful tool to measure extragalactic distances. Indeed, this type of supernovae results from a binary system: a carbon-oxygen white dwarf stars grows by accreting the matter of its binary companion, until its mass reaches the Chandrasekhar limit[19]. At this critical mass, white dwarfs are subject to thermo-nuclear explosion, which yields a constant peak luminosity (due to the uniform mass limit). As all of the SNe Type-Ia have the same intrinsic

[19]The maximum mass of a stable white dwarf star ($\sim 1.4 M_\odot$): for higher mass, the electron degeneracy pressure becomes unable to prevent catastrophic collapse.

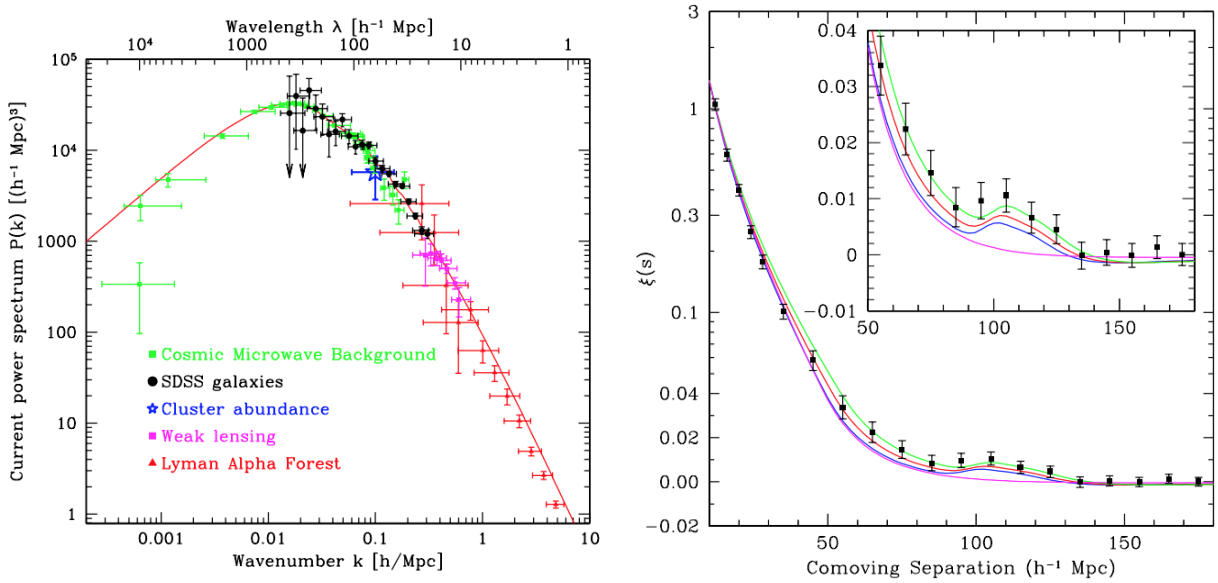

Figure 1.16 – Left panel: The matter power spectrum $P_\delta(k)$ constructed from observational results, as presented by Tegmark et al. (2004).
Right panel: the galaxy correlation function $\xi(\vec{r})$. This result is computed by using SDSS DR3 and Luminous Red Galaxy sample, as described in Eisenstein et al. (2005).

luminosity, it becomes easy to calculate their corresponding luminosity distance (they thus act as standard candles). Moreover, being very bright, they can be used to probe distances beyond the local Universe.

By studying the relations between SNe Type-Ia luminosity and its light curves, one can determine the luminosity distances of these events. They provide a clear evidence of the accelerating expansion of the Universe (Garnavich et al. 1998; Riess et al. 1998; Perlmutter et al. 1999; Aldering et al. 2004; Riess et al. 2009; Choudhury & Padmanabhan 2005; Hicken et al. 2009; Suzuki et al. 2012; Betoule et al. 2014). As illustrated in figure 1.17, the determination of distance-redshift relation of SNe-Ia is used to probe the cosmological parameters Ω_m and Ω_Λ.

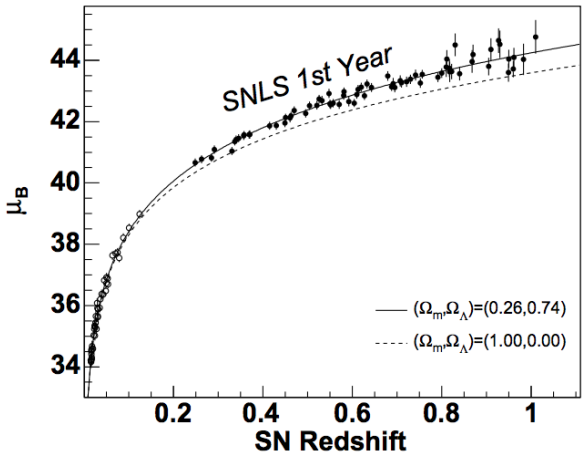

Figure 1.17 – Hubble diagram of Type Ia supernovae for two different cosmologies. The distance estimator μ_B is plotted as a function of the supernovae redshift z. This result comes from the measurements to 71 high redshift SNe Ia discovered during the first year of the 5-year Supernova Legacy Survey (SNLS) and nearby SNe Ia (Astier et al. 2005).

1.3.1.5 The evidence for dark matter

The presence of "dark matter" was first proposed by Zwicky (1933) to explain "missing mass" in the Coma cluster (Peebles 1970; Rood et al. 1972). It was revealed by estimating the masses of galaxy cluster by two different methods: first, through the kinematics of cluster galaxies, and secondly, by summing the mass of galaxies. The mass inferred from the velocities of galaxies (via the virial theorem) is about 400 times higher than the luminous mass.

Galaxy clusters, as the largest collapsed objects in the Universe, have been extensively studied to refine our understanding on this apparent "missing mass". Different observables are used to determine the mass of clusters: such as galaxy kinematics (see e.g. recently, Balestra et al. 2016), X-ray surface brightness[20], or gravitational lensing[21] (Parker et al. 2005; Mandelbaum et al. 2006a). By averaging over a large cluster sample, the total baryon mass (the stellar and hot gas components) within a radius r_{500} appears to represent only $\sim 13-14\%$ of the total gravitational mass (Gonzalez et al. 2007).

At the scale of a galaxy, the rotational velocity of stars as function of their distance to the galactic center, called rotation curves, can be used to evaluated the dynamic mass of galaxies (Ostriker & Mark 1968; Rubin et al. 1980, 1985; Begeman et al. 1991; Kravtsov et al. 1998; Moore et al. 1999b; Evans & Wilkinson 2000; Sofue & Rubin 2001). The velocity of stars is expected to decrease with the distance to the center of the galaxy, if considering the baryonic contribution alone. Indeed, by assuming a centrally dominated mass, the rotational velocity should decline with the distance to the center, as following a Keplerian dynamics[22]. Measurements of rotation curves of galaxies, reveal that the velocities of stars far from the center are not decreased, but are constant, as it is illustrated in figure 1.18 (by considering the Miky Way). To explain this particular shape of rotation curves, one might introduce an extra mass in the outer region of the galaxy, the halo of dark matter. In detail, the velocity profile on spiral galaxies appear to be well-modelled by a universal profile which consists of an exponential thin disk and a spherical halo (Salucci & Burkert 2000; Klypin et al. 2002; Salucci et al. 2007).

Finally, observations of the CMB give further evidence of the presence of dark matter: here, the anisotropies created by the collapse of dark matter, which are not affected by photon radiative pressure. Large-scale structure measurements provide further arguments in favour of a type of matter which interacts with other matter through gravitational force alone (i.e. dark matter). Taken as a whole, these elements indicative of a discrepancy between the mass estimated from object luminosities and their mass deduced by gravitational considerations, which hold for galaxies, galaxy groups, and galaxy clusters, have become a matter of fact at the beginning of the 20th century.

To explain this discrepancy, an invisible matter complement is admitted on the cosmological model, which corresponds to "dark matter". This unknown matter does not interact with ordinary matter and cannot therefore be detected directly: only through its gravitational effect can it be "seen". There is a wealth of dark matter description in the literature, for example the self-interacting dark matter (Spergel & Steinhardt 2000a) or the warm dark matter (Bode et al. 2001). For an overview of dark matter candidates, one might refer to Bertone et al. (2005). Scientific consensus has fallen on weakly interacting massive particles (WIMPs), as described by Jungman

[20] By considering the intra-cluster medium in hydrostatic equilibrium (balance between pressure and gravity), one can estimate cluster masses from their X-rays emissions (see e.g. Carlberg et al. 1996; Evrard et al. 1996; Mohr et al. 1999).

[21] As detailed in chapter 2, the gravitational lensing is a unique probe to estimate the total mass distribution of a massive foreground object (the lens) without making any assumptions of the nature or dynamical state of the matter.

[22] For a test mass in circular orbit around a massive object with a mass M, its equation of motion is $\frac{GM}{r^2} = \frac{V^2}{r}$, where r and V are respectively the radius of the circular orbit, and the tangential velocity of this mass test (Kepler's laws).

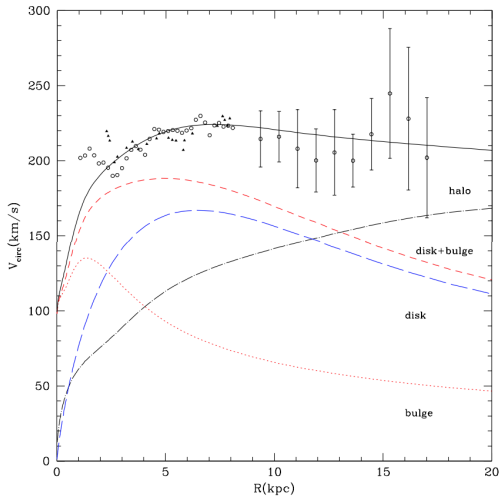

Figure 1.18 – The rotational velocity of stars within the Wilky Way have been model contributions from a bulge, disk, and dark matter halo. This figure comes from Klypin et al. (2002).

et al. (1996), which have a small cross section of interaction. Detecting dark matter annihilations and characterising the cross-section of dark matter interaction would provide decisive evidence and drastically reduce the large range of possible explanations. Characterizing dark matter behaviour on small scales[23] is therefore a key problem in the field of dark matter studies.

1.3.1.6 The combination of probes to constrain cosmological parameters

A combination of various cosmological probes allows to accurately constrain parameters of the ΛCDM model, as illustrated in figure1.19. As discussed above, the CMB, the BAO and the Type Ia SNe constitute main cosmological probes to constrain the dark energy (ω_Λ), and the density parameters of the baryons and dark matter (Ω_{DM},Ω_b). In addition, other cosmological probes such as cluster counts, and lensing (detail in chapter 2) are used to provide independent test of the cosmological model, and to break degeneracy in parameter characterisation. This is illustrated in figure 1.19.

1.3.2 Discrepancies on cluster and galactic scales

As cosmological measurements start to become accurate down to small scales ($< 10\,\mathrm{Mpc}\ h^{-1}$), the ΛCDM is tested at both galaxy and cluster scales. At these smaller scales, matter clustering becomes highly non-linear and is sensitive to possible interactions between dark and luminous matter. In addition, collisions and/or annihilation of dark matter particles could be revealed at these scales. In fact, characterising the different features of dark matter systems through observations at cluster and galactic scales leads to potential discrepancies with CDM predictions. We now discuss two main dark matter halo model properties, which seems to disagree with observations.

1.3.2.1 The cusp/core problem

We have seen that taking the dark matter component into account allows us to explain the global dynamics of galaxies within galaxy clusters and the stellar velocity distribution within galaxies. Focusing on the central region of dark matter haloes, the CDM model predicts a peaked internal density. Observational results, however, seem to favour a nearly isothermal profile with a constant density core (de Blok et al. 2001; Borriello & Salucci 2001; de Blok & Bosma 2002). Note that

[23] Many features of dark matter behaviour can best be seen at these scales.

Cosmological parameter	Planck results
Hubble constant H_0	67.74 ± 0.46
Matter density parameter Ω_m	0.3089 ± 0.0062
Dark energy density parameter Ω_Λ	0.6911 ± 0.0062
Fluctuation amplitude σ_8	0.8159 ± 0.0086
Spectral index n_s	0.9667 ± 0.0040

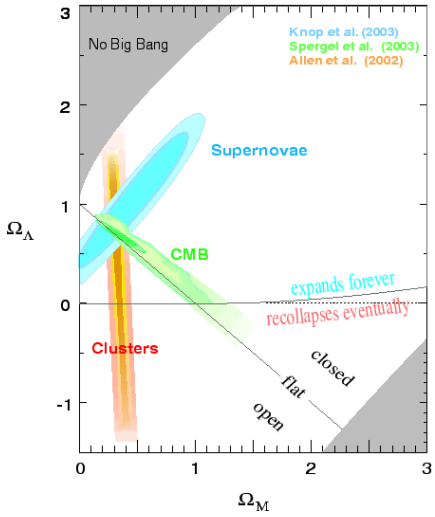

Figure 1.19 – Right: Cosmological parameters for the ΛCDM model as determined by Planck CMB power spectra, in combination with lensing reconstruction and external data (Planck Collaboration et al. 2016b)
Left: Combined constraints to cosmological densities Ω_m and Ω_Λ by using supernovae (SNIa), CMB and cluster abundance data. Credit to Supernovae Cosmology Project.

this is not the case for all galaxies: some studies are consistent with CDM predictions (van den Bosch et al. 2000).

Dwarf spheroids and low surface-brightness galaxies are expected to be ideal systems for testing the structure of dark matter haloes, because their baryonic fractions are supposed to be low in their internal regions (Burkert 1995). As illustrated in the left panel of figure 1.20, it appears that CDM models (via the NFW profile) over-predict the rotational velocity of stars in the internal region of galaxies (Moore 1994). In fact, spheroidal galaxies present, on average, a flatter slope in their core ($\alpha > -0.5$ for $\rho \propto r^\alpha$), than the expected steep power-law behaviour predicted by NFW or Einasto model (see e.g., Palunas & Williams 2000; Swaters et al. 2003; Gentile et al. 2004; de Blok et al. 2008). Recently, Oh et al. (2011) have estimated that the mean density slope in dwarf galaxies is around $\alpha \sim -0.29$, which strongly differs from the expected value of $\alpha \sim -1$ inferred form dark matter simulations (see also, Walker & Peñarrubia 2011). Moreover, Oman et al. (2015) highlight the complexity of the problem due to the diversity of rotation curves of dwarf galaxies.

There are different possible explanations for this unsolved "*cusp vs core*" controversy.

First, one can consider alternative dark matter nature such as self-interacting dark matter particles, thus changing the mass profile (closer to an isothermal core) and providing a better agreement with observations (Vogelsberger et al. 2012; Rocha et al. 2013; Weinberg et al. 2015). This approach remains controversial, as alternative dark matter studies do not always converge to the same conclusions (Zavala et al. 2013; Elbert et al. 2015).

Secondly, there is still room for debate over the method for measuring the slopes of mass profiles as inferred from kinematic data. Complex systematic effects can bias the mass profile estimation: non-circular motions, anisotropy velocity, galaxy inclination, projection effects, and asymmetry of the mass distribution can all contribute to such a bias (Swaters et al. 2003; Hayashi et al. 2004; Rhee et al. 2004).

Finally, properly modelling the impact of baryonic matter on the central mass profile may be the solution to reconcile the observed rotation curves of dwarf irregulars with the density profiles of haloes formed in the standard CDM scenario (Navarro et al. 1996a; Gnedin & Zhao 2002; Read

& Gilmore 2005; Mashchenko et al. 2006; Governato et al. 2012; Teyssier et al. 2013; Madau et al. 2014). These conclusion are strongly dependant of the efficiency on various baryonic processes, which are poorly-understood.

1.3.2.2 The missing satellite problem

The abundance of substructure within a dark matter halo has been estimated through N-body simulation (see 1.2.4.3). These predictions have been compared with the abundance of satellite galaxy in the Local Group (Moore et al. 1999a; Klypin et al. 1999) As illustrated in figure 1.20, it appears that the number of detected satellites around the Milky Way is much smaller than the number of dark matter clumps from CDM model (Klypin et al. 1999). We see that the abundance of massive satellite ($V_{circ} > 50\ km/s$) seems to agree with the CDM prediction, whereas the number of low-mass satellites appears over-predicted by about 1-2 orders of magnitude. This discrepancy became known as the "*missing satellites*" problem.

It was reduced with improvements in sensitivity leading to more satellite detections, which lead to the discovery of ultra-faint dwarf satellite galaxies (Belokurov et al. 2006; Irwin et al. 2007; Belokurov et al. 2009, 2010; Koposov et al. 2015; Drlica-Wagner et al. 2015). Indeed, the smaller number of directly observable satellites, could be due to the ultra-faint luminosity of these low-mass satellites. Physical processes taking place in these satellites, can potentially yield to extremely inefficient star formation rates, and thus reduce their expected luminosity (from the mass luminosity relation). For example, the reduction of star formation in low mass systems can be explained by gas heated via photo-ionization (Somerville 2002; Benson et al. 2002). By including models of the physics taking place in low-mass galaxies, Muñoz et al. (2009) estimated a lower number of expected luminous satellites. Improved models for the formation and evolution of dwarf spheroidal galaxies are crucial to investigate this science case.

In order to improve our understanding of their physics, the satellite galaxy luminosity function was measured via large galaxy survey such as SDSS (Koposov et al. 2008; Tollerud et al. 2008). These observations were then compared to numerical simulations with construct semi-analytical models to describe the galaxy satellite population and their properties (Guo et al. 2011; Starkenburg et al. 2013).

Taking into account both the detection limit of ultra faint galaxies and model formation rates of low-mass galaxies within CDM substructures can roughly reconcile the abundance of luminous satellites (Kravtsov 2009; Macciò et al. 2010; Kim et al. 2017). Note that changing the dark matter nature by self-interacting can also lead to solve the missing satellite problem (Zavala et al. 2013). Finally, the kinematics of the dwarf spheroidals appears also inconsistent with the properties of the dark satellites from numerical simulation (the too big to fail problem; Boylan-Kolchin et al. 2011).

1.3.2.3 Resolving these tensions

The comparison between theoretical predictions and current observational results at dark matter halo scales seems to show flaws in our understanding of dark matter. One might ask if this apparent small-scale crisis is related to baryonic physics, or if it is a real failure in the concordance model. Indeed, as gravitational force no longer dominates structure formation at these non-linear scales, full baryonic processes on galaxy formation and evolution must play a significant role. Pure dark matter prescriptions can therefore be one reason for these discrepancies between concordance model predictions and observational results. One might further ask if dark matter is in fact capable of self-interacting, or whether baryonic processes shape the physics of inner haloes? Can the over-prediction of dark matter clumps be reduced by baryonic physics, is it a question of detecting small massive objects, or is the very nature of dark matter itself in question? To answer

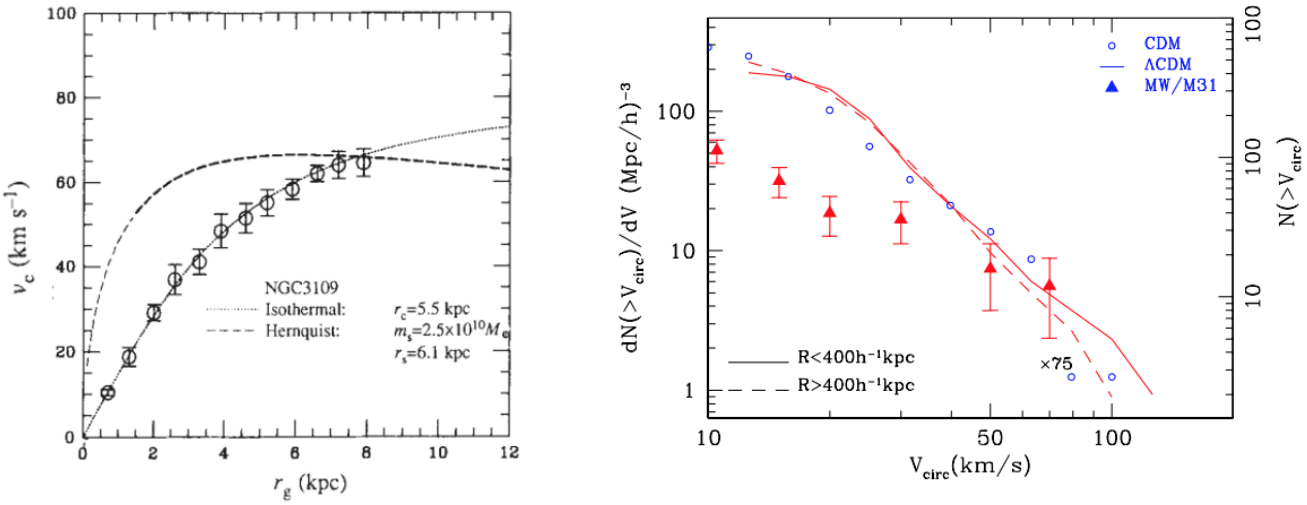

Figure 1.20 – Right: The rotation curve of a dwarf spiral galaxy. The dotted lines are the two types of fit: from a isothermal density profile ($\rho \propto r^{-2}$) and from the Hernquist profile ($\rho \propto r^{-1}$). This Figure is taken from (Moore 1994).
Left: The cumulative circular velocity distribution of satellites within $400kpc/h$ from the center of the host halo. Figure is taken from (Klypin et al. 1999).

these fundamental questions, we review the basics of numerical simulations as a crucial tool to describe the dark matter density field on both large and small scales.

1.4 Numerical simulations

As mentioned in section 1.2, numerical simulations are a necessary tools to compute the evolution of density fluctuations in the highly non-linear regime where $\delta \gg 1$. By considering initial conditions of a Gaussian primordial density field, one can numerically compute this evolution via gravitation dynamics in an expanding Universe.

1.4.1 Pure dark matter N-body simulations

Let us first describe the N-body approach as the discretisation of gravitational dynamical equations with a Newtonian approximation in an expanding space-time. Because dark matter is collisionless, we ignore here the pressure term. The Poisson-Vlasov system of equation for N-particles can be written as:

$$\text{For each dark matter particle i} \begin{cases} \ddot{\vec{x_i}} = -\vec{\nabla}\Phi(\vec{x_i})\,, \\ \Phi(\vec{x}) = -G\sum_{j=1}^{N} \dfrac{m_j}{|\vec{x}-\vec{x_j}|}\,. \end{cases} \tag{1.46}$$

where $\vec{x}_i$ is the comoving position of the particle with a mass m_i. It appears as non-linear differential equations of second order, which are hardly difficult to solve, even numerically. The natural first approach is to compute the gravitational force for each pair of particles, this is the particle-particle method (PP). This method needs large computational resources for a large particle number N, since the number of operation is N^2 at each time step. This direct N-body summation was used in the first simulation codes in the seventies. With the development of sophisticated numerical computation methods, more efficient approaches have emerged.

1.4.1.1 The PM and P^3M methods

The first optimisation, developed in the eighties, was to spread the particles distribution onto a 3-D regular grid (Hockney & Eastwood 1981; Efstathiou et al. 1985; Villumsen 1989; Bertschinger 1998). This approach allows us to smooth particle mass by using interpolation schemes (as described in Appendix A.3). The grid cells are defined by their density values, and the Poisson equation is solved on the grid by using Fourier Transform or via Multigrid solvers. The gravitational force field $\vec{F_g}$ is then inferred by derivation (finite difference), and is interpolated at each particle position. To move particles, we loop to the next time step. For example, by using leapfrog integration (Hut et al. 1995; Mikkola & Aarseth 2002), the updated velocity and position at the step i for each particles can be expressed as:

$$\vec{v}(t_{i+1/2}) = \vec{v}(t_{i-1/2}) + \Delta t\ \vec{F_g}(t_i)\,, \quad \vec{x}(t_{i+1}) = \vec{x}(t_i) + \Delta t\ \vec{v}(t_{i+1/2})\,, \tag{1.47}$$

where Δt is time value between two consecutive time steps. The velocity and position field are $\vec{v}$ and $\vec{x}$ respectively. This particle-mesh method (PM) is more efficient than PP method in terms of computational time, which is now proportional to $\mathrm{N_g} \log \mathrm{N_g}$, with $\mathrm{N_g}$ number of grid cells in one direction. Nevertheless, PM method tend to fail at small scales, *e.g.* structures smaller than cell size are smoothed out. It therefore necessitates a high spatial resolution. The accuracy of this N-body system evolution mainly depends of the used Poisson equation integrator, time-step and smoothing schema.

The hybrid code P^3M method - as a mix of PP and PM method - is based on the separation of the short- and long- range contribution of the gravitational force applied to a particle, such that $\phi(\vec{x}) = \phi^l(\vec{x}) + \phi^s(\vec{x})$ (Hockney & Eastwood 1981; Couchman 1991). The short-range part $\phi^s(\vec{x})$ is computed by directly summed the contributions of neighbour particles, as described in the PP method. The long-range contribution of the gravitational field $\phi^l(\vec{x})$ is supposed to be smooth and smaller, thus it can be well approximated by the PM method (computed on a grid). This way, we conserve the information on small scales and we are efficient on large scales.

1.4.1.2 Tree code

As non-linear clustering begins to take place, structures become denser and thus a direct computation of the short-range gravitational contribution become inefficient (summation over a large number of particles). To solve this problem, a tree code can be used (Barnes & Hut 1986).

The particles are organised following a tree structures over a hierarchy of cells. The first *cell*, which defines the main *branch* of the tree, is a large cube which incorporate all particles. Space is then split in order to obtain the same particle number in each sub-regions (or cells). The sub-division procedure occurs recursively (*branch* creation), until a threshold particle number is reached in each final cell (the *leaves*).

After building the tree, one can compute the gravitational force for each particle by going down the tree depending of an opening angle limit (free parameter). For cells which have an opening angle larger that the angle limit, we descend the tree (*opening branches*), to sum the individual contribution of nearby particles. In contrast, for distant cells where the opening angle is smaller than the threshold, all particles contained in a branch are regrouped into single massive particle.

This method yields an optimal computational time such that the gravitational force on a single particle needs $N_p \log N_p$ iterations. It should be noted that evaluating the forces by tree algorithm remains an approximation, where the error is controlled by the opening angle criterion. Furthermore, hybrid model have been created to speed up the computation, the Tree-PM model, where the short-range force is computed by the tree algorithm and the distant contribution via PM method (Springel 2005)

1.4.1.3 The successes and limits of N-body simulations

The main success of N-body simulations is to draw the global picture of the matter distribution on large scales, *i.e.* the cosmic web observed in the local Universe. Indeed, with the advent of high performance computing, cosmological simulations have been run in large volumes and with high DM mass resolution: as HORIZON 4π (Teyssier et al. 2009), Millenium I, II & XXL (Springel 2005; Boylan-Kolchin et al. 2009; Angulo et al. 2012), Horizon Run 3 (Kim et al. 2011), MultiDark (Klypin et al. 2016), or more recently, the Flagship simulation (Potter et al. 2017).

As presented in table 1.1, these simulations have different features in term of (length and mass) resolutions, box sizes, and computation codes[24]. For example, Horizon Run 3 has 20% more particles than Millenium-XXL, but 40 times poorer mass resolution. In addition, other characteristics have to be taken into account such as the force resolution, the initial redshift (redshift at which the simulation started), the simulation time step and the cosmological parametrisation. They all present different advantages, and are used to probe either larger scale, smaller objects, or local (old) Universe. With the advance of high performance computing, simulation box becomes larger, and Poisson solvers and integration methods becomes more accurate.

These large cosmological simulations are used to describe non-linear matter clustering, as shown figure 1.21. For example, in figure 1.15 we illustrate the large scale dark matter distribution from the Millenium simulation (in red), and see a good correspondence with the large galaxy surveys like the 2dF (in blue). As well, the statistics of the density field on large scales are predicted by N-body simulations such that the matter power spectrum (and the two-point matter correlation function) seem to match observations (e.g. Angulo et al. 2012). Moreover, we have seen that the properties of dark matter structure have been described through N-body simulations some of these properties include: the halo mass function, the density profile of DM haloes, and the concentration-mass relation (More et al. 2011; Prada et al. 2012; Watson et al. 2013; Ludlow et al. 2014; Sánchez-Conde & Prada 2014; Klypin et al. 2016).

To accurately characterise matter clustering at small scales, zoom-in N-body simulations have also been performed: Via Lactea (Kuhlen et al. 2008), Aquarius project (Springel et al. 2008b), Ghalo (Stadel et al. 2009), Phoenix (Gao et al. 2012). They have been used to predict the inner structure of Dark Matter haloes, the substructure mass function and the substructure spatial distribution.

Since baryons are expected to linearly follow the dark matter at large scales, the prediction of cosmological observables via N-body simulation seems to give a good match by a direct comparison with observational results, for typical scales larger than a few Mpc. Nevertheless, pure dark matter simulations cannot describe the impact of the baryonic physics on the underlying dark matter density field, which cannot be neglected on small-to-intermediate scales. Moreover, dark matter simulations do not reproduce the galaxy luminosity function which differs from the CDM halo mass function (Moster et al. 2010b). The simple prescription of a linear halo-galaxy mass relation fails, especially for low and high massive galaxies. Therefore, galaxy observables have to be predicted over simulations which consider the baryonic physics in addition to the DM clustering.

1.4.1.4 Populating the DM haloes with mock galaxies into N-body simulations

An alternative approach is to extend the results from DM-only N-body simulations by populating the DM haloes with mock galaxies. Indeed, it offers the opportunity to construct direct baryonic observables, which could be directly compared with observational results.

[24] Codes define how gravitational force will be computed, either on a grid (PM), or in particle approach (Tree code). Hybrid codes are usual for recent large N-body simulations. Different codes have very different Poisson solvers and integration methods.

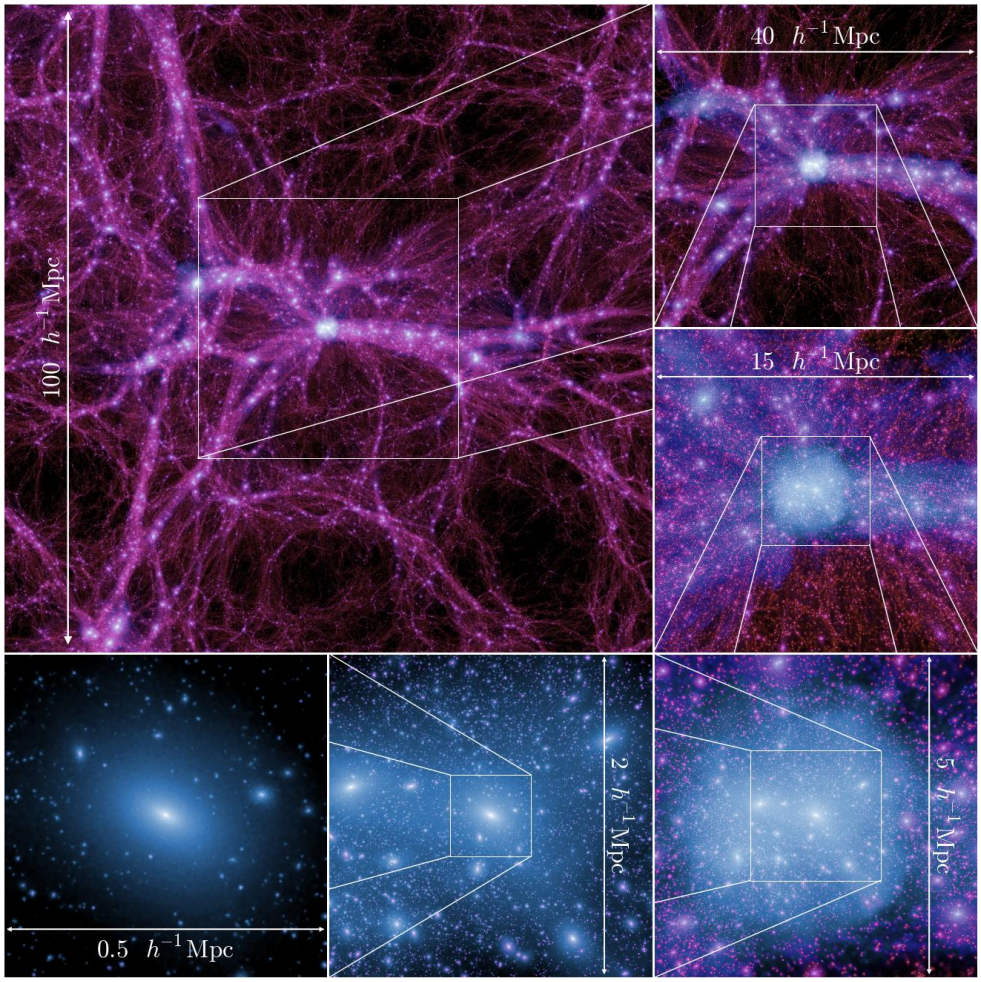

Figure 1.21 – The matter distribution at various scales from the Millennium-II Simulation, a very large N-body simulation. A zoom is realised around a massive dark matter halo at $z = 0$. Image credits: Boylan-Kolchin et al. (2009)

	Code	Box size (h^{-1}Gpc)	Mass resolution ($h^{-1}M_\odot$)	DM particles	Publication
Horizon Run 3	hybrid scheme (PM and Barnes-Hut octtree algorithm)	10.8	$\sim 2.4 \times 10^{11}$	7210^3	Kim et al., 2011
Millenium-XXL	Tree-PM code (GADGET-3)	3	$\sim 5.9 \times 10^9$	6720^3	Angulo et al., 2012
MultiDark	GADGET-2 and Adaptive Refinement Tree	1	$\sim 1.5 \times 10^9$	3840^3	Kyplin et al., 2016
Flagsphip	Pkdgrav3 GPU Hybrid	4	$\sim 1 \times 10^9$	15870^3	Potter et al., 2017

Table 1.1 – Comparison of recent pure DM N-body cosmological simulations.

To perform this mock galaxy catalogue, one must first select the dark matter haloes in the DM density field of the simulation, by using standard halo finding algorithms such as the friends-of-friends algorithm, SUBFIND algorithm, and subclump finder ADAPTAHOP (e.g. Aubert et al. 2004; More et al. 2011; Muldrew et al. 2011). One can cite Knebe et al. (2011), for a review of the different halo finders. The halo catalogues can then populated by the expected galaxy population via semi-analytic models (SAM) (White & Frenk 1991; Cole et al. 2000; Berlind & Weinberg 2002; Kravtsov et al. 2004; Bower et al. 2006; Croton et al. 2006b; De Lucia et al. 2006; Guo et al. 2011; Henriques et al. 2015). These SAMs assign the expected number of central and satellite galaxies to each halo, based on CDM prescriptions. They can finally assign as well galaxy properties (see e.g. Hearin et al. 2013; Shankar et al. 2014). Such modes have been calibrated over the observations such as the galaxy luminosities or stellar mass functions (see e.g. Coupon et al. 2015).

Current high-resolution cosmological simulations have used this method to provide coherent simulated galaxy catalogues (Angulo et al. 2012; Smith et al. 2017). Currently, in the perspective of the Euclid mission, complex SAM pipelines have been used on FLAGSHIP simulation and yield large mock galaxy data sets by accurately simulating galaxy properties such as color, luminosity, and shape. This large simulated galaxy catalogue is conceived of as a virtual universe, used to develop data processing and science analysis pipelines.

1.4.2 Hydrodynamical simulations

Hydrodynamical cosmological simulations attempt to give a comprehensive picture of galaxy formation and evolution over statistically representative volumes. This type of simulation is crucial to improve our understanding of the complex interplay between baryonic and dark matter components. Indeed, galaxy formation involves both dissipative gas physics and gravitational dynamics, e.g. stripping of gas by tidal fields. As it simultaneously treats the dark and luminous matter evolution, the computational resources required are much higher than N-body simulations (for the same volume and particle number). Thus, hydrodynamical cosmological simulations have to find a good balance between high resolution required to accurately model the galactic physics, and the large cosmological volume necessary to provide large statistics and describe galaxies in a cosmological framework.

1.4.2.1 The baryonic physics

Baryonic matter is treated as a collisional perfect fluid. The motion of the gas can be described by the standard hydrodynamical equations, the Navier–Stokes equations, which can be written as:

$$\begin{aligned} \frac{\partial \rho}{\partial t} + \vec{\nabla}.(\rho\vec{u}) = 0 \qquad & \text{conservation of mass}\,, \\ \frac{\partial \rho\vec{u}}{\partial t} + \vec{\nabla}.(\rho\vec{u}\times\vec{u}) + \nabla P = -\rho\vec{\nabla}\phi \quad & \text{conservation of momentum}\,, \\ \frac{\partial \rho E}{\partial t} + \vec{\nabla}.(\vec{u}(\rho E + P)) = -\rho\vec{u}.\vec{\nabla}\phi \qquad & \text{conservation of energy}\,, \end{aligned} \tag{1.48}$$

where ρ is the density, E is the internal energy per unit of mass, P is the pressure and $\vec{u}$ is the velocity of the gas. An equation of state is often imposed for the gas such as $P \propto \rho^{\gamma}$, such that the adiabatic index is $\gamma = 3/5$ for a ideal mono-atomic gas.

To jointly solve the dissipative gas physics and gravitational dynamics, numerical simulation codes often solve the gravitation on a grid, whereas the gas dynamics can be solved with a different approach. Indeed, current hydrodynamical cosmological codes threat the gas dynamics following either a Lagrangian approach by a discretization in mass, or a Eulerian approach by a discretization in space.

Based on a Lagrangian description, the smoothed particle hydrodynamics method (SPH, Monaghan 1992) codes discretize the gas in particles, and follows the particles over the computational times. The fluid dynamics are evaluated on a set of particles, a fluid element. The gas characteristics, e.g. the thermal energy or density, are modelled as continuous fields by interpolating over the fluid particle distribution. The main advantage of SPH codes is the high resolution induced naturally by this approach. Nevertheless, a significant drawback of these methods is that discontinuities are not accurately described (e.g gas shocks, (Evrard 1988; Agertz et al. 2007)). Famous SPH cosmological codes include GADGET code (Springel 2005), and GASOLINE (Wadsley et al. 2004).

In the Eulerian description, one can also solve the hydrodynamical equations on a grid. Gas properties (density, thermal pressure, internal energy) are discretized, and the thermodynamic equations are solved by imposing flux conservation on cells: conserved fluxes are those of mass, momentum and energy. Conservative numerical schemes are proposed in the literature to solve the differential equations on cells while accounting for the inter-cell boundary: these include the Godunov scheme (Gardiner & Stone 2005; Komissarov 1999). An important improvement on the computation of the gas physics on grid is to use an adaptively-refined grid: this is known as an adaptive mesh refinement (AMR). The mesh is refined according to a given criterion, usually the density or the mass within a cell. Therefore, when the density in a cell exceeds a given threshold, the cell is refined. This allows us to describe the denser regions at higher resolution, without extensively increasing the required computational resources. Nevertheless, AMR simulations remain limited by the maximum resolution of the grid. The main AMR codes available in the literature are: RAMSES (Teyssier 2002), AREPO (Springel 2010), ENZO Bryan et al. (2014) codes. Their differences result in various numerical approximations, which include the AMR grid geometry, the refined criteria, or the fluid conservation model (see e.g. Agertz et al. 2007, for a comparison of different codes).

1.4.2.2 Subgrid models

Because one cannot numerically resolve both the small scale baryonic structures (e.g. stars, black holes), and the cosmological structure (e.g. galaxy cluster formation), hydrodynamical cosmology simulations usually make a few assumptions on galactic baryonic physics. These are rolled into the so-called subgrid models. To achieve reasonable computational time, we have to select or roughly average some processes that are difficult to follow over the computational time, e.g. the radiative transfer. Therefore, phenomenological subgrid models are viewed as effective laws for unresolved scales to mimic astrophysical baryonic processes. The main subgrid models that are relevant for modelling the galaxy formation and evolution are described here:

- **Gas heating and cooling**:
  Heating and cooling source terms are added to the equation of energy conservation. In a plasma, radiative emissions are induced by atomic and metal collisions, and induce a loss of internal energy. To model this process, simulations use tables of cooling rate $\Lambda(\rho, z)$ available in the literature, which is a function of the gas density, and its thermal energy (see *e.g.* Sutherland & Dopita 1993). This subgrid model is necessary to provide the fragmentation of the gas, and thus the creation of stars. In addition, the heating of gas induced by the re-ionization is usually imposed by a homogeneous UV background after the re-ionisation $z \sim 10$ (see *e.g.* Haardt & Madau 1996).

- **Star formation**:
  Stars are obviously too small to resolve on the scale of cosmological simulations. Stellar

populations are thus treated as a particle which represents a single stellar population, *i.e.* typically one star particle is around $\sim 10^6$ $M_\odot$. Star formation is often modelled via the Kennicutt–Schmidt law (Kennicutt 1998). It relates the star formation rate $\dot{\rho_*}$ to the gas density ρ, such that: $\dot{\rho_*} = \epsilon\rho/\tau_{ff}$, where ϵ is the star formation efficiency (often approximated as 2%) and τ_{ff} is the free-fall time of the gas. Moreover, because stars form in regions with high densities of cold gas, the star formation is allowed in regions which exceed a given Hydrogen density threshold, typically $0.1H.cm^{-3}$. Note that the gas mass, that is converted into star particle, is removed from the parent gas cells.

- **Stellar evolution and feedback**:
  The evolution of star particles can be modelled by considering an initial stellar mass function. One must also model the stellar feedback to account for chemical enrichment, along with the thermal and kinetic energy transferred by the stars onto their ambient gas. The main stellar feedbacks which are commonly modelled are the stellar winds, type-Ia supernovae (Type Ia SNe) and type-II supernovae (Type II SNe). The physical feedback of stars remains complex to model and insufficiently understood. Thus various synthetic models are available to mimic stellar feedbacks by injecting momentum, mechanical energy and metals in the gas environment (such as starburst99 Leitherer et al. 1999).

- **Active Galactic Nuclei:**
  The formation of Black Holes (BH), treated as particles, generally require a density of gas and stars above a given threshold. The growth of the BH can be considered both by the Bondi-Hoyle-Lyttleton accretion rate and by the effective Eddington accretion rate. One can consider two different types of black halo feedback depending on the value of the gas accretion rate: the quasar and the radio modes. Low-accretion BH impact their surrounding environment by a bipolar outflow of matter (Omma et al. 2004), whereas high-accretion BH isotropically inject thermal energy into the gas. Details can be found in Dubois et al. (2012). Finally, black hole merging can occur when two BH particles are closer than a given threshold distance.

1.4.2.3 The production of a realistic galaxy population

The current main cosmological hydrodynamical simulations are: The Horizon AGN simulation (Dubois et al. 2014), The Eagle Project (Schaye et al. 2015), Massive Black II (Khandai et al. 2015), and Illustris TNG (Springel et al. 2018). These simulations give good descriptions of the formation and evolution of stellar systems and provide an estimation of the physical properties of galaxies, in the large scale environment and over the cosmic time.

In figure 1.2, I list the main cosmological hydrodynamical simulations and their different characteristics. First, one can separate hydrodynamical simulations depending of their type of code: either by a Lagrangian approach (SPH) as Eagle and Massive Black II (GADGET), or either by an Eulerian approach (adaptive mesh) such as Horizon-AGN (RAMSES) and Illustris (AREPO). Grid codes better reproduce discontinuities in gas (chocks, turbulences), whereas gas particle codes are unlimited in term of length resolution and require less computational resources in general. Obviously, depending of the box size, mass resolution and implemented physical processes, these different simulations are adapted to different cosmological investigations. Large hydrodynamical simulations with a reasonable mass resolution, such as Magneticum, are useful to study massive objects (large number of galaxy clusters) and to predict the properties of baryons at large scales[25]. In contrast, hydrodynamical simulations with box size around 100 Mpc are more accurate at galactic scales and are thus extensively used to investigate galaxy formation and

[25]For example, the gas density, metallicity, and temperature can be mapped over the LSS

evolution in LSS environment. In addition, the complex baryonic mechanisms (as SNe and AGN feedback) are simulated by different algorithms with different efficiencies from one simulation to an other. It leads to variant predictions of the density field statistics at intermediate and small scales (as detail below, see figure 1.24), and can also change the statistics of mock galaxy properties (*e.g.* figure 1.23 illustrates the impact of AGN feedback on galaxy mass function).

In general terms, hydrodynamical simulations provides a realistic mixture of galaxy morphology such as elliptical, irregular, and disc galaxies (Agertz et al. 2011; Vogelsberger et al. 2014; Genel et al. 2014; Sijacki et al. 2015; Kaviraj et al. 2017; Dubois et al. 2016). As illustrated in figure 1.22 [26], the simulated galaxy population tends to be similar in appearance to those observed in the Universe, with a large variety in colors, sizes, and morphologies.

In details, these large mock galaxy sample well reproduce observed galaxy properties, such as the bi-modality between passive and active galaxies, or the cosmic star formation history (Dubois et al. 2013; Vogelsberger et al. 2014; Furlong et al. 2015; Kaviraj et al. 2017). Indeed, the AGN feedback allows us to simulate a population of red massive elliptical galaxies. Without the BH activity, massive galaxies formed by merging tend to form a disc and to be highly star-forming (Dubois et al. 2013; Kaviraj et al. 2017). Inefficient star formation in low-mass galaxies, as introduced with the missing satellite problem, can be explained by stellar feedback (Hopkins et al. 2014).

As a result, galaxy stellar mass and luminosity functions predicted from hydrodynamical simulations can be considered a success. As illustrated in figure 1.23, the match of stellar mass function between simulations and observational results is strongly consistent (especially at low redshifts). The standard features of galaxy formation physics are more or less well-reproduced over the cosmic time, but some issues arise as depending on hydrodynamical simulation. For example, the Horizon-AGN simulation tends to over-predict the number of low-mass galaxies, and to produce too low galaxy stellar masses at high redshift (Kaviraj et al. 2017). These small disagreements can come from the accuracy limits of subgrid models, our ability to resolve smaller haloes, and our incomplete understanding of the galaxy formation and evolution.

Finally, the impact of the cosmic web environment on galaxy properties (morphology, luminosity, star forming) is accurately studied through these simulations (see also section 1.2.5.3). For example, it has been established that there is a correlation between the spin of a galaxy and its location in the filamentary structure (Navarro et al. 2004; Hahn et al. 2010; Dubois et al. 2014; Codis et al. 2015b). The intrinsic alignment of galaxies, *i.e.* the aligned of galaxies with the local density field, have been studied with hydrodynamical simulations (Codis et al. 2012b; Tenneti et al. 2014; Codis et al. 2015a; Chisari et al. 2017).

1.4.2.4 The impact of baryons on the underlying density field

Recently, it was shown that baryons have a non-negligible effect on the total matter clustering (Rudd et al. 2008; van Daalen et al. 2011; Vogelsberger et al. 2014; Hellwing et al. 2016; Springel et al. 2018). In figure 1.24, we present the deviation of the matter power spectrum predicted from hydrodynamical simulations, relative to collisionless results (DM only). Baryons tend to reduce the matter power spectra at intermediate scales ($k \sim 1h\,\mathrm{Mpc}^{-1}$) due to the baryonic pressure and AGN-driven outflows, and enhance the power amplitude at small scales ($k \sim 100h\,\mathrm{Mpc}^{-1}$), reflecting the baryonic collapse and star formation. We can also see that the resulting matter clustering depends on the considered hydrodynamical simulations, even if the global behaviour of the matter power spectrum remains similar. The upcoming EUCLID cosmological mission will measure the power spectrum on $0.1h\,\mathrm{Mpc}^{-1} < k < 10h\,\mathrm{Mpc}^{-1}$ scales, with a level of $\sim 1\%$

[26] the catalogue of mock galaxies from the Horizon AGN simulation is available here: http://www2.iap.fr/users/pichon/horizon-agn-galaxy-calalogue/index.html

	Code	Box size h^{-1}Mpc	DM mass resolution	DM particles	Publications
Horizon-AGN	RAMSES (AMR)	100	$\sim 8 \times 10^7$	1024^3	Dubois et al, 2014
Eagle	GADGET-3 (SPH)	100	$\sim 9.7 \times 10^6$	1504^3	Schaye et al, 2015
MassiveBlack II	P-GADGET (SPH)	100	$\sim 1.1 \times 10^7$	1792^3	Khandai et al, 2015
Illustris-1	AREPO (moving mesh)	~75	$\sim 6.3 \times 10^6$	1820^3	Nelson et al, 2015
Illustris-TNG300	AREPO (moving mesh)	~211	$\sim 5.9 \times 10^7$	2500^3	Nelson et al, 2019
BAHAMAS	GADGET-3 (SPH)	400	$\sim 4 \times 10^9$	1024^3	McCarthy et al, 2016
Magneticum Box 0 Box 1 Box 2	GADGET-3 (SPH)	 2688 896 352	 $\sim 4 \times 10^9$ $\sim 4 \times 10^9$ $\sim 6.9 \times 10^8$	 4536^3 1526^3 1584^3	Dolag et al, 2015

Table 1.2 – Comparison of recent cosmological hydrodynamical simulations.

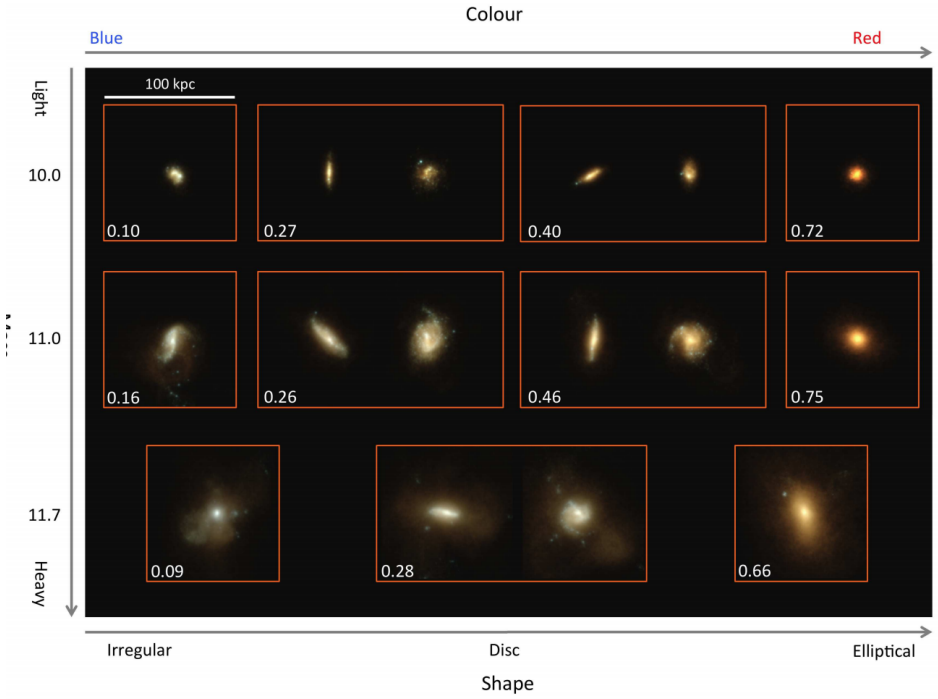

Figure 1.22 – Stellar emission of a sample of galaxies in the Horizon-AGN simulation at $z = 1.3$ observed through rest-frame u, g and i filters. Credit to Dubois et al. (2014).

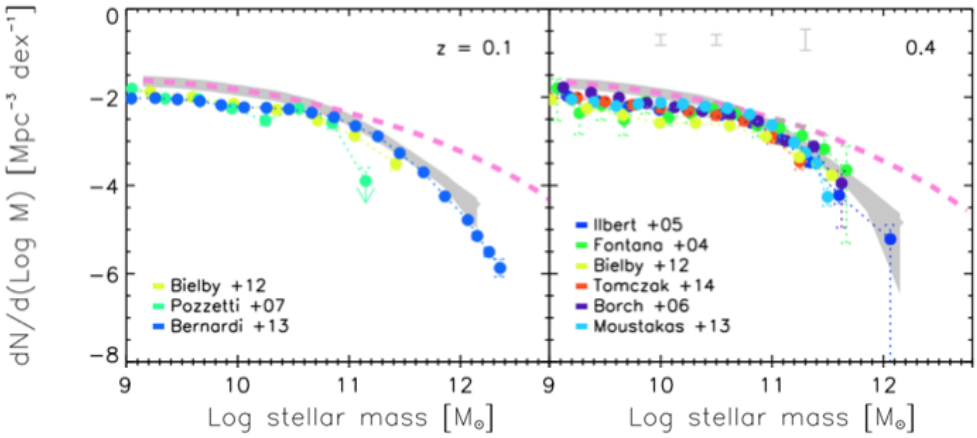

Figure 1.23 – The stellar mass function predicted from the Horizon-AGN as shown in the grey shaded regions, and the prediction from Horizon-noAGN are the pink curves. The various observational results are overlapping in colors. The figure comes from Kaviraj et al. (2017).

accuracy (Laureijs et al. 2011). The baryonic impact must thus be carefully investigated to provide accurate prediction of the matter clustering statistics at these relevant scales.

Focusing on the cluster and galactic scales, we find that baryonic physics significantly impact dark matter halo properties. In fact, supernova feedback can change the density profile of the dark matter halo from cusp into core (Pontzen & Governato 2012; Duffy et al. 2010; Teyssier et al. 2013; Di Cintio et al. 2014; Oñorbe et al. 2015; Schaller et al. 2015). The stellar feedback remains significant for low-mass galaxies. For massive galaxies, the AGN feedback noticeably reduces the slope of the density profiles in the inner regions (Peirani et al. 2017). The impact of baryonic processes on the underlying shape of dark matter also appears subtantial. As shown in figure 1.25 from Suto et al. (2017), the ellipticity of galaxy clusters seems to be significantly affected by the AGN feedback beyond the central region.

At smaller scales, the presence of baryons also impacts the small dark matter clumps which reside in halo. As shown in figure 1.26, the number of sub-haloes are reduced in the center of the hosting halo by the baryonic physics (Despali & Vegetti 2017). However, we see that these results differ depending on the specific baryonic physics being modelled (comparing EAGLE and Illustris simulation). In addition Dolag et al. (2009) shows that hot gas in galaxy clusters tends to decrease the sub-halo mass function relative to a corresponding dark-matter-only simulation.

Conclusion

The concordance model provides an accurate picture of the evolution of the matter density field over the cosmic time. It is verified through numerical simulations, which accurately account for non-linear matter clustering. This model agrees with the observations, especially at large scales. Nevertheless, some discrepancies are still present at cluster and galactic scales. Are these apparent gap between ΛCDM prediction and astronomical observations due to our lack of information on the nature the dark matter, or is it the result of complex baryonic physics relevant at these scales?

Baryonic components have a significant impact on the underlying matter at scales below a few Mpc. To better answer these questions, mock cosmological observable are constructed on state-of-art of cosmological simulations to provide a point of comparison for observations. In this thesis, I focus on gravitational lensing observables. Therefore, in the next chapter I will present in detail lensing theory and weak lensing observables.

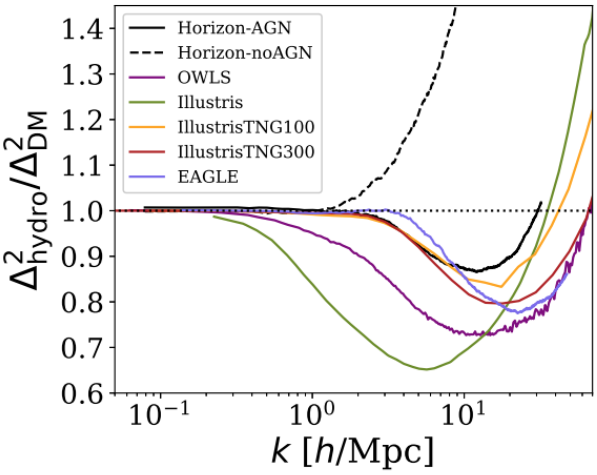

Figure 1.24 – Figure from Chisari et al. (2018): The impact of baryons and baryonic processes on the matter power spectrum at $z = 0$ by considering different hydrodynamical simulations.

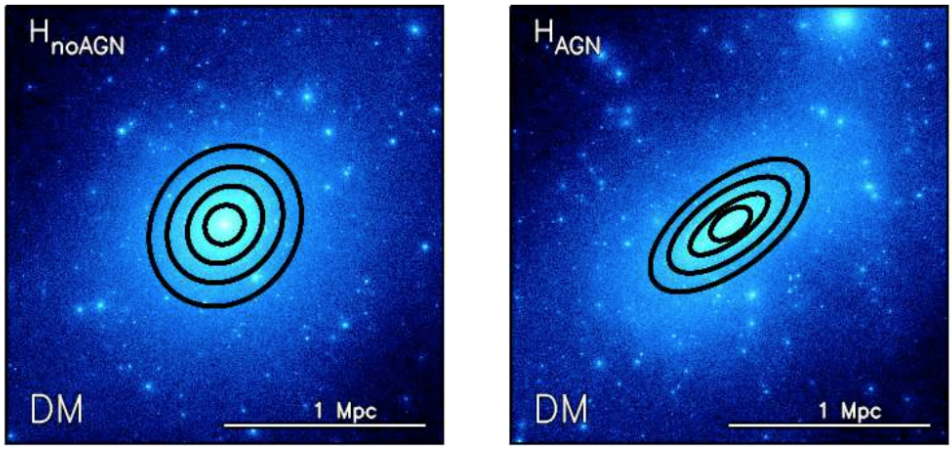

Figure 1.25 – Figure from Suto et al. (2017): The impact of AGN feedback on the projected dark matter distribution centered on haloes. These results came from the Horizon-AGN and Horizon-noAGN simulations.

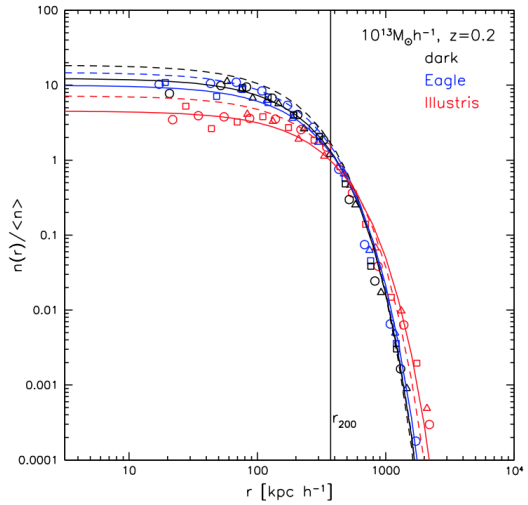

Figure 1.26 – The radial distribution of subhaloes as a function of their distance to the center of the parent halo. Comparison of these results for different numerical simulations are shown in (Pure dark matter, Eagles, Illustris). The figure comes from Despali & Vegetti (2017).

Chapter 2

Gravitational lensing

As predicted by General Relativity (Einstein 1916), light rays follow null-geodesic lines in space-time. The local matter-energy content curves the space-time metric, and massive bodies behave as gravitational deflectors. Light emitted from background sources is deflected by all the matter contained along their line-of-sight. Their resulting images appear to us displaced in the sky, and their shape is distorted. The first evidence of gravitational light bending occurred during a solar eclipse, when the light of sources behind the sun were observed (Dyson et al. 1920).

Major gravitational mirages can happen for efficient lenses, and for a strong alignment between the source, the lens and the observer, it is referred to as *strong lensing*. Such phenomena provide multiple images of the distant light source, or an intense stretching of an extended emitting source, giving rise to Einstein rings, or gravitational arcs. We had to wait until the eighties to detect the first extra-galactic strong lensing events. For exemple, in 1979, a double image of a lensed quasar by a galaxy was detected by Walsh et al. (1979). Shortly after, the strong distortions of background galaxies by galaxy clusters started to be characterised through observations. In particular, Soucail et al. (1987) identified a giant arc around the cluster Abell 370.

Conversely, when light bundles pass at the periphery of the lens, the gravitational potential weakly affects the photons path, resulting in a small deformation of the emitting sources. This so-called *weak* lensing effect cannot be observed directly, but can be seen after averaging over a large number of source shapes around the lens. By measuring the mean ellipticity of background galaxies, one can identify the underlying shear signal and then relate it to the projected density field. Because lensing equations make no assumption about the nature or the dynamical state of the lens, gravitational lensing constitutes a powerful tool to probe the total mass content of the Universe.

In addition, by cross-correlating the ellipticities of background galaxies, one can infer the lensing distortions induced by the large scale structure of the Universe (Wittman et al. 2000; Van Waerbeke et al. 2000a). This *cosmic shear* measurement is a important cosmological observable, as it encodes cosmological parameter values (for theoretical demonstration, see for examples Bernardeau et al. 1997; Jain & Seljak 1997a).

Due to the large potential of gravitational lensing in current cosmological investigations, large lensing data sets are planned for the future (Laureijs et al. 2012; Spergel et al. 2015). In particular, one can refer to the upcoming Euclid mission which will provide measurement of more than 1 billion of weak lensing sources (Laureijs et al. 2012).

In section 2.1 I will quickly review the theory of gravitational lensing, and its main assumptions. The section 2.2 presents the different lensing observables in the weak lensing regime.

These two first sections are inspired by: Bartelmann & Schneider (2001), Schneider et al. (1992), and Kilbinger (2015). The section 2.3 is centred on the existing numerical methods for the post-processing of cosmological simulations in order to simulate lensing signals.

2.1 The gravitational lensing formalism

Following the FLRW metric, the time of photon propagation is linked to the travel path, as follows:

$$c\ dt = \left(1 - \frac{2\phi}{c^2}\right) dr\,, \tag{2.1}$$

where ϕ is the 3-D Newtonian gravitational potential, such as $\phi \ll c^2$ in the weak gravitational field approximation. Analogously to the geometrical optics, one can identify in this relation the gravitational potential as a refraction medium with index $n = 1 - 2\phi/c^2$. It is this comparison which has led to the name of *gravitational lensing*. One can demonstrate (by using the Fermat's principle and Euler's equation), that the path of a light ray is continuously affected by the gravitational potential, so that the emission direction differs from the observed direction by a deflection angle:

$$\widehat{\alpha} = \frac{2}{c^2} \int \vec{\nabla}_\perp \phi\ dl\,. \tag{2.2}$$

Light deflection is thus proportional to the integral of the potential gradient along the ray path dl.

2.1.1 The lens equation

Let me now link the "*true*" angular coordinates of a source $\beta = (\beta_1, \beta_2)$ with the "*apparent* angular position $\theta = (\theta_1, \theta_2)$ of its image after being deflected by gravitational lensing. As illustrated in figure 2.1, one can consider the single thin lens model such that a source is located at distance D_S from the observer (which corresponds to the angular diameter distance), and the lens is located at angular distance D_L.

In the thin lens approximation, the light ray is deflected when it intersects the lens plane, *i.e.* the plane orthogonal to the line-of-sight which contains the lens. The 2-D physical coordinates η and ξ denote the position of the source in the source plane, and the position of the light ray in the lens plane, respectively. Obviously, we can relate the physical lengths to the angular positions, such as $\vec{\eta} = D_s\vec{\beta}$ and $\vec{\xi} = D_L\vec{\theta}$.

One can easily demonstrate by geometrical considerations that the lensing equation can be written in the small angle approximation as:

$$\vec{\eta} = \frac{D_S}{D_L}\vec{\xi} - D_{LS}\widehat{\alpha}(\vec{\xi})\,. \tag{2.3}$$

Or equivalently, by writing this equation in angular coordinates:

$$\vec{\beta} = \vec{\theta} - \frac{D_{LS}}{D_S}\vec{\widehat{\alpha}}(\vec{\theta}) = \vec{\theta} - \vec{\alpha}(\vec{\theta})\,, \tag{2.4}$$

where I introduced the reduced deflection $\alpha = \frac{D_{LS}}{D_S}\widehat{\alpha}$. I can re-write the deflection angle from Eq. 2.2 as:

$$\vec{\alpha} = \frac{2}{c^2}\frac{D_{LS}}{D_S} \int \vec{\nabla}_\perp \phi\ dl\,. \tag{2.5}$$

I thus define the lensing potential in the thin lens approximation:

$$\psi = \frac{2}{c^2}\frac{D_{LS}}{D_S D_L} \int \phi\ dl\,, \tag{2.6}$$

and the reduced deflection field takes the convenient form:

$$\vec{\alpha} = \vec{\nabla}_\theta \psi\,. \tag{2.7}$$

I have replaced the perpendicular gradient, according to $\vec{\nabla}_\perp = \vec{\nabla}_\theta / D_L$. The lensing equation is non-linear: one source position $\vec{\beta}$ can lead to multiple images $\vec{\theta}$.

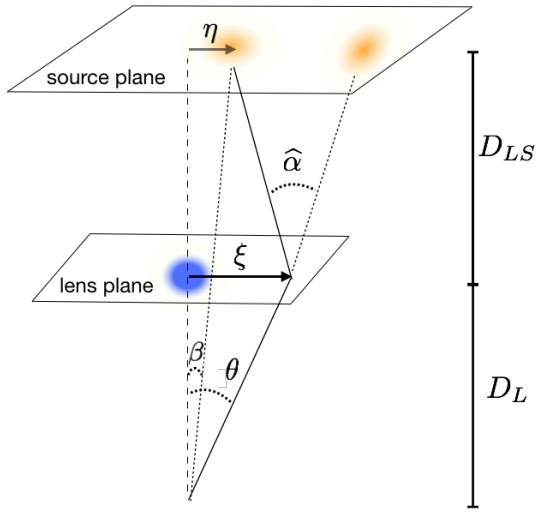

Figure 2.1 – Schematic view of the a gravitational lensing system in the thin lens approximation. Light ray emitted from the source at the coordinates $\vec{\beta}$, converges to the observer with the 'apparent' angular coordinates $\vec{\theta}$. At the intersection of the light ray and the lens plane, it is deviated by an 2-D angular vector $\vec{\widehat{\alpha}}$. The angular distances between the observer, the lens and the source are represented. The figure is inspired by Bartelmann & Schneider (2001). Note that in expending Universe, we have: $D_S \neq D_L + D_{LS}$.

2.1.2 Linearisation of the lens mapping

Having derived the lens equation 2.4, I can write the Jacobian of the transformation from the image to the source plane $\theta \rightarrow \beta(\theta)$ as:

$$A_{ij} = \frac{\partial \beta_i}{\partial \theta_j}\,, \tag{2.8}$$

$$= \delta_{ij} - \frac{\partial \alpha_i}{\partial \theta_j}\,, \tag{2.9}$$

$$= \delta_{ij} - \frac{\partial^2 \psi}{\partial \theta_i \partial \theta_j}\,. \tag{2.10}$$

The convergence and shear are introduced as function of the tidal field $\partial^2\psi/\partial\theta_i\partial\theta_j$:

$$\kappa = \frac{1}{2}\left(\frac{\partial^2\psi}{\partial\theta_1^2} + \frac{\partial^2\psi}{\partial\theta_2^2}\right)\,, \quad \gamma_1 = \frac{1}{2}\left(\frac{\partial^2\psi}{\partial\theta_1^2} - \frac{\partial^2\psi}{\partial\theta_2^2}\right)\,, \quad \gamma_2 = \frac{\partial^2\psi}{\partial\theta_1\,\partial\theta_2}\,. \tag{2.11}$$

Following these definitions, the magnification tensor can be rewritten as:

$$A = \begin{pmatrix} 1-\kappa-\gamma_1 & -\gamma_2 \\ -\gamma_2 & 1-\kappa+\gamma_1 \end{pmatrix}\,. \tag{2.12}$$

The diagonal part of the Jacobian, corresponding to the convergence κ, illustrates an isotropic deformation, *i.e.* by increasing or decreasing the size of the source.

In contrast, the traceless part of the matrix denotes an anisotropic stretching of source shape, and depends on the the shear components (γ_1, γ_2). Mathematically, the shear is a complex number which can be written as $\gamma = \gamma_1 + i\gamma_2 = |\gamma|e^{2i\varphi}$, where φ is the polar angle between the two shear components. The shear field is therefore a spin-2 quantity, due to the factor 2 in the exponential. It is invariant under a rotation by π, *i.e.* an ellipse rotated by π is transformed into itself. The behaviour of a circular source as sheared by γ_1, γ_2 components is illustrated in figure 2.2. One can re-express the shear relative to the peculiar center $\vec{\theta_r}$. Thus, one can define the tangential and the cross components of the shear $(\gamma_t, \gamma_\times)$ as:

$$\gamma_t(\vec{\theta};\vec{\theta_r}) = -\mathrm{Re}\left[\gamma e^{2i\phi}\right] \quad \text{and} \quad \gamma_\times(\vec{\theta};\vec{\theta_r}) = -\mathrm{Im}\left[\gamma e^{2i\phi}\right]\,, \tag{2.13}$$

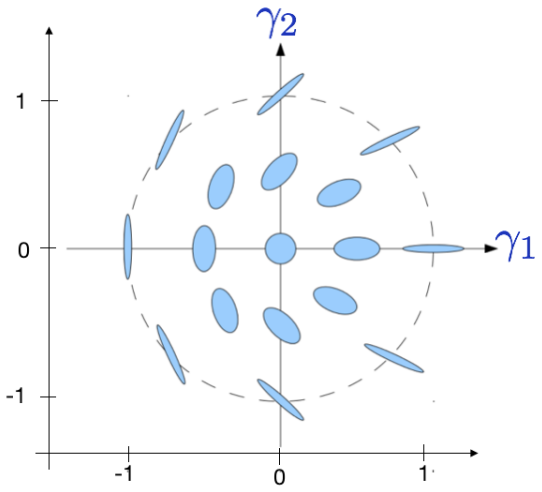

Figure 2.2 – Schematic view of a constant shear field γ deforming a circular source. The orientation of the deformation is given in the Cartesian coordinates of the shear γ_1, γ_2. The ellipse rotation is invariant by π, thus the shear is a 2-spin field as $\gamma = e^{i\varphi}$.

where ϕ is the polar angle between $\vec{\theta}$ and $\vec{\theta_r}$. Taking the center of the lens as a point of reference, we find that shear is purely tangential for a perfectly circular lens, whereas any departure from the circular symmetry in the mass distribution of the lens induces a cross-shear component.

I finally introduce the notion of the reduced shear $g = \gamma/(1-\kappa)$, which constitutes the measurement extracted form the ellipticity of galaxies. Indeed, one can rewrite the Jacobian matrix such as:

$$A = (1-\kappa)\begin{pmatrix} 1-g_1 & -g_2 \\ -g_2 & 1+g_1 \end{pmatrix}, \tag{2.14}$$

where $(1-\kappa)$ is a multiplicative factor. The actual distortion measured in the background galaxies is thus the reduced shear.

The convergence, which is the Laplacian of the lensing potential, can be related to the surface density Σ by considering the Poisson equation:

$$\left.\begin{array}{c} \Delta\phi_{2D} = 4\pi G\Sigma \\ \Delta\psi = 2\kappa \end{array}\right\} \kappa = \frac{4\pi G}{c^2}\frac{D_S}{D_L\ D_{LS}}\Sigma = \frac{\Sigma}{\Sigma_{\rm crit}}\,. \tag{2.15}$$

The convergence is a dimensionless surface density, where the critical surface density is:

$$\Sigma_{\rm crit} = \frac{c2}{4\pi G}\frac{D_L\ D_{LS}}{D_S}\,. \tag{2.16}$$

For a mass distribution close to the critical density, we are in the strong lensing regime.

Finally, notice that the equations 2.11 can be re-written in Fourier space (Kaiser & Squires 1993):

$$\widehat{\psi} = \frac{\widehat{\kappa}}{|l|^2}\begin{cases} \widehat{\gamma_1} = (l_1^2\ -\ l_2^2)\widehat{\psi}\,, \\ \widehat{\gamma_2} = 2i\ l_1\ l_2\ \widehat{\psi}\,, \\ \widehat{\alpha_1} = il_1\ \widehat{\psi}\,, \\ \widehat{\alpha_2} = il_2\ \widehat{\psi}\,, \end{cases} \tag{2.17}$$

where $\vec{l} = (l_1, l_2)$ represent the 2-D Fourier vector, and $\widehat{X}$ denotes the Fourier transform of X.

2.1.3 The conservation of surface brightness

An important feature of gravitational lensing is the conservation of surface brightness (Etherington 1933). The luminosity per unit solid angle in the source plane of an extended source is equal to the surface brightness observed in the image. Mathematically, it can be translated as:

$$I(\vec{\theta}) = I^s \left[\vec{\beta}(\vec{\theta})\right] , \tag{2.18}$$

where $I(\vec{\theta})$ and $I^s \left[\vec{\beta}(\vec{\theta})\right]$ are the brightness distributions in the lens and source planes, respectively. Locally, for a point $\vec{\theta_0}$ in an extended image, which corresponds to $\vec{\beta_0} = \vec{\beta}(\vec{\theta_0})$ in the source plane, we have:

$$I(\vec{\theta}) = I^s \left[\vec{\beta_0} + A(\vec{\theta_0})(\vec{\theta} - \vec{\theta_0})\right] . \tag{2.19}$$

This translates the fact that a circular source may become an ellipse in the lens plane.

2.1.4 Magnification

Magnification μ is defined as the ratio between the flux of the image and flux of the source. Mathematically, in the limit of a point source, the local magnification is given by the inverse of the determinant of the matrix A:

$$\mu^{-1} = \det A = (1-\kappa)^2 - \gamma^2 . \tag{2.20}$$

The eigenvalues of the magnification tensor are then the amplification in the tangential and in the radial direction:

$$\mu_t = \frac{1}{\lambda_t} = \frac{1}{1-\kappa-\gamma} , \tag{2.21}$$

$$\mu_r = \frac{1}{\lambda_r} = \frac{1}{1-\kappa+\gamma} . \tag{2.22}$$

When the determinant of the Hessian matrix vanishes, the magnification becomes infinite. This is not possible in practice, because sources have a finite size. The set of coordinates in the lens plane $\vec{\theta}$ where $\lambda_t \to 0$ (or $\lambda_r \to 0$) defines the tangential (or the radial) critical line (Blandford & Narayan 1986). Translating these curves in the source plane leads to the definition of the caustics: any sources close to the caustic will be extremely magnified and distorted. Only sources inside a caustic presents multiple images.

2.1.5 The mass-sheet degeneracy

Another important concept is the mass-sheet degeneracy (MSD) (Falco et al. 1985). By considering a shift of source location by a factor $\beta \to \lambda\beta$ in equation 2.4, one can preserve the image positions and shapes, and magnification ratios, by considering a different lens characterised by deflection angle α', such as:

$$\lambda\beta = \lambda\theta - \frac{D_{ls}}{D_s}\lambda\theta = \theta - \frac{D_{ls}}{D_s}\left(\lambda\alpha + \frac{D_s}{D_{ls}}(1+\lambda)\theta\right) \equiv \theta \ - \frac{D_{ls}}{D_s}\alpha' , \tag{2.23}$$

Thus, this degeneracy in the lens equation can be seen as a additional sheet of constant convergence $(1-\lambda)$:

$$\kappa \to \kappa' = \lambda\kappa + (1-\lambda) , \tag{2.24}$$

The so-called *mass-sheet degeneracy* appears as a limitation in mass determination by weak gravitational lensing. This degenerate relation is also present in the strong lensing regime, and can impact for example the determination of the Hubble constant (Schneider & Sluse 2013).

2.2 The variety of weak lensing observables

In this section, I give a brief overview of commonly-used lensing estimators along with the scale and the objects that we probe.

By using the weak lensing signal, one can investigate matter distribution on large scales. In particular, one can probe the statistics of the projected total density field of large scale structure by considering the cosmic shear. Moreover, by focusing on individual lenses (like galaxies and galaxy clusters), one can determine their density profile by measuring the tangential shear signal. The weak lensing regime is characterised by $\kappa, \gamma \ll 1$. The associate shear signal must therefore be statistically extracted by averaging over a large number of galaxy ellipticities.

2.2.1 Estimating the shear from background galaxies

In the weak gravitational lensing regime, the image of an elliptical source is also an ellipse. One can define the tensor of second moments of the surface brightness of an image:

$$Q_{ij} = \frac{\int d^2\theta \; I(\theta) \; (\theta_i - \overline{\theta}_i) \; (\theta_j - \overline{\theta}_j)}{\int d^2\theta \; I(\theta)} \,, \tag{2.25}$$

where $(\overline{\theta}_i, \overline{\theta}_j)$ is the barycentre of the image. From the surface brightness conservation equation eq. 2.19, it becomes that the moments of the image Q can be expressed as a function of the moments of the source Q^S such as:

$$Q_S = AQA^T \,. \tag{2.26}$$

The shape of an image can be described by the complex polarisation χ, or the complex ellipticity parameter ε:

$$\chi = \frac{Q_{11} - Q_{22} + 2Q_{12}}{Q_{11} + Q_{22}} \,, \qquad \varepsilon = \frac{\chi}{1 + \sqrt{1 - |\chi|^2}} \,. \tag{2.27}$$

Therefore, from the 2.26, the complex ellipticity of an background galaxy χ can be related to the complex ellipticity of the source χ^S (Schneider & Seitz 1995; Seitz & Schneider 1995, 1997), by the following relation:

$$\chi = \frac{\chi_S - 2g + g^2\chi_s^*}{1 + |g|^2 - 2R(g\chi_S^*)} \,, \tag{2.28}$$

where * denotes the conjugation of a complex number. From this transformation, one can also find the transformation between the ellipticity of an image and it intrinsic ellipticity (the unlensed galaxy shape), for $|g| < 1$:

$$\varepsilon = \frac{\varepsilon^S + g}{1 + g^*\varepsilon^S} \,. \tag{2.29}$$

In addition, galaxies are supposed to be randomly orientated in the sky, meaning that $\langle \varepsilon^S \rangle = 0$. Therefore, the shape of image galaxies is seen as an unbiased estimator of the reduced shear $\langle \varepsilon \rangle = g$ (Schneider & Seitz 1995). In the weak lensing regime, with $\kappa \ll 1$, one can approximate $\langle \varepsilon \rangle = \gamma$. The rms dispersion of the intrinsic ellipticity distribution is of the order $\sigma_\varepsilon \sim 0.3$. The noise induced by intrinsic galaxy shapes must be taken into account, and the shear signal to noise ratio is simply:

$$\left(\frac{S}{N}\right)_{shear} = \gamma\sqrt{N}/\sigma_\varepsilon \,, \tag{2.30}$$

where N is the number of background galaxies. Averaging over a large number of background galaxies is essential, so as to reduce the shape noise. For example, for a shear value of $\gamma \sim 0.03$, we need to average over 100 galaxies to get an estimate of the shear with $S/N \sim 1$. This source of uncertainty is a fundamental limitation in the accuracy of weak lensing measurements. Future

	CFHTLenS	KiDS (KiDS-450)	DES (Y1)	HSC-SSP (DR1)
Area (deg^2)	154 deg2	1500 (450)	5000 (1321)	1400 (100)
Photometric bands	ugriz	ugri	griz	grizy
Effective galaxy number density ($gal/arcmin^2$)	14	6 (8.53)	10	21.8
Pixel size at the focal plane (arcsec)	0.187	0.214	0.27	0.168
Publications	Heymans, 2012 Erben, 2013	Kuijken, 2015 (Hildebrandt, 2017)	DES collaboration, 2005 (Abbott, 2017)	Aihara, 2018a (Aihara, 2018b)

Table 2.1 – The features of CFHLenS, KiDS, DES and HSC-SSP

surveys will reduce this noise term by providing a larger number of detected sources, such as the density number of galaxy will be $n_g \sim 30$ galaxies/arcmin^2; this can be contrasted to current ground based data sets with $n_g \sim 5/20$ galaxies/arcmin^2.

2.2.2 Current and ongoing weak lensing galaxy surveys

In order to perform accurate weak lensing analyses, a large number of background galaxy shapes and redshift measurements is required to reduce the statistical uncertainties. In fact, large (photometric) weak lensing survey is often chosen to overlap with (spectroscopic) galaxy surveys which map the foreground galaxy distribution. I will briefly review the common current and upcoming weak lensing galaxy surveys, before presenting results on lensing observables in the next sections.

Shape measurement of background galaxies has been carried out in the past by different surveys such as the CFHTLenS (Heymans et al. 2012b; Erben et al. 2013). This survey is a 154 square degree multi-colour optical survey in *ugriz* bands, and based on the Canada France Hawaii Telescope Legacy Survey (CFHTLS) and optimised for weak lensing analysis[1].

At the present time, ongoing wide-area weak lensing surveys from ground-based experiments, such as Kilo-Degree Survey (KiDS, Kuijken et al. 2015), Dark Energy Survey (DES, The Dark Energy Survey Collaboration 2005), and the Hyper Suprime-Cam Subaru Strategic Program (HSC-SSP, Aihara et al. 2018a), start to provide their first data releases to the community (for example DES-Y1, HSC-DR1, DES Collaboration et al. 2017; Aihara et al. 2018b). The larger fraction of observed sky dramatically increases the number of galaxy shape measurements, and therefore reduces the shape noise on WL signal. The different features of these weak lensing surveys are gathered in table 2.1.

[1] in terms of data reduction (Erben & CFHTLenS Collaboration 2012), shape measurement (Miller & CFHTLenS Collaboration 2012), photometric redshifts (Hildebrandt et al. 2012), and systematic error analyses (Heymans et al. 2012a).

2.2.3 2-D mass map reconstruction from the ellipticity of background galaxies

Mapping the density field with weak lensing is a primordial tool as it allows to map the underlying dark matter distribution at various scales.

Technically, one can construct the shear map by detecting the observed galaxy shapes centred on a given structure (galaxy, galaxy cluster, or larger aperture). At this stage, one must keep in mind possible contaminations of the shear signal, which could be caused by effects such as atmospheric variations and instrumental biases. Methods to correct these biases can be found in the literature, such as the Kaiser, Squires & Broadhurst method (Kaiser et al. 1995; Luppino & Kaiser 1997; Hoekstra et al. 1998). Complementary information on weak lensing shear reduction can be found in Heymans et al. (2006).

The measured shear signal can be transformed into a convergence map by inverting the shear in Fourier-space, following equations 2.17:

$$\widehat{\kappa} = \frac{l_1^2 - l_2^2}{|l|^2}\widehat{\gamma_1} + \frac{2l_1 l_2}{|l|^2}\widehat{\gamma_1}\,. \tag{2.31}$$

The convergence field reconstruction is complex, as we have to use inversion algorithms (Kaiser & Squires 1993; Seitz & Schneider 1995). 2-D mass mapping algorithms have been proposed in the literature to resolve this inverse problem accurately and efficiently (Bartelmann 1995; Bradač et al. 2005; Starck et al. 2006; Pires et al. 2009). The noise of convergence maps can be estimated by considering the number density of background galaxies (van Waerbeke 2000).

Using advances in the field of mass reconstruction techniques (Kaiser & Squires 1993; Kaiser et al. 1995; Lombardi & Bertin 1998), mapping the projected matter density field by using gravitational lensing has become commonplace in observational cosmology (Clowe et al. 1998; Hoekstra et al. 1998, 2000; Clowe & Schneider 2001). Indeed, the total mass distribution of galaxy clusters reflects the properties and the nature of dark matter. Figure 2.3 illustrates a typical density map of a merging cluster (Clowe et al. 2006). We clearly observe that the total mass distribution from weak lensing differs from the hot gas mapping. This observation constitutes a direct evidence of the collisionless nature of the dark matter. Indeed, as we see, stars and dark matter are not affected by the past collision, whereas the gas (highly collisional) is chocked and slowed by the collision.

Projected density maps of galaxy clusters made through weak lensing observations can be completed with baryonic observables such as X-rays and galaxy mapping (Clowe et al. 2004; Markevitch et al. 2004; Clowe et al. 2006; Randall et al. 2008; Merten et al. 2011). These joint analyses of galaxy clusters are used to investigate the relationship between the astrophysical properties of clusters and their surrounding dark matter halos, such as the scaling relations between X-ray properties and the cluster masses.

In detail, cluster mass estimation is obtained by averaging the shear signal into radial shells centred on the cluster. Then, the tangential distortion profile can be fitted by spherical mass profile models (like the Navarro-Frenk-White, or singular isothermal sphere profile), to estimate the cluster mass, and cluster concentration, as defined in section 1.2.4.1 (Okabe et al. 2010; Bhattacharya et al. 2013). From these type of weak lensing analyses, the estimation of the mass-to-light ratios of clusters has been derived and calibrated (Parker et al. 2005; Mandelbaum et al. 2006a; Johnston et al. 2007). The inferred mean halo mass -richness (number of galaxies) and -luminosity relations appear to be well fit by a power-law relations. As expected rich clusters are more massive, and more luminous. In order to exploit clusters as cosmological probes[2], such cluster mass-observable relations have to be precisely calibrated in the first instance.

[2]The DM halos mass function is strongly influenced by the considered cosmological model.

Figure 2.3 – Composite image of the famous merging cluster of galaxies, named as the Bullet Cluster. The hot diffuse gas is draw in pink (detected by X-ray emission), the total mass distribution (reconstructed by weak lensing measurements) is in blue, and galaxy distribution is illustrated in background (optical bands). Credit to Markevitch (2006) and Clowe et al. (2006).

2.2.4 Galaxy-galaxy lensing

Galaxy-galaxy lensing (GGL) consists in the weak lensing effect induced by a massive foreground galaxy, on the distant galaxies. It probes the projected density of the lens, *i.e.* the radial density profile of foreground galaxies.

This approach consists in azimuthally averaging galaxy ellipticities in concentric annuli centred on the lens, to estimate the tangential shear $\gamma_T(|\vec{\theta}|)$ as a function of the angular separation to the lens. Because individual galaxies are not massive enough to produce a significant GGL effect (distortions of order 0.1%), one must stack the shear signal around a large number of foreground lens galaxies.

If the spectroscopic redshifts of foreground galaxies are available, one can then compute the excess of surface mass density $\Delta\Sigma$. Indeed, one can demonstrate that the mean tangential shear can be related to the mean surface density inside a circle and the mean density on the circle (Schneider et al. 1992):

$$\gamma_t(R) = \frac{\overline{\Sigma}(< R) - \overline{\Sigma(R)}}{\Sigma_{\rm crit}} \equiv \Delta\Sigma \; \Sigma_{\rm crit}^{-1} \, . \tag{2.32}$$

A common observational technique is to jointly analyse two overlapping galaxy surveys by considering the foreground lens galaxies from the spectroscopic one. The ellipticities of distant galaxies are given by a (photometric) survey. For example, GAMA (Driver et al. 2011) and KiDS (de Jong et al. 2013) surveys were cross-correlated to improve the accuracy of tangential shear measurement around galaxies (Velliscig et al. 2017; van Uitert et al. 2018) and galaxy groups (Viola et al. 2015).

As illustrated in figure 2.4, we show the GGL shear profile, averaged over a large sample of lens galaxies (Parker et al. 2007). Background galaxies appear tangentially aligned with the lens, whereas by symmetry the cross component is null on average. Fitting the mean tangential shear measurements with a parametric profile (like NFW or Einasto) allows us to estimate the mean halo mass and concentration of the lens sample (Kleinheinrich et al. 2006; Hoekstra et al. 2005; Mandelbaum et al. 2008). The ellipticity of dark matter haloes can also be investigated by

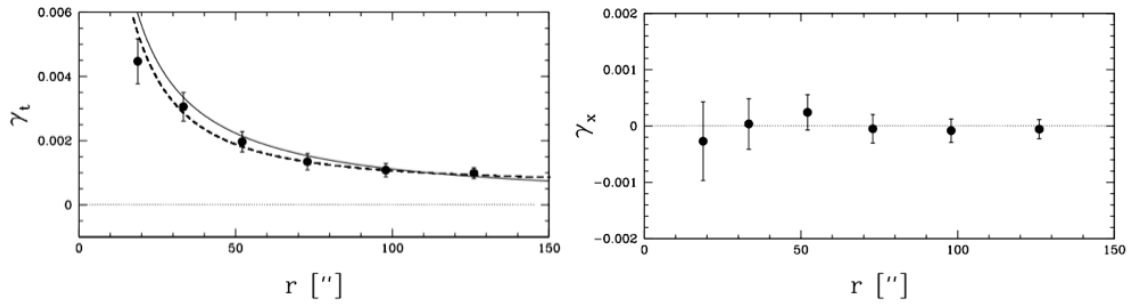

Figure 2.4 – The averaged tangential and cross shear as a function of radius around a sample of CFHTLS galaxies (Parker et al. 2007). The median lens redshift is 0.4 and the median source redshift is 0.9. The dashed and solid lines represents the fits by the Navarro-Frenk-White and isothermal profile, respectively. The best NFW fit corresponds to a halo with a scale radius $r_{200} = 150\ h^{-1}kpc$ and virial mass $M_{200} = 7.6\ 10^{11}\ h^{-1}M_{\odot}$.

galaxy-galaxy weak lensing (Mandelbaum et al. 2006a; Parker et al. 2007). The GGL signal is thus used to characterise the properties of dark matter halos at galactic scales.

One can further sub-divide the foreground lens galaxy samples depending of their properties: galaxy type, luminosity, stellar mass, morphology, satellite or central galaxies. This allows to probe the relationship between galaxy properties and their host dark matter halo. Such work was performed by Sheldon et al. (2004) using the SDSS: $\Delta\Sigma$ was evaluated for early and later type galaxies, separately. The correlation between galaxies and the tangential distortion of background sources was also explored by Mandelbaum et al. (2006b), who studied satellite fractions for late- and early- type galaxies. In this vein, the galaxy-mass correlation function was investigated by GGL to constrain the evolution of the galaxy population over cosmic time (Guzik & Seljak 2001; Mandelbaum et al. 2006b; Leauthaud et al. 2012; Velander et al. 2014; Hudson et al. 2015; Coupon et al. 2015). By studying the evolution of stellar-halo mass ratio M_*/M_h depending of the halo mass, it appears a characteristic halo mass M_h^{peak} for which star formation is most efficient. For lower and higher halo masses, complex physical mechanisms are responsible in quenching star formation (see section 1.2.5.2 galaxy-halo connection).

2.2.5 Two-point cosmic shear statistics

Besides the direct characterisation of mass distribution properties with shear measurement, we can consider the statistics of the shear signal. Indeed, since the first detections of weak gravitational lensing by large-scale structure (Van Waerbeke et al. 2000b; Bacon et al. 2000; Wittman et al. 2000), the statistics of the shear signal are widely used to probe the underlying cosmological model to constrain cosmological parameters. Here, I will mostly focus on the two-point statistics of the lensing signal.

The weak lensing power spectrum

The two-point correlation function (2PCF) of the convergence is written as $\langle\kappa(\vec{\vartheta})\kappa(\vec{\vartheta}+\vec{\theta})\rangle$, where $\vec{\theta}$ is the angular separation vector between two lines of sight. Assuming that the density field is homogeneous and isotropic (cosmological principle) and that the convergence is the projection of the density field along the line-of-sight, we deduce that the convergence correlation function is invariant under rotation and translation. $\langle\kappa(\vec{\vartheta})\kappa(\vec{\vartheta}+\vec{\theta})\rangle$ is therefore a function of the modulus of

the separation vector. It can be written in the Fourier space:

$$\langle \widehat{\kappa}(\vec{l})\widehat{\kappa}^*(\vec{l'})\rangle = (2\pi)^2\delta(\vec{l}-\vec{l'})P_\kappa(l)\,, \tag{2.33}$$

where $P_\kappa(l)$ is the convergence power spectrum, and l is the 2-D Fourier vector such as $\vec{l} = 2\pi/\vec{\theta}$. Note that we have assumed a flat sky, and did not use spherical harmonics.

One can relate the shear and the convergence in Fourier space by using the complex form of the shear:

$$\widetilde{\gamma} = \left(\frac{(l_1^2 - l_2^2)}{|l|^2} + \frac{(2il_1l_2)}{|l|^2}\right)\widetilde{\kappa} = e^{2i\phi_l}\widetilde{\kappa}\,, \tag{2.34}$$

where ϕ_l is the polar angle of the Fourier vector $\vec{l}$. Following this formula, it becomes evident that the shear and the convergence have the same power spectrum: $P_\kappa = P_\gamma$.

The cosmic shear power spectrum can be written as an integral of the 3-D matter power spectrum along the line-of-sight (Miralda-Escude 1991; Blandford et al. 1991; Kaiser 1992):

$$P_\kappa(l, z_s) = \left(\frac{3\Omega_{\rm m}H_0^2}{2c^2}\right)^2 \int_0^{\chi_{\rm s}} {\rm d}\chi \left(\frac{\chi(\chi_{\rm s}-\chi)}{\chi_{\rm s}a(\chi)}\right)^2 P_\delta\left(\frac{l}{\chi}, \chi\right)\,, \tag{2.35}$$

where $\chi_{\rm s}$ is the comoving distance between the source plane and the observer. The small-angle and flat-sky approximations are assumed in this formulation. It also supposed that $\vec{k} = \frac{\vec{l}}{\chi}$, meaning that only modes perpendicular to the line-of-sight are relevant. This is the so-called "Limber" approximation (Limber 1953).

Following this formulation, I predict the lensing power spectra for different source redshifts: the result is shown in figure 2.5. The matter power spectrum P_δ, in linear and non-linear regimes, have been predicted with the Cosmic Linear Anisotropy Solving System (CLASS) code (Blas et al. 2011; Lesgourgues 2011). This Boltzmann code numerically resolves the linear perturbation theory, and non-linear corrections, to provide an accurate estimation of cosmological observables, as depending of the cosmological parameters given in input. Then, I integrated matter power spectra under the Limber approximation. Note that equation (2.35) assumes all lensed galaxies are at the same redshift. One can also take into account the observed galaxy distribution in redshift $p(z)$, which is commonly expressed as a Gamma PDF of the form:

$$p(z) \propto \left(\frac{z}{z_0}\right)^{a-1} {\rm e}^{-z/z_0}\,, \tag{2.36}$$

where a, z_0 are free parameters estimated from galaxy observations. Recently, Laigle et al. (2016) estimated photometric redshift distributions with $a \simeq 2.1$ and $z_0 \simeq 0.51$ using the COSMOS2015 catalogue. The effective convergence power spectrum is therefore computed by weighting the contributions of the different source planes:

$$P_\kappa(l) = \int P_\kappa(l, z_s)\; p(z_s)\; dz_s\,. \tag{2.37}$$

Commonly, the measurement of lensing power spectrum is used to jointly constrain the matter density parameter Ω_m and the amplitude of the matter power spectrum σ_8. Recently, its characterisation at different source redshift, the so-called cosmic shear tomography, has also been used to probe the dark energy equation of state. The weak lensing power spectra have thus been extensively measured in large galaxy surveys (Brown et al. 2003; Heymans et al. 2005; Kitching et al. 2007; Lin et al. 2012; Kitching et al. 2014; Köhlinger et al. 2016; Abbott et al. 2016; Alsing et al. 2017; Köhlinger et al. 2017) .

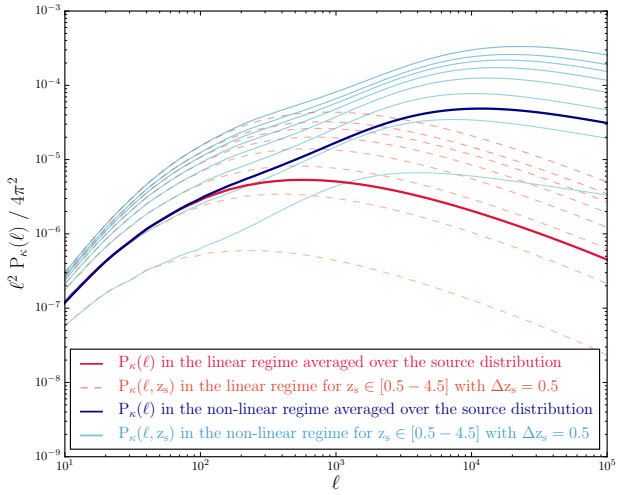

Figure 2.5 – The predicted lensing power spectra in linear and non-linear regimes.Prediction done by integrating P_δ from CLASS code in the the Limber approximation (Gouin et al. 2017)

The angular correlation of pairs of galaxy ellipticities

In addition to the lensing power spectrum, an even more direct observable quantity of weak lensing statistics is the two-point shear correlation function (2PSCF). The angular shear correlation is simpler to measure because it can directly be computed in real space. The correlation of the shear at two-points yields four quantities: $\langle\gamma_t\gamma_t\rangle$, $\langle\gamma_\times\gamma_\times\rangle$, $\langle\gamma_t\gamma_\times\rangle$ and $\langle\gamma_\times\gamma_t\rangle$. By parity conservation, one can show that $\langle\gamma_t\gamma_\times\rangle = \langle\gamma_\times\gamma_t\rangle = 0$.

Two-point correlation functions can be defined (Miralda-Escude 1991):

$$\xi_\pm(\theta) = \langle\gamma_t(\vec{\vartheta})\gamma_t(\vec{\vartheta}+\vec{\theta})\rangle \pm \langle\gamma_\times(\vec{\vartheta})\gamma_\times(\vec{\vartheta}+\vec{\theta})\rangle\,, \tag{2.38}$$

where isotropy and homogeneity considerations tell us that $\xi_\pm$ are only functions of the modulus of the separation vector $\vec{\theta}$. The shear correlation functions $\xi_\pm$ are related to the lensing power spectrum by the Hankel transform:

$$\xi_\pm(\theta) = \frac{1}{2\pi}\int_0^\infty dl\; l\; J_{0/4}(l\theta)P_\kappa(l)\,, \tag{2.39}$$

where J_ν is the Bessel function of order ν. This formulation allows us to predict the two-point correlation function via a numerical integration of the convergence power spectrum.

Observationally, one can estimate the shear correlation function by cross correlating the ellipticity of galaxy pairs, binning by separation angle between the pairs (Schneider et al. 2002):

$$\widehat{\xi_\pm}(\theta) = \frac{\sum_{ij}\omega_i\omega_j(\varepsilon_t^i\varepsilon_t^j \pm \varepsilon_x^i\varepsilon_x^j)}{\sum_{ij}\;\omega_i\omega_j}\,. \tag{2.40}$$

To each galaxy ellipticity ε^i can be assigned a weight depending on the accuracy of measurement ω_i. Galaxy pairs (i,j) located at angular positions $(\vec{\vartheta_i},\vec{\vartheta_j})$, are collected in bins of angular distance $|\vec{\theta}| = |\vec{\vartheta_i} - \vec{\vartheta_j}|$.

The shear correlation function has been measured on large galaxy surveys, such as in CFHTLenS (Heymans et al. 2013; Kilbinger et al. 2013), Deep Lens Survey (Jee et al. 2013), KiDS (Hildebrandt et al. 2017), and in DES (Troxel et al. 2017). The measurement made from CFHTLenS data sets is presented in figure 2.6 as an example (Kilbinger et al. 2013).

Recently, Hildebrandt et al. (2017) have constrained cosmological parameters from cosmic shear measurements made in the KiDS survey. This study used accurate theoretical models which take into account the intrinsic alignment of galaxies and the impact of baryon feedback.

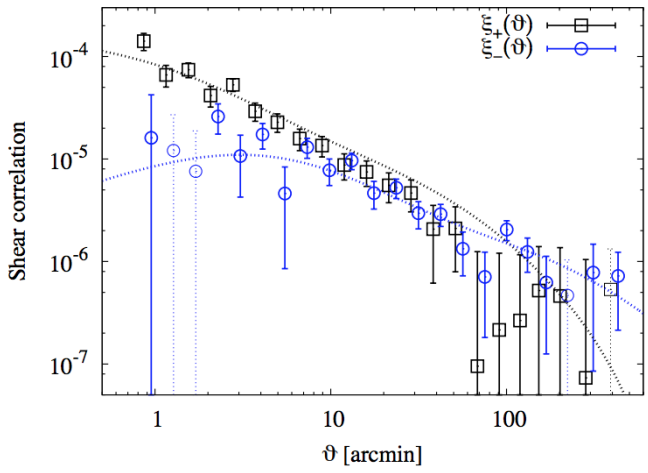

Figure 2.6 – The two-point shear correlation functions $\xi_{\pm}$ measured in CFHTLens. The dotted lines presented the non-linear model prediction. This figure comes from Kilbinger et al. (2013). Copyright 2013 Oxford University Press.

Indeed, cosmic shear tomography analyses constitute an important probe of the cosmological model, and leads to potential inconsistencies with the CMB results, as described in (MacCrann et al. 2015). Therefore, this analysis was made with a high level of accuracy (comparable to photo-z calibration) and a precise treatment of systematic errors (like measurement errors, sample variance, and covariance estimation).

2.2.6 The future Euclid weak lensing survey

Future large galaxy surveys such as Euclid (Laureijs et al. 2011), Large Synoptic Survey Telescope (LSST, Chang et al. 2013) and Wide-Field Infrared Survey Telescope (WFIRST, Spergel et al. 2015) will provide the unprecedented opportunity to improve our constrains on cosmological parameters by measuring the cosmic shear, and to better characterise the dark matter density field properties from large to galactic scales by using galaxy-galaxy lensing and mass mapping. In particular, my thesis project fits into the framework of the future Euclid mission with the ultimate goal to predict weak lensing observables with its expected level of precision. This mission aims to investigate the nature of dark energy and dark matter, by using two complementary cosmological probes: weak lensing and galaxy clustering.

The Euclid space mission will be launched around 2022, and will observe the sky far 6 years. Two main instruments will perform the Euclid galaxy catalogue: the VIS (optical imager), the Near Infrared Spectrometer Photometer (NISP). The VIS instrument will offer a high image quality (with a pixel size of 0.1 arcsec on the focal plane) and a very stable point-spread function (PSF)[3]. It will thus considerably improve galaxy shape measurements. The NISP instrument has a pixel size of 0.3 arcsec (on the focal plane), and will provide a Deep NIR photometry (3 near infrared band filters Y J and H). The near infrared spectrometer (NIS) will measure galaxy spectra with 4 different near infrared grisms (from 920 to 1850 nm).

The Euclid mission will perform two galaxy surveys: a wide survey which covers 15 000 square degrees of the sky, and a deep one (with 2 magnitude deeper) by covering around 40 deg^2. The wide survey will contain around 1.5 billion of galaxy shape measurements (> 30 galaxies per arcmin^2) with an unprecedented sensitivity, as it is illustrated in figure 2.7. Moreover, Euclid wide galaxy survey will be completed by ground base data sets to obtain photometric redshifts[4]

[3]This is an effect of the imaging system due to the instrument and the atmosphere. Anisotropic PSF induces artificial correlations of galaxy shapes. This contamination can be estimated by calibrating the PSF on a sample of stars, for example.

[4]Different of ground-based-imaging data, such as DES, are currently considered, and to complete the photometry measurements performed by Euclid, in order to improve the photometric redshift estimation of galaxies.

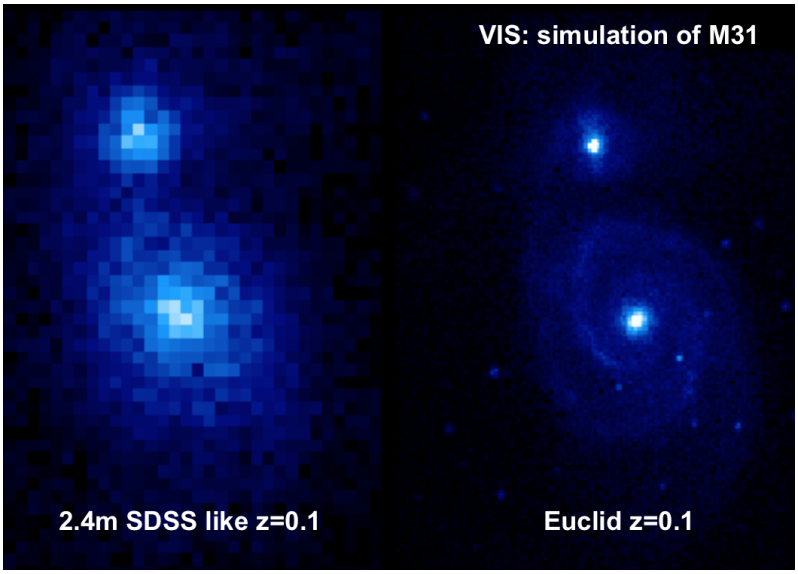

Figure 2.7 – Simulation of Euclid resolution for the observation of M51, compared to SDSS observations, from J. Brinchmann.

with $\Delta z = 0.05(1+z)$ accuracy out to redshift of ~ 2. In addition, the NIS will measure 35 million spectroscopic redshifts with 0.001 accuracy. The Deep Euclid survey will contain 1.5 million galaxies with shape and photo-z measurements, and 150 000 galaxies with spectroscopic redshifts.

In fact, Euclid mission is optimised for lensing surveys (knowledge of source redshift distribution and accurate source shape measurements) and will allow to address different gravitational lensing aspects (cosmic shear, galaxy-galaxy lensing, strong lensing events, microlensing...). In particular, with this wide field cosmic shear survey, the distribution of dark matter will be explored across the cosmic time, by weak lensing tomography over 10 redshift slices (in redshift range: $0 < z < 2$). Cosmic shear measurements will be used to probe the expansion history of the Universe, at the DM-dominated/DE-dominated transition period. Euclid aims to measure the cosmic expansion rate to better than 10% (for redshift $0.7 < \mathrm{z} < 2$) (Laureijs et al. 2011).

In addition, considering the expected selection function of cluster photometric survey, Sartoris et al. (2016) estimated that Euclid will detect around 2×10^5 galaxy clusters at $0.2 \leq z \leq 2$. This large cluster number density will lead to drastically improve constraints on dark energy)[5], by using cluster number counts, cluster power spectrum, and cluster scaling relation. Forecast results with Euclid clusters of galaxies is presented figure 2.8.

2.3 Numerical methods to predict the lensing signal

We have seen that Euclid mission will precisely probe the matter distribution until small scales ($k \sim 1h.\mathrm{Mpc}^{-1}$) via weak lensing and galaxy clustering. Therefore accurate predictions of these observables are required down to non-linear scales. As shown in chapter 1, an accurate description of the matter density field in this highly non linear regime requires numerical simulations. Therefore, substantial efforts are underway to accurately estimate lensing observables. Such predictions are essential to interpret observational results and to correctly extract cosmological information.

[5] A dynamical evolution of the dark energy can be described by a equation-of-state parameter ω such as $\omega(a) = \omega_0 + (1-a)\omega_a$.

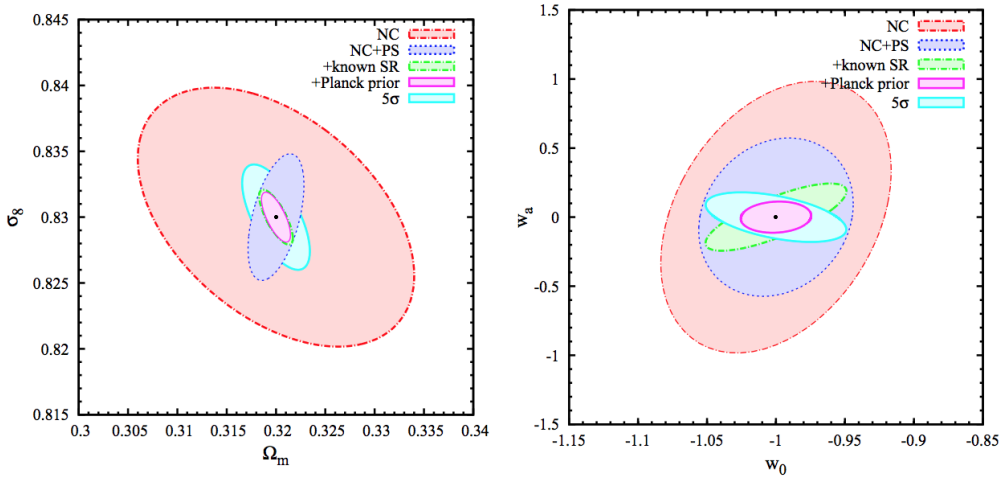

Figure 2.8 – Forecast results with the Euclid Galaxy Cluster Survey. Constraints at the 68% confidence level on the cosmological parameters Ω_m and σ_8 (left panel) and ω_0 and ω_a (right panel) realised by Sartoris et al. (2016). The cosmological probes are the cluster number count (NC), and the cluster power spectrum (PS), with/without a perfect knowledge of cluster scaling relation (SR).

Propagating light rays through dark matter simulations can be done to reproduce the deflection and distortions of light bundles and thereby other lensing observables such as convergence maps, 1-point PDFs, 2-point shear correlation functions, along with characteristics like peaks and voids was done early in the history of the field (eg Jain et al. 2000; Hamana & Mellier 2001; Vale & White 2003; Hennawi & Spergel 2005; Hilbert et al. 2007, 2009; Sato et al. 2009). Much progress has been made since on large and mildly non linear scales with the production of full sky maps with resolutions of a few arc minutes (eg Fosalba et al. 2015; Giocoli et al. 2016a; Takahashi et al. 2017a).

More recently, the impact of baryons and baryonic processes on the lensing signal was investigated through hydrodynamical simulations. Focusing on weak lensing statistics, Semboloni et al. (2011) showed that the 2-point shear correlation function can significantly be affected by the baryonic physics at scales below 10 arcmin. Even the number of convergence peaks is altered by the baryons, to a lesser extent than the power-spectrum (Yang et al. 2013).

Let me now give an overview of the current numerical methods used to implement gravitational lensing through cosmological simulations.

2.3.1 The propagation of light-rays

Light-cone simulation

Numerical predictions of the lensing signal can be done by propagating light-rays through a light-cone. We define a light-cone as a cut in the simulation box over different time steps in order to mimic the matter distribution along a line-of-sight (l.o.s). It is characterised by its opening angle and its direction on the simulation box. The periodic boundary conditions of the simulation box are used to construct coherent structures along the l.o.s. Various efficient methods have been developed to maximise the number of independent light cone realisations which can be made from a unique simulation (see eg. Carlson & White 2010). As an example, the light-cone of the Horizon-AGN simulation, over which I have propagated light-rays, is illustrated in figure 2.9.

Light-cones are registered into a series of slices, which can be extracted either on-the-fly

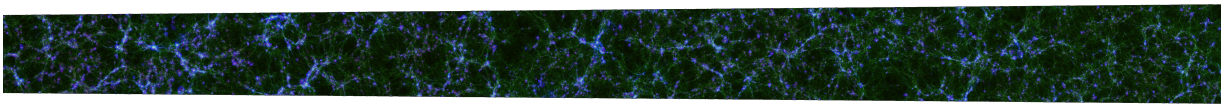

Figure 2.9 – The light-cone of the Horizon-AGN simulation, extracted on-the-fly. The opening angle of the cone is 2.25 deg out to redshift $z = 1$ and 1 deg all the way to $z = 8$.

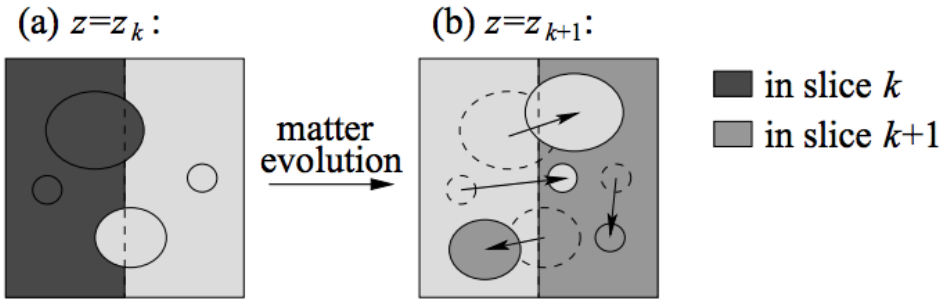

Figure 2.10 – Schematic view of the boundary between two light-cone slices k and $k + 1$. Halos located near a slice boundary are identified in a given slice based on the positions of their centres (a). They can cross the slice boundary between two time steps (b), and so halos included in slice k need to be excluded from the slice $k + 1$. Credit to Hilbert et al. (2009)

(during the run of the simulation), or from simulation outputs at different time step. The slice boundaries have to be carefully treated to avoid truncating structures, as illustrated in figure 2.10. In fact, for two given neighbouring slabs at two consecutive time steps, structures can be counted twice (or not at all) if the inclusion (or exclusion) of structures with large proper motions is not properly accounted for. In Chapter 4, I will go into more details on slice boundaries problems in the light-cone of the Horizon-AGN simulation.

The theory of light-ray propagation in a continuous matter distribution

Before discussing numerical approximations of the theory of light-ray propagation in a continuous matter distribution, let us spend some time by examining the theory. On cosmological scales, the path of a photon is continuously deflected by the gravitational potential ϕ along the line-of-sight, as light rays cross many over/under-dense regions at different locations. Therefore, the thin lens approximation does not hold, and one needs to fully integrate the trajectory of rays along their path.

For a given source plane at comoving distance χ_s, the source plane position of a ray, initially observed at position $\vec{\theta}$ is given by the continuous implicit (Voltera) integral equation (Jain & Seljak 1997b):

$$\vec{\beta}(\vec{\theta}, \chi_\mathrm{s}) = \vec{\theta} - \frac{2}{c^2} \int_0^{\chi_\mathrm{s}} \mathrm{d}\chi \, \frac{\chi_\mathrm{s} - \chi}{\chi_\mathrm{s} \, \chi} \vec{\nabla}_\beta \phi \left(\vec{\beta}(\vec{\theta}, \chi), \chi \right) . \tag{2.41}$$

To first order, one can evaluate the gravitational potential along an unperturbed path becomes:

$$\vec{\beta}(\vec{\theta}, \chi_\mathrm{s}) = \vec{\theta} - \frac{2}{c^2} \int_0^{\chi_\mathrm{s}} \mathrm{d}\chi \, \frac{\chi_\mathrm{s} - \chi}{\chi_\mathrm{s} \, \chi} \vec{\nabla}_\theta \phi \left(\vec{\theta}, \chi \right) . \tag{2.42}$$

This is known as the *Born approximation*, which is common to many diffusion problems of physics. It neglects the continuous deviation of light rays. It is generally an excellent approximation

for small deviations, ie in the weak lensing regime. Note that the Born approximation prevents any possible coupling between two deflectors at different redshift, which can occur when a far lens is already lensed by a nearby structure, and hence becomes more (or less) efficient at deflecting even more distant sources than it would be in the absence of the near source. An interesting property of the Born Approximation is that the relation between $\vec{\beta}$ and $\vec{\alpha}$ can be reduced to an effective thin lens identical to the eq. (2.1), allowing the definition of an effective convergence.

When the approximation does not hold, the relation between $\vec{\beta}$ and $\vec{\alpha}$ can no longer be reduced to a unique effective potential. Some curl-component may be generated, implying that the magnification tensor is no longer symmetric but requires the addition of a rotation term and so-called B-modes in the shear field. In this more general framework, the magnification tensor should be rewritten:

$$A_{ij}(\vec{\theta}) = \begin{pmatrix} 1-\kappa-\gamma_1 & -\gamma_2-\omega \\ -\gamma_2+\omega & 1-\kappa+\gamma_1 \end{pmatrix} . \tag{2.43}$$

The image plane positions where $\omega \neq 0$ are closely related to the lines of sight along which some substantial lens-lens coupling may have occurred.

The multiple-lens plane approximation

One common way to propagate light rays through a matter distribution is to sub-divide the line-of-sight into a series of lens planes with a small redshift interval. Thus, the light deflection occurs at each intersection of a light ray with a lens plane. Light rays are then deflected plane by plane from the observer to a fiducial source plane, as illustrated in figure 2.11. Hence, we ensure that all light rays converge to the observer, *i.e.* light rays are shot back. Between lens planes, light-rays follow straight lines.

We assume here that the lens planes are parallel to one another. This means that sky curvature is assumed to be negligible. This approximation is valid for small angular opening of the light cone (on the order of a few degrees). Instead of lens plane, spherical lens must be considered for large sky lensing predictions, on which spherical geometry is applied to compute lensing quantities (Fosalba et al. 2008; Das & Bode 2008; Teyssier et al. 2009; Becker 2013; Takahashi et al. 2017b; Kilbinger et al. 2017).

The formalism of the multiple lens plane approximation is well defined in the literature (Blandford & Narayan 1986; Schneider et al. 1992; Jain et al. 2000; Hilbert et al. 2009). Mathematically, one can re-write the integral of the light-ray deflection Eq. 2.41, by a direct summation of each small deflection induced by each lens plane:

$$\vec{\beta}^k = \vec{\theta} - \sum_n^{k-1} \frac{D_{nk}}{D_k} \vec{\alpha}^n(\vec{\beta}^n) , \tag{2.44}$$

where $\vec{\theta}$ is the angular position of a light-ray on the first lens plane, and $\vec{\beta}^k$ is it position on the lens plane k. The angular diameter distance from the observer to the k-th lens plane is noted D_k, and D_{nk} represents the angular diameter distance between the n-th and k-th planes. The initial conditions are defined as $\vec{\beta}^0 = \vec{\beta}^1 = \vec{\theta}$, and light rays started from the observer plane without initial deflection. This equation is recursive, and can be simplified by accounting only for the last two lens planes, such that:

$$\vec{\beta}^k = \left(1 - \frac{D_{k-1}\ D_{k-2;k}}{D_k\ D_{k-2;k-1}}\right) \vec{\beta}^{k-2} + \frac{D_{k-1}\ D_{k-2;k}}{D_k\ D_{k-2;k-1}}\ \vec{\beta}^{k-1} - \frac{D_{k-1;k}}{D_k}\ \vec{\alpha}^{k-1}(\vec{\beta}^{k-1}) . \tag{2.45}$$

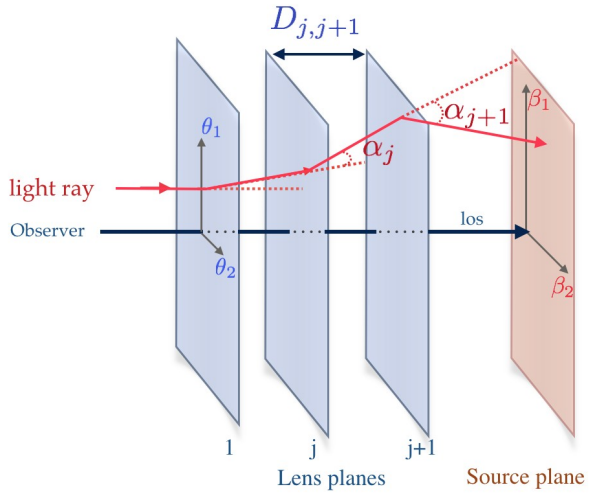

Figure 2.11 – Schematic view of the light ray propagation through multiple lens planes where D_{ij} is the angular diameter distance between the i- and j- lens planes. As illustrated, light rays are shooting back from the observer, with the first coordinates $\vec{\theta}$, to the source. For each i-lens plane, we compute the deflection field $\vec{\alpha}_i$ at the true position of the light $\vec{\beta}_i$, and therefore light rays are recursively deflected plane-by-plane.

.

Likewise, the magnification tensor can be re-expressed as a propagation of lens quantities (shear and convergence) by conserving the information of the last two planes.

$$A_{ij}^k = \left(1 - \frac{D_{k-1}\ D_{k-2;k}}{D_k\ D_{k-2;k-1}}\right) A_{ij}^{k-2} + \frac{D_{k-1}\ D_{k-2;k}}{D_k\ D_{k-2;k-1}} A_{ij}^{k-1} - \frac{D_{k-1;k}}{D_k} U_{ik}^{k-1} A_{kj}^{k-1} \,. \tag{2.46}$$

where U_{ij}^k is the shear tensor evaluated on the plane k, such that:

$$U_{ij}^k = \frac{\partial^2 \psi^k(\vec{\beta}^k)}{\partial\beta_i^k \partial\beta_j^k} = \frac{\partial \alpha_i^k(\vec{\beta}^k)}{\partial\beta_j^k} \,. \tag{2.47}$$

This recursive form is numerically more tractable than a direct summation, because we do not have to store all the lensing information along the light-of-sight.

For comparison, the light rays propagation in the Born approximation can be numerically made following this formulation:

$$\vec{\beta}^k = \vec{\theta} - \sum_n^{k-1} \frac{D_{nk}}{D_k} \vec{\alpha}^n(\vec{\theta}) \equiv \vec{\theta} - \vec{\alpha}^{\rm eff}(\vec{\theta}) \,. \tag{2.48}$$

In this case, the deflection angle is always evaluated at the unpertubated position θ. This simplification is equivalent to a single effective lens plane with an effective deflection $\vec{\alpha}^{\rm eff}(\vec{\theta})$, as described above. Likewise, the distortion matrix can also be re-written in the Born approximation such that:

$$A_{ij}^k(\vec{\theta}) = \delta_{ij} - \sum_n^{k-1} \frac{D_{nk}}{D_k} U_{ij}^n(\vec{\theta}) \,. \tag{2.49}$$

Properly tracing the light rays propagation has the advantage of taking the lens-lens coupling into account (the coupling between structures at different distances). This level of precision have been explored into large N-body simulations (Hilbert et al. 2009; Giocoli et al. 2016b). It results that the Born approximation is accurate enough (sub-percent) to predict the two-point shear (or convergence) statistics up to small scales. Note that beyond the plane approximation, ray-tracing can be also performed by modelling the 3-D gravitational potential (e.g. Couchman et al. 1999; Barreira et al. 2016).

2.3.2 Building the deflection field by mapping the projected mass

Simulations of weak lensing, either into a single- or multiple- lens plane approximation, requires a method to build lensing quantities on a plane. There are multiple ways to construct the deflection field in the lens planes. Depending on the simulation itself, the most basic method is to map the projected density into a plane, and then to solve the differential equation $\vec{\nabla}.\vec{\alpha} = 2\kappa$ in Fourier space.

Particles projected onto a grid

The previous simulations of gravitational lensing from N-body simulations smoothed the projected particle distribution on a grid using fixed kernels: Nearest-grid-point, Cloud-In-Cell, Triangular Shape Cloud, polynomial or Gaussian (See Appendix A) (e.g Wambsganss et al. 1998; Vale & White 2003; White & Vale 2004; Pace et al. 2007).

Any smoothing kernel W has to be normalised, such that: $\int d\vec{x} W(|\vec{x} - \vec{x}_i|, l_i) = 1$. The size of the kernel l_i can be either fixed or adaptive. Adaptive smoothing will be discussed. The smoothed projected density of N_{part} particles, is computed such that:

$$\Sigma(\vec{x}) = \frac{m_p}{A} \sum_{i=1}^{N_{part}} W(|\vec{x} - \vec{x}_i|, l_i)\,, \tag{2.50}$$

where A is the area of the projected mass map.

Note also that Bradač et al. (2004) proposed an alternative technique to compute the surface density maps based on the Delaunay tessellation method.

Particle Noise

As density is sampled with a limited number of point masses (particles), some shot noise is present. In fact, this discreteness noise inherent to particle distributions induces an additional small-scale lensing signal. Depending on the method used to construct the projected density field, one can estimate the contribution of particle shot noise in the computed lensing quantities (Vale & White 2003; Rau et al. 2013; Angulo et al. 2014). The noise level can be evaluated depending on the particle number, the particle size and the choice of smoothing algorithm. The particle noise on the surface mass density can be expressed such that:

$$\sigma^2_\Sigma(\vec{x}) = \frac{m_p^2}{A^2} \sum_{i=1}^{N_{part}} W^2(|\vec{x} - \vec{x}_i|, l_i)\,. \tag{2.51}$$

Derivation of the lensing quantities

In the grid-based approach, lensing quantities (gravitational potential, shear, deflection) are derived from the 2-D projected map using Fast Fourier Transforms (equations 2.17), which assume periodic boundary conditions. In particular, it is crucial to construct the deflection angle field to deviate light-rays. Knowing the deflection-angle field, we must then interpolate its values into the grid for each light-ray position. This is usually done with a bi-linear interpolation scheme.

Smooth particle lensing (SPL)

Li et al. (2006b) was one of the first to adapt the smoothing length of particles as a function of local density in order to improve the contrast of the computed lensing signal. The smooth particle lensing (SPL) technique, developed by Aubert et al. (2007), efficiently simulates gravitational

lensing from N-body simulations using a density-dependent particle smoothing. It can thus efficiently compute lensing quantities from a particle distribution by using a 2D-Tree domain decomposition.

This method is based on the fact that at a given point $\vec{r}$ (or a light ray position), one can compute the lensing signal by summing all particle contributions on its point, such as $\kappa(\vec{r}) = \sum \kappa_i(\vec{r})$ Each mass particle is described by a 2-D Gaussian function in the projected density, such that:

$$\kappa(\vec{r}) = \frac{m_p}{2\pi\sigma^2\Sigma_{\rm crit}} \exp\left(-\frac{r^2}{2\sigma^2}\right) , \tag{2.52}$$

where r is the distance between the light-ray position and the particle, and the width σ is adaptively assigned. The potential, deflection angle, and shear associated to a single particle are also expressed by smoothing kernels. For example, the associated deflection angle of a given particle is:

$$\alpha(\vec{r}) = \frac{m_p}{\pi\Sigma_{\rm crit}} \frac{\exp\left(-\frac{r^2}{2\sigma^2}\right) - 1}{r} . \tag{2.53}$$

This method thus computes lensing quantities (convergence, shear, potential, deflection) without the need for Fast Fourier transforms or any deflection-angle interpolation at each light ray-position.

To efficiently sum all particle contributions on a single position, we use a 2-D Tree of particle distribution. Going down the 2-D Tree structures, particles away from a given position are grouped into a single massive particle while closer particle are individually summed. This is illustrated figure in 2.12. For a given light ray, the smoothing length is constant for all particles:

$$\sigma = \left(\frac{N_\sigma r_{sph}}{N_{sph}}\right) , \tag{2.54}$$

where r_{sph} is the distance from the light-ray to N_{sph}-th nearest neighbour particle.

We thus have two free parameters N_{sph} and N_σ, the latter of which is a control parameter. Note that the approximation of a constant smoothing length by rays is not properly correct, but seems to be sufficient and reduces computational time which becomes of the order of $N_{ray}\log(N_{part})$. This method remains powerful to avoid FFT and to preserve the small scale features.

Based on this approach, high performance lensing codes have been performed, such as the GLAMER code (Metcalf & Petkova 2014; Petkova et al. 2014). Weak lensing forecasts were then proposed by running this type of code on large N-body simulation. For example, Giocoli et al. (2016b) have performed light-cones on the Big MultiDark simulation and traced light-rays in the multiple lens plane approximation with GLAMER. Their predictions of cosmic shear 2-points and 3-points statistics and halo-galaxy lensing are consistent with theoretical model. In grid-based approaches, Hilbert et al. (2009) traced light-rays through the Millennium simulation by using an adaptive smoothing kernel to quantify the impact of Born corrections in cosmic shear and galaxy-galaxy lensing.

Such methods remain restricted to Lagrangian simulations. Indeed, by considering different particle masses in hydrodynamical simulations, the Tree structure becomes hardly tractable. One must consider a 2-D Tree for each particle types (DM, star, gas, agn) to properly evaluate their separate contributions. This drastically increases computational costs.

To avoid this problem, I used the resolution level of the simulation to find the correct smoothing length. As explained in the chapter 4, I performed ray-tracing over an AMR grid. By recovering the resolution level around a given particle position from the neighbouring gas cells, I can bypass the time-consuming step of building a tree in the distribution of particles.

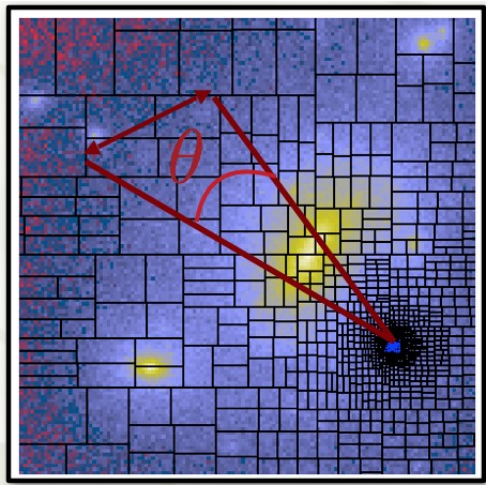

Figure 2.12 – A visual representation of how the space is splitting by a 2D-tree over a particle distribution. The opening angle criterion is also illustrated. Close to the region of interest (light ray position) the cells are opened, whereas particles distant to it position are grouped into larger cells. Credit to Aubert et al. (2007).

2.3.3 The construction of the deflection field by using the acceleration field

An alternative approach used in this thesis is to compute the deflection from the gravitational acceleration field (as detailed in chapter 4). Indeed, if the gravitational force computed in a numerical simulation is kept as part of its outputs, one can compute the deflection field by integrating the transverse component of the acceleration along the light of sight, according to Eq. (2.5).

I present this method for grid-based numerical simulation (either regular or refined). To do so, we have to consider, for each light-ray, the cells which intersect the ray, and compute the intersection length along the line-of-sight l_i. It is illustrated in figure 2.13.

Knowing the cell size δ_i and its orientation with respect to the line of sight, l_i is deduced with a simple Oriented-Box-Boundary (OBB) algorithm (*e.g.* Akenine-Möller et al. 2008). Indeed, fast algorithm are proposed in the literature to compute the intersection between a ray and a box which are not oriented perpendicularly to the ray, referred as Ray-OBB intersection algorithm. Our case is simpler because simulation cells are cubic, and are assumed to share the same orientation (flat sky approximation). In addition, light rays are parallel to the line-of-sight. One can therefore factorise out dot products between the normals to cell and the line of sight. The Ray-Cube intersection is illustrated in figure 2.14.

Finally, the deflection angle at a given position $\vec{\theta}$, can by computed by summing the gravitational force on cells weighting by their intersection lengths, such that:

$$\vec{\alpha}(\vec{\theta}) = \frac{2}{c^2} \sum_{i \in \mathcal{V}(\vec{\theta})} \vec{\nabla}_\perp \phi_i(\vec{\theta})\ l_i\ , \tag{2.55}$$

where $\mathcal{V}(\vec{\theta})$ denotes the projected vicinity of a sky position $\vec{\theta}$.

This method has the advantage of preserving the gravitational force that was used when evolving the simulation. In particular, the way shot noise is smoothed out in the simulation to recover the acceleration field from a mixture of Lagrangian particles (and Eulerian gas cells) is faithfully respected in the raytracing. In other words, the force felt by photons is the very same force as the one felt by particles in the simulation.

Furthermore, this method has the advantage to not first compute the convergence κ to then perform Fourier transforms. We do not need to assume periodic boundary conditions at the edge of the deflection map. Indeed, the force field contains information from regions outside the aperture considered, and so its boundaries are more valid than a deflection field obtained by mapping the density. Finally, the convergence and shear fields can be computed from the deflection field in real space via finite differences.

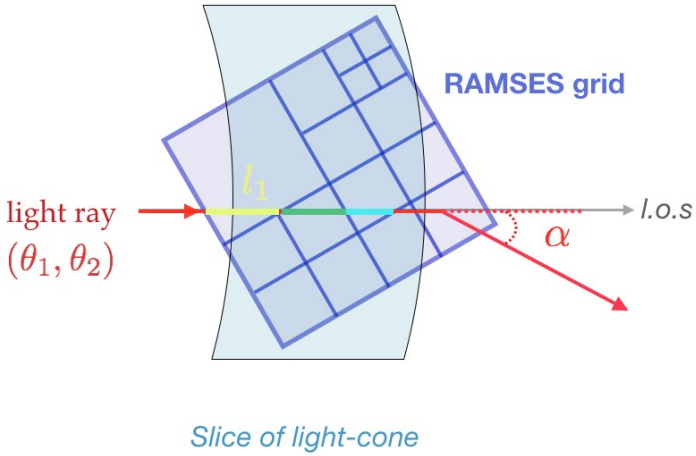

Figure 2.13 – Schematic view of an intersection between a light-ray and the simulation grid, which have been recorded in slices of the light-cone. The intersection length between a ray and a cell is noted l_i.

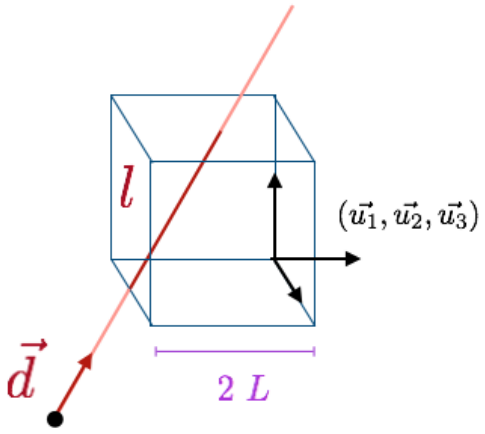

Figure 2.14 – Schematic view of the intersection between a ray and an orriented cubic box. The cube is defined by its orthonormal basis vectors $(\vec{u}_{1,2,3})$, its center, and its half-size L. The ray is defined by its origin and its direction $\vec{d}$.

2.4 Conclusion

In this chapter, I presented a brief review of gravitational lensing theory, along with classical lensing observables in the weak regime. I also presented some of the generic numerical methods I will use to predict the lensing signal from N-body and hydrodynamical simulations, which are implemented in the next chapters. In fact, we have seen that thanks to future weak lensing experiments such as the Euclid mission, weak lensing statistics analyses will be possible with an unprecedented accuracy (1.5 billion galaxies shapes for the Euclid mission) and down to small non-linear scales. In this context, predictions of cosmic shear and GGL have to be done with state-of-art hydrodynamical simulations (to quantify the significant impact of baryonic physics on these observables at intermediate and small scales). This is the research I address in chapter 4. In addition, upcoming wide weak lensing surveys will provide the opportunity to drastically improve statistics analyses on galaxy clusters and large scales structures. Sartoris et al. (2016) estimated that Euclid will detect around 2×10^5 galaxy clusters with a high detection thresholds (5σ galaxy overdensity). Therefore, in chapter 3, I present my study of the connection between the cosmic web and clusters using weak lensing as a probe and quantified on N body simulation the future detectability of this weak lensing signal in the context of Euclid.

Chapter 3

Multipolar moments of weak lensing signal around clusters

Weighing filaments in harmonic space

3.1 Context

In this chapter, I investigate the connection of galaxy clusters to the comic web using the weak lensing signal. Although the global filamentary structure of the Universe is well understood, a detailed study of its morphology allows us to further probe the underlying cosmology and improve our understanding of structure formation and evolution (Codis et al. 2018). It is particularly interesting to characterise cosmic filaments with lensing, an unbiased tracer of mass, because they are mainly composed of dark matter.

At the vicinity of clusters, the density contrast of filaments is more important; it is therefore the ideal place to detect them via weak lensing. However, detecting individual filaments with weak lensing is challenging given the weakness of their corresponding shear field. Only massive bridges of matter between two clusters have so far been detected by WL with some significance (see e.g. Dietrich et al. 2012). The WL signal can also be enhanced using various algorithms and methods described in the literature (see e.g. Maturi & Merten 2013), but its detection remains difficult on an object by object basis. In addition, the gravitational potential induced by the cluster has to be carefully modeled, in order not to over-estimate the filaments' detection. As a workaround, one can attempt to stack the WL signal induced by cosmic filaments. One possible avenue is the aperture multipolar moments of WL, as described by Schneider & Bartelmann (1997). It relies on a multipolar decomposition of the mass distribution to quantify asymmetries directly from the shear signal. An illustration of the multipolar decomposition is presented in figure 3.1.

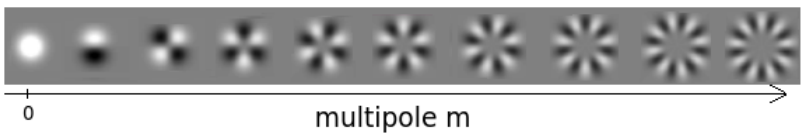

Figure 3.1 – An illustration of the multipolar decomposition as a function of order m. For example at the order $m = 0$, the matter distribution is isotropic (monopole), whereas the order $m = 1$ is the dipole, $m = 2$ the quadrupole, etc.

3.2 Paper presentation

I study the prospect of measuring with weak lensing the azimuthal dark matter distribution around galaxy clusters inside and outside their virial radius. I consider a sample of galaxy clusters, which I extracted from the PLUS[1] DM-only cosmological simulation made available to me by S Peirani at IAP.

In order to extract the angular symmetries around clusters, we considered the aperture multipole moments Q_m of this convergence field introduced by Schneider & Bartelmann (1997)

$$Q_m = \int_0^\infty \mathrm{d}r\, r^{1+m} w_m(r) \int_0^{2\pi} \mathrm{d}\varphi\, \mathrm{e}^{\imath m\varphi} \kappa(r,\varphi)\,. \tag{3.1}$$

where $w_m(r)$ is a radial weight function with a compact support so that $w_m(r)$ vanishes beyond some radius $R_{\rm max}$ and below some inner radius $R_{\rm min}$. The inner and outer cluster environments that we chose to analyse are defined as $[0.25-0.5]R_{\rm vir}$ and $[1-4]R_{\rm vir}$, respectively.

Because filaments are not very dense and weak lensing signal is generally a low signal-to-noise measurement, the moments cannot be directly measured on a cluster-by-cluster basis, which means that stacking many clusters will be needed for the signal to show up. Since clusters are not particularly aligned with one another, a crude stacking of the moments will completely wash the information out by symmetry. Instead, we got around this problem by stacking the modulus of these moments, and so as to obtain an harmonic power spectrum of multipolar moments $\langle|Q_m|^2\rangle$. This is the main observable that we explored in the paper. In particular, we extensively describe the amplitude and shape of these spectra as a function of multipolar orders m, as a function of cluster mass, radius and redshift, as a way to diagnose the shape and connectivity of halos. We also compare those spectra with similar spectra derived around random locations in the simulation box instead of the around cluster. The rest of this section summarises our main findings while Section 3.3 presents the technicals aspects and numerical tools, which I developed for this work and are not described in the paper.

Multipolar moment spectra computed around clusters present an m-independent boost of spectral amplitude compared to spectra computed around random locations. This first discrepancy between multipolar moment predictions from linear and non-linear regimes, is understood as arising from the non-linear evolution of the density field around density peak. Indeed, as gravitational clustering builds up, clusters attract matter in their vicinity. This induces an amplification of the density contrast around cosmic nodes, where the density fluctuations are locally evolving more rapidly. The overall excess of harmonic power near density peaks is understood and theoretically quantified by using the Zeld'ovich approximation and the spherical collapse.

Besides the overall boost of amplitude at all multipole orders, the quadrupole ($m=2$) prevails in cluster core relatively to the background density field. This is consistent with recent studies which use elliptical or triaxial models to describe dark matter haloes shape (Warren et al. 1992; Jing & Suto 2002; Despali et al. 2014). In fact, more massive haloes present a stronger harmonic power excess at quadrupole, which tends to indicate a stronger ellipsoidal symmetry on the core of haloes.

At the outskirts of clusters, harmonic distortions are spread on small angular modes, and thus, in contrast to the result of of the companion paper, appears to trace the non-linear sharpening of the filamentary structures. This harmonic power excess shows a mass dependence: more massive clusters provide stronger harmonic distortions, spread on larger angular scales. Theoretically, massive haloes are supposed to be connected to a larger number of filaments, as found by Pichon et al. (2010); Aragón-Calvo et al. (2010) and Codis et al. (2018). Ours results are in agreement with this global picture of cluster evolution: massive haloes are more likely to be in their early

[1] http://www2.iap.fr/users/peirani/PLUS/plus.htm

formation phase, and their shape is typically distorted by major mergers or accretion along the preferred direction set by their connecting filaments. Conversely, lower-mass haloes are formed at higher redshift and have had more time to relax. They typically lost the memory on their accretion history, and therefore the preferential directions induced by recent merging events.

To explore the evolution of cluster shape in the cosmic history, the statistics of $\langle|Q_m|^2\rangle$ are investigated for cluster progenitors over the cosmic time. I assume that the most massive clusters at different redshifts are progenitors. Their multipolar moments spectra are not significantly changed from $z = 0.9$ to $z = 0$. This suggests that the shape of the most massive haloes is fixed at early times, and keeps the memory of its initial conditions during its formation collapse (Bond et al. 1996). One might ask if the shape of lower massive clusters are changing with cosmic time. In fact, the disconnection of the halo from the cosmic web, induced by dark energy, should occur for less massive clusters (Pichon et al. 2010). As expected, we observe a decrease of the harmonic excess with the time, for lower massive haloes in both internal and external regions.

Finally, we also investigate the correlation of angular shape of galaxy clusters at small and large scales. To do so, I cross-correlated the multipolar moments for the two different annuli: $\langle Q_m(R_1)Q_n^*(R_4)\rangle$. It appears that only orders $m = n = 1, 2, 4$ present a significant correlation. This is probably because, typically, two branches of filaments are connected to a node of the cosmic web on small scales (Pogosyan et al. 2009). Further away from the nodes, bifurcation points appear and therefore increase the number of filaments.

In the last section of the article, I estimate the overall detectability of multipolar moment spectra as a function of the number of stacked clusters, cluster redshift and cluster mass. The main noise sources in the measurement of multipolar moments from shear data are: the noise induced by the intrinsic ellipticity of galaxy (shape noise), the additional lensing signal induced by the Large Scale Structure along the line of sight (LSS noise), and the variance of the harmonic power spectra due to the finite number of clusters.

Finally I model the detection of $\langle|Q_m|^2\rangle$ statistics for the upcoming Euclid survey (Laureijs et al. 2011; Sartoris et al. 2016). By estimating the number of detected clusters for a given range of redshift and mass, I estimated the expected signal-to-noise ratio on multipolar moments for both internal and external regions of galaxy clusters. Due to their abundance, lower mass clusters presented an higher signal-to-noise ratio. In addition, measurement of multipolar spectra on closest clusters is better due to the lowest noise contamination induced by the matter on the line-of-sight. The Euclid mission should provide all the necessary information for studying the cosmic evolution of the connectivity of the cosmic web around lensing clusters, and the azimuthal shape of cluster core, by using multipolar moment up to $m \sim 8$ and $z \sim 0.75$.

This study is compared with a companion paper (Codis et al. 2017), presented in Appendix B, in which the aperture multipolar moments are investigated in the linear and weakly non-linear regimes, assuming that clusters are simply the peaks of a 2D Gaussian Random Field. In particular, this complementary study shows that the amplitude of the harmonic spectra (with and without the condition to be centred on the peak) appears to be robust w.r.t. the linear growth of the structures. In addition, the harmonic distortions are robust with respect to the peak condition in linear regime for $m > 3$.

3.3 Details on the preliminary numerical work

I detail now different numerical processes and verifications that I developed, and which are not given in the paper.

3.3.1 The cluster sample

The cluster sample was first detected in the simulation box by S Peirani via a Friend-of-Friend (FoF) algorithm, which computes the mass of linked particles and the position of the center of mass of this collection of particles.

I extracted clusters from the simulation box by considering all the DM particles within a sphere centred on density peaks defined by the FoF catalogue. I performed numerical optimisations to improve on the estimate of the clusters' centre using the shrinking sphere method: starting with a large sphere centred on the FoF halo, I re-define the halo center as the center of mass and I reduced the radius of the sphere by 5%. This process is recursively repeated until convergence of the center's location. This step is necessary because the center derived by FoF algorithm is sensitive to the presence of massive substructures inside dark matter halos, and thus, it is not located at the density peak which is a better choice for the center [2]. As illustrated in figure 3.2, the FOF center (cyan point) differs from the one obtained of applying the shrinking sphere center refinement (magenta point).

In details, I have explored the impact of shrinking sphere parameters (the starting radius and the rate of sphere diminution) on the final center location, to ensure the convergence of this method. I tested the robustness of the shrinking sphere center by performing the radial density profile of some individual galaxy clusters. It produces a coherent radial density profile, in agreement with the NFW profile presented in figure 3.2.

By fitting an NFW profile, I obtained the concentration and the scale radius of clusters. This step is a validation of my mock cluster sample. I finally estimates the Virial mass and radius for each cluster. As an example, a typical 2-D density (or convergence) map of a cluster-mass dark matter halo in the PLUS simulation, is presented in the top left panel of figure 3.3, which also shows the different annuli considered, R_1 and R_4. One can also see maps of the corresponding lensing quantities for this cluster: the two shear components, the lensing potential and the deflection components. They are computed with Fast Fourier Transforms of the converge

3.3.2 Multipolar moments for test mass distributions

After extracting the cluster sample at different redshifts, I computed the multipolar moments by a direct summation of the dark matter particle contribution of each cluster. This step requires parallelisation, implemented in `openmp`.

In addition, I modelled and subtracted off the shot noise induced by the DM particles.

An example of the shot noise particle and its impact on the multipolar moments are illustrated figure 3.4 (left panel). In this example, I consider a typical matter distribution with an $m = 3$ angular symmetry, so that the surface density obeys $\Sigma(R, \theta) = \Sigma_0 \cos(3\theta)$. I also compute the multipolar moments for an elliptical mass distribution whose radial profile obeys:

$$\Sigma(R) = \frac{\Sigma_0}{2G} \frac{R_{cut}^2}{R_{cut}^2 - R_{core}^2} \left(\frac{1}{\sqrt{R_{core}^2 + R^2}} - \frac{1}{\sqrt{R_{cut}^2 + R^2}} \right) ,$$

where R_{cut} and R_{core} are two scale radii, in order to model the smoothly truncated Pseudo Isothermal Elliptical Mass Distribution (Kassiola & Kovner 1993, Kneib et al., 1996). As expected and illustrated in figure 3.4 (right panel), an elliptical mass distribution only generates even modes, especially Similarly, one can consider a mass distribution of the form

$$\kappa = \frac{\kappa_0}{(1 + s^2(1 + \varepsilon \cos(2\theta)))^\nu} ,$$

[2] Note that identifying the center of galaxy clusters is by itself a complex problem as it can be measured observationally as the Brightest Cluster Galaxy, the peak of X-ray emission, or the weak lensing convergence map or SZ emission. Typical offsets $\lesssim 10\%$ of the virial radius are commonly found between those observational choices

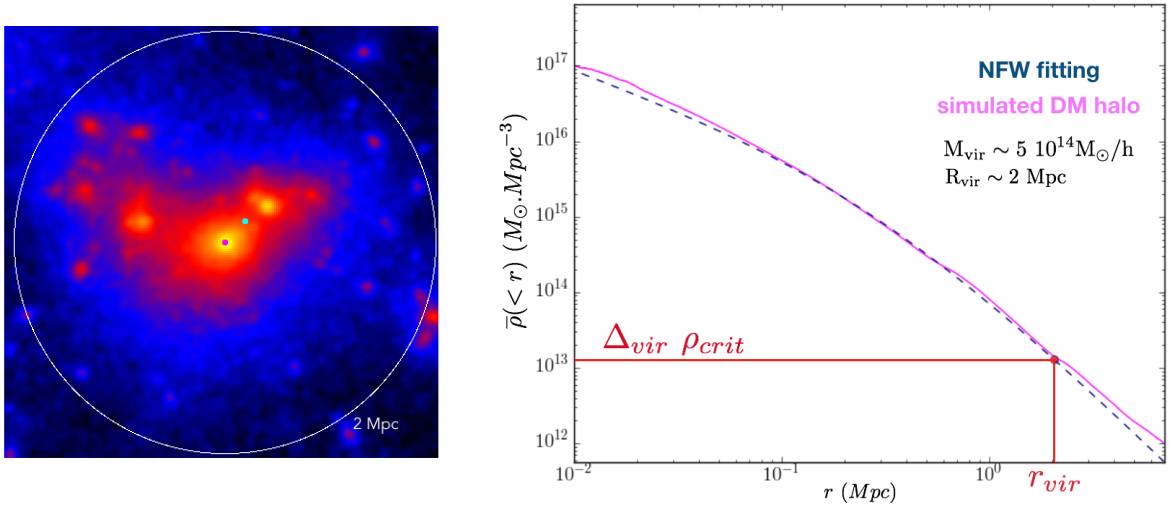

Figure 3.2 – Left panel: Example of the two different centres: FoF center in cyan and the shrinking sphere center in magenta for a massive cluster at $z = 0$. The cumulative mean density profile of this cluster is shown on the right panel.
The NFW profile is also fitted on the density profile of the halo. As illustrated, the Virial radius is defined as the distance at which $\rho(< r_{vir}) = \delta_{vir}\rho_{crit}$.

which has been extensively studied by Schneider & Weiss (1991), since it can easily be Taylor expanded around small values of the ellipticity ε. Here $s = r/r_c$, is the radius expressed in units of a particular core radius scale r_c. These authors show that the expansion generates terms

$$\kappa = \frac{\kappa_0}{(1+s^2)^\nu}\left[1 + \sum_{m=1}^{\infty}\frac{k_\nu}{m!}\left(\varepsilon\frac{s^2}{1+s^2}\cos(2\theta)\right)^m\right],$$

where the expression for k_ν can be found in Schneider & Weiss (1991). We readily see the $1/m!$ fall off of modes and the prevalence of the quadrupole, characteristic of elliptical symmetries. More precisely, on scales $r \gg r_c$, it can be shown that $Q_2 = \varepsilon\nu Q_0$, with $\nu \simeq 1/2$ for nearly isothermal mass distributions.

The impact of any mis-centering on the multipolar moments is another important effect that I quantified. Indeed, it produces odd multipolar moments, and in particular, increases the amplitude at the order $m = 1$. To do so, I apply random shifts to the center with respect to the reference fiducial shrinking sphere location and computed the corresponding multipolar moments. These offsets were uniformly drawn in various ranges depending on $R_{\rm vir}$. figure 3.5 shows the resulting multipolar moment spectra for various amplitudes of mis-centering, in the two annuli considered in the paper (left and right panel). Mis-centering affects the shape of the multipolar moments at small scales, in the internal region of clusters ($R \in [0.25 - 0.5]R_{\rm vir}$). For a sensible range $\pm 0.1\ R_{\rm vir}$ of offsets, even modes are not affected, but the deficit of power for odd orders is suppressed. This means that multipole moments could in principle be used to quantify the quality of the centering procedure. If we further increase this mis-centering, the complete shape of the power spectrum is distorted at all orders. Considering the external annulus ($R \in [1.0 - 4.0]R_{\rm vir}$), any realistic offset ($\lesssim 0.1\ R_{\rm vir}$), does not significantly impact the multipolar spectrum. I only show the distortions produced by large offsets. Again, even order are less affected.

I observe a substantial amplitude for $m = n = 1$ for the cross-correlation between the internal and external annuli (i.e. $\langle Q_m(R_1)Q_n^*(R_4)\rangle$). This is directly due to the condition to be centred on a density peak: this correlation is affected by any mis-centering of clusters. As expected,

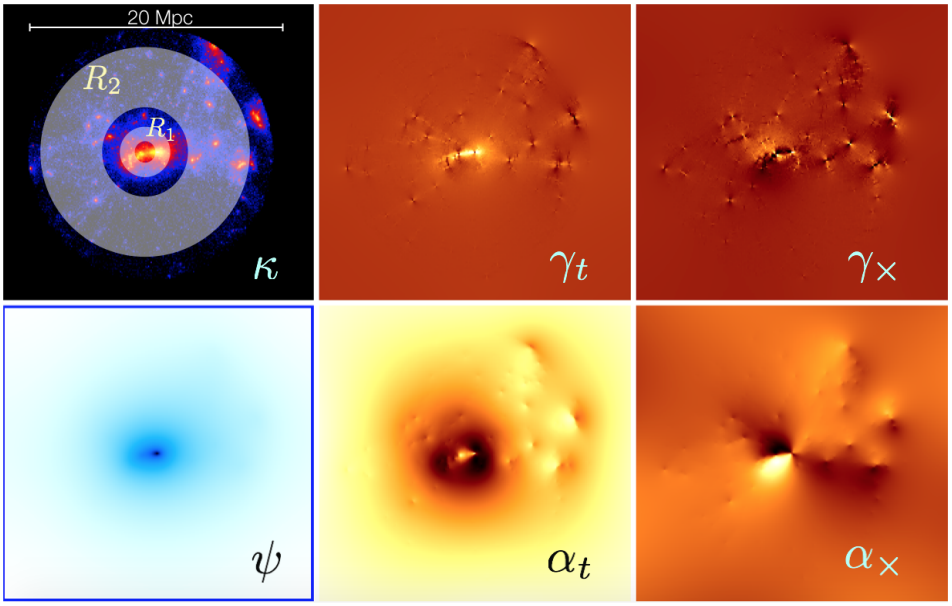

Figure 3.3 – The different lensing quantities of a massive simulated cluster are presented here. The convergence, the shear tangential and rotational, the 2-D potential and the deflection tangential and rotational are noted $\kappa, \gamma_t, \gamma_\times, \psi, \alpha_t, \alpha_\times$, respectively.

by computing this cross-correlation with various mis-centering, I observe that the amplitude of $\langle Q_1(R_1)Q_1^*(R_4)\rangle$ reduces as the mis-centering increases.

3.4 Overview of my different contribution

I carried out the post-processing of the simulation from the cluster sample extraction to the resulting harmonic spectra, including all numerical aspects described above. I also made the preliminary investigation of $\langle|Q_m|^2\rangle$ statistics in section 2.2.1, by integrating the linear and non-linear power spectra of the density contrast from the Boltzmann CLASS code (Blas et al. 2011; Lesgourgues 2011). The theoretical modelling of the power spectral amplitude boost α (section 2.3 and Appendix A) were performed by Sandrine Codis and Raphael Gavazzi. The introduction, discussion and interpretation of the results are carried by all of the authors. In section 4, the covariance matrix of the multipolar moments (equation 40, and the detail of the calculation given in Appendix C) the theoretical development were initiated by Raphael Gavazzi and validated by the other co-authors. I numerically performed the estimation of the different noise sources, and of the expected number of observed clusters by the Euclid mission (as function of mass and redshift). My implication on the companion paper was minor: it is the result of interaction with Sandrine Codis about the difference behaviour of $\langle|Q_m|^2\rangle$ statistics in linear and non-linear regimes, by comparing and discussing our results. I improved my theoretical skills and my comprehension of density field statistics thanks to this collaboration in this second paper.

3.5 Perspectives

In this paper, I present a new statistical estimator based on harmonic decomposition of the WL signal around clusters. I propose to use this estimator to probe the filamentary structures around clusters at large scales, along with the azimuthal shape of cluster core. I find that shear lensing

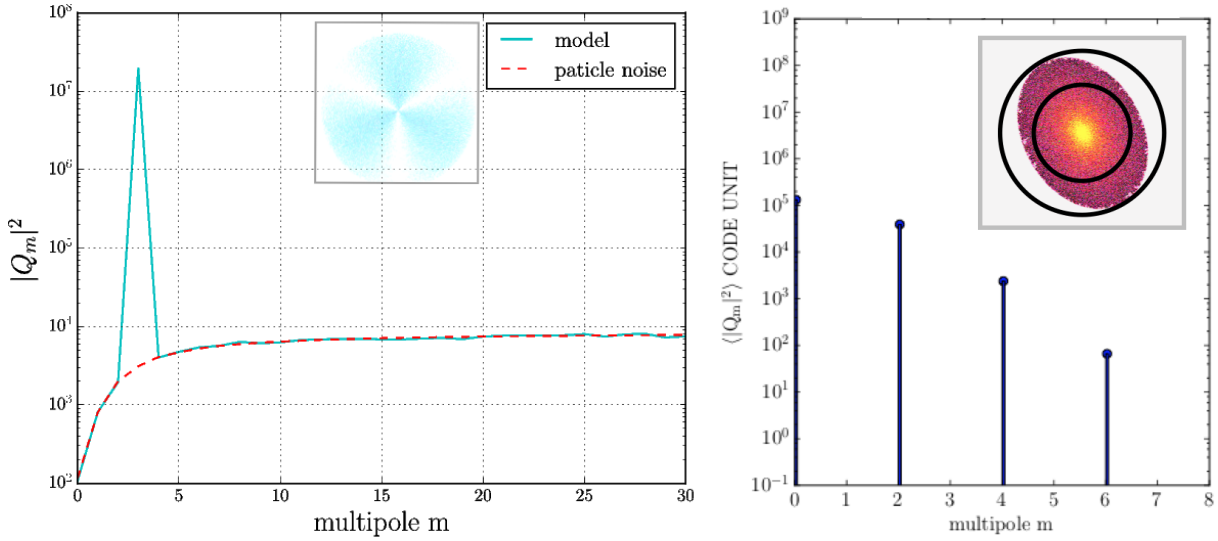

Figure 3.4 – Left panel: The multipolar moments $|Q_m|^2$ computed for a toy particle distribution (illustrated in the top). The angular symmetry on the projected density induces a high multipolar amplitude at $m = 3$. In addition, the particle shot noise also creates multipolar moments spread over all m order. As shown in the paper below, the particle noise corresponds to a constant projected density power spectrum and thus can be estimated and subtracted off.
Right panel: The multipolar moments $|Q_m|^2$ computed for an elliptical mass distribution (illustrated in the top insert). In this case, the shot noise is already subtracted. One can see the prevalence of the quadrupole $m = 2$ and that only even modes are non-null, with a fast $\sim 1/m!$ fall-off.

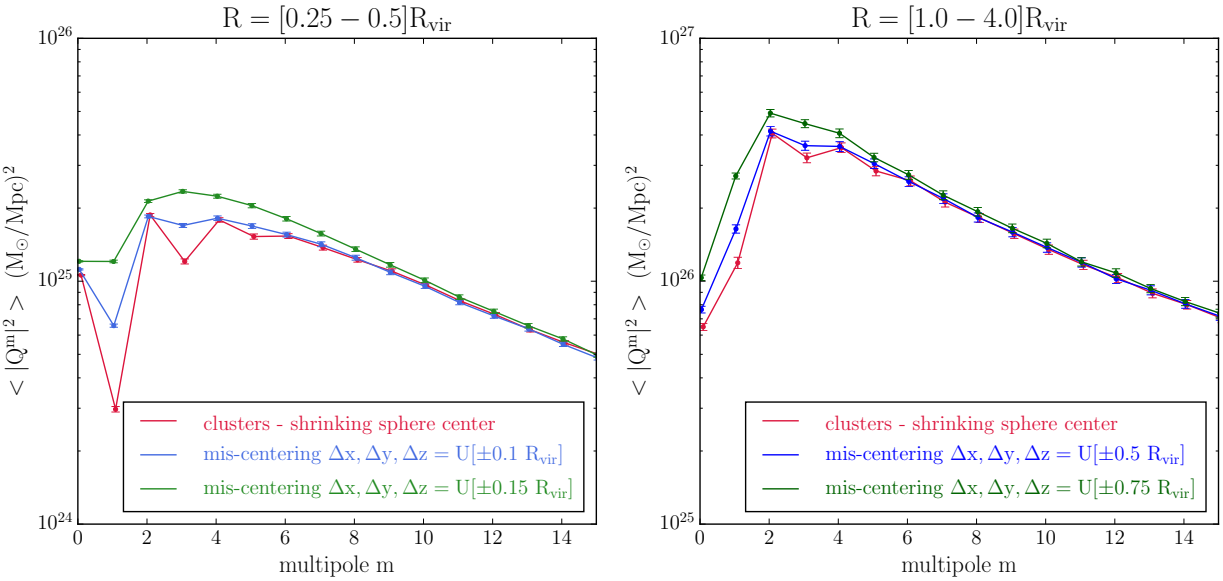

Figure 3.5 – Multipolar moment spectra of clusters for the mass bin M_1 at the two scales in the annuli $R \in [0.25 - 0.5]R_{vir}$ (left panel) and $R \in [1.0 - 4.0]R_{vir}$ (right panel). The two panels show the difference between a measurement of the spectrum with a good centering, compared to a measurement on clusters with a random offset of the center position. We observe the same effects for the other mass bins.

surveys can be used to measure the angular distribution of the convergence field around clusters of galaxies, to constrain their connectivity to the cosmic web. Indeed, Codis et al. (2018) has shown that the number of filaments connected to a given cluster is a natural probe for the growth of structure and the nature of dark energy in particular. The disconnection of filaments with cosmic time is driven by both gravitational clustering and dark energy, the latter of which stretches and disconnects neighbouring filaments through the increased expansion of voids. The multipolar moments of the shear signal therefore have to be predicted with different cosmologies, and with models involving different type of Dark Matter, in order to be measured with future lensing data sets, such as Euclid photometric survey.

At cluster core scales, the multipolar moment statistics can be affected by both the nature of dark matter (e.g. self-interacting dark matter should reduce the quadrupole) and by the baryonic physics. Complementary to this study, for the aforementioned scales, one must carry out hydrodynamical simulations to take the impact of baryonic component on the azimuthal shape of clusters into account. Indeed, connectivity is also paramount to understand galactic assembly at smaller scales. Cosmic filaments have a baryonic continuation within dark haloes, which connect closely the cosmic environment to their galaxies. Beyond the number of connected filaments, the mass load, geometry and advected torques are also worth investigating.

At these scales, the measurement of multipolar moments statistics can be already achieved on current shear surveys by considering a typical aperture of $R = [0.1 - 1]R_{vir}$. Such measurements on ground-based observations will be presented in a future work. For instance, Darragh Ford et al. (2018, in prep.) found that AGN feedback disconnects filaments, which in turn quenches bright central galaxies, by studying the star-formation efficiency of these galaxies at fixed group mass in the COSMOS catalogue.

Finally, this formalism can be applied to derive results for either cosmological observables, such as the galaxy distribution, or the X-ray emission. By computing the moment on different galaxy population, one can explore the relative bias of these populations inside filaments and into cluster haloes. Similarly, the multipolar moment of the X-ray emission can be easier measured (higher signal amplitude), and can be used to characterise warm-hot ionised baryons at the vicinity of galaxy clusters.

A&A 605, A27 (2017)
DOI: 10.1051/0004-6361/201730727

Astronomy & Astrophysics

Multipolar moments of weak lensing signal around clusters

Weighing filaments in harmonic space

C. Gouin[1], R. Gavazzi[1], S. Codis[2], C. Pichon[1,3], S. Peirani[1], and Y. Dubois[1]

[1] Institut d'Astrophysique de Paris, UMR 7095 CNRS & Université Pierre et Marie Curie, 98bis Bd Arago, 75014 Paris, France
e-mail: gouin@iap.fr
[2] Canadian Institute for Theoretical Astrophysics, University of Toronto, 60 St. George Street, Toronto, ON M5S 3H8, Canada
[3] Korea Institute of Advanced Studies (KIAS) 85 Hoegiro, Dongdaemun-gu, 02455 Seoul, Republic of Korea

Received 3 March 2017 / Accepted 11 May 2017

ABSTRACT

Context. Upcoming weak lensing surveys such as *Euclid* will provide an unprecedented opportunity to quantify the geometry and topology of the cosmic web, in particular in the vicinity of lensing clusters.
Aims. Understanding the connectivity of the cosmic web with unbiased mass tracers, such as weak lensing, is of prime importance to probe the underlying cosmology, seek dynamical signatures of dark matter, and quantify environmental effects on galaxy formation.
Methods. Mock catalogues of galaxy clusters are extracted from the N-body PLUS simulation. For each cluster, the aperture multipolar moments of the convergence are calculated in two annuli (inside and outside the virial radius). By stacking their modulus, a statistical estimator is built to characterise the angular mass distribution around clusters. The moments are compared to predictions from perturbation theory and spherical collapse.
Results. The main weakly chromatic excess of multipolar power on large scales is understood as arising from the contraction of the primordial cosmic web driven by the growing potential well of the cluster. Besides this boost, the quadrupole prevails in the cluster (ellipsoidal) core, while at the outskirts, harmonic distortions are spread on small angular modes, and trace the non-linear sharpening of the filamentary structures. Predictions for the signal amplitude as a function of the cluster-centric distance, mass, and redshift are presented. The prospects of measuring this signal are estimated for current and future lensing data sets.
Conclusions. The *Euclid* mission should provide all the necessary information for studying the cosmic evolution of the connectivity of the cosmic web around lensing clusters using multipolar moments and probing unique signatures of, for example, baryons and warm dark matter.

Key words. galaxies: clusters: general – large-scale structure of Universe – gravitational lensing: weak – methods: numerical – methods: statistical

1. Introduction

The large-scale structures of the Universe (hereafter LSS) have been observed for more than twenty years, first by the CfA catalogue (de Lapparent et al. 1986), and later by large spectroscopic surveys (e.g. the 2dF and SDSS surveys: Colless et al. 2003; Gott et al. 2005). These surveys emphasised a distribution of galaxies that is not homogeneous, but concentrated along filaments, sheets, and presents large underdense regions (voids). Structures grow highly anisotropically from primordial density fluctuations of dark matter under the effect of gravity. Large N-body simulations reproduce this picture, where dark matter particles arrange themselves in a network of filaments. Massive haloes are located at the intersection of filaments, and grow via successive merging as well as continuous accretion of surrounding matter following some preferential directions (Davis et al. 1985; Klypin & Shandarin 1993; Bond et al. 1996; Bond & Myers 1996).

The detection and study of cosmic filaments through observations and numerical simulations is a fundamental step in refining our understanding of structure formation history and cluster evolution. Indeed, filaments have a significant impact on the mass budget of the Universe, as they account for ∼40 per cent of all mass at $z = 0$ (Aragón-Calvo et al. 2010). Their dynamical evolution probes the underlying cosmological model. They also play an important environmental role on galaxy formation and galaxy properties (Hahn et al. 2007; Sousbie et al. 2008; Pichon et al. 2011; Codis et al. 2012; Malavasi et al. 2017; Laigle et al. 2017). However, given the low-density contrast of filaments, identifying them in observations has remained a challenge and, in this context, several observables have been devised to probe their mass distribution.

One of the main observables that has been used to detect filaments is X-ray emission, induced by the warm hot intergalactic medium (WHIM, Cen & Ostriker 1999). Detection remains difficult because X-rays could either come from the intergalactic medium, or past cluster mergers (e.g. Kull & Böhringer 1999; Durret et al. 2003), and often needs to be supported by other observables (Eckert et al. 2015). Recently, the *Planck* satellite has also claimed detection of the Sunyaev-Zeldovich effect of the WHIM in between pairs of galaxy clusters (Planck Collaboration Int. VIII 2013). Some studies reported the detection of filaments in the distribution of galaxies (Ebeling et al. 2004; Pimbblet et al. 2004). Yet this method is limited to relatively low redshifts ($z < 0.4$) and does not probe the physical properties of filaments, given that its main

components are the WHIM and dark matter. Zhang et al. (2013) proposed an algorithm to study the photometric properties of filaments by stacking galaxies' population in cluster pairs.

Gravitational lensing stands as a powerful complementary tool to investigate the entire structure of filaments because it probes dark and luminous matter, regardless of its dynamical state. However, early filament detections by weak lensing (WL) are still controversial. Some attempts have been made to detect them in between galaxy clusters (Clowe et al. 1998; Kaiser et al. 1998; Gray et al. 2002; Gavazzi et al. 2004; Dietrich et al. 2004; Heymans et al. 2008), but it is not clear how robust these results are against residual systematic galaxy alignments. Progress in mass reconstructions from WL (alone or in combination with strong lensing) have recently led to detections confirmed by other observables (Dietrich et al. 2012; Jauzac et al. 2012; Higuchi et al. 2017). Yet, direct measurements from individual (massive) filaments remain sparse due to the weakness of the corresponding shear field. To compensate, some studies also tried to characterise filaments by stacking WL signal (see e.g. Dietrich et al. 2005; Mead et al. 2010; Clampitt et al. 2016; Epps & Hudson 2017). Various WL algorithms amplifying filament detection are described in the literature. Maturi & Merten (2013) developed a WL filter tailored to their elongated extension. Simon et al. (2008) used higher-order correlations, like the galaxy-galaxy-shear three-point statistics. Likewise, aperture multipole moments were introduced by Schneider & Bartelmann (1997) to quantify asymmetries in the mass distribution directly from the shear signal carried by background galaxies. Dietrich et al. (2005) and Mead et al. (2010) studied the quadratic aperture moment of WL signal induced by cluster pairs.

Beyond the overall radial mass profile, the WL measurement of the ellipticity of haloes (their quadrupole) has drawn some attention in recent years. In particular, for galaxy haloes, it is possible to study the relative alignment and flattening of the host halo and its central galaxy (Parker et al. 2007; van Uitert et al. 2012; Schrabback et al. 2015; Clampitt & Jain 2016). Some attempts have also been made to measure the projected ellipticity of a few individual clusters of galaxies (Oguri et al. 2010) or to measure the mean ellipticity of an ensemble of clusters and groups of galaxies by stacking the signal (Evans & Bridle 2009; van Uitert et al. 2017). This latter approach requires assumptions to be made over the relative alignment and elongation between dark and luminous matter.

A visual inspection of the time evolution of N-body simulations allows us to anticipate the following: as gravitational clustering builds up, to first order, the cosmic nodes catastrophically attract matter in their vicinity. This induces an amplification of the contrast in the connected cosmic network, which is locally evolving more rapidly due to the induced density boost (when compared to typical filaments away from the nodes). At the level of this spherically contracting description there should be an excess harmonic power near the peaks. At second order, the filaments themselves induce anisotropic tides which boost up their own contrast by transversally collecting matter and substructures. This effect is also reinforced near peaks, as the radial and transverse tides add up and proto-haloes pass the collapse threshold more easily. The local cosmic filaments at the nodes are therefore amplified by non-linear gravity. This is the cluster-centric counterpart of the process described by Bond et al. (1996) for the field: the large-scale cosmic web is de facto already in place in the initial conditions and gravitational clustering amplifies it differentially. A relative harmonic analysis of the vicinity of clusters should therefore allow us to capture this gravitationally boosted primordial connectivity. The purpose of this paper is to quantify this effect via upcoming WL surveys.

This study will rely on aperture multipole moments at all orders to quantify the azimuthal repartition of matter at different scales, centred on galaxy clusters. We will use mock clusters extracted from a large N-body cosmological simulation to predict the statistical properties of multipolar moments. A new statistical estimator, the multipolar power spectrum will be implemented while stacking the modulus of aperture multipole moments. This method will allow us to quantify the angular distribution of matter around cosmic hubs, hence to detect the signature of filaments in the vicinity of clusters. Stacking power spectra instead of moments alleviates assumptions about the relative distribution of dark and luminous matter whose relation seems to depend on mass and scale (van Uitert et al. 2017).

The structure of this paper is as follows. Section 2 describes the aperture multipole moments following the formalism of Schneider & Bartelmann (1997) and relates the statistics of these moments with those of the underlying convergence fields. In this section, we also build a model for the expected boost in the harmonic power spectra. Section 3 then describes the computation of multipole moments using the dark halo clusters extracted from the PLUS cosmological constrained dark matter N-body simulation and explores how the power spectra depend on redshift, cluster mass and radius. Section 4 discusses the prospects of measuring this signal with WL data accounting for sample variance, shape noise (finite ellipticity of background sources), and intervening LSS, and then weighs the mass content of filaments near the nodes of the cosmic web. Finally, a summary is presented in Sect. 5.

2. Multipolar aperture moments

Let us first present the ingredients of cluster-centric weak gravitational lensing and introduce the corresponding expected statistical properties of the convergence field, which is related to the underlying matter distribution. Specifically, multipolar moments are introduced to measure the asphericity – which quantifies the projected departures from circular symmetry – around the nodes of the cosmic web. Since the focus is on how cluster environment deviates from random locations, the expected ratios will be presented in increasing order of theoretical complexity, starting from the assumption of constrained Gaussian random fields (GRFs) for the convergence. This will guide our understanding of the actual empirical numerical study discussed in the following section.

2.1. Definition of convergence multipoles

The focus of this paper lies in the azimuthal mass distribution at various scales around massive galaxy clusters. For a thin gravitational lens plane, the convergence κ at a given position $\boldsymbol{r}$ in the sky corresponds to the projected excess surface density expressed in units of the so-called critical density $\Sigma_{\rm crit}$

$$\kappa(\boldsymbol{r}) = \frac{1}{\Sigma_{\rm crit}} \int \mathrm{d}z \, (\rho(\boldsymbol{r}, z) - \overline{\rho}) \,, \tag{1}$$

with the convention that the line-of-sight corresponds to the z-axis and the plane of the sky $\boldsymbol{r}$ vector can be defined by polar coordinates (r, φ). The critical density involves distance ratios between a fiducial source at an angular diameter distance $D_{\rm s}$, the

distance to the lensing mass D_l and the distance between the lens and the source D_ls

$$\Sigma_\mathrm{crit} = \frac{c^2}{4\pi G}\frac{D_\mathrm{s}}{D_\mathrm{l}D_\mathrm{ls}}. \tag{2}$$

The lensing potential ψ can also be defined as

$$\psi(\boldsymbol{r}) = \frac{2}{c^2}\frac{D_\mathrm{l}D_\mathrm{ls}}{D_\mathrm{s}}\int \mathrm{d}z\,\Phi(\boldsymbol{r}, z), \tag{3}$$

where Φ is the three dimensional gravitational potential. One can then express the two components γ_1 and γ_2 of the complex spin-2 shear $\gamma = \gamma_1 + \imath\gamma_2$ and the scalar convergence κ as derivatives of the lensing potential

$$2\kappa = \psi_{,11} + \psi_{,22}, \tag{4}$$
$$2\gamma_1 = \psi_{,11} - \psi_{,22}, \tag{5}$$
$$\gamma_2 = \psi_{,12}. \tag{6}$$

Since the interest lies in convergence and shear patterns around a particular centre, let us introduce the tangential γ_t and curl $\gamma_\times$ shear components[1] as

$$\gamma_t = -\mathcal{R}(\gamma\,\mathrm{e}^{-2\imath\varphi}), \quad \gamma_\times = -\mathcal{I}(\gamma\,\mathrm{e}^{-2\imath\varphi}). \tag{7}$$

Following the formalism of Schneider & Bartelmann (1997), let us also define the aperture multipole moments Q_m of this convergence field as

$$Q_m = \int_0^\infty \mathrm{d}r\, r^{1+m} w_m(r) \int_0^{2\pi} \mathrm{d}\varphi\,\mathrm{e}^{\imath m\varphi}\kappa(r,\varphi). \tag{8}$$

There is substantial margin in the choice of the radial weight function. As one may want to have a different radial shape for different multipole orders m and it is desirable to consider a compact support so that $w_m(r)$ vanishes beyond some radius R_max and, possibly, below some inner radius $R_\mathrm{min} \equiv \nu R_\mathrm{max}$. For later use, the multipolar moments can be expressed as a function of the shear field (Schneider & Bartelmann 1997) in a local

$$Q_m = \int_0^\infty \mathrm{d}r\, r^{1+m}\int_0^{2\pi}\mathrm{d}\varphi\,\mathrm{e}^{\imath m\varphi} \times\left[w_m(r)\gamma_t(r,\varphi) + \imath\left(w_m(r) + \frac{r}{m}w_m'(r)\right)\gamma_\times(r,\varphi)\right], \tag{9}$$

and a non-local

$$Q_m = \int_0^\infty \mathrm{d}r\, r^{1+m}\int_0^{2\pi}\mathrm{d}\varphi\,\mathrm{e}^{\imath m\varphi} \times\left[(2W_m(r) - w_m(r))\,\gamma_t(r,\varphi) - \imath m W_m(r)\gamma_\times(r,\varphi)\right], \tag{10}$$

way, with the long-range weight function defined by

$$W_m(r) = \frac{1}{r^{m+2}}\int_0^r \mathrm{d}x\, x^{1+m} w_m(x), \tag{11}$$

where the prime denotes d/dr derivation. Any combination of these two estimators would yield the same answer but, in practice, a careful account of the various sources of noise and the range over which data (i.e. ellipticities of background galaxies) are available will drive the choice of $w_m(r)$. By considering the main source of noise that is due to the intrinsic non-zero ellipticity distribution of background galaxies, Schneider & Bartelmann (1997) found an optimal weight function for a mass density profile that can be approximated as a nearly isothermal mass distribution with $\rho(r) \propto r^{-2}$ or ($\kappa \propto r^{-1}$) and proposed the following form that we use, unless otherwise stated:

$$R_\mathrm{max}^{1+m}\, w_m(r) = \frac{1}{x^{1+m} + \nu^{1+m}} - \frac{1}{1+\nu^{1+m}} + \frac{(1+m)(x-1)}{(1+\nu^{1+m})^2}, \tag{12}$$

over the range $x = r/R_\mathrm{max} \in [\nu, 1]$ and zero elsewhere.

It is noteworthy that an elliptical mass distribution will generate only even moments with a fast decline of modes. Schneider & Weiss (1991) relate the harmonic expansion terms of the convergence or surface mass density with the ellipticity ϵ. In practice, for a power law mass distribution $\kappa \propto r^{-n}$, one can easily show that $Q_2/Q_0 = n\epsilon/2$.

2.2. The statistics of Q_m for a Gaussian random field

In this subsection, let us further assume that the convergence (or some projected density) field is Gaussian and fully characterised by its power spectrum $P_\kappa(\boldsymbol{k})$ so that the two-point expectation value for the Fourier modes $\hat{\kappa}(\boldsymbol{k})$ can be written as

$$\langle\hat{\kappa}(\boldsymbol{k})\hat{\kappa}^*(\boldsymbol{k'})\rangle = (2\pi)^2\delta_D(\boldsymbol{k}+\boldsymbol{k'})P_\kappa(|\boldsymbol{k}|). \tag{13}$$

2.2.1. Random locations

The convergence κ having zero mean value, the covariance between multipolar moments centred at random positions can readily be expressed by following the same method as Schneider et al. (1998) who explored the statistics of the M_ap statistic, which is a particular case of the $m = 0$ multipolar moments. Let us write

$$\langle Q_m Q_n^*\rangle = \int_0^\infty\!\!\int r\mathrm{d}r\, r'\mathrm{d}r' \int_0^{2\pi}\!\!\int \mathrm{d}\varphi\mathrm{d}\varphi'\; r^m w_m(r) r'^m w_n(r') \times \mathrm{e}^{\imath(m\varphi - n\varphi')}\langle\kappa(r,\varphi)\kappa(r',\varphi')\rangle, \tag{14}$$
$$= 2\pi\,\imath^{m-n}\int k\mathrm{d}k\, U_m(k)U_n(k)\,P_\kappa(k), \tag{15}$$
$$\equiv \imath^{m-n}A_{\kappa,mn}, \tag{16}$$

where the Hankel transform $U_n(\ell)$ of the radial weight function is defined by

$$U_m(\ell) = \int r\mathrm{d}r\, r^m w_m(r) J_m(\ell r), \tag{17}$$

and $J_m(x)$ are the first-kind Bessel functions.

Let us now consider a realistic convergence power spectrum derived from the non-linearly evolved matter spectrum, $P_\delta(\boldsymbol{k})$. The power spectrum of the density contrast is computed at various redshifts, using the Boltzmann code `CLASS` toolkit (Blas et al. 2011; Lesgourgues 2011) for the fiducial Planck Cosmology. For a given source redshift, the convergence power spectrum $P_\kappa(\ell, z_\mathrm{s})$ can be inferred from the three-dimensional matter power spectrum, considering the following integral (Blandford et al. 1991; Miralda-Escudé 1991; Kaiser 1992; Bartelmann & Schneider 2001; Simon 2007)

$$P_\kappa(\ell, z_\mathrm{s}) = \frac{9}{4}\Omega_m^2\left(\frac{H_0}{c}\right)^4\int_0^{\chi_s}\mathrm{d}\chi\frac{(\chi_\mathrm{s}-\chi)^2}{\chi_\mathrm{s}^2}\frac{P_\delta(\ell/\chi,\chi)}{a^2(\chi)}. \tag{18}$$

In addition, instead of using a single-source-plane redshift, the latest COSMOS2015 photometric redshift distribution

[1] In some cases, $\gamma_\times$ is referred to as a "radial" γ_r component which can be misleading for a spin-2 field.

(Laigle et al. 2016) is used to approximate the redshift distribution of sources as a Gamma PDF of the form

$$p(z_s) = \frac{e^{-z_s/z_0}}{z_0\Gamma(a)}\left(\frac{z_s}{z_0}\right)^{a-1}, \quad (19)$$

with $a \simeq 2.1$ and $z_0 \simeq 0.51$ for sources as faint as an AB magnitude $i = 25$, which is suitable for future experiments like *Euclid* or current deep ground-based imaging data. The effective convergence power spectrum is finally computed by weighting the contributions of the different source planes

$$P_\kappa(\ell) = \int P_\kappa(\ell, z_s)\, p(z_s)\, \mathrm{d}z_s. \quad (20)$$

For illustration purposes, Fig. 1 shows the convergence power spectrum and the corresponding multipolar moments for a fiducial choice of $R_{\max} = 10'$ and $\nu = 0.5$, which should correspond to the scale of a few virial radii for a massive cluster at redshift $z \sim 0.3$. In order to highlight the contrast between the linear and non-linear regime on the convergence power spectrum and on the associated multipolar moment spectrum, we illustrate these two cases. As expected, by adopting a non-linear matter power spectrum, the multipolar moment spectrum is significantly enhanced.

2.2.2. The statistics of Q_m under peak constraint

Even for a Gaussian random field, the statistics of Q_m should change significantly when centred on a cluster rather than a random location. The formalism must be updated to deal with a particular flavour of three-point statistics that accounts for the presence of a maximum with a specific height ν_p of the density field at the origin of the coordinate system. In brief, the companion paper (Codis et al. 2017) has shown that the effect of the peak constraint is to

- significantly boost the monopole (we are near a peak);
- significantly remove power from the dipole (we are now well centred on the peak);
- slightly suppress the power of the quadrupole;
- leave all other $m \geq 3$ multipoles unchanged.

These results rely on the assumptions that galaxy clusters can be mapped to peaks in the initial field smoothed at some scale R, which themselves can be characterised by their height (large excursion), gradient (forced to be null at the origin), and Hessian (two negative eigenvalues).

Our current purpose is to go beyond the Gaussian and peak approximation and describe the statistical properties of Q_m at late time by measuring them directly in simulations in Sect. 3. In the following section, we simply describe changes in the statistics of multipolar moments to be expected from simple arguments about the non-linear evolution around galaxy clusters.

2.3. The non-linear statistics of Q_m around clusters

Appendix A presents an approximate model based on the Zeldovich approximation and the spherical collapse, which shows that the small-scale density fluctuations in a shell at radius r falling onto a spherically symmetric proto-cluster will experience a boost of amplitude α with respect to the field. It is due to the contraction of fluctuations within the original Lagrangian shell induced by the tidal distortion field of the cluster overdensity. It implies for the 3D power spectrum

$$P_{\rm cluster}(\boldsymbol{k}) \equiv \alpha\, P_{\rm random}(\boldsymbol{k}), \quad \text{where} \quad \alpha \simeq \left(\frac{3M(<r)}{4\pi\bar{\rho}r^3}\right)^{2/3}, \quad (21)$$

where $\bar{\rho}$ is the mean background density. Once projected along the line-of-sight, fluctuations around a cluster should also produce a non-linear achromatic (m-independent) boost of multipolar moments spectra as compared to the field. This prediction is compared to measurements in simulations in Sect. 3.3 and despite a crude treatment of projection effects and the extension of the model deeply inside the core of the cluster, is shown to give a quantitative explanation for the boost.

This boost corresponds to the first order change on the multipolar moments expected for initial peaks evolving into clusters. The next step involves understanding any spectral distortion of $|Q_m|^2_{\rm cluster}$ with respect to $\alpha|Q_m|^2_{\rm random}$, as a second-order effect due to the non-linear coupling of modes involving specifically the filamentary structure around clusters. Finally, we recall that

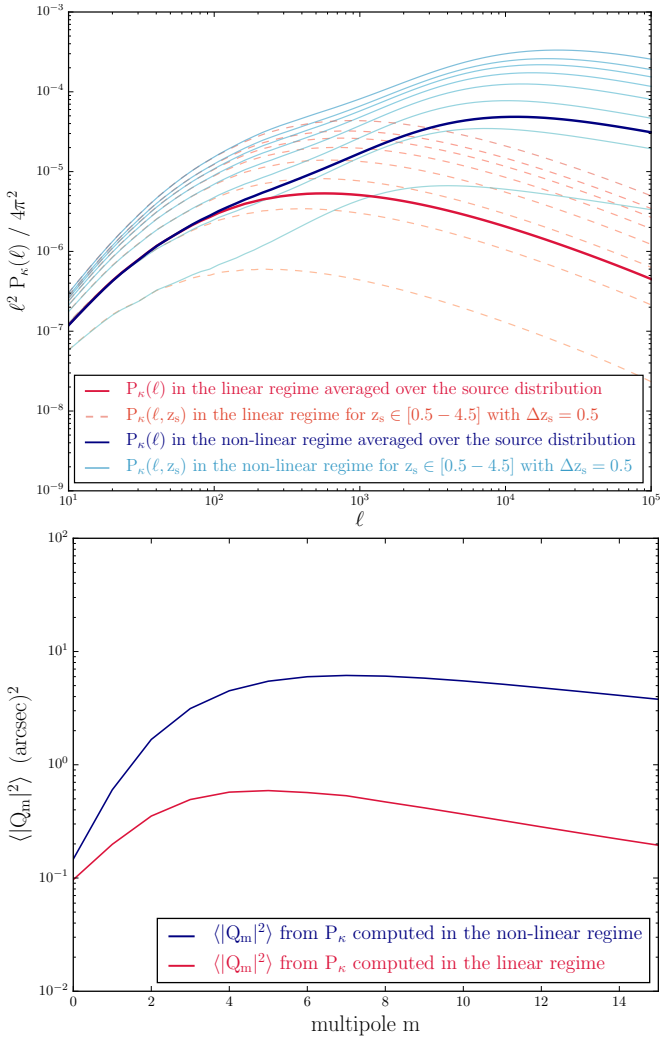

Fig. 1. *Top panel*: cosmological convergence power spectrum $P_\kappa(\ell)$ derived from the evolved matter power spectrum averaged over the source redshift distribution of Eq. (19). The red and blue curves represent the quantities induced by the linear and non-linear matter power spectrums, respectively. *Bottom panel*: corresponding multipolar moment spectra $\langle|Q_m^2|\rangle$ for the weight function in Eq. (12) and a choice of $R_{\max} = 10'$ and $\nu = 0.5$.

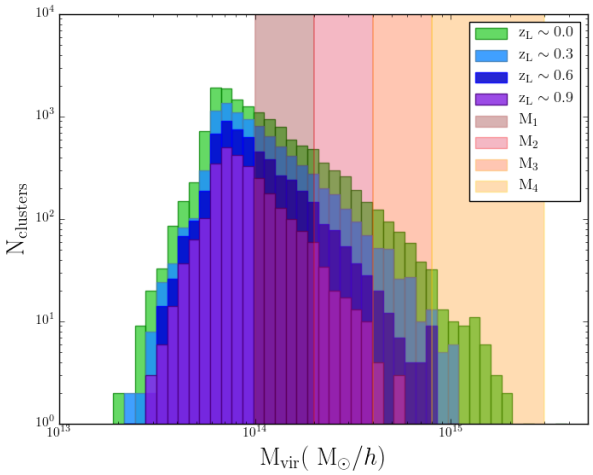

Fig. 2. Halo virial mass function in the PLUS simulation box (600 cMpc/h on a side) at four different redshifts (0, 0.3, 0.6 and 0.9) showing the content of the four mass intervals considered. Only haloes with a FOF mass greater than $5 \times 10^{13}\, h^{-1} M_\odot$ are shown here.

the linear power spectrum $P(k)$ should be updated when accounting for the peak condition at the origin of the coordinate system and that, in two dimensions, the multipoles $m \leq 2$ are impacted. A more thorough treatment of the asphericity around the cluster potential could possibly allow us to predict the actual shape of the $|Q_m|^2_{\rm cluster}$ spectrum at all m. This is left for future work, and from now on, we rely on N-body cosmological simulations to predict these spectra, both near the edge of clusters where our formalism should hold, but also deep inside the virial radius of those clusters.

3. Measuring multipolar moments in simulations

3.1. Dark matter haloes in the PLUS cosmological simulation

A cosmological simulation taken from the Paris Local Universe Simulation (PLUS)[2] project was analysed. It corresponds to a ΛCDM universe with the following set of cosmological parameters, $\Omega_{\rm m} = 0.3175$, $\Omega_\Lambda = 0.6825$, $\Omega_b = 0.049$, $H_0 = 67.11$ km s^{-1}/Mpc, $n_{\rm s} = 0.9624$ and $\sigma_8 = 0.8344$ (Planck Collaboration XVI 2014). The simulation was performed with Gadget2 (Springel 2005) in a periodic box of side $600\, h^{-1}$ Mpc and using 2048^3 dark matter particles (i.e., with a mass resolution of $\sim 2.2 \times 10^9\, h^{-1} M_\odot$). The adopted Plummer-equivalent force softening was 14.6 h^{-1} kpc and was kept constant in comoving units. The simulation started at $z = 49$ and ended at the present time $z = 0$. The initial conditions have been generated using the BORG algorithm (Bayesian Origin Reconstruction from Galaxies Jasche & Wandelt 2013; Lavaux 2015) aiming at modelling the local universe.

The dark matter halo catalogue was extracted at redshifts $z = 0, 0.3, 0.6$, and 0.9 with a Friend-of-Friend algorithm (FOF) using a linking length of 0.15 in units of the mean inter-particle separation and came up, for the $z = 0$ output, with about 14 000 groups and clusters with mass $M_{\rm FOF} > 5 \times 10^{13}\, h^{-1} M_\odot$. Then all the particles in the direct vicinity of these haloes are extracted and projected along a given direction. Hence, each extracted halo contains a cluster and its outer environment (Metzler et al. 2001). The additional effect of the uncorrelated background and foreground matter distribution along the line of sight to distant gravitationally lensed galaxies will be treated as an additional Gaussian random field acting as a noise contribution (see e.g. Hoekstra 2001, 2003).

- $M_{\rm FOF}$ is used as a first guess to define a virial radius $M_{\rm FOF} = 4/3\pi\Delta_{\rm vir}\rho_{\rm crit}R^3_{\rm vir}$.
- The centre of mass of the linked particles was used to extract all the particles within a comoving radius $R_{\rm H} = 4R_{\rm vir}$ about it. This radius is sufficiently large to capture the most relevant environment of clusters.
- We refine the definition of the centre by seeking the main peak of the density field with a shrinking sphere method. Starting from the previous value of $R_{\rm vir}$, let us compute the centre of mass therein. At each iteration, the sphere is shrunk by 2.5% and we update the center of mass accordingly. The process is stopped when the final mass is below 1% of the starting $M_{\rm FOF}$ value.
- By sorting particles in radius about this final centre, one can easily build the cumulative mean density profile $\overline{\rho}(<r)$. The final virial radius is the distance at which $\overline{\rho}(<R_{\rm vir}) = \Delta_{\rm vir}\rho_{\rm crit}$.

The above calculations rely on the fitting functions of Bryan & Norman (1998) to estimate the density contrast $\Delta_{\rm vir}$ above the critical density $\rho_{\rm crit}$ for our reference ΛCDM cosmology. Hence, the typical virial mass is on average 1.14 times greater than $M_{\rm FOF}$, the mass directly linked by the FOF algorithm. We investigate two different radial intervals, $R/r_{\rm vir} \in [0.25, 0.5]$ and $R/r_{\rm vir} \in [1, 4]$, in order to emphasise differences between the innermost, presumably relaxed, areas and the ones undergoing coherent infall motions, where filaments should be more prominent.

To study the influence of mass in this analysis, the sample of haloes is divided into four bins of virial mass $M_1 \in$ 1–2, $M_2 \in$ 2–4, $M_3 \in$ 4–8, and $M_4 \geq 8 \times 10^{14}\, h^{-1} M_\odot$ as shown in Fig. 2.

We also study the evolution of multipolar moments with redshift by considering simulation outputs at redshifts $z = 0, 0.3, 0.6, 0.9$. In order to follow the evolution of moments of a given population of haloes, we also consider the 100 most massive clusters. This selection in mass is a proxy for a population of haloes with the same rareness, $\nu_p = \delta/\sigma$. Indeed, the mass of non-linearity $M_\star$ (i.e. the peak of the Press-Schechter mass function) evolves with redshift. Picking the most massive haloes at each redshift therefore allows us to focus on a population of haloes which present a similar level of non-linearity[3], which should therefore be at the same stage of their evolution. As redshift takes values $z = 0, 0.3, 0.6$, and 0.9, the mean virial mass of the 100 most massive clusters successively takes values $M_{\rm vir} \simeq 10, 7, 5, 3 \times 10^{14}\, h^{-1} M_\odot$.

3.2. Multipoles from simulated haloes

The projected surface density of a discrete distribution of particles of mass M_j reads

$$\Sigma(r, \varphi) = \sum_j M_j\, \delta_{\rm D}(\boldsymbol{r} - \boldsymbol{r}_j), \tag{22}$$

where r and φ are the coordinates in the plane of the sky. Hence, translating Eq. (8) to a discrete distribution, the multipolar

[2] http://www2.iap.fr/users/peirani/PLUS/plus.htm

[3] Which amounts to having a constant variance $\sigma^2(M, z)$ at redshift z and scale M.

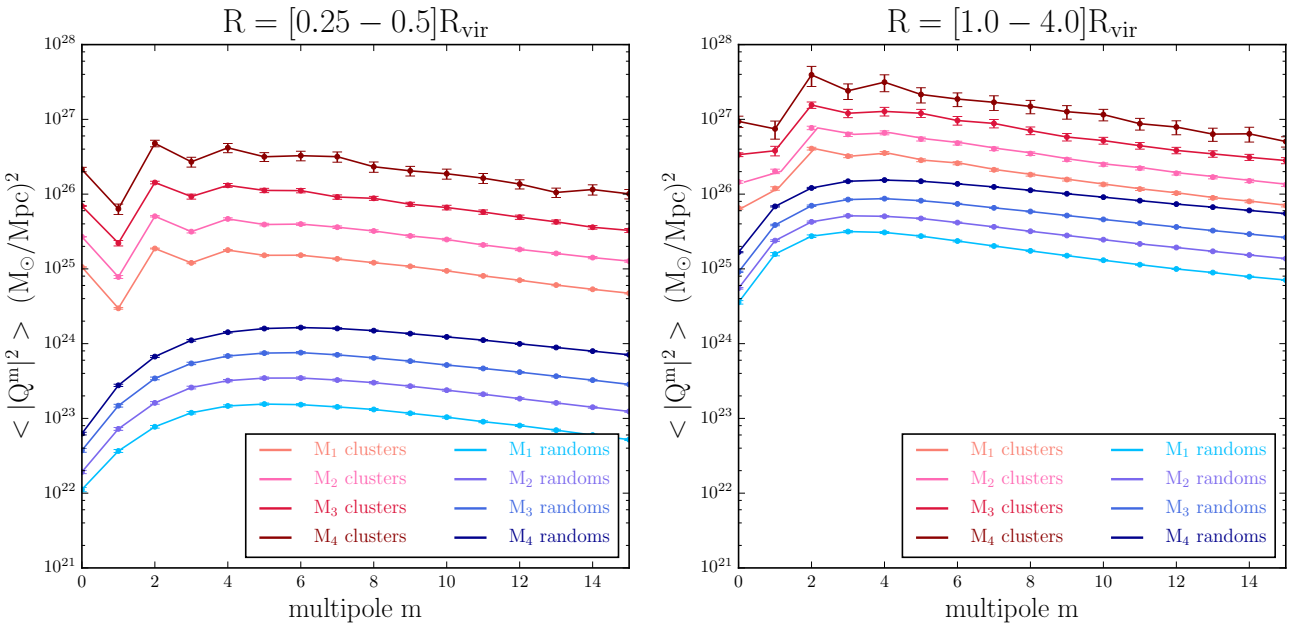

Fig. 3. Multipolar moments spectra around clusters (upper red curves) and around random location (lower blue curves) for the two annuli $0.25 \leq R/R_{\rm vir} < 0.5$ and $1 \leq R/R_{\rm vir} < 4$ (*left and right-hand panels* respectively) for the $z = 0$ simulation output. There is an excess of power around clusters as compared to random localisations, since the density field is denser. At large m (substructures scales), their spectra differ by a nearly constant multiplicative factor $\hat{\alpha}$, which is the first order signature of the dynamical evolution of the shape of clusters (see Sect. 3.3).

moments reads

$$Q_m = \int_0^\infty {\rm d}r r^{m+1} w_m(r) \int_0^{2\pi} {\rm d}\varphi \, {\rm e}^{{\rm i}m\varphi} \, \Sigma(r,\varphi), \\ = \sum_j M_j r_j^m w_m(r_j) {\rm e}^{{\rm i}m\varphi_j}. \quad (23)$$

Because of the spherical extraction of particles performed around each cluster, one needs to subtract off the contribution of the cosmological mean density, which simply reads

$$\Sigma_0(r) = 2\rho_{\rm mean} \sqrt{R_{\rm H}^2 - r^2}. \quad (24)$$

Since it does not depend on the azimuth φ, it only involves a non-zero correction $Q_0^{\rm bg}$ to the monopole term $m = 0$ in Eq. (23). As discussed, the practical measurement of these multipolar moments requires signal stacking and, by symmetry, the phases of Q_m will be lost in this process. Any departure from circular symmetry would thus be washed out. A simple workaround that does not depend on the visible baryonic mass in clusters is to consider the mean power of their multipolar moments in harmonic space. The focus is therefore on the statistics of $\langle |Q_m^2| \rangle$.

For each simulated cluster i, the projections along the three canonical (x, y, z) directions are averaged for a given annulus ΔR

$$3\,|Q_m^i|^2 = |Q_m^{i,x}|^2 + |Q_m^{i,y}|^2 + |Q_m^{i,z}|^2. \quad (25)$$

Finally, for a given mass bin ΔM, one averages the multipolar moments of haloes within the same mass bin to compute the spectrum of multipolar moments

$$\langle |Q_m|^2 \rangle (\Delta M, \Delta R) = \frac{1}{N_{\rm haloes}} \sum_i^{N_{\rm haloes} \in \Delta M} |Q_m^i|^2 (\Delta R). \quad (26)$$

In order to explore how the background cosmology affects $\langle |Q_m|^2 \rangle$, these multipoles are also computed for spheres drawn randomly inside the simulation box. For each position, a virial radius (and mass) is randomly assigned from the parent halo catalogue and the multipolar moments of these random "haloes" is measured. This allows us to contrast the growth of moments near clusters to the overall cosmic growth of structures cast into the particular filtering of the density field as given by Eq. (8). In order to limit the noise in these reference moments, many more random positions than haloes are drawn. Appendix B checks that this approach yields results that are consistent with a formal integration of the power spectrum of the density contrast $P_\delta(\boldsymbol{k})$.

At this stage, these (centred or random) spectra are not corrected from the shot noise contribution due to the finite number of particles in the simulation that are sampling the density field. This correction is only substantial at low mass, on small scales (the smallest ΔR annulus), and for the largest multipole orders m. Shot noise corresponds to a white convergence (or surface density, here) power spectrum that is independent of the wave vector $\boldsymbol{k}$ as described in Sect. 2.2

$$P(k) \equiv P_0 = \langle \Sigma_0(r) \rangle \, M_{\rm part}, \quad (27)$$

with $\langle \Sigma_0(r) \rangle$ the mean projected density for $r \in [R_{\rm min}, R_{\rm max}]$. For multipoles centred on clusters, this latter equation is multiplied by $1 + \langle Q_0^{\rm cluster} \rangle / \langle Q_0^{\rm bg} \rangle$ to get the correct shot noise amplitude. Here the average accounts for cluster-to-cluster variations of $R_{\rm max}$ (due to $M_{\rm vir}$ variations within that mass range).

Figure 3 presents the shape of the $\langle |Q_m|^2 \rangle$ spectrum of multipolar moments at redshift $z = 0$ as a function of multipolar order m, and for the four mass bins and two radial bins. In order to highlight the effect that a galaxy cluster has on the statistics of $\langle |Q_m|^2 \rangle$, we also display the same quantity for random locations.

3.3. Overall excess of power

There is an obvious excess of power in Fig. 3 at almost all multipoles and scales around clusters as compared to random locations of similar size since the density field is denser due to the

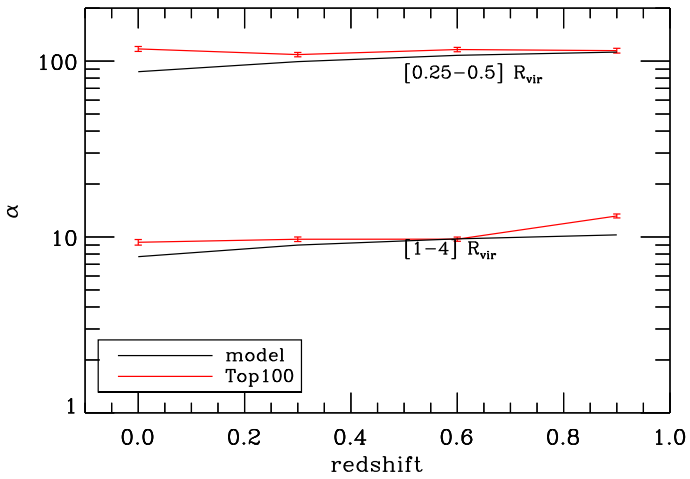

Fig. 4. Evolution with redshift of the normalisation factor $\hat{\alpha}$ of multipolar moments spectra for the 100 most massive haloes (red solid lines). The theoretical prediction of α is overlaid in black. The model reproduces the variations with time, mass and scale remarkably well, despite a crude treatment of projections and the limited validity of the spherical collapse model.

presence of the central cluster. Clusters and random locations differ by a nearly constant multiplicative factor, which is the first order signature of the dynamical evolution of the shape of clusters, as quantified in Sect. 2.3. This multiplicative factor $\hat{\alpha}$ (the 2D counterpart of the boost factor α of Sect. 2.3) is estimated empirically by focussing on the $m \in [15-30]$ multipole range, since it is on the smallest angular scales that the assumptions behind the Zeldovich boost are most sensible:

$$\log \hat{\alpha} = \frac{1}{16} \sum_{m=15}^{30} \left(\log \langle |Q_m|^2 \rangle_{\rm cluster} - \log \langle |Q_m|^2 \rangle_{\rm random} \right). \qquad (28)$$

Figure 4 shows the evolution of $\hat{\alpha}$ with redshift and as a function of scale for the 100 most massive clusters in the simulation box. This boost, of order $\sim$100 on the small $R \in [0.25, 0.5]R_{\rm vir}$ scale, and of order $\sim$10 in the larger $R \in [1, 4]R_{\rm vir}$ scale, is, of course, of key importance for the detectability of $|Q_m|^2$.

A comparison with the prediction of α based on the spherical contraction of a Lagrangian shell presented in Sect. 2.3 is overlaid. It shows a remarkable agreement, given the limited validity of the extension of this model deeply inside virialised haloes and the lack of modelling of projection effects. Since we use apertures that scale with the virial radius, α should not evolve much with time or mass (up to a mild change with time and mass of the halo concentration, see Appendix A). This is clearly seen and reproduced in Fig. 4.

3.4. Harmonic distortions

In order to highlight spectral distortions that are in excess of the overall boost, Fig. 5 shows the normalised spectra $\langle |Q_m|^2 \rangle_{\rm clusters} / (\alpha \langle |Q_m|^2 \rangle_{\rm random})$ as a function of halo mass at redshift zero in the top panels, and as a function of redshift for the 100 most massive haloes in the bottom panels.

A residual excess of power is found on large angular scales $m \lesssim 8$, possibly extending slightly further for the outermost radial bin and for more massive haloes. Systematically, odd orders carry less power. This should be the signature of the peak constraint (that was only affecting $m = 1$ for a GRF). The centering reduces the power excess at odd multipolar orders, mainly at $m = 1, 3$. Mis-centering will thus reduce the contrast between odd and even orders. We explored the amplitude of this effect by applying random offsets of the order $0.1\,R_{\rm vir}$, and only found noticeable differences on small-scale moment spectra whereas offsets as large as $0.5R_{\rm vir}$ are required to substantially change moments in the $1-4R_{\rm vir}$ range. The main effect of mis-centering on small-scale moments is to reduce the contrast between odd and even orders, leaving the latter ones almost unchanged.

Comparing small ($0.25 \leq R/R_{\rm vir} < 0.5$) and large-scale ($1.0 \leq R/R_{\rm vir} < 4.0$) annuli, respectively, on the left and right panels of Fig. 5, a similar excess is found suggesting that the small- and large-scale shape might be correlated (see Sect. 3.5 below). The faster damping with m inside haloes represents a noticeable difference, tracing the higher level of symmetry in the core of virialised structures. It can indeed be approximated by an ellipsoid (with possibly some amount of $m = 4$ boxiness). In fact, the inner quadrupole $m = 2$ presents a higher amplitude relative to the monopole than in the outskirts of clusters (right panel). This is consistent with recent studies which use elliptical or triaxial models to describe dark matter haloes shape (Warren et al. 1992; Jing & Suto 2002; Despali et al. 2014).

More massive haloes are more sensitive to the anisotropic environment they formed in. Interpreting this excess of power as the non-linear sharpening of the filamentary structure of haloes sitting at the nodes of the cosmic web, one may infer that these haloes are connected to a larger number of filaments, as already found by Pichon et al. (2010) and Aragón-Calvo et al. (2010). Massive haloes are more likely to be in their early formation phase, and their shape is typically distorted by major mergers or accretion along the preferred direction set by their connecting filaments. Conversely, lower-mass haloes are formed at higher redshift and have had more time to relax. They typically lost the memory on their accretion history, and therefore the preferential directions induced by recent merging events.

Following the same haloes with time (bottom panels), that is, at constant initial overdensity while compensating for progenitor bias (e.g. Sheth & Tormen 2004), one can see that no significant evolution of the multipole is observed. This suggests that the shape of haloes is settled early in the cosmic history, probably in the initial conditions, as anticipated in Sect. 3.1 (and discussed in e.g. Bond et al. 1996). Though one might have expected to observe a disconnection of dark haloes through the dark-energy-induced stretching of the cosmic web (Pichon et al. 2010), it turns out that the most massive clusters of the simulation have not had time to disconnect from the cosmic web nor fully relax. Their outskirts are still imprinted by their initial environment, whose azimuthal geometry displays power on a fairly wide range of multipoles triggered by the connected filaments and walls. Both large- and small-scale moments are frozen in shape from the initial conditions and only grow with time at the cosmic rate captured by the boost. Their excess multipole seems qualitatively consistent with the expected number of connected filaments (peaking at 2–4) inferred from the initial conditions (Pichon et al. 2010), keeping in mind that multipoles are mass weighted.

3.5. Radial correlations

Let us investigate now whether the angular shape of galaxy clusters at small and large scales are correlated. A cross-spectrum of multipoles at varied scales would tell us how far the filaments plunge into the haloes. Figure 6 shows the reduced cross-spectrum of multipolar moments at radii $R \in [0.25-0.5]R_{\rm vir}$ and

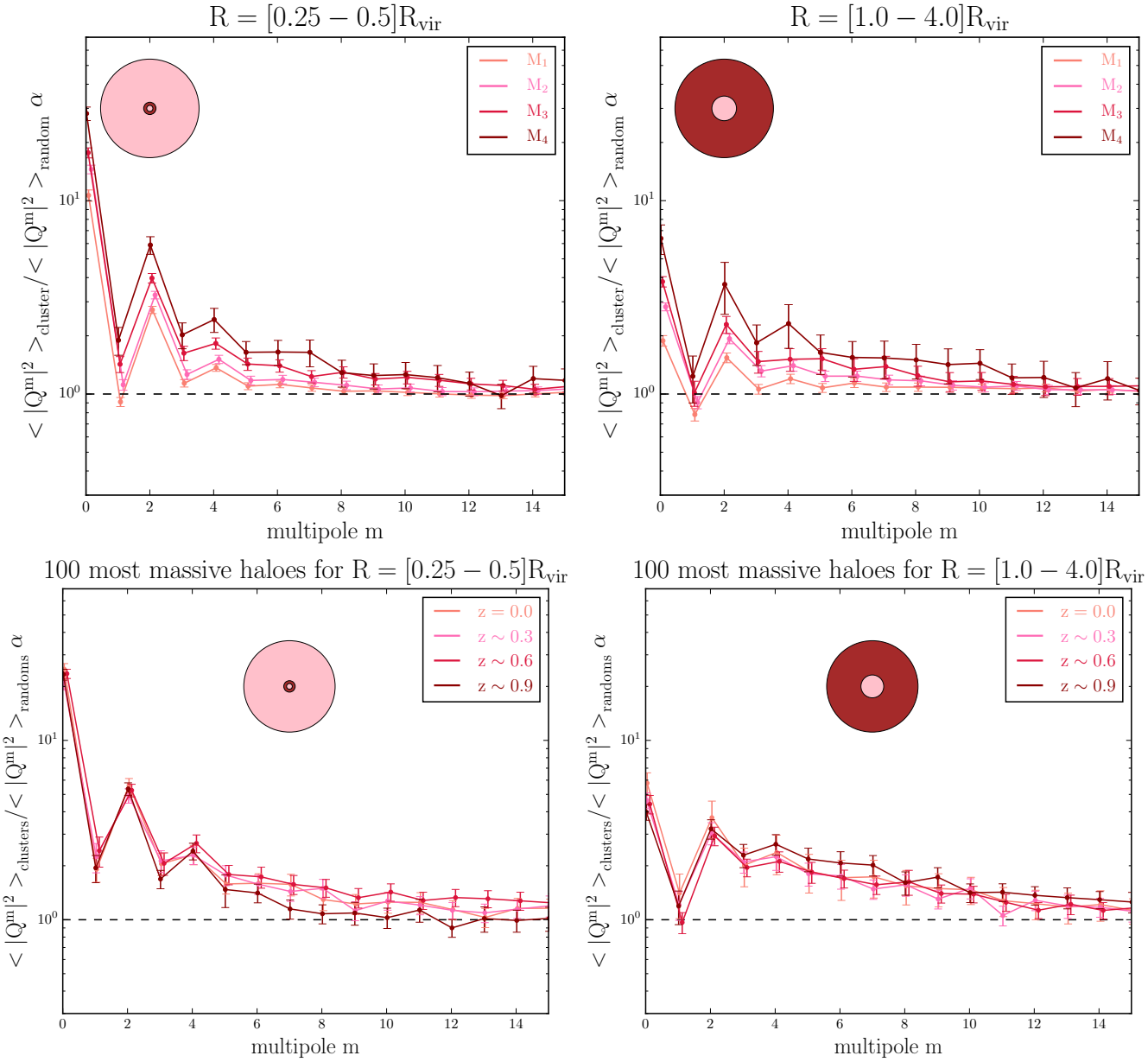

Fig. 5. *Top panels*: multipolar moments spectra (normalised by random profiles) for the annulus $0.25 \leq R/R_{\rm vir} < 0.5$ (*left*) and $1 \leq R/R_{\rm vir} < 4$ (*right*) at redshift $z = 0$ as a function of halo mass. In the internal region, the quadrupole prevails, and reflects the ellipsoidal symmetry of the core. In the external region, the residual power excess at $2 < m < 10$, not predicted by GRF approximation, should represent the non-linear sharpening of the filamentary structure. *Bottom panels*: multipolar moments spectra (normalised by random profiles) for the annulus $0.25 \leq R/R_{\rm vir} < 0.5$ (*left*) and $1 \leq R/R_{\rm vir} < 4$ (*right*) for the 100 most massive haloes for the $z = 0$, $z \sim 0.3$, $z \sim 0.6$ and $z \sim 0.9$ simulation outputs. Comparing a population of haloes with the same level of non-linearity (or the same rareness), the shape of haloes appears to be settled early in the cosmic history.

$R \in [1{-}4]R_{\rm vir}$ for the M_1 mass bin. This reads

$$\rho_{1,4}(m,n) = \frac{\langle (Q_m(R_1)Q_n^*(R_4)\rangle - \delta_{m0}\delta_{n0}\langle Q_0(R_1)\rangle\langle Q_0(R_4)\rangle}{\sigma_{Q_m(R_1)}\,\sigma_{Q_n(R_4)}}. \quad (29)$$

The disconnected part (product of the means) is subtracted to highlight the relative fluctuations between annuli and multipolar orders. In contrast to what was done for the auto-spectra $\langle |Q_m|^2\rangle$ for which the mean $\langle Q_0\rangle^2$ was not subtracted off because it contributes to the overall signal amplitude and to its detectability (Sect. 4). Without subtraction, $\langle Q_0(R_1)\rangle\langle Q_0(R_4)\rangle$ would induce a large correlation $\rho_{1,4}(0,0) \geq 0.5$.

Except for the diagonal $m = n = 1, 2, 4$ terms, no significant correlation is observed. A similar trend is found at higher masses although the signal to noise is even lower. Apart from the quadrupole, the shapes seem to decorrelate. Hence there is no strong angular coherence between the structures found at $R \in [0.25{-}0.5]R_{\rm vir}$ and $R \in [1{-}4]R_{\rm vir}$ beyond the quadrupole. The non-zero cross-correlation at $m = 1$ is induced by the condition to be centred on a density peak. We also checked that miscentring has the effect of reducing the $\langle Q_1(R_1)Q_1^*(R_4)\rangle$ term. In order to reach a factor 2 decline in correlation amplitude, one needs to reach offsets of the order $0.2\,R_{\rm vir}$.

4. Measuring multipolar moments from shear data

Let us now quantify our ability to estimate the power spectrum of multipolar moments from real WL data. They involve a set of background galaxies whose light is deflected by a foreground

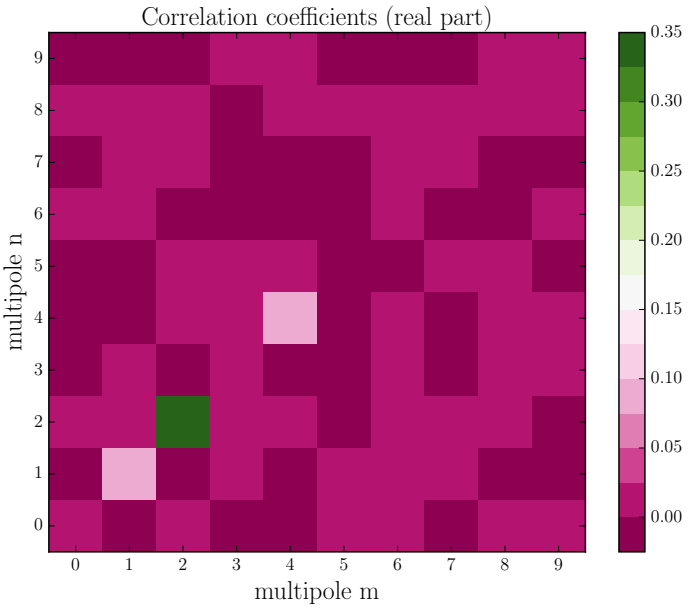

Fig. 6. Cross-correlation of multipolar moments between annuli $R \in [0.25, 0.5]R_{\rm vir}$ and $R \in [1{-}4]R_{\rm vir}$ for the M_1 mass bin. Apart from $m = n = 1, 2, 4$ terms, no significant correlation is found.

Table 1. Critical lensing surface density used to convert Sect. 3 multipolar moments expressed in terms of mass into moments expressed in terms of convergence.

Lens redshift	0	0.3	0.6	0.9
$\langle\Sigma_{\rm crit}^{-1}\rangle^{-1}$ $[10^{15}\,M_\odot\,{\rm Mpc}^{-2}]$	∞	3.330	4.413	7.585

galaxy cluster. Since very few detections of filaments, and little evidence for a departure from circular symmetry have been reported so far, there is a dire need to investigate how to measure the mean excess power spectrum of multipolar moments from a set of galaxy clusters. The aim is, in particular, to quantify the expected signal to noise ratio as a function of redshift, scale, and mass.

Three leading sources of noise must be considered here: the shape noise coming from the unknown intrinsic ellipticity of background sources, the lensing gravitational potential due to the LSS along the line-of-sight, and the sample variance due to the finite number of clusters one can average over to infer the mean multipolar spectrum. One expects some internal variability due to the relative dynamical age of these massive structures undergoing merger, being fed by a variable number of filaments. The derivation we use follows Schneider et al. (1998) who studied the statistical properties of the aperture mass $M_{\rm ap}$ estimators, but neglects the effects of Poisson fluctuations in the number of background sources. This is legitimate for large-scale cluster lensing with deep wide-field imaging.

One first needs to rescale the multipolar moments previously inferred from simulations in terms of mass per Mpc since the convergence was replaced by the surface density in Eq. (23). Therefore the moments will be multiplied by the mean inverse critical density $\langle\Sigma_{\rm crit}^{-1}(z)\rangle$, averaged over the same redshift distribution of background sources as that assumed in Sect. 2.2. The corresponding values for the fiducial lens redshifts are listed in Table 1.

4.1. Covariance of multipolar moment spectrum estimators

The convergence field around a cluster should be replaced by three uncorrelated fields

$$\kappa \longrightarrow \kappa + \kappa^{\rm s} + \kappa^{\rm L}, \tag{30}$$

where κ is the signal produced by the cluster, $\kappa^{\rm s}$ is the contribution from the intrinsic ellipticity of background sources and $\kappa^{\rm L}$ is due to the uncorrelated LSS along the line-of-sight. The LSS that is not physically correlated to the direct cluster environment (beyond 10 Mpc, or so) will nevertheless give rise to a cosmological convergence field that will act as an additive source of noise plaguing the multipolar moment (or more generally the convergence field sourced by the clusters) to be measured. This so-called cosmic shear signal has to be taken into account for the detectability of multipolar moments as it is a substantial source of noise for overall cluster-mass measurements (Hoekstra 2001, 2003). Section 2.2 already showed the two-point properties of this component $\kappa^{\rm L}$ through the Eq. (14). In the remainder, the statistical properties of $\kappa^{\rm L}$ are approximated as those of a GRF (with null kurtosis) since the focus is on the statistics of κ.

The convergence field is not directly observable; ellipticities are used to measure shear. The observed complex ellipticity ϵ of a galaxy with intrinsic source plane ellipticity $\epsilon_{\rm s}$ and carrying a complex shear signal γ is simply: $\epsilon = \epsilon_{\rm s} + \gamma$. Since for an ensemble of galaxies with random intrinsic orientation, the mean $\epsilon_{\rm S}$ is null, one can write:

$$\langle\epsilon_i\rangle = \gamma_i, \tag{31}$$

$$\langle\epsilon_i\epsilon_j\rangle = \gamma_i\gamma_j + \gamma_i^{\rm L}\gamma_j^{\rm L} + \sigma_\epsilon^2\delta_{ij}, \tag{32}$$

where the one-dimensional rms dispersion of intrinsic source ellipticities $\sigma_\epsilon \simeq 0.25$ was introduced. In practice, measurement errors that depend on the quality of images (correction for smearing by the Point Spread Function, signal-to-noise...) would also increase this dispersion to a value that we shall take to be $\sigma_\epsilon \equiv 0.3$ in the remainder.

Following again Schneider & Bartelmann (1997), let us consider the local estimator of Q_m from measured shear as defined by Eq. (9) and in which only background galaxies projected into a given annulus of inner and outer radius $\nu R_{\rm max}$ and $R_{\rm max}$ are used to estimate the multipolar moments in that aperture. The non-local estimator, involving shear measurements outside that aperture, may increase the sensitivity but at the expense of introducing large correlations between annuli. The remainder of this work only explores the merits of the local estimator Eq. (9) that is rewritten in the same way as Schneider & Bartelmann (1997)

$$Q_m = \int {\rm d}^2\boldsymbol{r}\left[\frac{b_{t,m}(r)}{r}\gamma_t(r,\varphi) + \imath\frac{b_{\times,m}(r)}{r}\gamma_\times(r,\varphi)\right]{\rm e}^{\imath m\varphi}, \tag{33}$$

with

$$b_{t,m}(r) = r^{m+1}w_m(r), \tag{34}$$

$$b_{\times,m}(r) = r^{m+1}\left(w_m(r) + \frac{r}{m}w_m'(r)\right). \tag{35}$$

For a finite number N of sources inside a given annulus $[\nu R_{\rm max}, R_{\rm max}]$, the discrete version of Eq. (33) reads

$$\hat{Q}_m = \frac{1}{\overline{n}}\sum_k^N {\rm e}^{\imath m\varphi_k}\left[\frac{b_{t,m}(r_k)}{r_k}\epsilon_{{\rm t},k} + \imath\,\frac{b_{\times,m}(r_k)}{r_k}\epsilon_{\times,k}\right], \tag{36}$$

where $\overline{n}$ is the mean number density of background sources, for which a typical value $\overline{n} = 30\,{\rm arcmin}^{-2}$. Even though the sources

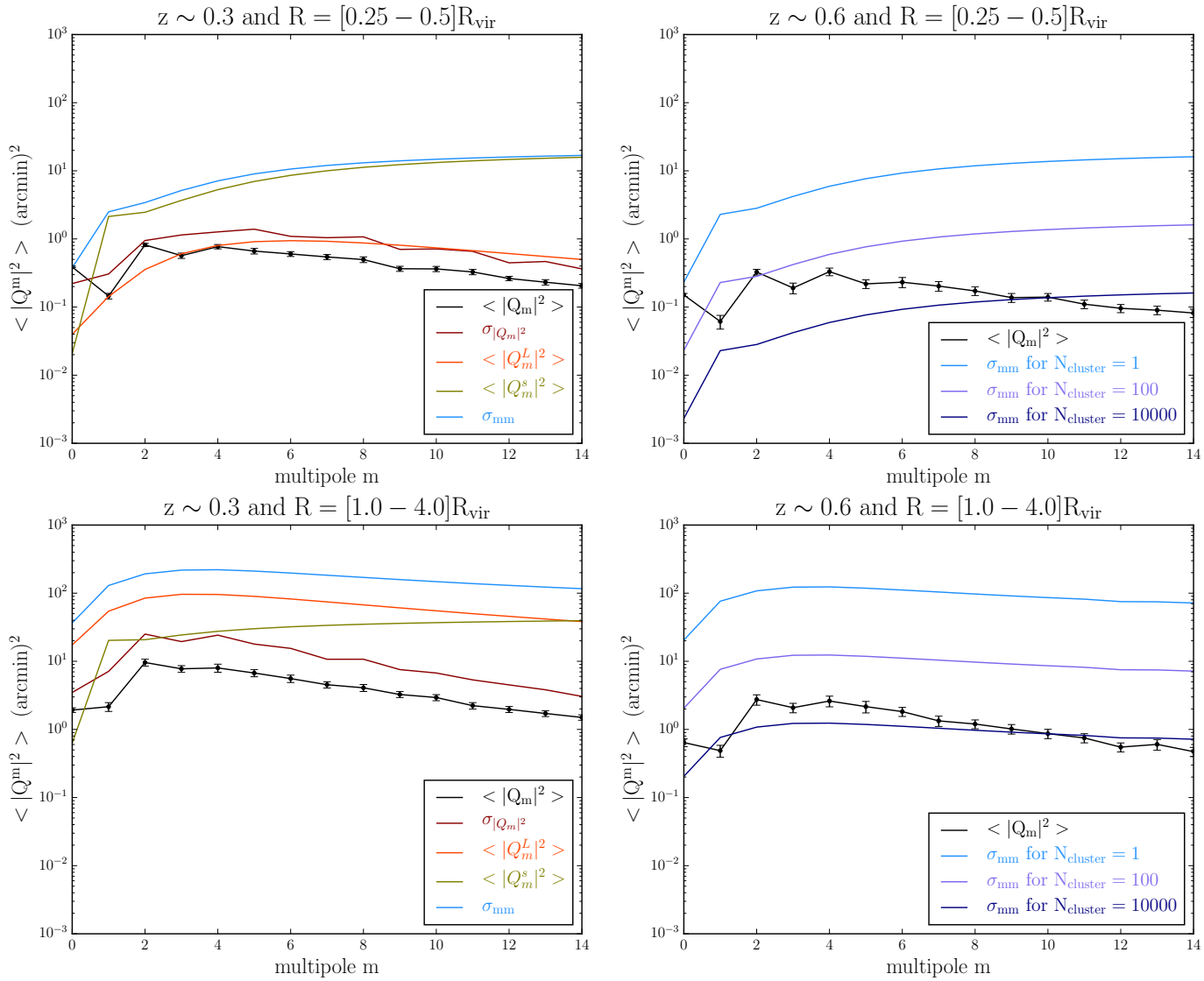

Fig. 7. Multipolar moment spectra of clusters for the mass bin M_3 and the noise contribution at two scales in the annuli ΔR_1 (*top panel*) and ΔR_4 (*bottom panel*) and for two redshift values $z = 0.3$ and 0.6, respectively, *from left to right*. *The left-hand panels* show the different sources of noise as described in Sect. 4. On *the right-hand panels*, the total noise profile $\sigma_{\rm mn}$ is shown once divided by $\sqrt{N_{\rm clusters}}$ in order to mimic the shot noise obtained by stacking the spectra of $N_{\rm clusters}$ clusters.

are randomly oriented, the ensemble average of the quadratic estimator $|\hat{Q}_m|^2$ of $|Q_m|^2$ will contain a shape noise and a LSS noise contribution that must be subtracted off

$$\langle|\hat{Q}_m|^2\rangle = |Q_m|^2 + |Q^{\rm s}_m|^2 + |Q^{\rm L}_m|^2. \tag{37}$$

As shown in Schneider & Bartelmann (1997), this shape noise mean power spectrum is

$$|Q^{\rm s}_m|^2 = \frac{\sigma^2_\epsilon}{\bar{n}^2}\sum_k^N \frac{b^2_{t,m}(r_k) + b^2_{\times,m}(r_k)}{r^2_k}, \tag{38}$$

$$= \frac{\pi\sigma^2_\epsilon}{\bar{n}}\int_{\nu R}^R {\rm d}r \frac{b^2_{t,m}(r) + b^2_{\times,m}(r)}{r}. \tag{39}$$

This mean noise spectrum gives us a sense of our ability to measure multipolar moments. But one really needs to compute the covariance of the estimator by following the calculations made for cosmic shear correlation functions (Schneider et al. 1998, 2002) and consider the covariance matrix of the multipolar moments

$$\begin{aligned}\sigma^2_{mn} &\equiv \langle|\hat{Q}_m|^2|\hat{Q}_n|^2\rangle - \langle|\hat{Q}_m|^2\rangle\langle|\hat{Q}_n|^2\rangle,\\ &= \delta_{mn}|Q^{\rm s}_m|^2\left[|Q^{\rm s}_m|^2 + 2|Q_m|^2 + 2|Q^L_m|^2\right]\\ &\quad + \delta_{m0}\delta_{n0}|\tilde{Q}^{\rm s}_0|^2\left[|\tilde{Q}^{\rm s}_0|^2 + 2|Q_0|^2 + 2|Q^L_0|^2\right]\\ &\quad + 4A_{\kappa,mn}A_{\kappa^{\rm L},mn}\\ &\quad + \langle|Q_m|^2|Q_n|^2\rangle - \langle|Q_m|^2\rangle\langle|Q_n|^2\rangle\\ &\quad + \langle|Q^{\rm L}_m|^2|Q^{\rm L}_n|^2\rangle - \langle|Q^{\rm L}_m|^2\rangle\langle|Q^{\rm L}_n|^2\rangle.\end{aligned} \tag{40}$$

The first two terms in Eq. (40), containing $Q^{\rm s}_m$, correspond to the shape noise. They are diagonal and dominate for $m = 0$. Their derivation along with the definition of the modified moments $|\tilde{Q}^{\rm s}_m|^2$ are detailed in Appendix C. The last three terms correspond to the mixture of sampling variance and LSS noise contributions. If both κ and $\kappa^{\rm L}$ were GRFs, these three terms would simplify to $2(A_{\kappa,mn} + A_{\kappa^{\rm L},mn})^2$, with A_{mn} defined in Eq. (14).

4.2. Overall detectability

The left-hand panels of Fig. 7 compare the amplitude of $|Q_m|^2$, $|Q_m^{\rm s}|^2$ and $|Q_m^{\rm L}|^2$ along with the rms dispersion of $|Q_m|^2$ for a single cluster of galaxies in the intermediate mass bin ($M \in [4-8]\times10^{14}\,h^{-1}\,M_\odot$) at redshift $z \sim 0.3$. The total combination of diagonal terms $\sigma_{\rm mm}$ in Eq. (40) is also overlaid. It appears that for the internal regions (top panel), the shape noise – coming from the intrinsic ellipticities of the background galaxies – dominates, whereas on large scales, the dominant source of noise is the line-of-sight density fluctuations $|Q_m^{\rm L}|^2$. Hoekstra (2003) also found a similar radial behaviour of the relative importance of shape noise and LSS for measuring overall cluster masses. Obviously, detectability is easier in the central region than at the outskirts of clusters, since the density field is stronger. The signal-to-noise declines also as redshift increases and mass decreases. The overall signal-to-noise is quite low for a single cluster, with values of order 0.1 for the most favourable multiples ($m = 0, 2, 4$). On small scales, using a non-local multipole estimator might slightly reduce shape noise contributions, but on large scales, LSS will dominate anyway, suggesting that very deep observations with a low shape noise level would not be of much help. We must therefore consider stacking the lensing signal of many clusters.

On the right panels of Fig. 7, the amplitude of $\langle|Q_m|^2\rangle$ is compared to the total noise contribution $\sigma_{\rm mm}$ for a single cluster in the mass bin $\rm M_3$ at $z \sim 0.6$ at small and large radii. Instead of splitting the noise budget into its components, the total overall noise level is scaled by a factor 0.1 or 0.01 as it should naturally decrease if one considers 100 or 10 000 clusters instead of just one. Besides, at higher redshift, the signal-to-noise decreases due to the rise of the critical density with redshift (see Table 1).

The *Euclid* photometric galaxy cluster survey will contain about 2×10^5 clusters between $z = 0.2$ and $z = 2$ (Sartoris et al. 2016). The authors provide an estimate of the number of galaxy clusters to be detected for a given range of redshift and minimum mass by carefully accounting for the *Euclid* cluster selection function. This allows us to predict the expected number of clusters in each mass bin and for three redshift intervals, hence the expected signal-to-noise ratio on multipolar moments. This is shown in Fig. 8 for both internal and external regions of galaxy clusters. Higher signal-to-noise can be achieved for lower mass clusters because of their larger abundance. More specifically, multipolar moments measured at the outskirts of clusters should accurately be detected by stacking clusters with $M_{\rm vir} \leq 8\times10^{14}\,h^{-1}\,M_\odot$ and $z \leq 0.75$. In the internal regions, we estimate that the angular symmetries on cluster cores could be probed for all cluster masses for $z \lesssim 0.75$.

In order to improve the signal-to-noise and permit detections on a shorter timescale, one can consider a broader annulus $R = [0.1-1.0]\,R_{\rm vir}$ that probes the high-density regions, the corresponding list of signal-to-noise ratios for 100 clusters in Table 2. A detection of the multipoles from $m = 0$ to $m = 4$ is possible in this annulus, stacking the signal over about 100 galaxy clusters, for all mass bins at $z \sim 0.3$ and for the most massive clusters. At $z \sim 0.6$, the measurement is possible for clusters of similar mass but only up to the quadrupole.

Table 2. Signal-to-noise ratio on multipolar moment spectra for $N_{\rm cluster} = 100$ when the annulus $R \in [0.1, 1.0]\,R_{\rm vir}$ is considered.

Redshift	Mass bin	Multipole m					
		0	1	2	3	4	5
0.3	M_1	9	0.6	1.8	0.4	0.4	0.2
	M_2	12	1.2	3.4	1.0	1.0	0.5
	M_3	14	2.4	5.4	2.1	2.2	1.1
	M_4	11	3.2	7.1	3.6	3.7	2.1
0.6	M_1	8	0.3	0.9	0.2	0.2	0.08
	M_2	10	0.6	2.0	0.5	0.5	0.2
	M_3	12	1.4	3.7	1.0	1.1	0.4
	M_4	17	3.1	4.9	2.0	2.4	0.8
0.9	M_1	5	0.1	0.3	0.01	0.01	0.003
	M_2	8	0.2	0.9	0.2	0.2	0.06
	M_3	10	1.0	1.9	0.5	0.5	0.24

5. Summary and conclusions

The multipolar moments of the convergence were used to quantify asymmetries in the projected density field around galaxy clusters. The multipoles were computed within annuli centred on mock clusters of galaxies, extracted from a large dark matter simulation. The power spectra of these moments, $\langle|Q_m|^2\rangle$, were studied in detail, noticeably via their evolution with redshift, cluster mass and radial aperture.

We quantified the degree of angular symmetries around clusters that is in excess of the background density field. To this end, we compared the multipolar moment spectra centred on clusters to those of random locations. To first order, the non-linear evolution of mass shells sinking towards the centre of clusters induces a boost of power at all angular scales due to the contraction of the Lagrangian patch initially encompassing the mass fluctuations. When the density field is nearly Gaussian, only $m \leq 2$ moments are affected by the peak constraint, as demonstrated in Codis et al. (2017), while in the quasi-linear regime this paper also predicts, perturbatively, the achromatic boost. In the highly non-linear regime, a simple model based on the spherical collapse model was presented, and is found to be in good agreement with measurements on massive haloes extracted from the PLUS Dark Matter cosmological simulation.

Looking at the harmonic distortions occurring on top of the overall boost, we found an angular power excess at orders $m \lesssim 10$ in the outer shell, which traces the azimuthal shape of the projected density. The excess chromatic power in the multipoles seems qualitatively consistent with the predicted number of connected filaments in the outskirts of clusters (Pichon et al. 2010; Pogosyan et al., in prep.), keeping in mind that the harmonic analysis is mass weighted. We also found a higher amplitude for the quadrupole in the central regions, which reflects the ellipsoidal symmetry of the core of haloes (see also, e.g. Despali et al. 2014). Given the similarity in the excess power in internal and external regions, we examined the cross-correlation of multipolar moments between these two annuli. Except for the quadrupole, angular shapes at small and large scales seem to be uncorrelated. This is probably because, typically, two branches of filaments are connected to a node of the cosmic web on small scales (Pogosyan et al. 2009). Further away from the nodes, bifurcation points appear and therefore increase the number of filaments. We therefore expect the quadrupole to be correlated between small and large scales but correlations beyond the quadrupole to be suppressed on small scales. Therefore, the steeper profile of the small-scale multipoles compared to their large-scale counterpart is fully consistent with this idea that the cosmic connectivity is smaller on small scales.

We also studied the evolution of multipolar spectra at different redshifts (from $z = 0$ to $z \sim 0.9$) and found that following the same population of haloes, that is, with the same initial rareness

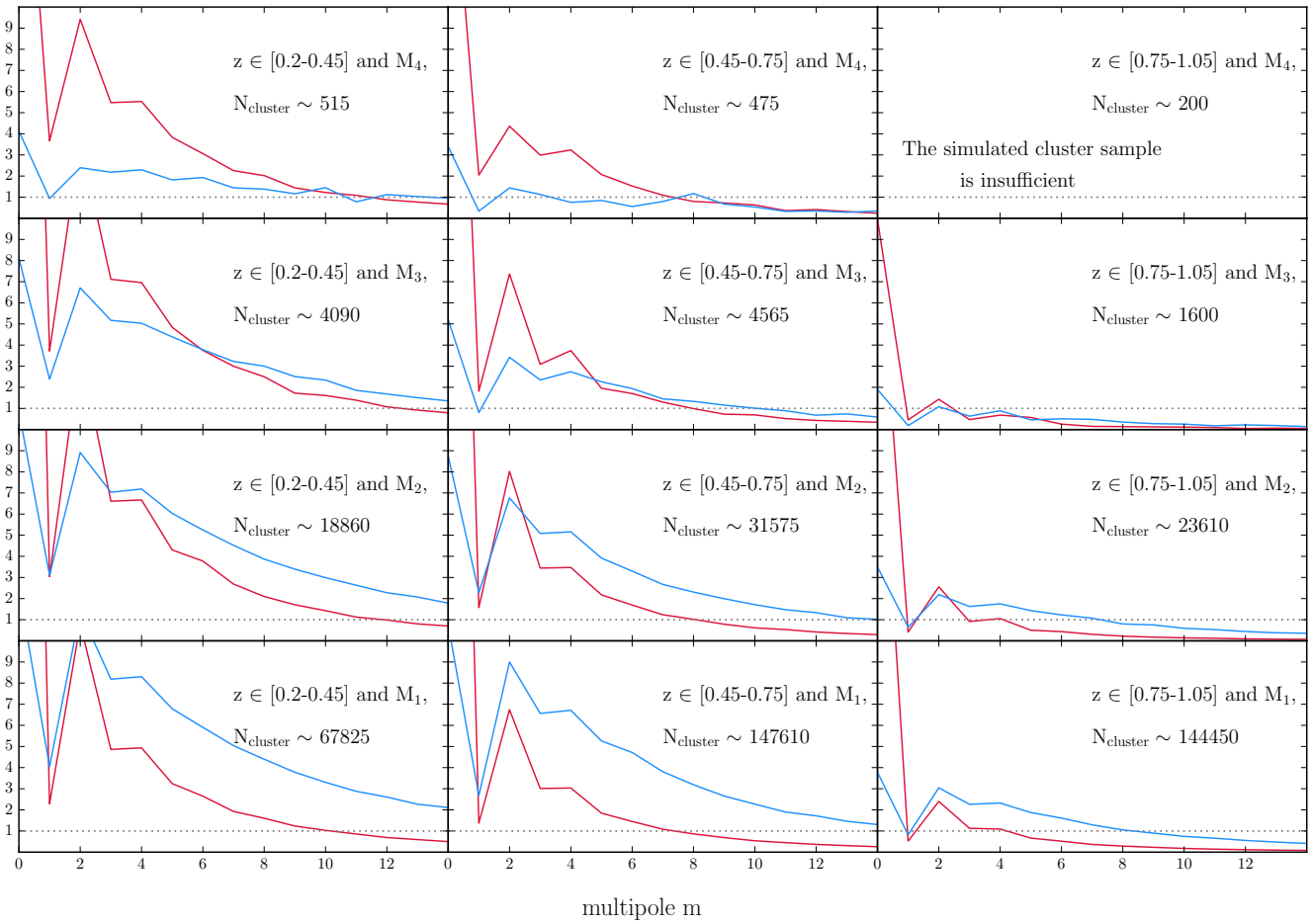

Fig. 8. Expected signal-to-noise ratio of multipolar moment spectra that one could obtain by stacking the total number of galaxy clusters $N_{\rm cluster}(z, M)$, that will be uncovered in the future *Euclid* survey (Sartoris et al. 2016). Red and blue curves represent the signal-to-noise ratio for the annuli $R_1 \in [0.25{-}0.5]R_{\rm vir}$ and $R_4 \in [1{-}4]R_{\rm vir}$, respectively. Three different ranges of redshift are considered (∼0.3, ∼0.6 and ∼0.9 from *left to right*), together with four fiducial cluster mass intervals ($M_4, \cdots M_1$, *from top to bottom*).

level, the multipolar moments measured in an annulus that follows the growth of the virial radius grow at a rate that is similar to the cosmic rate (implying no change of the spectra normalised by α). This suggests that the larger-scale shape in the vicinity of the halo is fixed at early times in its formation history, and keeps the memory of its initial conditions during collapse (Bond et al. 1996). Indeed, the dark-energy-induced disconnection from the cosmic web (Pichon et al. 2010) has not yet occurred for this most massive population of clusters. We note that, as expected, for a less massive population of haloes, we observe a decrease of the harmonic excess in both internal and external regions with time. This decrease is due to a virialisation of the core and a disconnection of the halo from the cosmic web, at the respective scales. Globally, these quantitative estimates are consistent with dynamical expectation drawn from the visual inspection of simulations.

Finally, we estimated the detectability of these harmonics using WL data, taking into account different sources of noise such as the shape noise (intrinsic ellipticity of the background galaxies), the impact of the LSS along the line-of-sight, and the sample variance. As expected, the amplitude of the signal-to-noise ratio increases with halo mass and depends on the aperture and the cluster redshift (see Fig. 7). On small scales (within the virial radius), shape noise dominates whereas additional deflections due to matter along the line-of-sight dominate the noise budget on larger scales (outside the virial radius). Due to the weakness of the signal, one has to stack the multipolar moment spectra over a larger number of clusters. Hence, one should consider current detections of filaments with WL with caution.

With the upcoming *Euclid* mission (Laureijs et al. 2011), multipolar moment spectra will be detected with a good degree of precision up to $m \sim 10$ in central and external regions. On a shorter timescale, considering a broader annulus ($R = [0.1{-}1]R_{\rm vir}$), harmonic components should be measured at orders $m = 0, 2, 4$, by stacking ∼100 massive clusters up to $z \sim 0.6$. Such measurements on ground-based observations will be presented in a forthcoming companion paper (Gavazzi et al., in prep.). Upcoming investigations should extend this study to varying cosmological models. Cosmology can have an impact on multipolar moment spectra but the overall amplitude is governed by the cluster mass profile, which is better constrained by a direct stacking of the tangential shear or a stacking of Q_0 values. Cosmological effects related, for instance, to the growth rate and dark energy, may have an effect on the relative amplitude of moments. One could extend those measurements to cosmological hydrodynamical simulations in which baryonic physics, such as gas cooling and feedback from active galaxy nuclei, will substantially change the shape of the total mass distribution on small scales (Teyssier et al. 2011; Suto et al. 2017). These scales may be more efficiently probed by strong lensing observables (following, e.g. Peirani et al. 2008). Additionally, models involving warm or self-interacting dark matter may leave an interesting

footprint on the spectrum of multipolar moments, as departure from vanilla CDM would tend to make haloes rounder. We thus expect these spectra to be a valuable Dark Matter probe on small scales. Finally, we expect that comparisons between multipolar moments measured with lensing and similar moments measured on different populations of galaxies of different types may shed new light on the relative bias of these populations inside filaments and as they sink into cluster haloes. The key role of environment on the quenching of star formation in galaxies around clusters may hence be probed.

Acknowledgements. The authors would like to thank K. Benabed, J.-F. Cardoso, M. Kilbinger, G. Lavaux for valuable discussions. This work was supported by the Agence Nationale de la Recherche (ANR) as part of the SPIN(E) ANR-13-BS05-0005 and Jeune Chercheur AMALGAM projects, and by the Centre National des Études Spatiales (CNES). This work has made use of the Horizon Cluster hosted by the Institut d'Astrophysique de Paris. We thank S. Rouberol for running the cluster smoothly for us.

References

Aragón-Calvo, M. A., van de Weygaert, R., & Jones, B. J. T. 2010, MNRAS, 408, 2163
Bartelmann, M., & Schneider, P. 2001, Phys. Rep., 340, 291
Blandford, R. D., Saust, A. B., Brainerd, T. G., & Villumsen, J. V. 1991, MNRAS, 251, 600
Blas, D., Lesgourgues, J., & Tram, T. 2011, J. Cosmol. Astropart. Phys., 7, 034
Bond, J. R., & Myers, S. T. 1996, ApJS, 103, 1
Bond, J. R., Kofman, L., & Pogosyan, D. 1996, Nature, 380, 603
Bryan, G. L., & Norman, M. L. 1998, ApJ, 495, 80
Cen, R., & Ostriker, J. P. 1999, ApJ, 519, L109
Clampitt, J., & Jain, B. 2016, MNRAS, 457, 4135
Clampitt, J., Miyatake, H., Jain, B., & Takada, M. 2016, MNRAS, 457, 2391
Clowe, D., Luppino, G. A., Kaiser, N., Henry, J. P., & Gioia, I. M. 1998, ApJ, 497, L61
Codis, S., Gavazzi, R., & Pichon, C. 2017, A&A, in press, DOI: 10.1051/0004-6361/201630091
Codis, S., Pichon, C., Devriendt, J., et al. 2012, MNRAS, 427, 3320
Colless, M., Peterson, B. A., Jackson, C., et al. 2003, ArXiv e-prints [arXiv:astro-ph/0306581]
Davis, M., Efstathiou, G., Frenk, C. S., & White, S. D. M. 1985, ApJ, 292, 371
de Lapparent, V., Geller, M. J., & Huchra, J. P. 1986, ApJ, 302, L1
Despali, G., Giocoli, C., & Tormen, G. 2014, MNRAS, 443, 3208
Dietrich, J. P., Clowe, D., Schneider, P., Kerp, J., & Romano-Díaz, E. 2004, in Outskirts of Galaxy Clusters: Intense Life in the Suburbs, ed. A. Diaferio, IAU Colloq. 195, 34
Dietrich, J. P., Schneider, P., Clowe, D., Romano-Díaz, E., & Kerp, J. 2005, A&A, 440, 453
Dietrich, J. P., Werner, N., Clowe, D., et al. 2012, Nature, 487, 202
Durret, F., Lima Neto, G. B., Forman, W., & Churazov, E. 2003, A&A, 403, L29
Ebeling, H., Barrett, E., & Donovan, D. 2004, ApJ, 609, L49
Eckert, D., Jauzac, M., Shan, H., et al. 2015, Nature, 528, 105
Epps, S. D., & Hudson, M. J. 2017, MNRAS, 468, 2605
Evans, A. K. D., & Bridle, S. 2009, ApJ, 695, 1446
Gavazzi, R., Mellier, Y., Fort, B., Cuillandre, J.-C., & Dantel-Fort, M. 2004, A&A, 422, 407
Gott, III, J. R., Jurić, M., Schlegel, D., et al. 2005, ApJ, 624, 463
Gray, M. E., Taylor, A. N., Meisenheimer, K., et al. 2002, ApJ, 568, 141
Hahn, O., Porciani, C., Carollo, C. M., & Dekel, A. 2007, MNRAS, 375, 489
Heymans, C., Gray, M. E., Peng, C. Y., et al. 2008, MNRAS, 385, 1431
Higuchi, Y., Oguri, M., Tanaka, M., & Sakurai, J. 2017, MNRAS, submitted [arXiv:1503.06373]
Hoekstra, H. 2001, A&A, 370, 743
Hoekstra, H. 2003, MNRAS, 339, 1155
Jasche, J., & Wandelt, B. D. 2013, MNRAS, 432, 894
Jauzac, M., Jullo, E., Kneib, J.-P., et al. 2012, MNRAS, 426, 3369
Jing, Y. P., & Suto, Y. 2002, ApJ, 574, 538
Kaiser, N. 1992, ApJ, 388, 272
Kaiser, N., Wilson, G., Luppino, G., et al. 1998, upublished [arXiv:astro-ph/9809268]
Klypin, A., & Shandarin, S. F. 1993, ApJ, 413, 48
Klypin, A., Yepes, G., Gottlöber, S., Prada, F., & Heß, S. 2016, MNRAS, 457, 4340
Kull, A., & Böhringer, H. 1999, A&A, 341, 23
Laigle, C., McCracken, H. J., Ilbert, O., et al. 2016, ApJS, 224, 24
Laigle, C., Pichon, C., Arnouts, S., et al. 2017, MNRAS, submitted [arXiv:1702.08810]
Laureijs, R., Amiaux, J., Arduini, S., et al. 2011, ArXiv e-prints [arXiv:1110.3193]
Lavaux, G. 2015, IAU General Assembly, 22, 2245818
Lesgourgues, J. 2011, ArXiv e-prints [arXiv:1104.2932]
Malavasi, N., Arnouts, S., Vibert, D., et al. 2017, MNRAS, 465, 3817
Maturi, M., & Merten, J. 2013, A&A, 559, A112
Mead, J. M. G., King, L. J., & McCarthy, I. G. 2010, MNRAS, 401, 2257
Metzler, C. A., White, M., & Loken, C. 2001, ApJ, 547, 560
Miralda-Escudé, J. 1991, ApJ, 380, 1
Navarro, J. F., Frenk, C. S., & White, S. D. M. 1997, ApJ, 490, 493
Oguri, M., Takada, M., Okabe, N., & Smith, G. P. 2010, MNRAS, 405, 2215
Parker, L. C., Hoekstra, H., Hudson, M. J., van Waerbeke, L., & Mellier, Y. 2007, ApJ, 669, 21
Peirani, S., Alard, C., Pichon, C., Gavazzi, R., & Aubert, D. 2008, MNRAS, 390, 945
Pichon, C., Gay, C., Pogosyan, D., et al. 2010, in AIP Conf. Ser. 1241, eds. J.-M. Alimi, & A. Fuözfa, 1108
Pichon, C., Pogosyan, D., Kimm, T., et al. 2011, MNRAS, 418, 2493
Pimbblet, K. A., Drinkwater, M. J., & Hawkrigg, M. C. 2004, MNRAS, 354, L61
Planck Collaboration XVI. 2014, A&A, 571, A16
Planck Collaboration Int. VIII. 2013, A&A, 550, A134
Pogosyan, D., Pichon, C., Gay, C., et al. 2009, MNRAS, 396, 635
Sartoris, B., Biviano, A., Fedeli, C., et al. 2016, MNRAS, 459, 1764
Schneider, P., & Bartelmann, M. 1997, MNRAS, 286, 696
Schneider, P., & Weiss, A. 1991, A&A, 247, 269
Schneider, P., van Waerbeke, L., Jain, B., & Kruse, G. 1998, MNRAS, 296, 873
Schneider, P., van Waerbeke, L., Kilbinger, M., & Mellier, Y. 2002, A&A, 396, 1
Schrabback, T., Hilbert, S., Hoekstra, H., et al. 2015, MNRAS, 454, 1432
Sheth, R. K., & Tormen, G. 2004, MNRAS, 350, 1385
Simon, P. 2007, A&A, 473, 711
Simon, P., Watts, P., Schneider, P., et al. 2008, A&A, 479, 655
Sousbie, T., Pichon, C., Colombi, S., Novikov, D., & Pogosyan, D. 2008, MNRAS, 383, 1655
Springel, V. 2005, MNRAS, 364, 1105
Suto, D., Peirani, S., Dubois, Y., et al. 2017, PASJ, 69, 14
Teyssier, R., Moore, B., Martizzi, D., Dubois, Y., & Mayer, L. 2011, MNRAS, 414, 195
van Uitert, E., Hoekstra, H., Schrabback, T., et al. 2012, A&A, 545, A71
van Uitert, E., Hoekstra, H., Joachimi, B., et al. 2017, MNRAS, 467, 4131
Warren, M. S., Quinn, P. J., Salmon, J. K., & Zurek, W. H. 1992, ApJ, 399, 405
Zhang, Y., Dietrich, J. P., McKay, T. A., Sheldon, E. S., & Nguyen, A. T. Q. 2013, ApJ, 773, 115

Appendix A: Towards the non-linear statistics of Q_m

Let us first consider the weakly non-linear regime for the statistics of Q_m around clusters before turning to its strong non-linear counterpart.

A.1. The weakly non-linear regime

For simplicity, let us first focus on the statistics of density fluctuations in a 3D shell of matter located at a radius r from the centre of a cluster of galaxies. This shell is falling onto the cluster at a rate that can be derived from the spherical collapse model or the Zeldovich approximation. It was originally located at a Lagrangian radius q. Specifying the initial potential $\psi(\boldsymbol{q}) = \psi^{\rm l}(\boldsymbol{q}) + \psi^{\rm c}(\boldsymbol{q})$, where $\psi^{\rm c}$ is the potential generated by the peak at the centre and $\psi^{\rm l}$ is due to matter fluctuations in the original shell, the mapping between the Eulerian coordinate $\boldsymbol{r}$ and its corresponding Lagrangian position $\boldsymbol{q}$ is

$$\boldsymbol{r} = \boldsymbol{q} - D'\boldsymbol{\nabla}_q\psi(\boldsymbol{q}), \tag{A.1}$$

with $D' = D(a)/4\pi G\bar{\rho}a^3$, $D(a)$ the linear growth rate, and $\bar{\rho}$ the mean comoving cosmic density. The evolved density contrast is given by the Jacobian of this transformation

$$1 + \delta = \left|\delta_{ij} - D'\psi^{\rm c}_{,ij} - D'\psi^{\rm l}_{,ij}\right|^{-1}, \tag{A.2}$$

with $|\ |$ the determinant of its argument. Taylor expanding this relation around small values of $\psi^{\rm l}$ and defining the distortion tensor $\Gamma_{ij} = \delta_{ij} - D'\psi^{\rm c}_{,ij}$, allows us to rewrite Eq. (A.2) as

$$1 + \delta = \left|\Gamma_{ij}\right|^{-1}\left(1 + D'{\rm Tr}(\Gamma^{-1}_{ij}\psi^{\rm l}_{,ij})\right), \tag{A.3}$$

where Tr is the trace of its argument. Accounting now for the spherical symmetry of $\psi^{\rm c}$, the Γ matrix reads

$$\Gamma = {\rm Diag}\left(1 - D'\psi^{\rm c}_{,qq}, 1 - D'\frac{1}{q}\psi^{\rm c}_{,q}, 1 - D'\frac{1}{q}\psi^{\rm c}_{,q}\right), \tag{A.4}$$

in spherical coordinates. Let us now also neglect the anisotropy of Γ by assuming that the radial compression of fluctuations occurring as the shell shrinks does not significantly depart from the angular compression, so that $\Gamma_{ij} = (1 - D'\frac{1}{q}\psi^{\rm c}_{,q})\,\delta_{ij}$. This is only strictly valid for a uniform initial overdensity but any departure from it would leave no imprint on angular fluctuations over the surface of the shell. Then, taking into account that the potential perturbations are related to the local initial density contrast through Poisson's equation $D'{\rm Tr}(\psi^{\rm l}_{,ij}) = D(a)\delta^{\rm l,i}$, we can write

$$D'\,{\rm Tr}(\Gamma^{-1}_{ij}\psi^{\rm l}_{,ij}) \simeq D(a)\delta^{\rm l,i}\left(1 + D'\frac{1}{q}\psi^{\rm c}_{,q}\right). \tag{A.5}$$

In Eqs. (A.2), (A.3), $1 + \delta$ refers to the contrast with respect to the background mean density. However, we are interested in the contrast of fluctuations in the shell that are in excess of the smooth cluster contribution $1 + \delta^{\rm c}$. We can therefore multiply Eq. (A.3) by $|\Gamma|$. We also simplify terms involving the derivatives of the potential by considering the small initial cluster density contrast $\delta^{\rm c,i}$ (at radius q) and the mean initial density contrast $\bar{\delta}^{\rm c,i}$ (averaged inside the sphere of radius q)

$$D'\frac{\psi^{\rm c}_{,q}}{q} = \frac{D(a)\,\bar{\delta}^{\rm c,i}}{3} \equiv \frac{D(a)}{q^3}\int_0^q \delta^{\rm c,i}p^2{\rm d}p. \tag{A.6}$$

When expressed relative to the smooth cluster density, Eq. (A.3) becomes

$$\frac{1+\delta}{1+\delta^c} = |\Gamma|\,(1+\delta) \simeq 1 + D(a)\delta^{\rm l,i}\left[1 + D(a)\frac{\bar{\delta}^{\rm c,i}}{3}\right], \tag{A.7}$$

noticing that without the cluster one would recover the classical linear theory result $\delta = D(a)\delta^{\rm l,i}$. Local fluctuations experience a multiplicative boost factor corresponding to the term in brackets in Eq. (A.7), and thus the power spectrum of local fluctuations in the cluster vicinity can be written as

$$P_{\rm cluster}(\boldsymbol{k}) = P_{\rm random}(\boldsymbol{k})\left[1 + \frac{D(a)\,\bar{\delta}^{\rm c,i}}{3}\right]^2 \equiv \alpha\; P_{\rm random}(\boldsymbol{k}). \tag{A.8}$$

In this equation, $P_{\rm random} = D(a)^2P_0$, as expected from linear theory. We nevertheless assume below that the relation still holds for the non-linearly evolved $P_{\rm random}$.

Equation (A.8) simply quantifies the boost imposed by the peak condition in the initial conditions $\bar{\delta}^{\rm c,i}$. This is consistent with the perturbative approach of Codis et al. (2017) who showed that gravitational evolution induces a non-linear bias at all multipoles proportional to the peak height ν, the amplitude of fluctuations $\sigma_0 \propto D(a)$ and the rescaled three-point function $\xi^{(3)}$. The agreement between both approaches follows from the $D(a)\bar{\delta}^{\rm c,i} \leftrightarrow \sigma_0\nu$ correspondence. From Eq. (A.8) and Codis et al. (2017), it appears that the excess amplitude of harmonics scales like $D(a)$ at first order. However, these predictions are only valid in the weakly non-linear regime.

A.2. The highly non-linear regime

The above formalism can be extended to a fully non-linear regime, where gravitational clustering boosts all multipoles in proportion, through the convergence of the flow towards the central peak. In practice, one needs to relate $P_{\rm cluster}(\boldsymbol{k})$ and $P_{\rm random}(\boldsymbol{k})$ to the cluster environment at late time. In the Zeldovich approximation (or in the spherical collapse model before shell crossing), the Lagrangian radius q is related to its evolved Eulerian counterpart r via

$$\boldsymbol{r} = \boldsymbol{q}\,\rho(<r)^{-1/3}, \tag{A.9}$$

if the mass enclosed by this falling shell is constant $M(<q) = M(<r)$. Writing $q = \lambda r$, where $\lambda = \rho(<r)^{1/3}$ is related to the mean density within the sphere of radius r, the solution for λ is

$$\lambda = 1 + \frac{D(a)\,\bar{\delta}^{\rm c,i}}{3}, \qquad \text{at early time,} \tag{A.10}$$

$$= \left(\frac{3M(<r)}{4\pi\bar{\rho}r^3}\right)^{1/3}, \qquad \text{at late time.} \tag{A.11}$$

The boost of power α previously defined in Eq. (A.8) was found to be $\alpha = \lambda^2$ at early time and we assume here it should remain $\alpha = \lambda^2$ at late time. At late time, it is also convenient to assume a NFW density profile (Navarro et al. 1997) for the equilibrium state of the clusters, which is characterised by is virial mass $M_{\rm vir}$ and concentration c. These two parameters are correlated and slowly change with time. This allows us to express the density enclosed in the sphere of radius r as

$$\rho(<r) = \rho_{\rm vir}\frac{f_{\rm NFW}(cr/R_{\rm vir})}{f_{\rm NFW}(c)}, \tag{A.12}$$

with $\rho_{\rm vir}$ the mean density inside the virial radius $R_{\rm cir}$ and $f_{\rm NFW}(x) = [\log(1+x) - x/(1+x)]/x^3$, which relates the mean

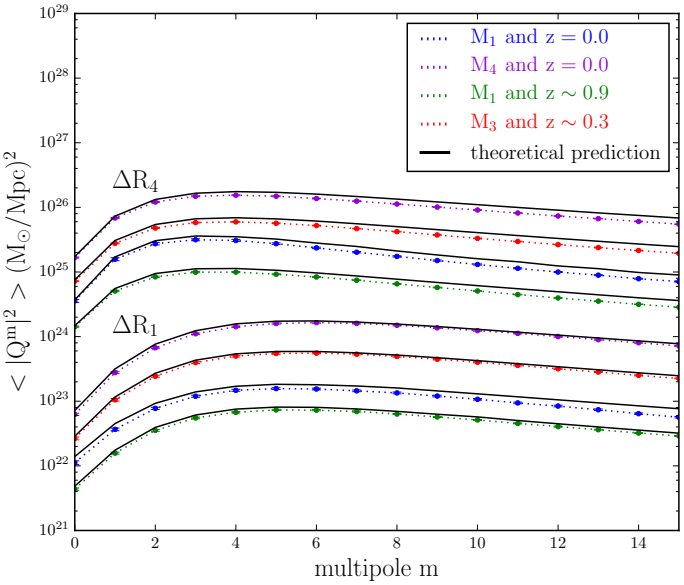

Fig. B.1. Comparison between the analytical (solid lines) and the measured (dotted lines with tiny error bars) spectrum of multipolar moments for annuli taken at random positions in the simulation box. The bottom (resp. top) curves correspond to small $R \in [0.25\text{–}0.5]\,R_{\rm vir}$ (resp. large $R \in [1\text{–}4]\,R_{\rm vir}$) annuli. Four mass and redshift values are overlaid for each radius.

density contrast at radius r to the contrast at the virial radius. We finally get

$$\alpha = \left[\frac{\rho_{\rm vir}}{\bar{\rho}}\frac{f_{\rm NFW}(cr/R_{\rm vir})}{f_{\rm NFW}(c)}\right]^{2/3}. \tag{A.13}$$

where $\bar{\rho}$ is the mean background density. Equation (A.13) only depends on time via the (weak) time and mass dependence variation of the concentration parameter (Klypin et al. 2016). This can be see in Fig. 4.

Appendix B: Spectrum of multipolar moments at random location

The spectrum of multipolar moments calculated at random locations can be inferred from the power spectrum of density fluctuations and compared to the spectrum measured in simulations. In Sect. 2.2.1, we related the spectrum of multipolar moments with the power spectrum of the underlying two-dimensional density (or, there, convergence) field. We thus need to compute the power spectrum of the projected density $\Sigma(\boldsymbol{R})$ from the power spectrum of the three-dimensional density fluctuations $P_\delta(\boldsymbol{k})$. Since we excise spheres of size $R_{\rm H} = 4R_{\rm vir}$, the statistical properties of the projected density from this sphere are not stationary because the radial extent a over which the density is integrated is a function of the projected radius R, $a = a(R) = \sqrt{R_{\rm H}^2 - R^2}$. Therefore, the two-dimensional spectrum reads

$$P_\Sigma(k_\perp, R) = \frac{2a^2\,\bar{\rho}^2}{\pi}\int_{-\infty}^{\infty}{\rm d}k_\parallel\; P_\delta\left(\sqrt{k_\perp^2 + k_\parallel^2}\right)\,{\rm sinc}\,(k_\parallel a)^2. \tag{B.1}$$

Figure B.1 compares this analytical prediction with the measurements made in the simulation for different masses, annuli and redshifts. For this calculation, we again use the Boltzmann code CLASS toolkit (Blas et al. 2011; Lesgourgues 2011) for the fiducial Planck Cosmology. To simplify the expression of the theoretical prediction, we approximate $a(R) = \sqrt{R_{\rm H}^2 - \bar{R}^2}$ with $\bar{R} = \sqrt{R_{\rm min}\,R_{\rm max}}$, the geometrical mean radius of the annulus. The agreement is quite satisfactory. The small mismatch is due to the simplifying assumptions used to conduct the analytical integration (approximation on $a(R)$), and to the theoretical uncertainties on the non-linear power spectrum P_δ on the smallest scales.

Appendix C: Covariance of multipolar moments

Let us present here the details of the derivation of the four-point statistical properties of the shape noise contribution to the local multipolar moments in Eq. (40), by following the same notations as Schneider et al. (1998). Let us neglect terms that are due to the finite number of sources carrying shear. No coherent shear is carried by galaxies either. Hence, uncorrelated galaxy ellipticities satisfy

$$\langle\epsilon_{i\alpha}\rangle = 0, \quad \langle\epsilon_{i\alpha}\epsilon_{j\beta}\rangle = \sigma_\epsilon^2\delta_{ij}\delta_{\alpha\beta}, \tag{C.1}$$

with Latin indices $i \in 1\ldots N$ labelling different galaxies in an annulus $[\nu R_{\rm max}, R_{\rm max}]$ and Greek indices labelling ellipticity components $\alpha \in \{t, \times\}$, hence following the notations of Schneider et al. (2002) with the distinction that σ_ϵ is, here, the one-dimensional dispersion of source ellipticities. The four-point expectation value of ellipticities is

$$\langle\epsilon_{i\alpha}\epsilon_{j\beta}\epsilon_{k\mu}\epsilon_{l\nu}\rangle = \sigma_\epsilon^4\left(\delta_{ij}\delta_{\alpha\beta}\delta_{kl}\delta_{\mu\nu} + \delta_{ik}\delta_{\alpha\mu}\delta_{jl}\delta_{\beta\nu} + \delta_{il}\delta_{\alpha\nu}\delta_{jk}\delta_{\beta\mu}\right).$$

This will be useful for averaging over source ellipticities the multipolar moment power spectrum

$$|Q_m|^2 = \frac{1}{\bar{n}^2}\sum_{jk}{\rm e}^{\imath m(\varphi_j-\varphi_k)}\Big[\left(\beta^m_{jt}\beta^m_{kt}\epsilon_{jt}\epsilon_{kt} + \beta^m_{j\times}\beta^m_{k\times}\epsilon_{j\times}\epsilon_{k\times}\right) + \imath\left(\beta^m_{j\times}\beta^m_{kt}\epsilon_{j\times}\epsilon_{kt} - \beta^m_{jt}\beta^m_{k\times}\epsilon_{jt}\epsilon_{k\times}\right)\Big], \tag{C.2}$$

adopting the convention $\beta^m_{j\alpha} = b_{\alpha,m}(r_j)/r_j$. In the absence of shear, the expectation value of Eq. (C.2) is simply

$$\langle|Q_m|^2\rangle \equiv |Q^{\rm s}_m|^2 = \frac{\sigma_\epsilon^2}{\bar{n}^2}\sum_{k=1}^{N}\left(\beta^{m,2}_{kt} + \beta^{m,2}_{k\times}\right). \tag{C.3}$$

Accounting for symmetries and arranging terms, the four-point moments reads

$$\langle|Q_m|^2\,|Q_n|^2\rangle = \langle|Q_m|^2\rangle\,\langle|Q_n|^2\rangle + |K^+_{mn}|^2 + |K^-_{mn}|^2, \tag{C.4}$$

where

$$K^\pm_{mn} \equiv \frac{\sigma_\epsilon^2}{\bar{n}^2}\sum_k{\rm e}^{\imath(m\mp n)\varphi_k}\left(\beta^m_{kt}\beta^n_{kt} \pm \beta^m_{k\times}\beta^n_{k\times}\right). \tag{C.5}$$

We highlight that the averaging over source positions within the annulus yields

$$\langle K^+_{mn}\rangle = \delta_{mn}|Q^{\rm s}_m|^2, \quad \langle K^-_{mn}\rangle = \delta_{m0}\delta_{n0}\tilde{Q}^{\rm s2}_0, \tag{C.6}$$

with the modified moments defined by

$$|Q^{\rm s}_m|^2 = \frac{\pi\sigma_\epsilon^2}{\bar{n}}\int_{\nu R}^{R}{\rm d}r\frac{b^2_{t,m}(r) + b^2_{\times,m}(r)}{r}, \tag{C.7}$$

$$|\tilde{Q}^{\rm s}_m|^2 = \frac{\pi\sigma_\epsilon^2}{\bar{n}}\int_{\nu R}^{R}{\rm d}r\frac{b^2_{t,m}(r) - b^2_{\times,m}(r)}{r}. \tag{C.8}$$

Chapter 4

Gravitational lensing in the Horizon-AGN simulation light-cone

4.1 Weak lensing in the Horizon-AGN simulation light-cone: Small scale baryonic effects (Article submitted to Astronomy & Astrophysics)

Context

For scales below few Mpc, the density field is non-linearly impacted by baryons and their associated physics, as shown in Chapter 1. Yet, with the advent of high performance hydrodynamics, it is now becoming possible to model the complex interplay of baryons and dark matter at these non-linear scales. Hence I focus in the second part of my thesis on mocking weak lensing observables down to these scales through the post-processing of state-of-the-art of hydrodynamical cosmological simulations. I also construct statistical estimators which I validate on these mocks.

Such predictions are crucial for upcoming lensing surveys surveys such as Euclid, LSST and WFIRST, which will measure the lensing signal with an new level of accuracy in order to achieve the nominal level of accuracy on the dark energy parameters. In anticipation of these future data sets, lensing observables need to be calibrated and characterised while including baryonic physics. Semboloni et al. (2011) showed that weak lensing statistics can significantly differ between pure-DM predictions and those which include the impact of baryonic physics. In addition, the number of convergence peaks itself is altered by taking account the baryonic component, as described by Yang et al. (2013).

As detailed in chapter 2, significant progress has been made to efficiently predict lensing observables up to non-linear scales with large cosmological simulations. Regarding works using pure N-body simulations, one can cite the production of WL full sky maps with angular resolutions of a few arcmin (e.g. Fosalba et al. 2015; Giocoli et al. 2016b; Takahashi et al. 2017b). Such realisations are used to accurately predict the variance of weak lensing statistics (by reducing the cosmic variance). Predicting lensing observables from hydrodynamical simulations is more complex, as we must take into account different matter particles (stars, BH, DM) which have different masses, as well as the gas component which could be either cells (Eulerian code) or particles (Lagrangian code). Nevertheless, the advance of hydrodynamical simulations and numerical ray tracing methods, prediction of lensing signal from such simulation have started. For instance, Velliscig et al. (2017) recently predicted the galaxy-galaxy lensing signal on the EAGLE simulation, and found a significant agreement with the GAMA+KiDS data (Dvornik et al. 2017).

Paper presentation

In the paper below, I investigate the impact of baryons on the weak lensing observable in the Horizon-AGN simulation (Dubois et al. 2014). This is a full physics cosmological hydrodynamical simulation based on the AMR code RAMSES, as described in chapter 1. In particular, to mimic all deviations of light-rays along a mock light-of-sight, light rays are propagated trough the light cone of the simulation.

To perform the light rays propagation the multiple-lens-plane approximation is applied, i.e., the light cone is partitioned into a series of lens planes and light rays are deflected plane by plane (Hilbert et al. 2009, see for example). Light-ray are also propagated in the Born approximation (only one effective thin lens plane), to quantify the impact of lens-lens coupling on weak lensing statistics.

In this study, two different algorithms are used to evaluate the deflection of light rays on each lens plane. The first method accurately integrates the acceleration along the path of light rays on each cell of the AMR simulation (called after OBB method). This new method has the advantage of providing an estimation of the deflection at a resolution level similar to the simulation grid. The second one, inspired from the Smooth Particle Lensing method (Aubert et al. 2007), adaptively smooths particles depending of the total local density. This more standard approach allow to distinguish the individual impact of dark and baryonic matter on the lensing signal. Both methods are then used to deflect light-rays along the light-cone, and are compared.

From the computed lensing signal toward the light cone, I predict the standard weak lensing statistics: convergence power spectrum, two-point shear correlation and galaxy-galaxy lensing. Standard cosmic shear statistics are estimated for the total matter, and by considering the DM particles only. Convergence power spectra are impacted by the baryonic component: at the 10% level for angular scales below a few arcmin. Note that due to the weak opening angle of the light-cone (1 square degree) the prediction of weak lensing statistics on large scale are strongly noised by the cosmic variance. In addition, the impact of the reduced shear approximation ($g = \gamma/(1-\kappa) \sim \gamma$) on the two-point shear correlation function is also estimated: $\xi_-^g/\xi_-^\gamma > 5\%$ for scales lower than 1 arcmin.

The magnification bias is also quantified on the galaxy-shear correlation, i.e. the magnification of lens by all of the matter between the lens and the observer. A proper propagation of light-rays is necessary to accurately model the magnification of lens. The galaxy-galaxy lensing (GGL) predictions are compared to current measurements realised by Leauthaud et al. (2017) on the CMASS sample of galaxies at z ~ 0.55. Tacking into account the magnification bias induced on the stellar mass estimation of lens galaxies, a good agreement is found between GGL predictions and the measurements of Leauthaud et al. (2017). By considering galaxy lenses at higher redshift $z_L \geq 1$, the impact of magnification bias on GGL signal is relevant for separations greater than 1 Mpc.

Finally, this paper is a first step towards building a full end-to-end generation of lensed mock images from large cosmological hydrodynamical simulations, as explained in section 2.

Details of the numerical work

In this study, I perform light-ray propagation in the multiple-lens plane approximation and with two methods of deflection field reconstruction, as detailed in the paper below. Because some numerical aspect is discussed in that paper explicitely, while others have been discussed in Chapter 2, I will not get into too much details here.

Nevertheless, I would like to focus on the problem of missing (and excess) cells in the light cone, which arose during the development and testing of the OBB method (see section 3.4 of the paper). When the light cone slice is written to disk during the run of the simulation, some cells are missing or appear twice. This is due to the fact that cells at the edge of a slice can be refined or de-refined from one time step to the next, and this effect is not properly accounted for. This problem is illustrated in figure 4.1.

I thus spent a few months to identify, characterise and attempt to correct this problem. Yet, eventually I chose not to, given its complexity: the light cone is computed on the fly, so I cannot re-run the light cone realisation. Instead, I recommended identifying all cells with this problem and correcting it. While more tractable, this approach still requires considerable quantities of work, computational time and memory. Nevertheless, I have convinced myself that the impact of this error is minor, while the OBB method overall presents significant advantages [1] and could be used in any light cone (knowing the simulation grid, either regular or AMR).

In addition to the OBB method, I also calculated lensing quantities using a more standard approach, by smoothing particle masses on a 2-D grid to obtain the surface density. Considering the level of accuracy that I reach in this study, adaptative smoothing is necessary, which is implemented using a version that I wrote inspired by the SPL code of Aubert et al. (2007). Such codes are indeed well-suited to treat single components of matter (either DM, star, BH or gas). It thus directly run for each component at each time step, which involves very long computational times, as it requires building a tree in the distribution of particle for each component. In my study, I had already reconstructed the AMR grid in the light cone when using the OBB method. I thus already have the information of the resolution level around a given particle. Tacking the advantage of this information, I smooth particle by a 2-D gaussian kernel for which the standard deviation σ is proportional to the RAMSES grid resolution at the location of the particle.

This numerical aspect made use of high performance computing, including OPEN-MP/MPI parallelisation and code optimisation. Overall 300,000 hours of CPU were used on the Horizon Cluster hosted by the Institut d'Astrophysique de Paris.

Overview of my different contribution

I am also the main architect of this paper: I realised the post-processing of the light cone including the ray-tracing, and the lens plane construction with the two methods. I also computed the cosmic shear statistics, including the convergence power spectra and the 2-point shear correlation function. The galaxy shear correlation and magnification bias investigations were done jointly by Raphael Gavazzi and me. The first three authors contributed actively to writing the paper. For example, I wrote the first draft of the introduction, which was then modified in turn by Raphael Gavazzi and Christophe Pichon.

Perspectives of this study

In this paper, I predict the weak lensing statistics with stat-of-the-art of hydrodynamical cosmological simulation, and quantify the impact of baryons and baryonic physic on the cosmic shear lensing signal. These predictions take advantageously into account all the matter along the line-of-sight (from $z \sim 7$ to $z = 0.05$), is resolved up to scales relevant for the impact of baryons (angular resolution of 0.1"), and take care of all relevant numerical approximations (propagation over a large number of planes, and impact of deflection field reconstruction).

By using the lensing quantities computed here, one can already extend my study to the strong lensing regime. Strong lensing predictions, which include a realistic physic of baryons, are

[1] as detailed in the paper: the mass distribution outside the light cone is consistently taken into account, and it provides the deflection directly

important as they provide information on the core of the lens, where baryonic component cannot be negligible. Indeed, current studies reconcile observations with dark matter halo models by incorporating baryonic physics inside simulations addressing scientific issues such as the cusp-core problem or sub-haloes abundance problem. For instance, Peirani et al. (2018) already showed that the innermost parts of Horizon-AGN galaxies are consistent with the strong lensing observations of Sonnenfeld et al. (2013) and Newman et al. (2013, 2015).

In addition, I am currently incorporating my ray-tracing results to mock images produced by Clotilde Laigle (Kaviraj et al. 2017). The corresponding project will be detailed at the end of this chapter. This work will allow me to extract the true gravitational lensing signal form observations. Such forecasts are crucial in order to prepare future surveys such as Euclid or LSST.

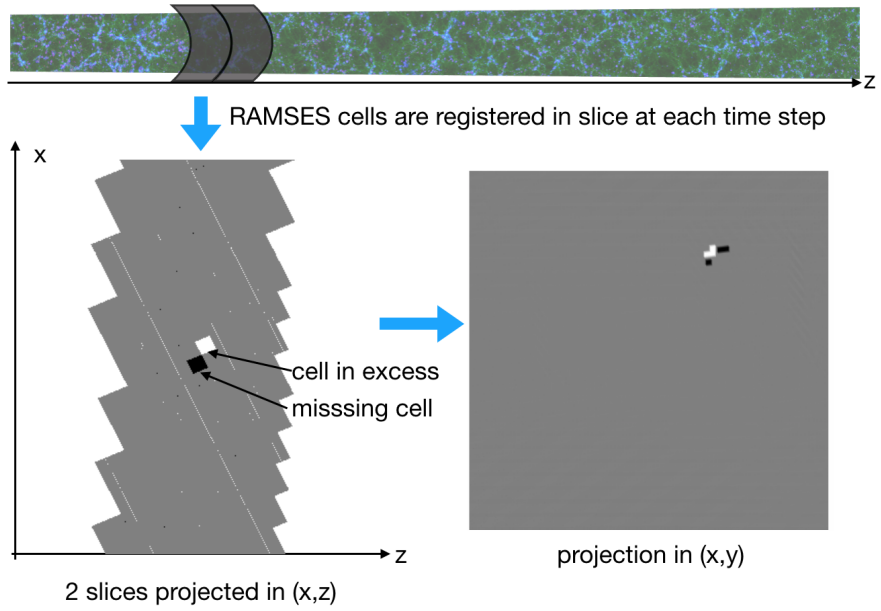

Figure 4.1 – Schematic view of the missing (and excess) cells found at the edge between two light cone slices, presented along two distinct views. In addition, this picture illustrates the orrientation of RAMSES cells relatively to the line-of-sight.

A&A 626, A72 (2019)
https://doi.org/10.1051/0004-6361/201834199

Astronomy & Astrophysics

Weak lensing in the Horizon-AGN simulation lightcone

Small-scale baryonic effects

C. Gouin[1,2], R. Gavazzi[1], C. Pichon[1,3,4], Y. Dubois[1], C. Laigle[5], N. E. Chisari[5], S. Codis[1], J. Devriendt[5], and S. Peirani[6]

[1] Institut d'Astrophysique de Paris, UMR7095 CNRS & Sorbonne Université, 98bis Bd Arago, 75014 Paris, France
e-mail: celine.gouin@ias.u-psud.fr, gouin@iap.fr
[2] Institut d'Astrophysique Spatiale, CNRS/Université Paris-Sud, Université Paris-Saclay, Bâtiment 121, 91405 Orsay, France
[3] Korea Institute of Advanced Studies (KIAS) 85 Hoegiro, Dongdaemun-gu, Seoul 02455, Republic of Korea
[4] Institute for Astronomy, University of Edinburgh, Royal Observatory, Blackford Hill, Edinburgh EH9 3HJ, UK
[5] Sub-department of Astrophysics, University of Oxford, Keble Road, Oxford OX1 3RH, UK
[6] Université Côte d'Azur, Observatoire de la Côte d'Azur, CNRS, Laboratoire Lagrange, Bd de l'observatoire, 06304 Nice, France

Received 5 September 2018 / Accepted 26 April 2019

ABSTRACT

Context. Accurate model predictions including the physics of baryons are required to make the most of the upcoming large cosmological surveys devoted to gravitational lensing. The advent of hydrodynamical cosmological simulations enables such predictions on sufficiently sizeable volumes.
Aims. Lensing quantities (deflection, shear, convergence) and their statistics (convergence power spectrum, shear correlation functions, galaxy-galaxy lensing) are computed in the past lightcone built in the Horizon-AGN hydrodynamical cosmological simulation, which implements our best knowledge on baryonic physics at the galaxy scale in order to mimic galaxy populations over cosmic time.
Methods. Lensing quantities are generated over a one square degree field of view by performing multiple-lens plane ray-tracing through the lightcone, taking full advantage of the 1 kpc resolution and splitting the line of sight over 500 planes all the way to redshift $z \sim 7$. Two methods are explored (standard projection of particles with adaptive smoothing, and integration of the acceleration field) to ensure a good implementation. The focus is on small scales where baryons matter most.
Results. Standard cosmic shear statistics are affected at the 10% level by the baryonic component for angular scales below a few arcminutes. The galaxy-galaxy lensing signal, or galaxy-shear correlation function, is consistent with measurements for the redshift $z \sim 0.5$ massive galaxy population. At higher redshift $z \gtrsim 1$, the effect of magnification bias on this correlation is relevant for separations greater than 1 Mpc.
Conclusions. This work is pivotal for all current and upcoming weak-lensing surveys and represents a first step towards building a full end-to-end generation of lensed mock images from large cosmological hydrodynamical simulations.

Key words. large-scale structure of Universe – gravitational lensing: weak – methods: numerical

1. Introduction

Gravitational lensing has become a versatile tool for probing the cosmological model and scenarios of galaxy evolution. From the coherent distortions, generated by the intervening matter along the line of sight, of the last scattering surface (e.g. Planck Collaboration VIII 2018) or intermediate-redshift galaxies (Bartelmann & Schneider 2001; Kilbinger 2015), to the inner parts of massive galaxies (Treu 2010), lensing directly measures the fractional energy density in matter of the Universe. Because it does not rely on assumptions about the relative distribution between the galaxies and the underlying dark matter (DM), which drives the dynamical evolution of cosmological structures, weak lensing plays a key role in recent, ongoing, or upcoming ground-based imaging surveys, such as the Canada France Hawaii Lensing Survey (Heymans et al. 2012), the Dark Energy Survey (Dark Energy Survey Collaboration 2005; Abbott et al. 2016), the Kilo-Degree Survey (KiDS: Kuijken et al. 2015), the Hyper Suprime-Cam Subaru Strategic Survey (Miyazaki et al. 2012), and the Large Synoptic Survey Telescope (LSST Science Collaborations 2009). It is also at the centre of the planned Euclid and WFIRST satellites (Laureijs et al. 2012; Spergel et al. 2015).

The statistical power of these experiments dramatically increases and drives on its way enormous efforts for the control of systematic effects. One of them concerns the accuracy to which theoretical predictions on the statistical properties of the matter distribution when it has evolved into the non-linear regime can be made on a small scale. Arguably, cosmological N-body numerical simulations have been playing a key role in solving the complex dynamical evolution of DM on scales smaller than a few Megaparsec (e.g. Springel et al. 2006). The upcoming Euclid or LSST missions require an extreme accuracy on the matter density power spectrum and the associated covariances that may enter a likelihood analysis of these data. The effort is currently culminating with the Flagship simulation, for instance (Potter et al. 2017). It also motivated earlier very large simulations such as Horizon-4π (Teyssier et al. 2009; Pichon et al. 2010), DEUS (Rasera et al. 2010), or MICE (Fosalba et al. 2015a), however. It has early been envisioned to propagate light rays through such DM simulations in order to reproduce the deflection and distortions of light bundles in a lumpy universe. The motivation is to derive lensing observables such as convergence maps and one-point probability distribution functions of this field or its topological properties (peaks, voids, etc.) or two-point shear correlation functions

(Jain et al. 2000; Pichon et al. 2010; Hamana & Mellier 2001; Vale & White 2003; Hennawi & Spergel 2005; Hilbert et al. 2007, 2009; Sato et al. 2009). Much progress has since been made on large and mildly non-linear scales with the production of full-sky maps with an angular resolution of a few arcminutes (e.g. Fosalba et al. 2015b; Giocoli et al. 2016; Takahashi et al. 2017).

In order to make the most of the upcoming surveys, the matter distribution for Fourier modes as large as $k \sim 10\,h\,\mathrm{Mpc}^{-1}$ must be predicted to the percent accuracy, which today still represents a challenge (Schneider et al. 2016). Furthermore, at these scales, the physics of baryons can differ from the dynamics of DM, and even though it amounts to ∼17% of the total cosmological matter budget, it has to be taken into account (van Daalen et al. 2011). For weak-lensing statistics, Semboloni et al. (2011) showed that the modelling of the two-point shear correlation function can be significantly biased when the baryons are simply treated like the collision-less DM. Even the number of convergence peaks itself is altered by baryons, but to a lesser extent than the power spectrum (Yang et al. 2013).

Recently, significant progress has been made on hydrodynamical simulations, which are now able to reproduce a morphological mix of galaxies in a cosmological context by considering baryonic physics such as radiative cooling, star formation, and feedback from supernovae and active galactic nuclei (AGN). Despite the balancing act that is required to be achieved between the high-resolution needs for properly describing the galaxies that formed at the centre of DM halos and the necessity of simulating sizeable cosmological volumes, recent simulations such as Horizon-AGN (Dubois et al. 2014), Illustris/Illustris-TNG (Vogelsberger et al. 2014; Pillepich et al. 2018), or EAGLE (Schaye et al. 2015) have now reached volumes of about 100 Mpc on a side and a resolution of about 1 kpc. This opens the possibility to quantify the effect of baryons (experiencing adiabatic pressure support, dissipative cooling, star formation, feedback, etc.) on the total matter distribution and its effect on lensing cosmological observables (see e.g. van Daalen et al. 2011; Tenneti et al. 2015; Hellwing et al. 2016; Springel et al. 2018; Chisari et al. 2018). Prescriptions to account for this effect (e.g. Semboloni et al. 2013; Schneider & Teyssier 2015; Mead et al. 2015; Rabold & Teyssier 2017) have been explored, and some start to be incorporated into cosmic shear studies (Hildebrandt et al. 2017).

In this paper, we further investigate the effect of baryons on lensing observables in the Horizon-AGN simulation. By taking advantage of the lightcone that is generated during the simulation run, we are able to fully account for projection effects (mixing physical scales) and small-scale non-linearities occurring in the propagation of light rays (e.g., Born approximation, lens-lens coupling, corrections for shear – reduced shear) that may be boosted by the steepening of the gravitational potential wells that are caused by cooled gas that sinks to the bottom of DM halos. This extends the analysis of Chisari et al. (2018), who mostly focused on the effect of baryons on the three-dimensional matter power spectrum and compared the Horizon-AGN results with those of Illustris, OWLS, EAGLE, and Illustris-TNG and found a broad qualitative agreement. The common picture is that hot baryons that are prevented from sinking into halos like DM induce a deficit of power inside halos (in a proportion of about $\Omega_\mathrm{b}/\Omega_\mathrm{M}$), and at still smaller scales ($k \gtrsim 30\,h\,\mathrm{Mpc}^{-1}$), baryons in the form of stars (and to a lesser extent, cooled gas) dramatically boost the amplitude of density fluctuations. However, even though these results seem to converge from one simulation to another, they substantially depend on the assumptions about sub-grid physics, and in particular, about AGN feedback.

In addition to these encouraging successes at quantifying the nuisance of baryons on cosmological studies, hydrodynamical simulations entail a wealth of information on the relation between galaxies or galaxy properties and the halo they live in. It is therefore a way to understand the large-scale biasing of these galaxies with respect to the overall total matter density field. We also explore the small-scale relation between galaxies and their surrounding gravitational potential that sources the lensing deflection field. In particular, the correlation between galaxies and the tangential distortion of background sources (so-called galaxy-galaxy lensing signal, GGL) has proven to be a way to constrain the galaxy-mass correlation function (e.g. Brainerd et al. 1996; Guzik & Seljak 2001; Mandelbaum et al. 2006, 2013; Leauthaud et al. 2012; Velander et al. 2014; Hudson et al. 2015; Coupon et al. 2015). In this vein, Velliscig et al. (2017) recently showed that the GGL around $z \sim 0.18$ galaxies in the EAGLE simulation is consistent with the GGL measured around the Galaxies And Mass Assembly (GAMA) groups using KiDS data (Dvornik et al. 2017).

Finally, subtle observational effects entering GGL by high-redshift deflectors ($z \gtrsim 0.8$) are investigated from the lensing information over the full past lightcone of the Horizon-AGN simulation. The magnification bias affecting the selection of deflectors (Ziour & Hui 2008) complicates the interpretation of GGL substantially. Currently, no such high-z lens sample has been studied because even higher faintly lensed sources that carry the shear signal are scarce, but the situation may change with Euclid. Its slit-less grism spectroscopy will provide a large sample of Hα emitters in the $0.9 \leq z \leq 1.8$ redshift range. A thorough understanding of the clustering properties of this sample may be achieved with the GGL measurement of this sample by using the high-z tail of the shape catalogue obtained with the visible imager (VIS) for Euclid. Some ray-tracing through cosmological simulations (Hilbert et al. 2009; Fosalba et al. 2015b) has briefly mentioned some aspects of the problem of magnification bias that was raised by Ziour & Hui (2008). The Horizon-AGN lightcone is a good opportunity to quantify these effects in order to correctly interpret upcoming GGLs. In this paper, cosmic shear or GGL quantities are directly measured from the lensing quantities obtained by ray-tracing methods. They are not inferred from the shape of galaxies, as is done in observations. A forthcoming paper will present the generation of mock wide-field images including lensing distortions from the full view of Horizon-AGN lightcone and the light emission predicted for the simulated stars, taking us one step closer to a full end-to-end generation of mock lensing observations.

The paper is organised as follows. Section 2 presents the Horizon-AGN hydrodynamical simulation, the structure of its lightcone, and some properties of the galaxy population therein. Section 3 describes the methods we implemented to generate the deflection field on thin lens planes and to propagate light rays through them. Section 4 describes the one- and two-point statistics of the resulting convergence and (reduced-)shear fields. The validity of the ray-tracing method is quantified by comparing our results with independent methods. Section 5 measures the GGL around the galaxies in the Horizon-AGN simulation. A comparison with observations is made for low-redshift deflectors. The problem of magnification bias is investigated for future observations of high-z GGL. Section 6 summarises our results.

2. Horizon-AGN simulation lightcone

2.1. Characteristics

The Horizon-AGN simulation is a cosmological hydrodynamical simulation performed with RAMSES (Teyssier 2002). The details of the simulations can be found in Dubois et al. (2014). We first briefly summarise the main characteristics. Horizon-AGN contains 1024^3 DM particles with a mass resolution of $8 \times 10^7\, h^{-1}\, M_\odot$ in a box of comoving size $L_{\rm box} = 100\, h^{-1}$ Mpc on a side. The gravity and hydrodynamics are treated in RAMSES with a multiscale approach with adaptive mesh refinement (AMR): starting from a uniform 1024^3 grid, cells are then adaptively refined when the mass inside the cell exceeds eight times the initial mass resolution. Cells are recursively refined (or de-refined according to the refinement criterion) down to a minimum cell size of almost constant 1 proper kpc (an additional level is triggered at each expansion factor $a = 0.1, 0.2, 0.4, 0.8$). The underlying cosmology is a standard ΛCDM model consistent with the WMAP7 data (Komatsu et al. 2011), with total matter density $\Omega_{\rm m} = 0.272$, dark energy density $\Omega_\Lambda = 0.728$, amplitude of the matter power spectrum $\sigma_8 = 0.81$, baryon density $\Omega_{\rm b} = 0.045$, Hubble constant of $H_0 = 70.4\,{\rm km\,s^{-1}\,Mpc^{-1}}$, and scalar spectral index $n_{\rm s} = 0.967$.

The evolution of the gas is solved on the RAMSES grid using a Godunov method with the approximate Harten-Lax-van Leer-Contact Riemann solver on the interpolated conservative hydrodynamical quantities, which are linearly interpolated at cell boundaries from their cell-centred values using a MinMod total variation diminishing scheme. In addition, accurate models of unresolved sub-grid physics have been implemented. The gas heating comes from a uniform UV background that started at the re-ionisation $z_{\rm reion} = 10$ (Haardt & Madau 1996). The cooling function of the gas follows Sutherland & Dopita (1993), from H and He collision and from the contribution of other metals. Star formation is modelled following the Schmidt law (Kennicutt 1998), with a constant star formation efficiency of 2% per free fall time. It occurs when the density of the gas exceeds the threshold $0.1\,{\rm H\,cm^{-3}}$. The temperature at gas densities higher than $0.1\,{\rm H\,cm^{-3}}$ is modified by a polytropic equation of state with polytropic index of 4/3 and scaling temperature of 10^4 K (Springel & Hernquist 2003). Stellar evolution is performed assuming a Salpeter (1955) initial stellar mass function. The sub-grid physics also includes stellar winds and supernova feedback in the form of heating, metal enrichment of the gas, and kinetic energy transfer to the ambient gas (see Kaviraj et al. 2017, for more details). Finally, black holes (BH) are created when the gas density exceeds $0.1\,{\rm H\,cm^{-3}}$, and when no other BH lies in the close environment. They grow by direct accretion of gas following an Eddington-limited Bondi-Hoyle-Littleton accretion rate, and by merger when BH binaries are sufficiently close. The AGN feedback is treated by either an isotropic injection of thermal energy, or by a jet as a bipolar outflow, depending on the ratio between the Bondi and the Eddington accretion rates (see Dubois et al. 2012; Volonteri et al. 2016, for details).

The past lightcone of the simulation was created on-the-fly as the simulation was running. Its geometry is sketched in Fig. 1. The opening angle of the cone is 2.25 deg out to redshift $z = 1$ and 1 deg all the way to $z = 8$. These two values correspond to the angular size of the full simulation box at these redshifts. We can therefore safely work in the flat sky (or infinitely remote observer) approximation. Up to $z = 1$, the volume of the cone is filled with about 7 replicates of the box. Between $z = 0$ and $z = 4$, the narrow cone contains about 14 replicates of the box, and the union of the two cones contains about 19 copies. This should be kept in mind when the statistical robustness of our results is quantified.

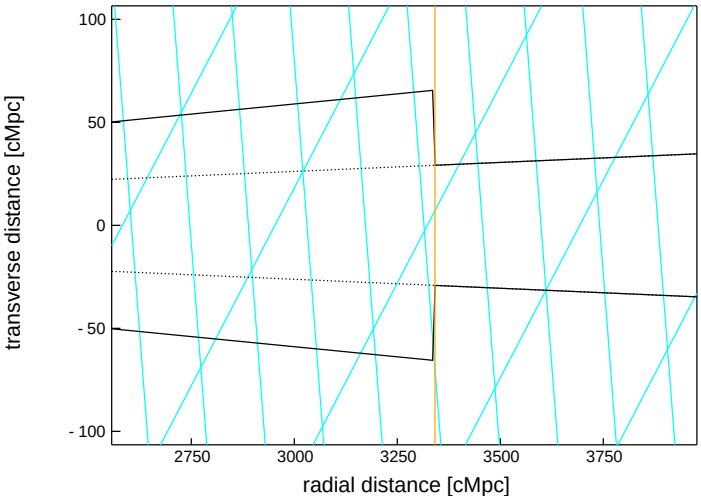

Fig. 1. 2D sketch of the past lightcone around redshift $z = 1$ (orange vertical line). Each mesh is a replicate of the Horizon-AGN simulation box (bounded with cyan lines). The tiling is performed all the way up to redshift $z \sim 8$.

In order to limit projection effects, a non-canonical direction was chosen for the past lightcone, but in order to preserve periodic boundary conditions between replicates, no random rotation was applied. Projection effects will still be present and induce characteristic spectral distortions on large scales that must be taken into account. Particles and AMR cells were extracted on-the-fly at each coarse simulation time step (when all levels were synchronized in time because a factor 2 of subcycling is used between levels) of the simulation according to their proper distance to a fiducial observer located at the origin of the simulation box. The lightcone of the simulation thus consists of 22 000 portions of concentric shells. Each of them contains stellar BH DM particles (with their position and velocity, mass, and age), along with AMR Eulerian cells storing the gas properties (position, density, velocity, temperature, chemical composition, and cell size) and the total gravitational acceleration vector.

2.2. Properties of galaxies and host halos

The AdaptaHOP halo finder (Aubert et al. 2004) was run on the lightcone to identify galaxies from the stellar particle distribution. The local stellar particle density was computed from the 20 nearest neighbours, and structures were selected with a density threshold equal to 178 times the average matter density at that redshift. Galaxies resulting in fewer than 50 particles ($\simeq 10^8\, M_\odot$) were not included in the catalogue. Because the identification technique is redshift dependent, AdaptaHOP was run iteratively on thin lightcone slices. Slices overlapped to avoid edge effects (i.e. cutting galaxies in the extraction) and duplicates were removed. In a second step, DM haloes were extracted independently from the DM particle distribution, with a density threshold of 80 times the average matter density, and keeping only haloes with more than 100 particles. The centre of the halo was temporarily defined as the densest particle in the halo, where the density was computed from the 20 nearest neighbours. In a subsequent step, a sphere of the size of the virial radius was drawn around it and a shrinking sphere method (Power et al. 2003) was implemented to recursively find the centre of mass

of the halo. In each iteration, the radius of the halo was reduced by 10%. The search was stopped when a sphere three times larger than our spatial resolution was reached. Each galaxy was matched with its closest halo.

The simulation contains about 116 000 galaxies and halos in the simulation box at $z = 0$, with a limit of about $M_* \gtrsim 2 \times 10^9\, M_\odot$. These yields have been extensively studied in previous papers of the Horizon-AGN series. For instance, Kaviraj et al. (2017) compared the statistical properties of the produced galaxies, showing a reasonable agreement with observed stellar mass functions all the way to $z \sim 6$. The colour and star formation histories are also well recovered, and so are the BH – bulge relations and duty-cycles of AGNs (Volonteri et al. 2016).

Following up on an earlier work (Dubois et al. 2013) that focused on a handful of zoomed galaxy simulations with RAMSES, Dubois et al. (2016) confirmed with a much greater statistical significance in Horizon-AGN that the morphological diversity of galaxies is well reproduced (fraction of rotation- versus dispersion-supported objects, and how this dichotomy maps into the star-forming versus quiescent dichotomy). Taking advantage of a parallel simulation run with the same initial conditions and in which the AGN feedback is turned off (Horizon-noAGN), the key role of the latter in shaping the galaxy morphology was emphasised. Furthermore, Peirani et al. (2017) studied the effect of AGN feedback on the innermost density profiles (stars, gas, DM, and total) and found a good agreement of the density profile, size-mass relation, and DM fraction inside the effective radius of galaxies with observations. In particular, Peirani et al. (2019) showed that the innermost parts of Horizon-AGN galaxies are consistent with strong-lensing observations of Sonnenfeld et al. (2013) and Newman et al. (2013, 2015).

Populating the lightcone yields a volume-limited sample of 1.73×10^6 galaxies in the narrow 1 deg cone. However, a large portion of the low-mass high-redshift galaxies would not be of much practical use in a flux-limited survey, as shown in Fig. 2, which plots the redshift-dependent limit in stellar mass that is attained with several i-band apparent limiting magnitudes. This was obtained using the COSMOS2015 photometric catalogue of Laigle et al. (2016).

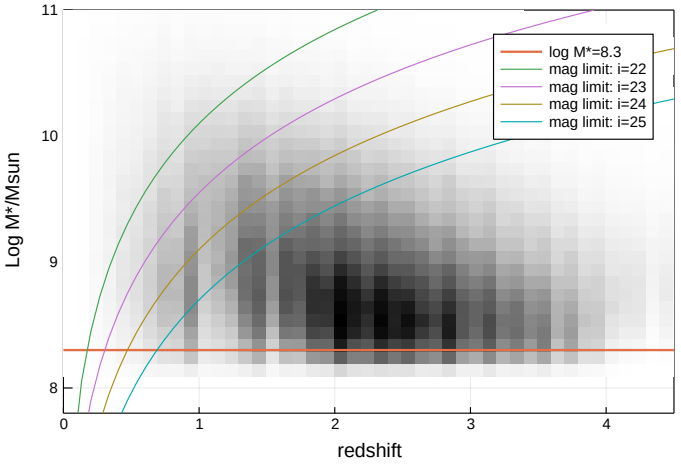

Fig. 2. Distribution in the redshift – stellar mass plane of the 1.7 million galaxies in the Horizon-AGN lightcone. For guidance, the stellar mass limit for completeness is shown as well as fiducial cuts in mass that would be obtained with a flux-limited survey of various i-band limiting magnitudes.

3. Ray-tracing through the lightcone

After briefly describing the basics of the propagation of light rays in a clumpy universe and the numerical transcription of this formalism, we now describe the ray-tracing computation in the Horizon-AGN lightcone. Our implementation of the multiple lens plane (but also the Born approximation) builds on similar past efforts (Hilbert et al. 2008; Metcalf & Petkova 2014; Petkova et al. 2014; Barreira et al. 2016). It has been tailored for the post-treatment of the Horizon-AGN past lightcone, but provided the flat-sky approximation holds, our implementation could readily be applied to any other RAMSES lightcone output (Teyssier et al. 2009).

As detailed below, two methods are investigated to infer deflection angles from either the distribution of various particle-like matter components or the total gravitational acceleration stored by RAMSES. The light rays are then propagated plane by plane (both within and beyond the Born approximation) for these two different estimates of the deflection field.

3.1. Thin lens plane

We define $\boldsymbol{\beta}$ the (un-perturbed and unobservable) source plane angular position and $\boldsymbol{\theta}$ the observed angular position of a light ray. Considering a unique thin lens plane, the relation between the angular position of the source $\boldsymbol{\beta}$, the deflection angle $\boldsymbol{\alpha}$, and the image $\boldsymbol{\theta}$ is

$$\boldsymbol{\beta} = \boldsymbol{\theta} - \frac{D_{\rm ls}}{D_{\rm s}} \boldsymbol{\alpha}(\boldsymbol{\theta}), \tag{1}$$

where $D_{\rm ls}$ and $D_{\rm s}$ are the angular diameter distance between the source and the lens, and between the observer and the source, respectively. The deflection angle $\boldsymbol{\alpha}(\boldsymbol{\theta})$ is obtained by integrating the gravitational potential $\Phi(\boldsymbol{r})$ along the line of sight (here, radial proper coordinate x_3),

$$\boldsymbol{\alpha}(\boldsymbol{\theta}) = \frac{2}{c^2} \int \boldsymbol{\nabla}_\perp \Phi(\boldsymbol{\theta}, x_3)\, {\rm d}x_3. \tag{2}$$

Hence, across a thin lens plane, the lensing potential $\phi(\boldsymbol{\theta})$ is related to the deflection field by the Poisson equation:

$$\Delta\phi = \boldsymbol{\nabla} \cdot \boldsymbol{\alpha} \equiv 2\kappa, \tag{3}$$

where the convergence κ is the projected surface mass density $\Sigma(\boldsymbol{\theta})$ in the lens plane expressed in units of the critical density $\Sigma_{\rm crit}$

$$\Sigma_{\rm crit}\, \kappa(\boldsymbol{\theta}) = \Sigma(\boldsymbol{\theta}) \equiv \int \rho(\boldsymbol{\theta}, z)\, {\rm d}z. \tag{4}$$

The critical density reads

$$\Sigma_{\rm crit} = \frac{c^2}{4\pi G} \frac{D_{\rm s}}{D_{\rm l} D_{\rm ls}}, \tag{5}$$

with $D_{\rm l}$, the angular diameter distance between the observer and the lens. In the above equations, all distances and transverse gradients are expressed in physical (proper) coordinates.

A Taylor expansion of the so-called lens Eq. (1) yields the Jacobian of the $\boldsymbol{\theta} \rightarrow \boldsymbol{\beta}$ mapping, which defines the magnification tensor (e.g. Bartelmann & Schneider 2001)

$$a_{ij}(\boldsymbol{\theta}) = \frac{\partial \boldsymbol{\beta}}{\partial \boldsymbol{\theta}} = \left(\delta_{ij} - \phi_{,ij}\right) \equiv \begin{pmatrix} 1 - \kappa - \gamma_1 & -\gamma_2 \\ -\gamma_2 & 1 - \kappa + \gamma_1 \end{pmatrix}, \tag{6}$$

where δ_{ij} is the Kronecker symbol, and the two components $\gamma_{1/2}$ of the complex spin-2 shear have been introduced. We note that

subscripts following a comma denote partial derivatives along that coordinate. Both shear and convergence are first derivatives of the deflection field $\boldsymbol{\alpha}$ (or second derivatives of the lensing potential)

$$\kappa = \frac{1}{2}(\alpha_{1,1} + \alpha_{2,2}), \tag{7}$$

$$\gamma_1 = \frac{1}{2}(\alpha_{1,1} - \alpha_{2,2}), \tag{8}$$

$$\gamma_2 = \alpha_{1,2} = \alpha_{2,1}. \tag{9}$$

Therefore, starting from pixelised maps of the deflection field $\alpha_{1/2}(i, j)$ in a thin slice of the lightcone, we can easily derive $\gamma_{1/2}(i, j)$ and $\kappa(i, j)$ with finite differences or fast Fourier transforms (FFTs), even if α is only known on a finite aperture, without periodic boundary conditions. Conversely, starting from a convergence map $\kappa(i, j)$, it is impossible to integrate Eq. (3) with FFTs to obtain α (and then differentiate again to obtain γ) without introducing edge effects if the periodic boundary conditions are not satisfied. Additionally, we also introduce the scalar magnification μ, which is the inverse determinant of the magnification tensor $a_{i,j}$ of Eq. (6).

3.2. Propagation of rays in a continuous lumpy universe

On cosmological scales, light rays cross many over- or underdense extended regions at different locations. Therefore, the thin lens approximation does not hold. The transverse deflection induced by an infinitely thin lens plane is still given by the above equations, but the trajectory of rays along their path needs to be fully integrated. For a given source plane at comoving distance χ_s, the source plane position of a ray, initially observed at position $\boldsymbol{\theta}$, is therefore given by the continuous implicit (Voltera) integral equation (Jain & Seljak 1997)

$$\boldsymbol{\beta}(\boldsymbol{\theta}, \chi_s) = \boldsymbol{\theta} - \frac{2}{c^2}\int_0^{\chi_s} \mathrm{d}\chi\, \frac{\chi_s - \chi}{\chi_s\,\chi} \boldsymbol{\nabla}_{\beta}\phi\left(\boldsymbol{\beta}(\boldsymbol{\theta}, \chi), \chi\right). \tag{10}$$

To first order, the gravitational potential along an unperturbed path can be evaluated, so that

$$\boldsymbol{\beta}(\boldsymbol{\theta}, \chi_s) = \boldsymbol{\theta} - \frac{2}{c^2}\int_0^{\chi_s} \mathrm{d}\chi\, \frac{\chi_s - \chi}{\chi_s\,\chi} \boldsymbol{\nabla}_{\theta}\phi\left(\boldsymbol{\theta}, \chi\right). \tag{11}$$

This is known as the Born approximation, which is common in many diffusion problems of physics. An interesting property of the Born approximation is that the relation between $\boldsymbol{\beta}$ and $\boldsymbol{\alpha}$ can be reduced to an effective thin lens identical to Eq. (1) allowing the definition of an effective convergence, which is the divergence of the effective (curl-free) deflection field: $2\kappa_{\rm eff} = \boldsymbol{\nabla} \cdot \boldsymbol{\alpha}_{\rm eff}$.

When the approximation does not hold, the relation between $\boldsymbol{\beta}$ and $\boldsymbol{\alpha}$ can no longer be reduced to an effective potential and some curl-component may be generated, implying that the magnification tensor is no longer symmetric but requires the addition of a rotation term ω and so-called B-modes in the shear field. In this more general framework, the magnification tensor should be rewritten

$$a_{ij}(\boldsymbol{\theta}) = \begin{pmatrix} 1 - \kappa - \gamma_1 & -\gamma_2 - \omega \\ -\gamma_2 + \omega & 1 - \kappa + \gamma_1 \end{pmatrix}. \tag{12}$$

3.3. Multiple lens planes approximation

The numerical transcription of Eq. (10) in the Horizon-AGN past lightcone requires the slicing of the latter into a series of parallel transverse planes, which could simply be the 22 000 slabs dumped by RAMSES at runtime every coarse time step. These are too numerous and can safely be stacked into thicker planes by packing together 40 consecutive slabs[1]. Here 500 slices of varying co-moving thickness were produced all the way to redshift $z = 7$ to compute either the deflection field or the projected surface mass density as described below.

The discrete version of the equation of ray propagation (10) for a fiducial source plane corresponding to the distance of the plane $j + 1$ reads

$$\boldsymbol{\beta}^{j+1} = \boldsymbol{\theta} - \sum_{i=1}^{j} \frac{D_{i;j+1}}{D_{j+1}} \boldsymbol{\alpha}^i(\boldsymbol{\beta}^i), \tag{13}$$

where $\boldsymbol{\alpha}^i$ is the deflection field in the lens plane i, D_{j+1} is the angular diameter distance between the observer and the plane $j + 1$, and $D_{i;j+1}$ is the angular diameter distance between planes i and $j + 1$. Therefore, as sketched in Fig. 3, rays are recursively deflected one plane after the other, starting from unperturbed positions on a regular grid $\boldsymbol{\theta} \equiv \boldsymbol{\beta}^1$.

The practical implementation of the recursion in Eq. (13) is computationally cumbersome and demanding in terms of memory because the computation of the source plane positions $\boldsymbol{\beta}^{j+1}$ requires holding all the j previously computed source plane positions. Instead, this paper follows the approach of Hilbert et al. (2009), who showed that Eq. (13) can be rewritten as a recursion over only three consecutive planes[2]

$$\boldsymbol{\beta}^{j+1} = \left(1 - \frac{D_j}{D_{j+1}}\frac{D_{j-1;j+1}}{D_{j-1;j}}\right)\boldsymbol{\beta}^{j-1} + \frac{D_j}{D_{j+1}}\frac{D_{j-1;j+1}}{D_{j-1;j}}\boldsymbol{\beta}^{j} - \frac{D_{j;j+1}}{D_j}\boldsymbol{\alpha}^j(\boldsymbol{\beta}^j). \tag{14}$$

In addition to this thorough propagation of light rays, the source plane positions and associated quantities (convergence κ, shear γ, and rotation ω) were additionally computed using the Born approximation, following the discrete version of Eq. (11):

$$\boldsymbol{\beta}^{j+1} = \boldsymbol{\theta} - \sum_{i=1}^{j} \frac{D_{i;j+1}}{D_{j+1}} \boldsymbol{\alpha}^i(\boldsymbol{\theta}). \tag{15}$$

The deflection maps in each lens plane were computed on a very fine grid of pixels of constant angular size. In order to preserve the spatial resolution of about 1 kpc that is allowed by the simulation at high redshift, 36 000 × 36 000 deflection maps were built in the narrow 1 deg lightcone. The deflection maps in the low-redshift 2.25 sq deg wide cone that reach $z = 1$ were computed on a coarser 20 000 × 20 000 pixel grid because the actual physical resolution of the simulation at low redshift does justify the 0.1 arcsec resolution of the narrow 1 sq deg field of view. Even though the image plane positions $\boldsymbol{\theta} = \boldsymbol{\beta}^1$ are placed on the regular pixel grid, the deflections they experience must be interpolated in between the nodes of the regular deflection map as they progress backward to a given source plane. This was done with a simple bilinear interpolation scheme.

[1] This number was chosen as a tradeoff between the typical number of CPU cores in the servers used to perform the calculations and the preservation of the line-of-sight native sampling of the lightcone.

[2] This recursion requires the introduction of an artificial $\boldsymbol{\beta}^0 \equiv \boldsymbol{\beta}^1 = \boldsymbol{\theta}$ slice in the initial setup.

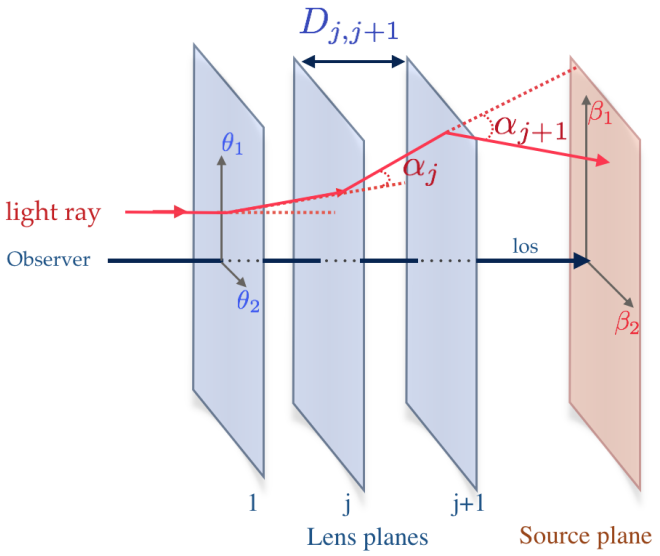

Fig. 3. Schematic view of the propagation of a light ray through a lightcone sliced into multiple discrete lens planes. The ray (red line) is deflected at each intersection with a thin lens plane. The deflection field is defined for each plane depending of the angular position on this plane $\boldsymbol{\alpha}^j(\boldsymbol{\beta}^j)$.

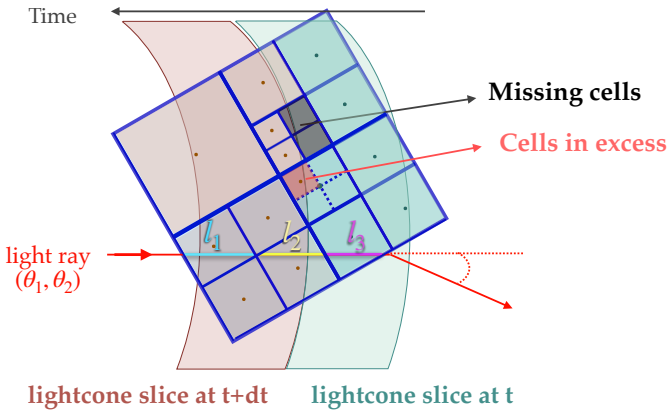

Fig. 4. Schematic view of the problem induced by cells at the boundary of slabs j and $j+1$, which become refined between time t and $t + \mathrm{d}t$. Missing cells (devoid of dots) or cells in excess (overlapping dotted cells of different colour) can end up as lightcone particles. A fiducial light ray is drawn to illustrate the intersection length l_i between the ray and RAMSES cells.

3.4. Total deflections from the RAMSES accelerations

We now describe how we obtained α that we used in Eqs. (14) and (15). The first method uses the gravitational acceleration field, which is registered on each (possibly refined) grid location inside the lightcone. The very same gravitational field that was used to move particles and evolve Eulerian quantities in RAMSES was interpolated at every cell position and was therefore used to consistently derive the deflection field. The merits of the complex three-dimensional multi-resolution Poisson solver are therefore preserved and the transverse components of the acceleration fields can readily be used to infer the deflection field. By integrating the transverse component of the acceleration along the light of sight, we can compute the deflection field according to Eq. (2).

To do so, gas cells that intersect the ray were considered for each light ray, and the intersection length along the line-of-sight l_i was computed. Knowing the cell size δ_i, and its orientation with respect to the line of sight, we deduced l_i with an oriented-box-boundary (OBB) algorithm (e.g. Akenine-Möller et al. 2008) that assumes that all cells share the same orientation (flat-sky approximation), and we factorised out expensive dot products between normals to cell edges and the line of sight,

$$\boldsymbol{\alpha}(\boldsymbol{\theta}) = \frac{2}{c^2} \sum_{i \in \mathcal{V}(\boldsymbol{\theta})} \boldsymbol{\nabla}_\perp \phi_i(\boldsymbol{\theta})\, l_i, \tag{16}$$

where $\mathcal{V}(\boldsymbol{\theta})$ denotes the projected vicinity of a sky position $\boldsymbol{\theta}$. As shown in Fig. 4, a fiducial light ray is drawn: at each lens plane, the deviation of the light is calculated as the direct sum of the transverse acceleration components recorded on the cells i, weighted by the intersection length l_i. Here, the field of view is small and we can safely assume that light rays share the same orientation (flat-sky approximation) and are parallel to the line of sight.

This method has the main advantage that it preserves the gravitational force that was used when the simulation was evolved. In particular, the way shot noise is smoothed out in the simulation to recover the acceleration field from a mixture of Lagrangian particles and Eulerian gas cells is faithfully respected in the ray-tracing. In other word, the force felt by photons is very similar to the force felt by particles in the simulation. Acceleration is also local, in the sense that the deflection experienced by a light ray (and related derivatives leading to e.g. shear and convergence) depends only on the acceleration of cells that this ray crosses. The mass distribution outside the lightcone is therefore consistently taken into account through the acceleration field.

However, this method is sensitive to small artefacts that are present at the lightcone generation stage (i.e. simulation runtime) and that could not be corrected without a prohibitive post-processing of the lightcone outputs. When the simulation dumps two given neighbouring slabs at two consecutive time steps, problems can arise if cells on the boundary between the two slabs have been (de-)refined in the mean time. As illustrated in Fig. 4, such cells can be counted twice or can be missing if they are refined (or de-refined) at the next time step. These bumps and dips in the deflection map translate into saw-tooth patterns in the convergence maps. They are quite scarce and of very modest amplitude, however.

A 100 arcsec wide zoom into the convergence map obtained with this method is shown in the left panel of Fig. 5. The source redshift is $z_s = 0.8$. A few subdominant artefacts due to missing acceleration cells are spotted. They induce small correlations on scales smaller than a few arcseconds and are otherwise completely negligible for our cosmological applications.

3.5. Projection of smoothed particle density

The second method of computing the deflection maps in thin lens planes is more classical: it relies on the projection of particles onto surface density maps that are then turned into deflection maps. If the line-of-sight integration is performed under the Born approximation, the Fourier inversion going from the projected density to the deflection is just done once starting from the effective convergence. Otherwise, with the full propagation, many FFT inversions on projected density maps that do not fulfil the periodic boundary condition criterion imply an accumulation of the inaccuracies in the Fourier inversion.

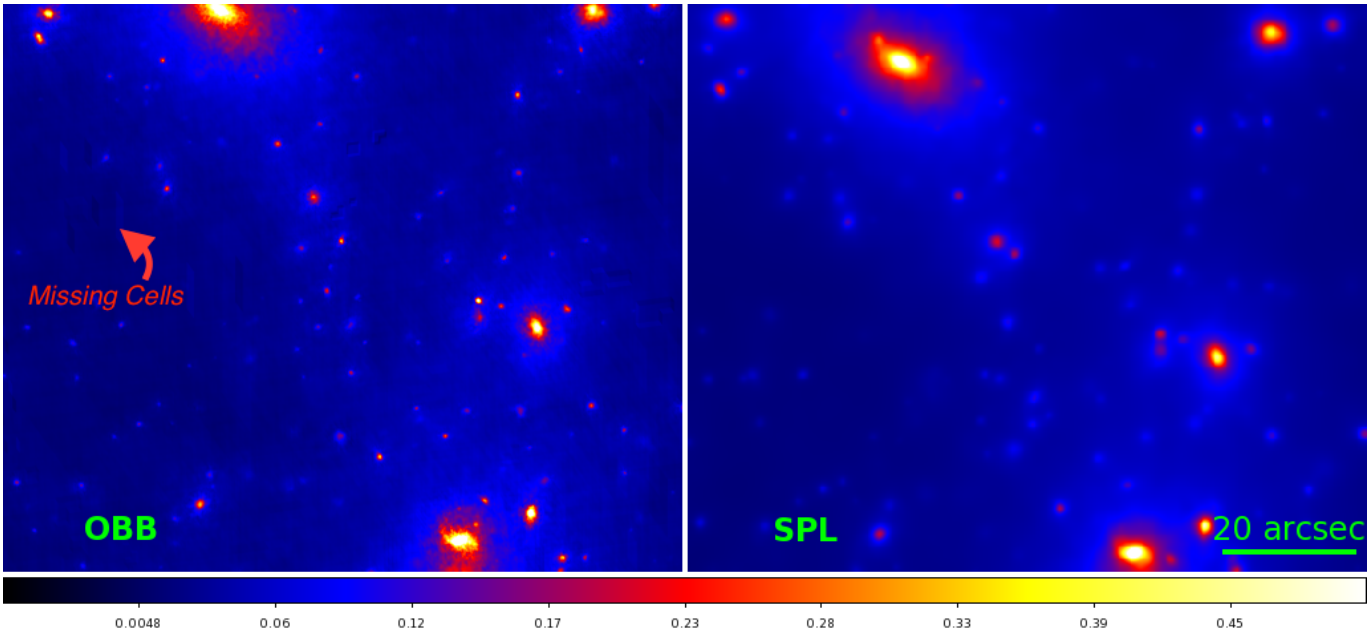

Fig. 5. Comparison of $z_s = 0.8$ convergence maps obtained with the OBB method (integration of transverse accelerations in cells, *left*) and with the SPL method (projection of particles onto convergence planes after adaptative Gaussian smoothing, *right*). The latter method applies a more aggressive smoothing that better erases shot noise. Inaccuracies of long-range deflections in the SPL method that are due to edge effects translate into a global shift for some galaxies, as compared to OBB. With this method, some missing acceleration cells occasionally produce modest artefacts on a small scale.

First of all, this method allows us to separate the contribution of each matter component from the total deflection field. We can therefore compute the contribution of stars or gas to the overall lensing near a given deflector. This is not possible with the acceleration method because only the total acceleration is computed by the simulation.

In addition, particles can be projected with an efficient and adaptive smoothing scheme. Instead of a standard nearest grid point or cloud-in-cell projection, a Gaussian filter (truncated at four times the standard deviation σ) is used in which the width of the smoothing filter σ is tuned to the local density, hence following the smooth particle lensing (SPL) method of Aubert et al. (2007). Because the AMR grid of `RAMSES` is adaptive, the resolution level around a given particle position from the neighbouring gas cells can be recovered. This thus bypasses the time-consuming step of building a tree in the distribution of particles, which is at the heart of the SPL method.

To illustrate the merits of this method and for comparison with the previous one, we show the same region of simulated convergence fields for a source redshift $z_s = 0.8$ in the right panel of Fig. 5. This adaptive Gaussian smoothing (referred to as SPL method below) seems more efficient at smoothing the particle noise out. Between the two methods, we note small displacements of some galaxies of a few arcseconds. They are due to the long-range inaccuracies generated by the Fourier inversions.

3.6. Lensing of galaxy and halo catalogues

In order to correlate galaxies (or halos) in the lightcone with the convergence or shear field around them and, hence, measure their GGL, their catalogue positions $\boldsymbol{\beta}$ (which are intrinsic source plane coordinates) need to be shifted and their observed lensed image plane positions $\boldsymbol{\theta}$ need to be inferred. These are related by the thorough lens Eq. (10), or its numerical translation (13). However, this equation is explicit only for the $\theta \rightarrow \beta$ mapping. The inverse relation, which can be multi-valued when strong lensing occurs, has to be solved numerically by testing for every image plane mesh $\boldsymbol{\theta}_{ij}$ whether it surrounds the coordinates $\boldsymbol{\beta}^{\rm gal}$ of the deflected galaxy when cast into the source plane $\boldsymbol{\beta}_{ij}$ (e.g. Schneider et al. 1992; Keeton 2001; Bartelmann 2003). Because the method should work in the strong-lensing regime, regular rectangular meshes may no longer remain convex in the source plane and it is therefore preferable to split each mesh into two triangles. These triangles will map into triangles in the source plane and we can safely test whether $\boldsymbol{\beta}^{\rm gal}$ is inside them. In order to speed up the test on our large pixel grids, the image plane was partitioned into a quad-tree structure that recursively explores finer and finer meshes. The method is very fast and yields all the image plane antecedents of a given galaxy position $\boldsymbol{\beta}^{\rm gal}$. This provides us the updated catalogues of halos and galaxies. Obviously, when the GGL signal is measured in the Born approximation, catalogue entries do not need to be deflected and therefore source plane and image plane coordinates are identical.

3.7. Summary of the generated deflection maps

Table 1 summarises the main advantages and drawbacks of the OBB and SPL methods. Altogether, 2×2 (OBB/SPL and Born approximation/full propagation) deflection maps were generated for each of the 246 source planes all the way to $z = 1$ in the wide opening angle field. Likewise, we obtained 2×2 maps for each of the 500 source planes all the way to $z = 7$ in the narrow opening angle field.

4. Cosmic shear

This section assesses the validity of our ray-tracing methods by measuring one- and two-point statistics of the lensing quantities such as convergence and (reduced-)shear. It also compares these finding with other methods.

Table 1. Summary of the main properties of the SPL and OBB methods ray-tracing methods.

	OBB	SPL
Deflection (per plane)	Integration of transverse acceleration	Particles adaptively smoothed and projected onto density planes
Large scale	Matter outside the lightcone is taken into account	Edge effects due to Fourier transforms
Small scale	Uses the multi-scale RAMSES potential	Smoothing reduces small-scale features
Cells missing/in excess	Produces small-scale artefacts	Unaffected
Matter component	Only for the total matter	Can individually consider DM, stars, and gas

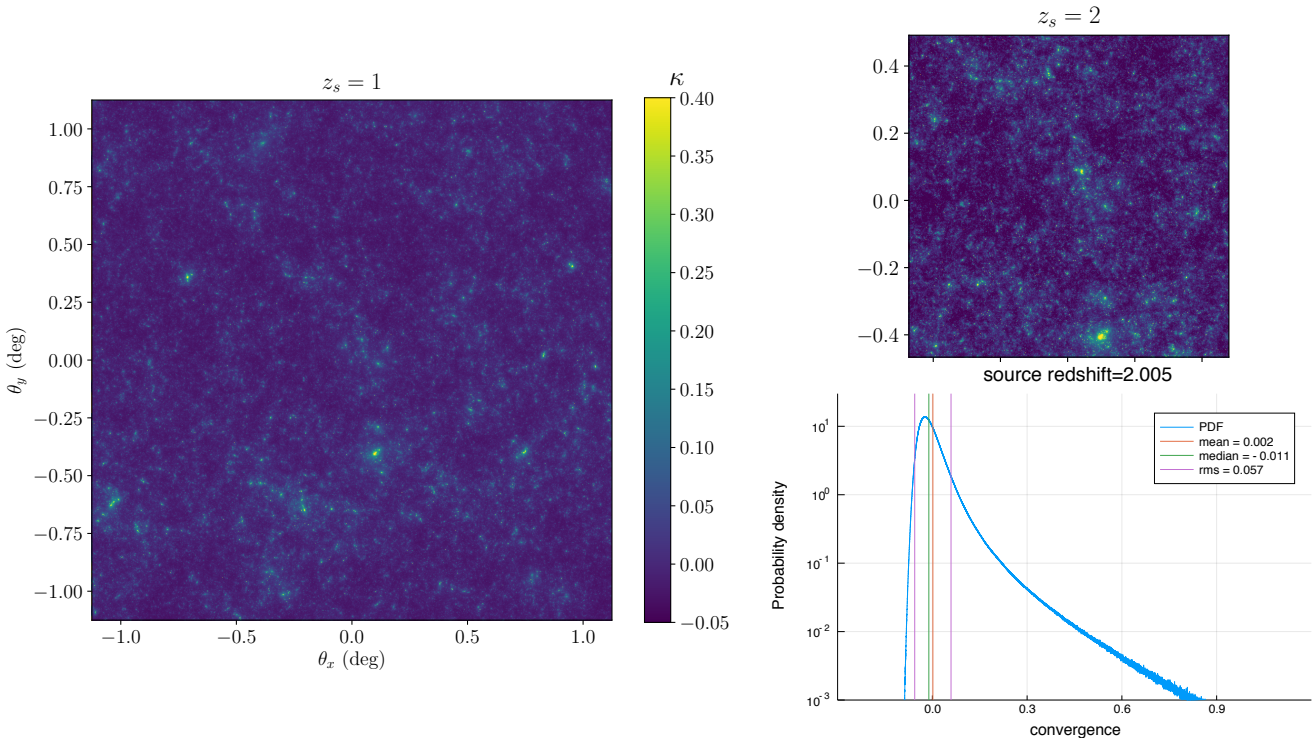

Fig. 6. *Left panel*: convergence map generated with a 0.′1 pixel grid over a 2.25×2.25 sq. deg. field of view for a fiducial source plane at $z_s \sim 1$. *Right panel*: convergence map with a field of view of 1 sq. deg. at $z_s \sim 2$, and its corresponding convergence PDF showing the characteristic skewed distribution.

The focus is on the effect of baryons on small scales for multipoles $\ell \gtrsim 2000$ to check whether the baryonic component is connected to other non-linear effects like the shear – reduced shear correction and beyond-Born treatments.

4.1. Convergence of one-point statistics

The most basic quantity that can be derived from the convergence field shown in the right panel of Fig. 6 is the probability distribution function (PDF) of the convergence. The Fig. 6 shows this quantity, which is extremely non-Gaussian at the $\sim 1''$ resolution of the map. The skewness of the field is visible, with a prominent high-end tail and a sharp decrease in negative convergence values.

4.2. Convergence power spectrum

In Fourier space, the statistical properties of the convergence field are commonly characterised by its angular power spectrum $P_\kappa(l)$,

$$\langle \hat{\kappa}(\boldsymbol{\ell})\, \hat{\kappa}^*(\boldsymbol{\ell}')\rangle = (2\pi)^2\, \delta_D(\boldsymbol{\ell} - \boldsymbol{\ell}')\, P_\kappa(\ell), \tag{17}$$

where $\delta_D(\boldsymbol{\ell}$ is the Dirac delta function. For two fiducial source redshifts ($z_s = 0.5$ and $z_s = 1$), Fig. 7 shows the angular power spectrum of the convergence obtained with the two ray-tracing techniques: the OBB and SPL methods (solid magenta and solid cyan curves, respectively). The low-redshift methods are based on the 2.25 deg wide lightcone. They are thus more accurate on larger scales $\ell \lesssim 10^3$, even though the large sample variance will not permit quantitative statements. On small scales ($\ell \sim 2 \times 10^5$), the additional amount of smoothing implied by the SPL projection of particles onto the lens planes induces a deficit of power with respect to the less aggressive softening of the OBB method in which shot noise has not been entirely suppressed (see Fig. 5).

The middle panel of Fig. 7 shows the difference between power spectra inferred using the Born approximation or with the full multiple lens plane approach for the OBB method. For angular scales $\ell \lesssim 8 \times 10^4$, we find differences between the two propagation methods that are smaller than about 0.5%, which is totally negligible given possible numerical errors and sampling variance limitations. At lower angular scales $\ell \gtrsim 10^5$, departures rise above the few percent level. We note that this scale also corresponds to the scale where shot noise (from

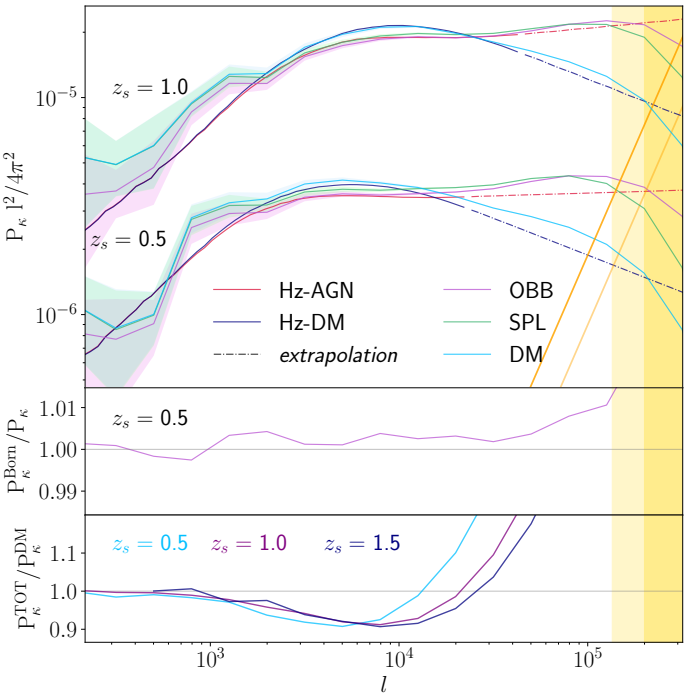

Fig. 7. *Upper panel*: convergence power spectra for source redshift $z_s = 1$ (*top*) and $z_s = 0.5$ (*bottom*) derived with the OBB (magenta) and the SPL (green) methods. The more aggressive smoothing of this latter method translates into a faster high-ℓ fall-off. The cyan curves (DM) only account for the DM component (rescaled by $1 + \Omega_b/\Omega_M$). The red curve corresponds to the direct integration of the three-dimensional total matter power spectrum (Limber approximation) in the Horizon-AGN simulation (Hz-AGN). The blue curves are the direct integration of the Horizon-DM (DM-only) matter power spectrum (Hz-DM). Dashes reflect regimes where the three-dimensional spectra of Chisari et al. (2018) were extrapolated by a simple power law (extrapolation). The yellow lines show the particle shot-noise contribution at two different redshifts. *Middle panel*: ratio of the $z_s = 0.5$ convergence power spectra obtained with the Born approximation and the proper multiple lens plane integration showing only very small changes up to $\ell \sim 10^5$. *Bottom panel*: ratio of the DM-only to total convergence power spectra at $z_s = 0.5$, 1.0, and 1.5 for the SPL method.

DM particles) and convergence power spectral are of equal amplitude (yellow shaded area). Below these very small scales, close to the strong-lens regime, the Born approximation may start to break down (Schäfer et al. 2012).

Under the Limber and Born approximations, the convergence power spectrum can be expressed as an integral of the three-dimensional non-linear matter power spectrum P_δ (Limber 1953; Blandford et al. 1991; Miralda-Escudé 1991; Kaiser 1992) from the observer to the source plane redshift or corresponding co-moving distance χ_s:

$$P_\kappa(\ell) = \left(\frac{3\Omega_m H_0^2}{2c^2}\right)^2 \int_0^{\chi_s} \mathrm{d}\chi \left(\frac{\chi(\chi_s - \chi)}{\chi_s a(\chi)}\right)^2 P_\delta\left(\frac{\ell}{\chi}, \chi\right), \tag{18}$$

where a is the scale factor and where no spatial curvature of the universe was assumed for conciseness and because the cosmological model in Horizon-AGN is flat. As a validation test of our light-deflection recipes, the lensing power spectrum derived from the actual ray-tracing was compared to an integration of the three-dimensional matter power spectrum measured by Chisari et al. (2018) in the Horizon-AGN simulation box. The red curve is the direct integration of $P_\delta(k)$ power spectra, and the dashed parts of the lines corresponds to a power-law extrapolation of the $P_\delta(k)$ down to smaller scales. In the range $3000 \lesssim \ell \lesssim 3 \times 10^5$, an excellent agreement is found between the red curve and the spectra inferred with our two ray-tracing techniques. On larger scales, the cosmic variance (which is different in the full simulation box and the intercept of the box with the lightcone) prevents any further agreement. This is also the case for $\ell \gtrsim 3 \times 10^5$, where some possibly left-over shot noise in the ray-tracing maps and the hazardous high-ℓ extrapolation of the three-dimensional power spectra complicate the comparison. In addition, the low-ℓ oscillations of the spectrum is likely to originate from the replicates of the simulation box throughout the past lightcone.

Chisari et al. (2018) also measured matter power spectra in the Horizon-DM simulation at various redshifts. This simulation is identical to Horizon-AGN in terms of initial conditions, but has been run without any baryonic physics in it after the mass of DM particles was rescalded to conserve the same total matter density (Peirani et al. 2017; Chisari et al. 2018). The integration of this DM-only power spectrum allows us to obtain a sense on the effect of baryons in the DM-distribution itself. In the same way as the red curve showed the result of the Limber integral in Eq. (18) for Horizon-AGN, the dark blue curve shows the same integral for Horizon-DM. The latter has much less power for $\ell \gtrsim 2 \times 10^4$ than either the integration of the full physics Horizon-AGN matter power spectrum (red) or that derived directly from ray-tracing (purple or green). The boost of spectral amplitude is due to cool baryons in the form of stars at the centre of halos. Moreover, we note a deficit of power on scales $2 \times 10^3 \lesssim \ell \lesssim 2 \times 10^4$ for the full physics simulation. As pointed out by Semboloni et al. (2011), the pressure acting on baryons prevents them from falling onto halos as efficiently as DM particles, hence reducing the depth of the potential wells when compared to a DM-only run. This effect has previously been investigated with more sensitivity on the three-dimensional matter power spectrum in the Horizon-AGN simulation (Chisari et al. 2018), and a clear dip in the matter density power spectrum of the full physics simulation is observed on scales $1 \lesssim k \lesssim 10\,h\,\mathrm{Mpc}^{-1}$. Here, the projection somewhat smears out this dip over a larger range of scales, but a ∼15% decrease in amplitude is typically observed for $\ell = 10^4$ at $z_s = 0.5$. In order to show the changes due to the inclusion of the baryonic component more clearly, we traced rays through the lightcone by considering only the DM particles of the Horizon-AGN run with the SPL method. For this particular integration of rays trajectories, we multiplied the mass of the DM particules by a factor $1 + \Omega_b/\Omega_{DM}$ (where $\Omega_{DM} = \Omega_m - \Omega_b$) to obtain the same overall cosmic mean matter density. The cyan curve in the upper panel shows the resulting convergence power spectrum. The ratios between the total full physics convergence power spectrum and the rescaled DM contribution of this power spectrum at $z_s = 0.5, 1.0$ and 1.5 are shown in the bottom panel and further illustrate the two different effects of baryons on intermediate and small scales.

By considering two raytracing methods to derive the convergence power spectrum, and by asserting that consistent results are obtained by integrating the three-dimensional matter power spectrum, we now search for small scale effects that involve the possible coupling between the baryonic component and shear – reduced shear corrections.

4.3. Shear – reduced shear corrections to two-point functions

In practical situations, rather than the convergence power spectrum, which is not directly observable, wide field surveys give

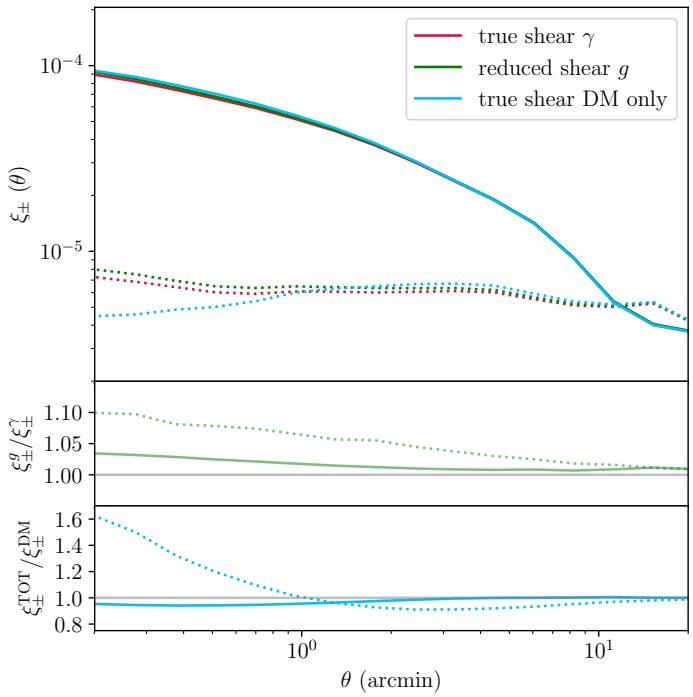

Fig. 8. *Upper panel*: two-point shear correlation functions ξ_+ (solid lines) and ξ_- (dotted lines) for a fiducial source redshift $z_s = 0.5$. We either correlate actual shear (red) or reduced shear (green) in the calculation to highlight the small-scale effect of baryons on this non-linear correction. *Middle panel*: ratio of shear correlation functions for the two cases. *Bottom panel*: ratio of shear correlation functions for a ray-tracing that only includes rescaled DM particles or all the components.

access to the angular correlation of pairs of galaxy ellipticities. The complex ellipticity[3] ε is directly related to the shear γ. The relation between the ensemble mean ellipticity and the shear is

$$\langle\varepsilon\rangle = g \equiv \frac{\gamma}{1-\kappa} \simeq \gamma, \tag{19}$$

with g the so-called reduced shear. Therefore, the two point correlations of ellipticities and shear only match when the convergence κ is small. Because the regions of large convergence are typically the centres of halos where the contribution of cooled baryons is highest, we might expect a coupling between the inclusion of baryons and the shear – reduced-shear corrections needed to properly interpret the cosmological signal carried by the two-point statistics (e.g. White 2005; Kilbinger 2010)

Owing to the spin-2 nature of ellipticity, we can define the angular correlation functions $\xi_\pm$

$$\begin{aligned}\xi_\pm(\theta) &= \langle\gamma_+(\vartheta+\theta)\gamma_+(\vartheta)\rangle_\vartheta \pm \langle\gamma_\times(\vartheta+\theta)\gamma_\times(\vartheta)\rangle_\vartheta,\\ &= 2\pi\int \mathrm{d}\ell\,\ell J_{0/4}(\theta\ell)P_\kappa(\ell),\end{aligned} \tag{20}$$

where γ_+ and $\gamma_\times$ are defined with respect to the separation vector between two galaxies or, here, any two image plane positions at separation θ. J_0 and J_4 are zeroth- and fourth-order Bessel functions.

Instead of the shear, observers can only measure associated ellipticities ϵ, which should thus replace γ in Eq. (20) in practical measurements. The reduced shear maps were computed together with shear and convergence maps, so as to measure the modified ξ_+ and ξ_- angular correlations to compare them with the actual correlation functions. For efficiency, the `Athena` code[4] was used to compute correlation functions.

The results are shown in Fig. 8 for a fiducial source redshift $z_s = 0.5$. Here ξ_+^g and ξ_+^γ only depart from one another at the ∼2–3% level on angular separations ∼1′. The effect is slightly stronger for ξ_- , which is known to be more sensitive to smaller non-linear scales than ξ_+, but is also more difficult to measure in the data because of its lower amplitude. On 1′ scales, $\xi_-^g/\xi_-^\gamma - 1 \simeq 7$–8%. Like for the power spectra in the previous subsection, the cyan curves represent the correlations $\xi_\pm^\gamma$ for the rescaled DM contribution. The bottom panel shows the ratio of rescaled DM over full physics reduced shear correlation functions, further illustrating the effect of baryons on small scales. Again, ξ_- responds more substantially to the inclusion of baryons. The deficit of correlation amplitude when baryons are taken into account peaks at 3–4′ and is of about 10%. Below 1′, the effect starts to increase, but those scales are never used in practical cosmic shear applications. We show in the next section that these scales remain perfectly relevant for galaxy evolution studies by means of the galaxy-galaxy weak-lensing signal.

5. Galaxy-galaxy lensing

Focussing further on DM halos, we now investigate the yields of the simulation in terms of the galaxy-galaxy weak-lensing signal. The tangential alignment of background galaxies around foreground deflectors is substantially altered by the aforementioned baryonic physics, and we also expect a strong signature in this particular lensing regime.

For a circularly symmetric mass distribution $\Sigma(R)$, we can relate shear, convergence, and the mean convergence enclosed inside a radius R centred on a foreground galaxy or halo as

$$\bar\kappa(<R) = \frac{2}{R^2}\int_0^R \kappa(R')R'\mathrm{d}R' = \kappa(R) + \gamma(R). \tag{21}$$

Using the definition of the critical density given in Eq. (5), we can define the excess density

$$\begin{aligned}\Delta\Sigma(R) &= \frac{M(<R)}{\pi R^2} - \Sigma(R),\\ &= \Sigma_{\rm crit}\gamma(R).\end{aligned} \tag{22}$$

The previous section has shown that the lensing convergence or shear maps have adequate statistical properties, and in Sect. 3.6 we showed how to use the associated deflection maps to map our lightcone galaxy catalogue into the image plane. In addition, galaxies are also expected to become magnified when lensed. Future extensions of this work will include the realistic photometry of the Horizon-AGN galaxies. We can easily account for the magnification bias by multiplying stellar masses by the magnification μ, however, as if luminosity or flux were a direct proxy for stellar mass. In the following, we refer to M_* for the intrinsic and μM_* for the magnified mass proxy.

For any given source redshift, we average the tangential shear around galaxies of any given stellar mass M_* (or more realistically magnified stellar mass μM_*), in order to estimate the GGL around Horizon-AGN galaxies. This is done around deflected galaxy positions.

[3] $\varepsilon = (a-b)/(a+b)\mathrm{e}^{2i\varphi}$, with a and b the major and minor axis of a given galaxy, respectively, and φ is the orientation of the major axis.

[4] http://www.cosmostat.org/software/athena

5.1. Comparison with CMASS galaxies

We first compared the GGL around Horizon-AGN galaxies with the GGL excess mass profiles obtained by Leauthaud et al. (2017), who analysed the spectroscopic CMASS sample of massive galaxies in the footprint of the CFHTLS and CS82 imaging surveys, which covered ∼250 deg^2. These authors paid particular attention to quantifying the stellar mass of the CMASS galaxies that are centred around lens redshift $z \sim 0.55$. The CMASS sample is not a simple mass selection, and includes a set of colour cuts, which makes this just a broad comparison. These results are somewhat sensitive to the detailed distribution in stellar mass above that threshold. The sample mean mass only slightly changes with redshift, but remains close to $3 \times 10^{11}\,M_\odot$.

In order to match this lens sample, we extracted from the wide low-redshift lightcone the galaxies in the redshift range $0.4 \leq z \leq 0.70$, and with a stellar mass above a threshold that was chosen to match the CMASS mean stellar mass. Even though these galaxies centred around lens redshift $z \sim 0.52$ were treated as lens galaxies, they experience a modest amount of magnification (they behave like sources behind the mass distribution at yet lower redshift, see Sect. 5.2). We therefore chose galaxies that satisfy $\mu M_* > 1.7 \times 10^{11}\,M_\odot$. At this stage, selecting for M_* or μM_* does not make any significant difference ($\lesssim$4%) because of the relatively low redshift of the lens sample. By doing so, we obtained the same sample mean stellar mass as the CMASS sample.

We then measured the mean tangential shear around these galaxies for a fiducial unimportant source redshift $z_s = 1$ and converted shear into excess density $\Delta\Sigma$. The result is shown in Fig. 9. A good agreement between our predictions (OBB method, green with lighter envelope) and the observations of Leauthaud et al. (2017) (blue dots) is found, further suggesting that Horizon-AGN galaxies live in the correct massive halos ($M_h \simeq 10^{13}\,M_\odot$), or at the very least, produce the same shear profile as CMASS galaxies around them. We note that we split the 2.25 deg field of view into four quadrants and used the dispersion in these areas to compute a rough estimate of the model uncertainties.

On scales $R \lesssim 0.2\,h^{-1}$ Mpc, the shear profile is 10−15% above the observations. Answering whether the discrepancy is due to faulty subgrid baryonic physics, a missing cosmological ingredient (or not perfectly adequate cosmological parameters), or leftover systematics in the data will certainly require more GGL observations, possibly combined with yet smaller scale strong-lensing and kinematical data (e.g. Sonnenfeld et al. 2018). Small-scale GGL clearly is a unique tool for addressing these issues (e.g. Velliscig et al. 2017), and asserting that the galaxy-halo connection is correctly reproduced by the simulations all the way to $z \gtrsim 1$ is arguably one of the foremost goals of galaxy formation models.

Figure 9 also shows our GGL results for the same population of lenses at the same redshift, but as inferred from the SPL method (solid black), which allows us to split the total lensing signal into its DM (blue and baryonic components (red). First of all, the agreement between the two methods for the total lensing signal is remarkable, except on scales $\gtrsim$2 Mpc ∼ 5′ , where differences begin to exceed the percent level. As we described in the previous section, this is due to inaccuracies of the Fourier transforms performed with the SPL method. We can use this latter technic to compare the contribution of DM and baryons (stars+gas), however. Clearly, the total and DM profiles look very similar beyond ∼0.2 Mpc up to a ∼17% renormalisation of the matter density. Only below these scales begin cooled baryons

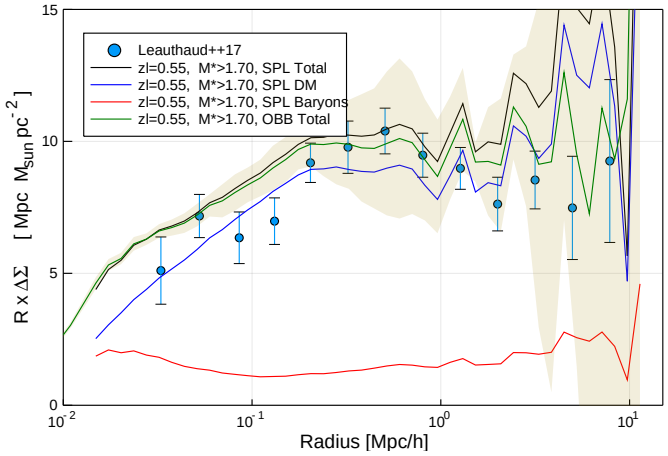

Fig. 9. Comparison of the GGL tangential shear signal around $z = 0.55$ Horizon-AGN galaxies (green curve surrounded by a light green ribbon) and the GGL observations of Leauthaud et al. (2017) (blue dots with error bars). Units are all physical (and not comoving!). Model uncertainties in the simulation past lightcone are roughly estimated by splitting the 2.25 deg wide field of view into four quadrants. They may be underestimated beyond 1 h^{-1} Mpc. Cuts in stellar mass are expressed in units of $10^{11}\,M_\odot$. Black, blue, and red curves show the GGL shear signal predicted with the SPL method for the total, DM, and baryonic mass distributions, respectively. For clarity, uncertainties are omitted. They are similar to those in the case of the OBB method (green).

(stars) to contribute substantially. We predict an equal contribution of DM and stars to the total shear signal near a radius ∼15 kpc. We refer to Peirani et al. (2017) for further details about the innermost density profiles around Horizon-AGN galaxies in the context of the cusp-core problem.

5.2. High-redshift magnification bias

For $z_l \gtrsim 0.6$, the lens population begins to be lensed by yet nearer structures. This can lead to a magnification bias, which was studied by Ziour & Hui (2008).

The spatial density of a lensed population of background sources can be enhanced or decreased by magnification as light rays travel through over- or under-dense sight-lines (e.g. Moessner & Jain 1998; Moessner et al. 1998; Ménard & Bartelmann 2002; Scranton et al. 2005). Furthermore, the fraction of sources that are positively or negatively magnified depends on the slope of the luminosity function of the population. If it is very steep (typically the bright end of a population), we can observe a dramatic increase in the number of bright lensed objects. These deflectors appear brighter than they actually are Fig. 10 shows the mean magnification experienced by Horizon-AGN lightcone galaxies above a given stellar mass threshold (mimicking a more realistic flux limit) as a function of redshift and minimum mass. The upper panel does not take into account the effect of magnification bias, whereas the lower panel does. Those that are consistently magnified and pass a given threshold (bottom panel) are slightly magnified on average, whereas the top panel only shows a tiny constant $\mu \sim 1$−3% systematic residual magnification. This residual excess does not depend on wether the SPL or OBB method are used, or whether we properly integrate rays or use the Born approximation. This is likely because the replicates of the simulation box fill up the lightcone, which slightly increases the probability of rays leaving an over-dense region to cross other over-dense regions on their way to the observer. This residual magnification is however

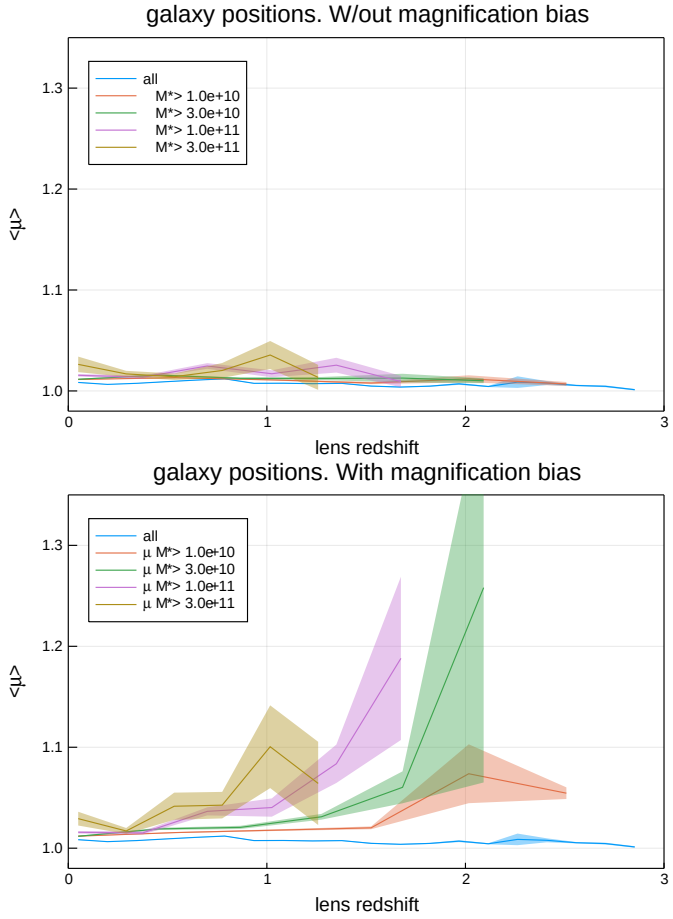

Fig. 10. Average magnification experienced by presumably foreground deflectors including (*bottom*) or excluding (*top*) for magnification bias effect that mostly affects the rapidly declining high end of the stellar mass function. Without magnification bias, a flat nearly unity mean magnification at all redshifts is recovered to within ∼1%. When the magnification bias is turned on, as expected in actual observations, no rapid rise is found (∼10% at $z \sim 1$ for the most massive or luminous galaxies). Cuts in stellar mass are expressed in units of $10^{11}\,M_{\odot}$.

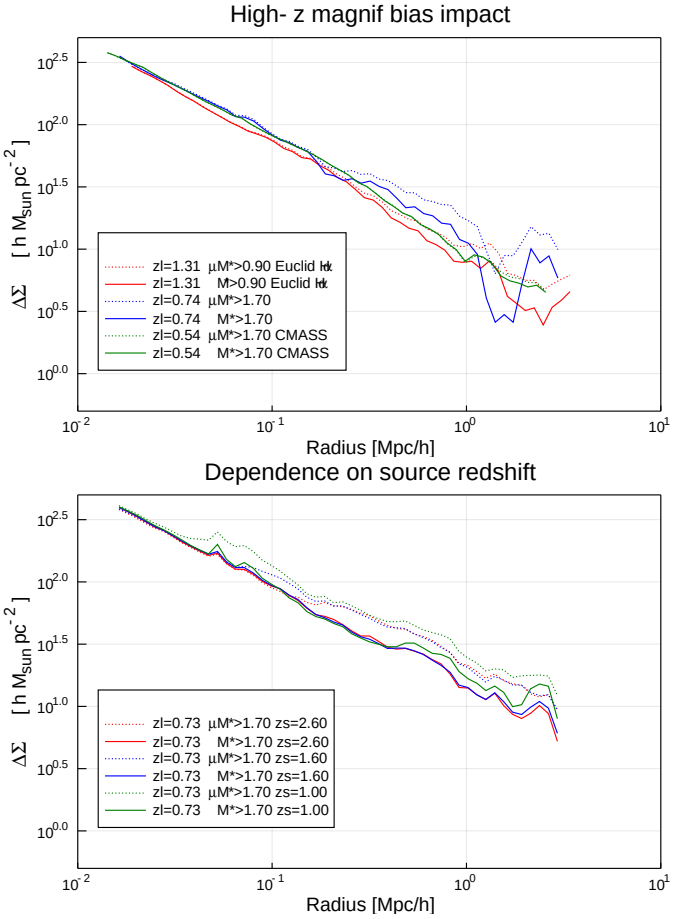

Fig. 11. *Upper panel*: effect of magnification bias on GGL for several high-z fiducial lens samples showing an increase in excess density $\Delta\Sigma$ (or tangential shear) for $R \gtrsim 1$ Mpc. Solid curves ignore the magnification, whereas dotted lines account for it. *Lower panel*: dependence of this effect on the source redshift. In both panels, cuts in stellar mass are expressed in units of $10^{11}\,M_{\odot}$.

tiny for sight-lines that are populated by galaxies, and it completely vanishes for rays coming for random positions.

The massive end of the galaxy stellar mass function appears tobe significantly magnification biased. A ∼8% effect for galaxies at $0.6 \leq z \leq 1.2$ and $M_* \gtrsim 2 \times 10^{11}\,M_{\odot}$ is typical. It can be as high at ∼20−50% at $1.5 \leq z \leq 2$ for $\mu M_* \gtrsim 3 \times 10^{11}\,M_{\odot}$. A thorough investigation of the effect of this magnification bias when we try to place constraints on the high end of the $z \gtrsim 2$ luminosity function from observations is left for a forthcoming paper.

Taking the magnification bias into account, we now explore three fiducial populations of massive deflectors to highlight the changes induced in the projected excess density profiles. The first population consists of the CMASS galaxies at $z = 0.54$ and $\mu M_* \geq 1.7 \times 10^{11}\,M_{\odot}$, the second case corresponds to the same lower limit on the mass, but pushed to $z = 0.74$. In both cases, the excess density is measured for source redshift $z_s = 0.8$. The last lens sample corresponds to the population of Hα emitters in the $0.9 \leq z \leq 1.8$ redshift range that will be detected by the Euclid slit-less grism spectrograph above a line flux of $\sim 2 \times 10^{-16}\,\mathrm{erg\,s^{-1}\,cm^{-2}}$. About 2000 such sources per square degree are expected; therefore the 2000 most massive Horizon-AGN lightcone sources are picked in that redshift interval to crudely mimic an Hα line flux selection. To account for magnification bias, the selection was also made on μM_*, and the source redshift for this populations was set to $z_s = 2$. Results for these three populations are shown in the top panel of Fig. 11, where we distinguish the excess density profiles that include (dotted) or exclude (solid) for magnification. As anticipated, no significant change is obtained for the $z = 0.54$ CMASS-like sample (green), but differences are more noticeable as lens redshift increases, and on large scales ($R \gtrsim 1$ Mpc), we observe a 20−50% increase in $\Delta\Sigma$, consistent with the large-scale linear scale-invariance bias model used by Ziour & Hui (2008). Between $z = 0.54$ and $z = 0.74$, galaxies of the same mass seem to live in halos of the same mass (very little evolution of the $M_* - M_h$ relation), leading to no evolution of $\Delta\Sigma$ below ∼200 kpc. The only difference occurs farther out where the two-halo term starts to be important in this galaxy-mass correlation function. There, galaxies of the same mass at $z = 0.54$ and $z = 0.74$ live in rarer excursions of the initial density field, and are thus more highly biased, which leads to an increase of $\Delta\Sigma$ on the large scale. For the Euclid-like distant lens population, the trend is similar, and the amplitude of the magnification bias effect would suggest a bias of the lens population about 30% higher than it really is.

The lower panel of Fig. 11 shows the evolution of the magnification-bias-induced excess density profile with source

redshift for massive deflectors at $z = 0.74$. In principle, according to Eq. (22), the excess density should not depend on source redshift. However, the magnification bias favours over-densities in front of deflectors. The response of distance sources carrying shear to these over-densities will depend on the source redshift in a way that is not absorbed by Eq. (22). Hence, a scale-dependent distortion of the profiles is observed. The closer the source redshift from the deflector, the smaller the scale it kicks in. As already stressed by Ziour & Hui (2008), this hampers a direct application of shear-ratio tests with high-redshift deflectors (e.g. Jain & Taylor 2003).

6. Summary and prospects

Using two complementary methods for projecting the density or gravitational acceleration field from the Horizon-AGN lightcone, we propagated light rays and derived various gravitational lensing observables in the simulated field of view. The simulated area was 2.25 deg^2 out to $z = 1$ and 1 deg^2 all the way to $z = 7$. The effect of baryons on the convergence angular power spectrum $P_\kappa(\ell)$ was quantified, together with the two-point shear correlations $\xi_\pm(\theta)$ and the galaxy-galaxy lensing profile around massive simulated galaxies.

For cosmic shear, the inclusion of baryons induces a deficit of power in the convergence power spectrum of about 10% for $10^3 < \ell < 10^4$ at $z_s = 0.5$. The amplitude of the distortion is about the same at $z_s = 1$, but is slightly shifted to roughly twice as high ℓ multipole values. On yet higher multipoles, the cooled baryons, essentially in the form of stars, produce a dramatic boost of power, nearly a factor 2 for $\ell \sim 10^5$. As emphasised in Chisari et al. (2018), it is worth stressing that detailed quantitative statements on such small angular scales may still depend on the numerical implementation of baryonic processes.

For galaxy-galaxy lensing, the projected excess density profiles for a sample of simulated galaxies consistent with the CMASS sample at $z \sim 0.52$ (analysed by Leauthaud et al. 2017) were found to be in excellent agreement. To properly analyse this signal around high-redshift deflectors, the magnification bias affecting the bright end of a population of distant galaxies was carefully taken into account, showing a large-scale increase of the signal as high as 30% beyond 1 Mpc for lenses at $z \gtrsim 1$. This type of effect is particularly pronounced for future samples of distant deflectors, such as the spectroscopic Euclid sources that are detected based on their Hα line intensity.

Peirani et al. (2019) have shown that the innermost parts of Horizon-AGN galaxies are consistent with strong-lensing observations of Sonnenfeld et al. (2013) and Newman et al. (2013, 2015) at $z_{\rm lens} \lesssim 0.3$. We intend to make more predictions on the optical depth for strong lensing in the Horizon-AGN lightcone with our implemented ray-tracing machinery. Likewise, in a forthcoming paper we will present the results of the deflection field applied to simulated images derived from the light that is emitted by the stars that are produced in the simulation, hence enabling the possibility of measuring lensing quantities (shear, magnification, etc.) in the very same way as in observations: shape measurement in the presence of noise, PSF, pixel sampling, photometric redshift determinations, realistic galaxy biasing, and more generally, directly predicted galaxy-mass relation, and also the intrinsic alignment of galaxies and their surrounding halos (Codis et al. 2015; Chisari et al. 2015, 2016).

Acknowledgements. The authors would like to thank D. Aubert for making his SPL code available to us. We acknowledge fruitful discussions with K. Benabed, S. Colombi, M. Kilbinger, and S. Prunet in early phases of the project. We also thank G. Lavaux, Y. Rasera, and M-A Breton for stimulating interactions around this project. We are also grateful to A. Leauthaud for constructive comments about the comparison with her GGL lensing results. CL is supported by a Beecroft Fellowship. This work was supported by the Agence Nationale de la Recherche (ANR) as part of the SPIN(E) ANR-13-BS05-0005 (http://cosmicorigin.org) ERC grant 670193, and AMALGAM ANR-12-JS05-0006 projects, and by the Centre National des Etudes Spatiales (CNES). NEC is supported by a RAS research fellowship. This research is also funded by the European Research Council (ERC) under the Horizon 2020 research and innovation programme grant agreement of the European Union: ERC-2015-AdG 695561 (ByoPiC, https://byopic.eu). This work has made use of the Horizon Cluster hosted by the Institut d'Astrophysique de Paris. We thank S. Rouberol for running the cluster smoothly for us.

References

Abbott, T., Abdalla, F. B., Allam, S., et al. 2016, Phys. Rev. D, 94, 022001
Akenine-Möller, T., Haines, E., & Hoffman, N. 2008, Real-Time Rendering 3rd Edition (Natick, MA, USA: A. K. Peters, Ltd.), 1045
Aubert, D., Pichon, C., & Colombi, S. 2004, MNRAS, 352, 376
Aubert, D., Amara, A., & Metcalf, R. B. 2007, MNRAS, 376, 113
Barreira, A., Llinares, C., Bose, S., & Li, B. 2016, JCAP, 5, 001
Bartelmann, M. 2003, ArXiv e-prints [arXiv:astro-ph/0304162]
Bartelmann, M., & Schneider, P. 2001, Phys. Rep., 340, 291
Blandford, R. D., Saust, A. B., Brainerd, T. G., & Villumsen, J. V. 1991, MNRAS, 251, 600
Brainerd, T. G., Blandford, R. D., & Smail, I. 1996, ApJ, 466, 623
Chisari, N., Codis, S., Laigle, C., et al. 2015, MNRAS, 454, 2736
Chisari, N., Laigle, C., Codis, S., et al. 2016, MNRAS, 461, 2702
Chisari, N. E., Richardson, M. L. A., Devriendt, J., et al. 2018, MNRAS, 480, 3962
Codis, S., Gavazzi, R., Dubois, Y., et al. 2015, MNRAS, 448, 3391
Coupon, J., Arnouts, S., van Waerbeke, L., et al. 2015, MNRAS, 449, 1352
Dark Energy Survey Collaboration 2005, ArXiv e-prints [arXiv:astro-ph/0510346]
Dubois, Y., Devriendt, J., Slyz, A., & Teyssier, R. 2012, MNRAS, 420, 2662
Dubois, Y., Gavazzi, R., Peirani, S., & Silk, J. 2013, MNRAS, 433, 3297
Dubois, Y., Pichon, C., Welker, C., et al. 2014, MNRAS, 444, 1453
Dubois, Y., Peirani, S., Pichon, C., et al. 2016, MNRAS, 463, 3948
Dvornik, A., Cacciato, M., Kuijken, K., et al. 2017, MNRAS, 468, 3251
Fosalba, P., Crocce, M., Gaztañaga, E., & Castander, F. J. 2015a, MNRAS, 448, 2987
Fosalba, P., Gaztañaga, E., Castander, F. J., & Crocce, M. 2015b, MNRAS, 447, 1319
Giocoli, C., Jullo, E., Metcalf, R. B., et al. 2016, MNRAS, 461, 209
Guzik, J., & Seljak, U. 2001, MNRAS, 321, 439
Haardt, F., & Madau, P. 1996, ApJ, 461, 20
Hamana, T., & Mellier, Y. 2001, MNRAS, 327, 169
Hellwing, W. A., Schaller, M., Frenk, C. S., et al. 2016, MNRAS, 461, L11
Hennawi, J. F., & Spergel, D. N. 2005, ApJ, 624, 59
Heymans, C., Van Waerbeke, L., Miller, L., et al. 2012, MNRAS, 427, 146
Hilbert, S., White, S. D. M., Hartlap, J., & Schneider, P. 2007, MNRAS, 382, 121
Hilbert, S., White, S. D. M., Hartlap, J., & Schneider, P. 2008, MNRAS, 386, 1845
Hilbert, S., Hartlap, J., White, S. D. M., & Schneider, P. 2009, A&A, 499, 31
Hildebrandt, H., Viola, M., Heymans, C., et al. 2017, MNRAS, 465, 1454
Hudson, M. J., Gillis, B. R., Coupon, J., et al. 2015, MNRAS, 447, 298
Jain, B., & Seljak, U. 1997, ApJ, 484, 560
Jain, B., & Taylor, A. 2003, Phys. Rev. Lett., 91, 141302
Jain, B., Seljak, U., & White, S. 2000, ApJ, 530, 547
Kaiser, N. 1992, ApJ, 388, 272
Kaviraj, S., Laigle, C., Kimm, T., et al. 2017, MNRAS, 467, 4739
Keeton, C. 2001, ArXiv e-prints [arXiv:astro-ph/0102340]
Kennicutt, Jr., R. C. 1998, ApJ, 498, 541
Kilbinger, M. 2010, A&A, 519, A19
Kilbinger, M. 2015, Rep. Prog. Phys., 78, 086901
Komatsu, E., Smith, K. M., Dunkley, J., et al. 2011, ApJS, 192, 18
Kuijken, K., Heymans, C., Hildebrandt, H., et al. 2015, MNRAS, 454, 3500
Laigle, C., McCracken, H. J., Ilbert, O., et al. 2016, ApJS, 224, 24
Laureijs, R., Gondoin, P., Duvet, L., et al. 2012, Proc. SPIE, 8442, 84420T
Leauthaud, A., Tinker, J., Bundy, K., et al. 2012, ApJ, 744, 159
Leauthaud, A., Saito, S., Hilbert, S., et al. 2017, MNRAS, 467, 3024
Limber, D. N. 1953, ApJ, 117, 134
LSST Science Collaborations (Abell, P. A., et al.) 2009, ArXiv e-prints [arXiv:0912.0201]
Mandelbaum, R., Seljak, U., Kauffmann, G., Hirata, C. M., & Brinkmann, J. 2006, MNRAS, 368, 715

Mandelbaum, R., Slosar, A., Baldauf, T., et al. 2013, MNRAS, 432, 1544
Mead, A. J., Peacock, J. A., Heymans, C., Joudaki, S., & Heavens, A. F. 2015, MNRAS, 454, 1958
Ménard, B., & Bartelmann, M. 2002, A&A, 386, 784
Metcalf, R. B., & Petkova, M. 2014, MNRAS, 445, 1942
Miralda-Escudé, J. 1991, ApJ, 380, 1
Miyazaki, S., Komiyama, Y., Nakaya, H., et al. 2012, in Ground-based and Airborne Instrumentation for Astronomy IV, Proc. SPIE, 8446, 84460Z
Moessner, R., & Jain, B. 1998, MNRAS, 294, L18
Moessner, R., Jain, B., & Villumsen, J. V. 1998, MNRAS, 294, 291
Newman, A. B., Treu, T., Ellis, R. S., & Sand, D. J. 2013, ApJ, 765, 25
Newman, A. B., Ellis, R. S., & Treu, T. 2015, ApJ, 814, 26
Peirani, S., Dubois, Y., Volonteri, M., et al. 2017, MNRAS, 472, 2153
Peirani, S., Sonnenfeld, A., Gavazzi, R., et al. 2019, MNRAS, 483, 4615
Petkova, M., Metcalf, R. B., & Giocoli, C. 2014, MNRAS, 445, 1954
Pichon, C., Thiébaut, E., Prunet, S., et al. 2010, MNRAS, 401, 705
Pillepich, A., Springel, V., Nelson, D., et al. 2018, MNRAS, 473, 4077
Planck Collaboration VIII. 2018, A&A, submitted [arXiv:1807.06210]
Potter, D., Stadel, J., & Teyssier, R. 2017, Comput. Astrophys. Cosmol., 4, 2
Power, C., Navarro, J. F., Jenkins, A., et al. 2003, MNRAS, 338, 14
Rabold, M., & Teyssier, R. 2017, MNRAS, 467, 3188
Rasera, Y., Alimi, J. M., Courtin, J., et al. 2010, in AIP Conf. Ser., eds. J. M. Alimi, & A. Fuözfa, 1241, 1134
Salpeter, E. E. 1955, ApJ, 121, 161
Sato, M., Hamana, T., Takahashi, R., et al. 2009, ApJ, 701, 945
Schäfer, B. M., Heisenberg, L., Kalovidouris, A. F., & Bacon, D. J. 2012, MNRAS, 420, 455
Schaye, J., Crain, R. A., Bower, R. G., et al. 2015, MNRAS, 446, 521
Schneider, A., & Teyssier, R. 2015, JCAP, 12, 049
Schneider, P., Ehlers, J., & Falco, E. E. 1992, Gravitational Lenses (Berlin Heidelberg New York: Springer-Verlag)
Schneider, A., Teyssier, R., Potter, D., et al. 2016, JCAP, 4, 047
Scranton, R., Menard, B., Richards, G. T., et al. 2005, ApJ, 633, 589
Semboloni, E., Hoekstra, H., Schaye, J., van Daalen, M. P., & McCarthy, I. G. 2011, MNRAS, 417, 2020
Semboloni, E., Hoekstra, H., & Schaye, J. 2013, MNRAS, 434, 148
Sonnenfeld, A., Treu, T., Gavazzi, R., et al. 2013, ApJ, 777, 98
Sonnenfeld, A., Leauthaud, A., Auger, M. W., et al. 2018, MNRAS, 481, 164
Spergel, D., Gehrels, N., Baltay, C., et al. 2015, ArXiv e-prints [arXiv:1503.03757]
Springel, V., & Hernquist, L. 2003, MNRAS, 339, 289
Springel, V., Frenk, C. S., & White, S. D. M. 2006, Nature, 440, 1137
Springel, V., Pakmor, R., Pillepich, A., et al. 2018, MNRAS, 475, 676
Sutherland, R. S., & Dopita, M. A. 1993, ApJS, 88, 253
Takahashi, R., Hamana, T., Shirasaki, M., et al. 2017, ApJ, 850, 24
Tenneti, A., Mandelbaum, R., Di Matteo, T., Kiessling, A., & Khandai, N. 2015, MNRAS, 453, 469
Teyssier, R. 2002, A&A, 385, 337
Teyssier, R., Pires, S., Prunet, S., et al. 2009, A&A, 497, 335
Treu, T. 2010, ARA&A, 48, 87
Vale, C., & White, M. 2003, ApJ, 592, 699
van Daalen, M. P., Schaye, J., Booth, C. M., & Dalla Vecchia, C. 2011, MNRAS, 415, 3649
Velander, M., van Uitert, E., Hoekstra, H., et al. 2014, MNRAS, 437, 2111
Velliscig, M., Cacciato, M., Hoekstra, H., et al. 2017, MNRAS, 471, 2856
Vogelsberger, M., Genel, S., Springel, V., et al. 2014, Nature, 509, 177
Volonteri, M., Dubois, Y., Pichon, C., & Devriendt, J. 2016, MNRAS, 460, 2979
White, M. 2005, Astropart. Phys., 23, 349
Yang, X., Kratochvil, J. M., Huffenberger, K., Haiman, Z., & May, M. 2013, Phys. Rev. D, 87, 023511
Ziour, R., & Hui, L. 2008, Phys. Rev. D, 78, 123517

4.2 Production of lensed mock images

In order to produce mock observational images for lensing analysis, we have to model the light emission of all star particles along the light-cone, to stack them and put them on a regular grid, to lens them and finally to add observational PSF and noise. In complement of the creation of the deflection maps described above, this requires computing the corresponding number of 2D-luminosity maps. This computation is described below. The realisation of 2D-luminosity maps is done with my collaborator Clotilde Laigle.

4.2.1 Modelling light emission from star particles

In the simulation, each star particle (with a mass of $\sim 3 \times 10.^6 \mathrm{M}_\odot$) is assumed to behave like a single stellar population (SSP), i.e. a population of stars born at the same time from the same gas cloud. The light emitted by a given SSP depends essentially on the initial mass function (IMF) of the stellar population, its current mass, age and metallicity, and on the chosen stellar evolution model and stellar template library. Different weights given to specific phases of stellar evolution (for example the AGB, post-AGB or Wolf-Rayet stars), but also different stellar feedback and supernova models can lead to dramatically different SSP spectra.

In this work, in order to model the light emitted by Horizon-AGN stellar particles, we use the BC03 single stellar population templates from Bruzual & Charlot (2003), with a Chabrier IMF (Chabrier 2003). In brief, we want that each particle is attached a BC03 SSP, which matches the particle in terms of age and metallicity. However, because of the different metallicity and age sampling in either Horizon-AGN or the BC03 model, BC03 SSPs are logarithmically interpolated to reproduce the desired Horizon-AGN values.

The BC03 SSP is also rescaled to match the initial stellar mass of the particle, and stellar mass losses are then treated according to the BC03 model instead of the stellar evolution model implemented in Horizon-AGN, since they are slightly different. This step is important for the purpose of treating mocks as real observed images. In fact, if the initial mass of the SSP is not rescaled, systematic offsets will occur in the photometry, and the galaxy masses estimated through SED-fitting from the simulated photometry will also be systematically offset from the intrinsic masses (defined as the sum of the stellar particle masses).

In addition it should be noted that the choice of the IMF is not insignificant, as it controls both the stellar mass loss prescription and the overall mass-to-light ratio (magnitudes beeing ~ 0.4 dex fainter with a Salpeter (Salpeter 1955) IMF compared to a Chabrier one). Although stellar mass loss prescriptions are implemented using a Salpeter IMF in Horizon-AGN, the Chabrier IMF is preferred here for the photometry computation because it brings the simulated galaxy counts in much better agreement with observed galaxy counts.

Re-normalisation of the metallicity As discussed in Kaviraj et al. (2017), the relatively low resolution reached in Horizon-AGN implies a delayed enrichment of star-forming clouds, which induces an underestimation of the gas phase metallicity compared to observations. To correct for this underestimation, a redshift-dependent boosting factor (varying from 4 at $z \sim 0$ to 2.4 at $z \sim 3$) has been computed in order to brings the simulated mass-gas phase metallicity relation with observations from Mannucci et al. (2010) at $z = 0$, 0.7, 2.5 and Maiolino et al. (2008) at $z = 3.5$. This factor is redshift dependent: $Z = Z_{\mathrm{old}} + 4.08430 - 0.213574z - 0.111197z^2$.

Dust extinction and IGM absoprtion At this stage, dust extinction could be added as a screen in front of each particle. Although dust extinction has been successfully implemented when

computing the total photometry around individual galaxies (see e.g. Kaviraj et al. 2017), it is much more computationally heavy to implement at the creation stage of the full cone 2D-luminosity maps. As a matter of fact, computing dust extinction requires to compute the dust column density from of each star particle, while taking the gas mass metallicity distribution as a proxy for the dust distribution. When working with individual galaxies, it is enough, for each particle, to compute the dust column density over the galaxy virial radius. When producing full-cone image, a variable length (scaling with the galaxy virial radius the particle is attached to) should be used to compute the dust column density. Although this is easy to implement, it requires changing the current structure of the mock creation code, which is still an-going project. Therefore in the following only the dust-free 2D-luminosity maps are presented.

Beyond the attenuation by dust within the interstellar-medium, galaxy luminosities are impacted by absorption along the line-of-sight due to intervening gas clouds in the intergalactic-medium (IGM), mainly through the Lyman-α forest. Consistently implementing IGM absorption is doable in the Horizon-AGN lightcone, since the distribution of gas in the foreground of each star particle is known all the way to $z \sim 0$. Attenuation by the IGM is not negligible at high redshift. The mean transmitted flux in the Lyman-α forest evolves from 0.83 to 0.71 between redshift 2 and 3, and will impact the rest-frame UV band blue-ward to the Lyman-α wavelength. For instance, at $z \sim 3$, magnitudes in the apparent B-band are on average 0.3 dex fainter with IGM absorption. However, IGM absorption is still much less important than dust extinction. This will be implemented in the mock images in the future .

4.2.2 Mock image production

From stellar particles to pixels We then perform the mapping between the stellar particle distribution and the cartesian grid of the 2D-luminosity maps. The lightcone is sliced in the same number of parallel transverse planes as done for the deflection maps computation, i.e in 500 slices (of varying comoving thickness), all the way to $z \sim 6$, with an angular resolution of 0.1arcsec. Therefore 500 2D-luminosity maps are produced, which will be deflected and magnified in a second step described below.
In order to map star particles to the 2D cartesian grid, the most straightforward way to proceed is to use a cloud-in-cell interpolation. However this leads to considerable shot noise at low redshift in the weakly populated outskirts of galaxies, when the angular resolution of the luminosity maps is better than the physical resolution of the AMR grid. The resulting image is unrealistic, and the lensing signal strongly polluted. To overcome this issue, each star particle is spread with a normal distribution over a sphere around its initial position, the radius of which being calibrated on the local gas density. By summing in this way the SED of all the SSPs falling in a pixel (the SSPs being weighted by the weight of the star particle in the cell), we finally get a SED for each pixel of the 500 2D-luminosity maps, ranging from 91 to 16×10^5Å, with a resolution of 3 Å from 3200 Å to 9500 Å, and a lower resolution outside this range. The SED is then shifted according to its redshift and converted to get apparent flux unit. Eventually, the photometric images are obtained by convolving the SED with some chosen filter passbands. In order to make predictions for various current and future surveys, we choose optical (u, r, z) filters from SDSS, NIR filters from Euclid and UltraVista, and the broad band optical filter from Euclid (riz). It is obviously easy to produce images in the photometric baseline of any desired survey. For illustration, a mock composite image of the Horizon-AGN lightcone, realised by Clotilde Laigle is displayed in figure 4.2.

Distortion of images The lensing deflection field is then applied to the 500 2D surface brightness maps in order to distort then. For each such source plane, the corresponding deflection, integrating all the mass contribution between the observer and that plane is used. For instance,

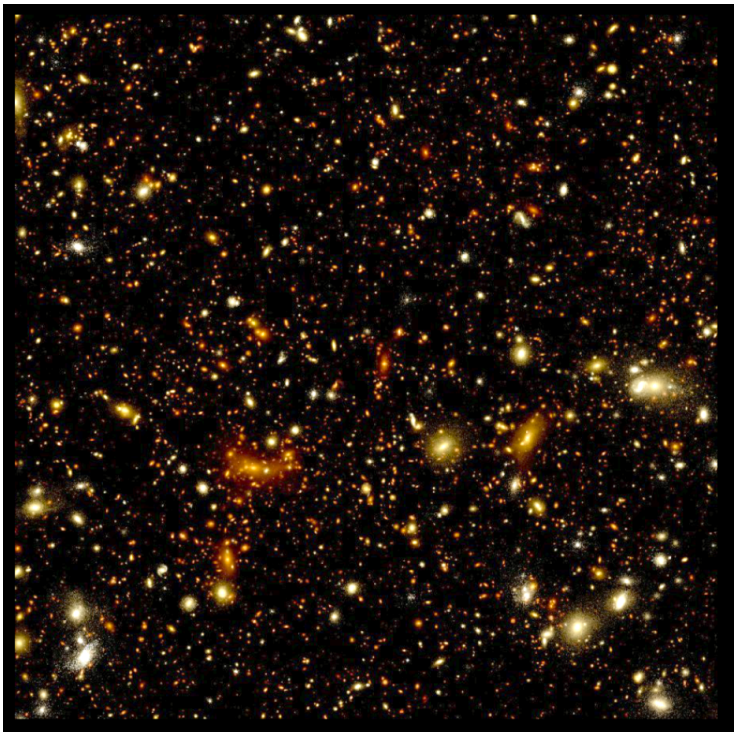

Figure 4.2 – A 14 arcmin^2 simulated composite image from the Horizon-AGN lightcone, in the u, r and z filters. The resolution is 0.15"/pixel and the image is computed using star particles in the redshift range $0.1 < z < 5.8$. Credit to Clotilde Laigle, and published in Kaviraj et al. (2017).

the 30th luminosity map is deflected by the lensing signal computed for 29 $\alpha(\theta)$ previous deflection planes.

Since deflection moves light rays away from the original image plane pixel grid, one has to perform a interpolation of intensity values of source plane pixel values around the source plane position. The luminosity in source planes $I_s(\vec{\beta})$ is transposed to the image positions $\vec{\theta}$ by using the conservation of surface brightness:

$$I(\vec{\theta}) = I_s(\vec{\beta}) = I_s(\vec{\theta} - \vec{\alpha}(\vec{\theta}))\,. \tag{4.1}$$

This requires an bi-linear interpolation $\vec{\beta} \rightarrow \vec{\theta} - \vec{\alpha}(\vec{\theta})$, for each pixel. Since the gravitational lensing effect is achromatic, the interpolation is identical for all the possible filters we considered to derive source plane intensity maps.

By doing so, the full lens equation is solved and, therefore, all the regimes of distortions are incorporated, which means that strong lensing as well as weak lensing are taken into account.

This can be seen in Figure 4.4, where faint background sources are not only sheared but also curved (so-called flexion regime), occasionally leading to arcs or ring-like features.

Towards realistic mock lensed observations Figure 4.3 presents a composite lensed image of 1 square degree of the Horizon-AGN lightcone in the apparent band u, r and z, and with a resolution of 0.1 arcsec. The right panel shows the corresponding lensing convergence map for a fiducial source plane at $z_s = 1.5$.

Although these images already appear to resemble observed images, the pipeline is still missing some ingredients in order to produce fully realistic mock images. Observed images are indeed intrinsically limited by the point spread function (PSF), which depends both on the atmospheric conditions and the instrument, and can vary as a function of wavelength but also spatially over a field from tile-to-tile. In order to consistently implement all the uncertainties arising in the observations, our mock images need to be convolved by the PSF corresponding to the instrument from which they are miming the observations.

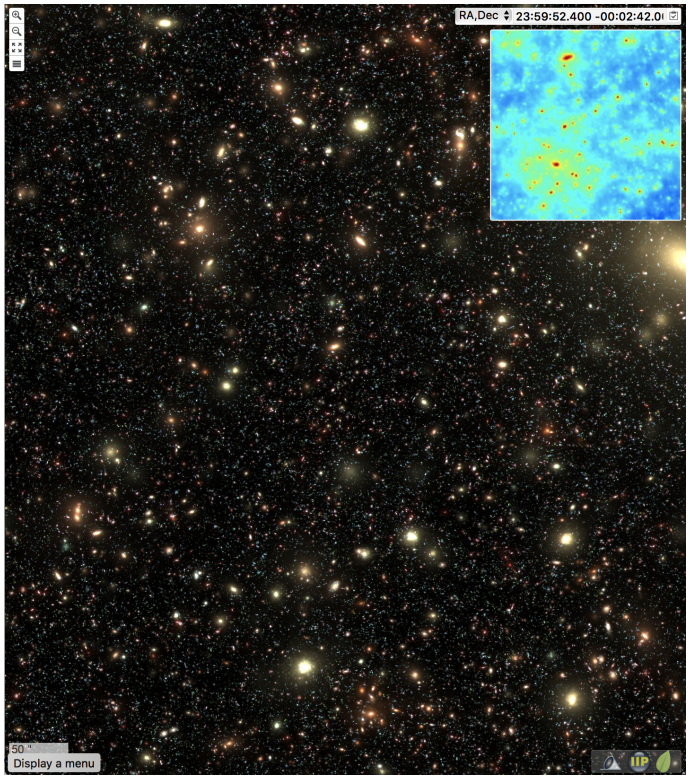

Figure 4.3 – Simulated distorted image at large scales and the corresponding zoom in the convergence map in the top right window. This image is 36000×36000 pixels in size.

Observations are also inevitably surface-brightness limited and noise diluted, and so should our mock images. Noise can be modelled in a first approach as gaussian/poissonian noise, and the flux value of each pixel can be replaced by a random value taken from a Gaussian distribution with the mean being the intrinsic flux and of a given σ. In addition, we will add in the image the emission by point sources objects, in particular nearby stars which easily saturate and pollute the photometry of close-by objects.

4.2.3 Summary and perspectives

I have produced mock lensed images from a simulated light-cone, reproducing a realistic diversity of galaxies in terms of morphology and photometry, but also in terms of spatial distribution and lensing. Theses aspects are extremely important in order to conduct end-to-end comparison of galaxy properties and distribution in the simulations with the same quantities in observations. This work is therefore pivotal for current and upcoming surveys relying on lensing analysis for constraining the cosmology. It will also be useful for all surveys focused on galaxy formation and evolution which rely on galaxy photometry to derive their physical properties, and for which lensing is either a pollution or on alternatively a tool to detect the first galaxies in the Universe (which would remain unseen if they would not be magnified).
The extensions of this work, which are still on-going and will presented in future publications, include:

Quantifying the contribution of intrinsic alignments to lensing and the contamination of the signal by observational limitations The first natural outcome of our work will be to test the purity of the extracted lensing signal in the context of current and upcoming surveys, i.e.

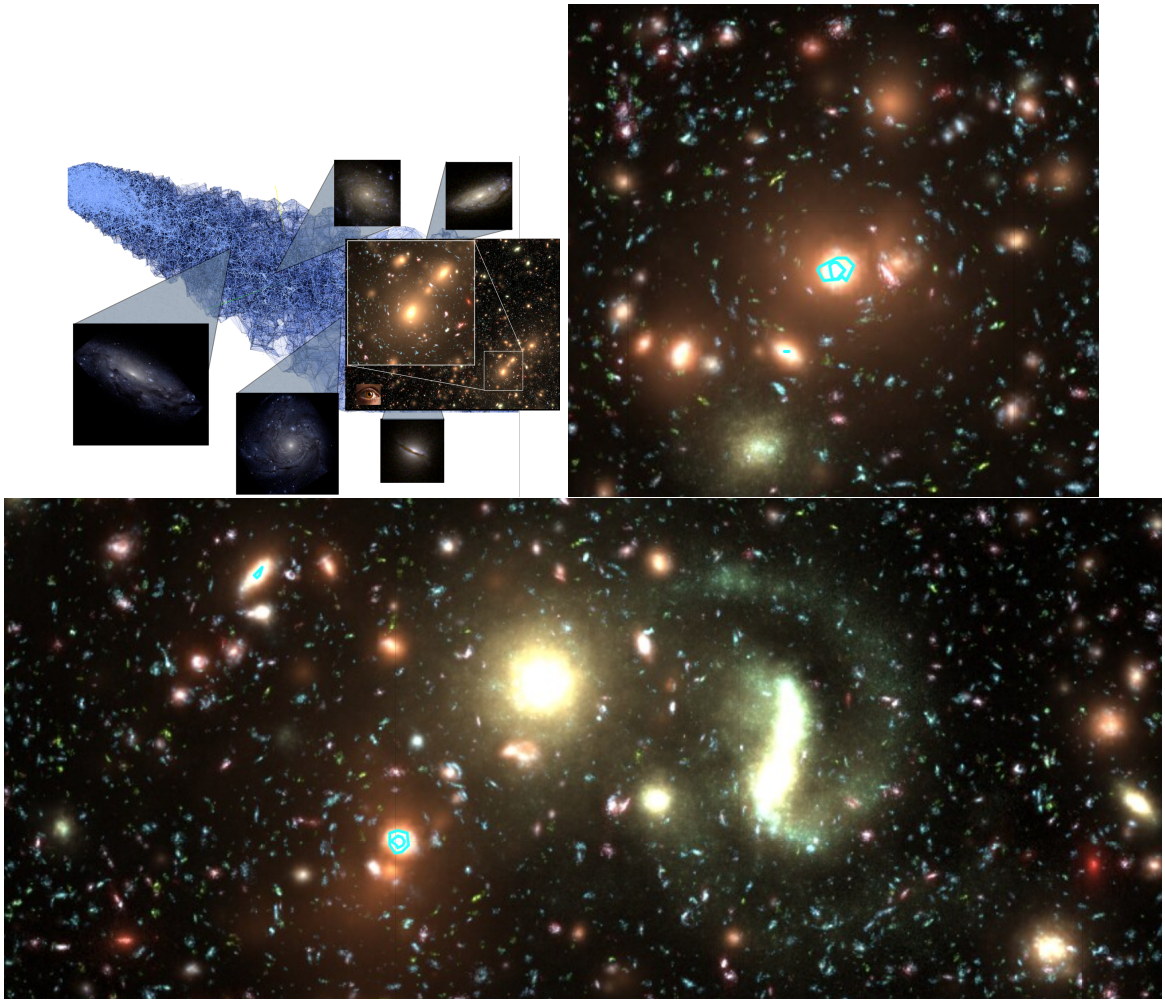

Figure 4.4 – Example of simulated distorted images from the Horizon-AGN light-cone in observational bands r,u,g, zoomed around the massive objects of the light-cone. The resolution is 0.1 arc-second/pixel. The critical lines for two redshift sources are overlapped: in light-blue $z_s = 1.2$ and in dark-blue $z_s = 3.5$.

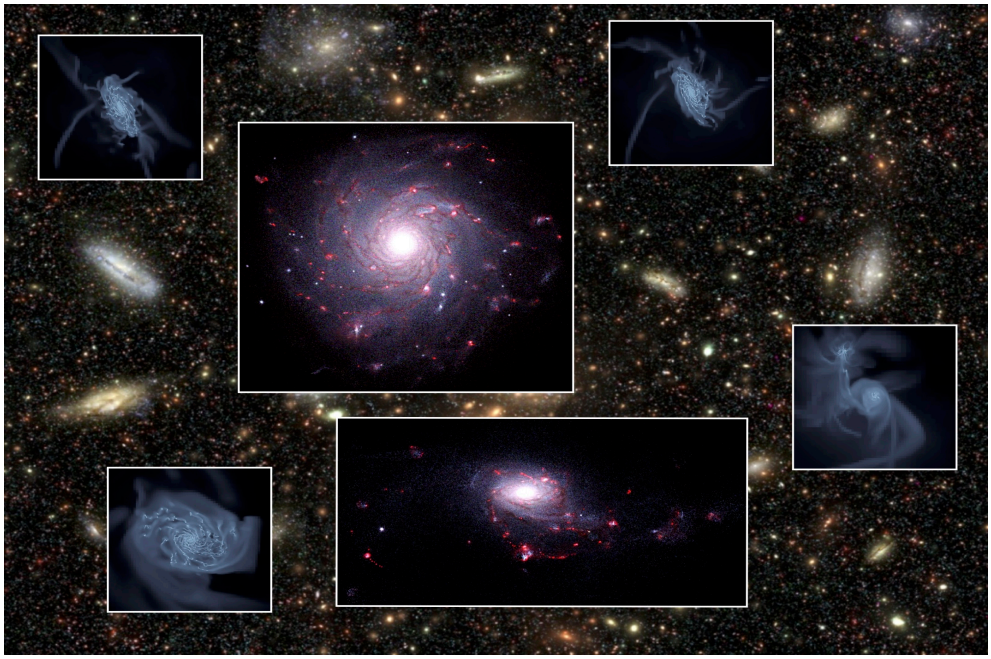

Figure 4.5 – Mock galaxies produced by the New-Horizon simulation, painted in the large framework of Horizon-AGN mock images.

how well the galaxy-galaxy lensing signal can be recovered from observed images. In particular, I will test the impact of the PSF, noise and blending in measuring the shear and magnification of galaxies. In addition, because the intrinsic alignment of galaxies is consistently reproduced in the Horizon-AGN lightcone, we will also be able to measure the contamination to the lensing signal in realistic conditions, as a follow up of previous works based on the Horizon-AGN shapshots (Codis et al. 2015a; Chisari et al. 2016). This work will naturally form part of the current collaborative effort of the Euclid consortium, in order to make optimal use of the upcoming wealth of all-sky photometric data.

Measuring the impact of lensing distortion, displacement and magnification on galaxy morphologies, mass function and clustering While quantifying the contamination of intrinsic alignment to the lensing signal is of prime importance for cosmology, the inverse operation, i.e. quantifying the contamination of lensing to the measurement of galaxy intrinsic alignment is also very relevant for galaxy formation. As a matter of fact, numerous works (e.g. Dubois et al. 2014; Lee et al. 2018; Ganeshaiah Veena et al. 2018) have investigated the process of galaxy alignment with the cosmic web in order to understand galaxy angular momentum acquisition and in turn the origin of the Hubble sequence. In short, large-scale matter flows crossing from walls generate multipolar high-vorticity quadrants in filaments (Laigle et al. 2015). Structure (haloes and galaxies) which are forming in these flows will end up with an angular momentum aligned with that vorticity and consequently with the filament. They will accrete matter through secondary infall with a coherent rotational motion, up to a specific transition mass, beyond which inflow will start to advect misaligned angular momentum. Subsequent mergers along the filaments lead to galaxy spin-flip ,and the most massive structures end up azimuthally aligned (and see also Welker et al. 2014; Codis et al. 2015b). Finally, satellites caught by massive halos settle into a plane around their central galaxy (Welker et al. 2018).
Observationally, measuring galaxy alignment with the cosmic web is difficult, in particular because estimating galaxy spin orientation remains a challenge, though some attempts have proven to be

successful at low redshift (especially in the SDSS Tempel et al. 2013; Zhang et al. 2013; Chen et al. 2018). At higher redshift and in the absence of high-resolution spectroscopy or IFU observations, one needs to rely on the two-dimensional shapes of the galaxies as a proxy for their orientations. Obviously in this case, the spin measurement will be polluted by rotation and shearing from lensing. In this project, we will measure galaxy shape and orientation both in the mock lensed and unlensed images. This will directly allow us to quantify how much the lensing signal contaminates galaxy shape and orientation measurements. Estimating the systematics it creates will help us to sharpen the intrinsic alignment signal measured in photometric surveys, and will be a determining step for the study of galaxy angular momentum acquisition in the Universe.

Beyond shearing and rotating galaxies, lensing cause displacements and magnification. For example, at $z \sim 1$, galaxies can be coherently displaced of the order of the arcminute (e.g. Chang & Jain 2014). A follow-up of the project will therefore to estimate how magnification biases 1-point statistics and displacement biases 2-point statistics. These biases are generally not taken into account in galaxy evolution studies relying either on the mass function (e.g. Davidzon et al. 2017) or on angular clustering measurements (Hatfield et al. 2016) to follow galaxy population evolution across cosmic time and to connect galaxies to their dark halos. In the era of upcoming large-field photometric surveys such that LSST and Euclid, taken these effects into account will be crucial to improve our current constraints on galaxy evolution.

Testing our ability to observe high-z galaxies through gravitational lensing Massive clusters can play the role of natural gravitational telescopes and can reveal, through magnification, background galaxies at very high redshift which would otherwise remain too faint to be detected (see e.g. GLASS Treu et al. 2015, amongst others), pushing the instruments to their faintest limits and reaching luminosities of at least 2 or 3 order of magnitudes beyond the normal limit. However, once detected, estimating the right magnification, a crucial step in order to accurately determine the galaxy mass, is very hard. In addition, correcting from the distortion in the case of strong lensing remains a challenge. in order to properly use gravitational lensing to perform a deep study of the high-redshift Universe, making accurate forecasts and estimating systematic uncertainties is in order.
In this project, we will combine the ray-tracing procedure that we have developped on the Horizon-AGN lightcone with current state-of-the art very high-resolution simulations of star-forming galaxies at $z = 6$ and above (Rosdahl et al. 2018, Katz et al. in prep). Mock images of these high-z simulated galaxies will be placed in background of the Horizon-AGN lightcone with various orientations and at various random positions, with clustering properties corresponding to the one expected for this population. In a second time, the images will be distorted and magnified as described above, and convolve with the PSF of current (e.g. HST) and future facilities (e.g. JWST Zackrisson 2011). The photometry of these high-z galaxies will then be extracted and analysed in the exact same way as done in observations, and possibly testing how well different code perform to extract the photometry and compute the physical properties of the galaxies. Taking advantage of the realistic clustering of galaxies in the lightcone, we will also be able to test the impact of blending on extracting the photometry. This work will be a crucial step in preparation and exploitation of upcoming missions. Indeed, our work will help to choose the ideal targets in current NIR facilities which could be followed up with ELT spectrocopy (e.g. with MOSAIC) or JWST, in order to optimize the detection and study of high-z candidates. In turn, it should help answering long-standing key questions about the time and modality of the reionisation of the Universe.

Lensing of the lyman-α forest The Horizon-AGN lightcone does not only allow to create mock photometric images, but also mocks of the lyman-α forest. Lyman-α forest observations are

precious to map the distribution of neutral Hydrogen in the Universe. It is now routinely used to test cosmology, but it is also a promising tool to map the cosmic web at high redhsift (e.g. Pichon et al. 2001; Lee et al. 2014, Laigle et al. in prep) with future facilities such that PFS (Takada et al. 2014) and MOSAIC on the ELT (Evans et al. 2012). Its power lies in particular in the fact that, instead of galaxies, it allows to sample uniformly high and low density regions of the matter field. Naturally, gravitational lensing deflects the position of emitting background galaxies and quasars, the spectra of which is used to trace the lyman-α forest. Each absorption feature in the Lyman-α forest corresponds to an overdensity at a precisely known redshift, and can be considered as a source for gravitational lensing. Gravitational lensing will therefore distort the image of the IGM. Should the Lyman-α forest signal-to-noise ratio allow to measure this distortion, lensing from the lyman-α forest could be use to constrain Cosmology. In particular, it has the advantage to involve a three-dimensional source field (compared to CMB lensing) and does not require galaxy shape measurement. Furthermore, it will allow us to probe matter distribution at a higher redshift than the one accessible from galaxy shear. As postulated by Croft et al. (2018), it can therefore become a complementary cosmological probe.

Chapter 5

Conclusion

5.1 Context

In the introduction and the first chapter of this thesis dissertation, we have seen that cosmology is more than ever confronted to the challenges of understanding the nature of Dark Matter and Dark Energy. Both the accelerated expansion of the Universe and the growth of the large scale cosmological structure at all scales must be characterised in detail. This is a prerequisite in order to make progress on the (possibly time varying) equation of state of DE, to better constrain the mass of neutrinos or the amount of Warm Dark Matter, if any, or even to test modifications of General Relativity.

The recent completion of the Planck mission has almost entirely starved the information content on the early stages of the Universe one can extract from the cosmic microwave background[1]. More emphasis is now being put on the thorough description of the matter distribution at later cosmic time, and on smaller scales, since it entails a wealth of statistical power to refine the cosmological model. This has motivated enormous observational efforts in the form of ongoing or upcoming wide field imaging and spectroscopic surveys like DES, DESI and soon Euclid, LSST or SKA.

These investigations require accurate theoretical predictions which are particularly difficult to obtain on small and intermediate scales due to the strong non-linearities imposed by the gravitational instability together with baryonic physics. In chapter 1, I explained why simulations are essential to correctly describe matter clustering in the concordance ΛCDM model in the highly non-linear regime. They bridge theories and observations, and are thus extensively used to refine expected cosmological observables. On large scales, the global behaviour of the large scale structure, the so-called cosmic web, is well reproduced in simulations. For collapsed systems such as clusters and galaxies, however, we have seen that our understanding remains incomplete, because these are governed by both the uncertain behaviour of dark matter on small scales and the complex dissipative physics of baryons, which is strongly impacted by mostly unknown stellar and AGN feedback. This results in discrepancies between models and observations: uncertainties in the dark matter halo properties (density profile, morphology, substructure) and galaxy population (evolution over cosmic time, luminosity distribution, environmental dependence) etc. Such issues are open and under rigorous study in the community: the relation between halo and host galaxies, possible self-interaction of dark matter, the feedback of the baryonic physics on the underlying matter distribution etc... are all fertile fields of research at the time of writing.

In this framework, high-resolution hydrodynamical cosmological simulations are one of many recent undertakings which aim to improve our understanding of the complex interplay between

[1] Constraining the amount of tensor modes generated during inflation remains a key goal, which only CMB polarisation experiments will be able to tackle

dark and luminous matter, and to provide a realistic picture of the Universe down to galactic scales. Such high performance simulations allow for the modelisation of the effect of complex processes while accounting for non-linear scale coupling, and to decide quantitatively which non-linear process dominates when and how. In addition, they permit to produce (large) virtual surveys so as to build and validate effective estimators and model biases.

Over the last decades, gravitational lensing has emerged as a unique tool in cosmology because of its ability to relate the total gravitational potential with the more directly accessible but difficult to predict distribution of galaxies. Lensing provides us with a way to quantify the total matter distribution, and to explore the connection between galaxies and total matter on a broad range of scales: from the linear galaxy bias at large scales, to the characterisation of dark matter in the core of clusters, galaxies and the substructures (or satellites) therein.

Notably, recent cosmic shear measurements like KiDS and DES have demonstrated the power of the joint analysis of galaxy shapes and positions (the so-called 3 times two-point correlation functions) to break well-known degeneracies with nuisance parameters and constrain simultaneous galaxy biasing, intrinsic alignments and cosmology (DES Collaboration et al. 2017; van Uitert et al. 2018). In addition, lensing can potentially shed light on possible modifications of General Relativity by testing the validity of the Poisson equation on cosmological scales.

However, reaching these goals requires to properly model lensing observables, which is all the more challenging as lensing is very sensitive to small scales where non-linearities and gastrophysics (in particular feedback processes) make any analytical modelling very difficult and challenging. Here again, numerical simulations provide us with an incredible tool to understand better this non-linear regime of structure formation. In particular, they represent an excellent testbed for the theoretical models used in cosmological inference pipelines which can be refined and improved thanks to the comparison with these numerical experiments. For instance, it is quite standard to try and increase the regime of validity of analytical techniques (such as perturbation theory) down to smaller scales by adding new free parameters (Carrasco et al. 2012). However, the number of free parameters rapidly explodes making any practical implementation useless. In this context, simulations can be used to find which of these parameters are the most relevant and find sometimes relations between them, therefore reducing the number of degree of freedom left in the analysis. Similarly, one can use numerical simulations to try and define the optimal strategy to model effectively the impact of baryons on lensing observables.

For these reasons, my thesis focused on the construction of lensing observables from numerical simulations with, in mind, the ultimate goal of reaching the percent accuracy up to $k \sim 10h/\mathrm{Mpc}$ that is needed for the Euclid mission (Laureijs et al. 2011). The Euclid consortium, that I joined in the course of my PhD, is actively working on large dark matter only N-Body simulations to improve our understanding of the imprint of non-linear matter evolution on cosmic shear signal on scales greater than a few Mpc. Here, reaching the required precision is already challenging and an effort is currently being made to assess the convergence of ray tracing techniques. Among other things, the dark matter simulations produced by the consortium are used to estimate the complex covariance matrices entangling lensing, galaxy clustering observables, and the biasing of halos with respect to the total matter distribution; in different cosmologies, and possibly, with modifications of gravity.

In this context however, the limited computing power available does not allow us to produce neither end-to-end nor even DM only Euclid mocks. Indeed, the number of required simulations is far beyond our current capabilities given the large volume of parameter space (we want to vary cosmological parameters within LCDM and beyond) and the large number of realisations needed to estimate covariance matrices with sufficient accuracy. The use of faster approximate

methods in this case is currently tested (Lippich et al. 2018; Blot et al. 2018; Colavincenzo et al. 2018). Of course, parallel analytical effort is being conducted on those relatively large scales (Standard perturbation theory, effective field theory, response approach...). Inspired by simulations, theoretical models are now trying to also include the effect of baryons on e.g the matter power spectrum (Schneider & Teyssier 2015) which is a key ingredient for cosmic shear predictions. There is no doubt that an hybrid approach between analytical modelling and numerical simulations will be the optimal way of analysing the data.

5.2 Summary and immediate objectives

My thesis work is complementary to this ongoing effort as it focuses on smaller deeply non-linear scales where baryonic physics starts playing a significant role. It will allow the community to estimate the cutoff in k below which semi analytic post processing of dark matter simulations should not be trusted. Accurately predicting the weak lensing signal below cluster scales requires hydrodynamical cosmological simulations. Indeed, even if the impact of baryonic processes on lensing signal was early acknowledged (Semboloni et al. 2011), its quantification remains uncertain. Only recently, the first "full physics" cosmological hydrodynamical simulations have been run and allow for the first time to directly predict the level of impact of baryons on cosmological observables (clustering and lensing). I therefore undertook a minute propagation of light rays through the past lightcone of the Horizon-AGN hydrodynamical cosmological simulation, which had been obtained by my colleagues at IAP, my host institute. The derivation of lensing observables and the exploitation of these results for a number of direct applications was at the core of this thesis work. This constitutes the material of Chapter 4. This intensive numerical study required substantial investment in parallel programming for the post-treatment of several terabytes of simulation outputs, on a distributed cluster of computers at IAP, which can be summarised as high-performance computing.

In order to acquire those skills and develop my own tools, I started by a project involving the extraction of numerical data around galaxies clusters on a pure N-body simulation. Chapter 3 presented this work, which focused on the use of statistical methods for cosmic web analysis at cluster scales. Characterising the connection between clusters and the surrounding large filamentary structures is a promising way to probe the underlying cosmology and to improve our understanding of structure formation history and cluster evolution. I thus projected particles around clusters to derive lensing observables, such as convergence and the more direct shear signal and used an harmonic decomposition of the 2D matter distribution to investigate the signature of filaments at the outskirts of clusters. I developed a new statistical tool to suitably stack the low amplitude aperture multipolar moments of this particular weak lensing signal. In practice, I found that the stacking of the power spectra of these moments for a large number of clusters provides us with a good method to measure the connectivity of clusters without relying on visible tracers like galaxies or gas. I also quantified the prospects of measuring this signal in the Euclid data with a careful analysis of all possible sources of noise and given the expected number of clusters to be uncovered in the Euclid survey. This work was the subject of my first publication in Astronomy and Astrophysics (Gouin et al. 2017), reproduced in Chapter 3. An interpretation of the origin of these moments is present in this paper and I also participated to a more theoretical investigation of the connectivity of convergence peaks (ie clusters), which is further explored in a companion paper (Codis et al. 2017) led by S Codis. This paper is also reproduced in Appendix B.
I intend to extend this statistical tool to other observables like the distribution of galaxies around clusters, the Sunyaev-Zeld'ovitch effect or the X-rays emission for which I expect a greater

signal-to-noise ratio than the weak lensing signal. This will give insights on the relative bias of galaxies and hot and warm gas inside filaments.

Equipped with those numerical tools, I went one step further in technicality by exploiting the lightcone of the Horizon-AGN simulation, as presented in Chapter 4. Compared to previous work, the propagation of light rays through such a simulation involved developing more complex tools to slice the volume in multiple lens planes, perform the propagation of rays, deal with more sophisticated numerical data for different physical components. All those developments are gathered in Section 2.3 and in an paper that has just been submitted to Astronomy & Astrophysics, reproduced in Chapter 4. Arguably, the main technical novelty resides in the use of the gravitational acceleration to infer the lensing deflection. The robustness of this ray-tracing technics was assessed with a comparison with more commonly used methods. For the first time, a state-of-the-art hydrodynamical simulation was used to build those lensing observables over a large field-of-view and with exquisite angular resolution able to resolve the internal structure of galaxies.

A first application of the deflection and convergence maps I derived from the simulated Horizon-AGN field is presented in the submitted article. It quantifies the impact of baryons on cosmic shear two-point statistics which is of paramount importance for Euclid. On scales smaller than a few arcminutes, baryons suppress correlation at the 10% level. The exact amplitude of the effect may depend somewhat on the details of the sub-grid physic but this will undoubtedly bias a cosmological analysis that would neglect baryons. It is thus very likely that a survey like Euclid will restrict the cosmic shear analysis to larger scales. However, this small scale information, which will be available at high signal-to-noise, can be used for other purposes like the relation between galaxies and their host dark matter halo to understand galaxy bias. This can be done with the Galaxy-Galaxy lensing signal that we also analysed in the submitted paper. At this stage, Horizon-AGN may still be too small to make relevant predictions for Euclid but we checked that this simulation produces the right galaxies in the right halos by comparing our shear profiles around massive galaxies with recent Galaxy-Galaxy lensing observations.

The mentioned results only scratch the surface of possible extensions of my work to other scientific lensing applications of the lensing signal in the Horizon-AGN lightcone. Indeed, the second section of the Chapter 4 presents the production of mock observations that are distorted by the lensing deflection field I obtained in Horizon-AGN as a second extension. The light cone of this simulation contains galaxies in which the emission of stellar particles have been calculated by my collaborators. I distorted those images and, after adding realistic observational defects (noise, convolution by a Point-Spread Function...), I should soon be in a position to apply all the techniques currently used to extract weak and strong lensing from actual multi-band optical or near infrared data. This will prove essential to check for possible biases entering the analysis pipeline, especially on small scales where the impact of the baryons is dominant (shape and ellipticity measurement, extraction and de-blending of sources for accurate photometry and subsequent photometric redshifts...). The different investigations which wait to be explored with the mock lensed (and un-lensed) images are detailed at the end of the chapter 4. This kind of end-to-end approach is also actively being conducted by the Euclid consortium over much larger fields of view for statistical power but without the advantages of an hydrodynamical simulation which provides complex galaxies in specific environments.

5.3 Perspectives

What could be the future developments of my thesis work on a larger time scale? We saw that some of the conclusions still lack statistical power to reach the ultimate accuracy that a mission

like Euclid demands. For instance, our $100h$/Mpc on a side box does not contain any dark matter halo more massive than $3 \times 10^{14}\,\mathrm{M}_{\odot}$ and thus does not allow me to study the impact of baryons on galaxy clusters. Such objects are currently being investigated with zoomed simulations elsewhere. But one may want to simulate larger volumes ($\gtrsim 1\,\mathrm{Gpc}^3$) with a resolution comparable or even better than Horizon-AGN, to better understand lensing and galaxy clustering. This may not be reachable for the coming years, especially as we want to run many such simulations with different cosmologies and different prescriptions for the subgrid physics. For instance, one can expect that changing the small scale properties of dark matter (eg adding a pressure term due to self-interactions, free-streaming, Bose-Einstein condensates, etc) will modify the density profile near the center of galaxies and clusters. However, a modification of subgrid baryonic processes (AGN or supernova feedback) might lead to similar profile modifications...

Such degeneracies should be explored thoroughly in the coming years. Some of them may not require very large volumes, but the spatial or mass resolution in the simulations should definitely be varied. This path has started to be explored by my colleagues responsible of the Horizon-AGN simulation in the form of the New-Horizon and Obelics simulations (20 Mpc zooms into the Horizon-AGN box with 20 pc resolution centred on a quiet region of the box and a cluster resp, see figure 4.5). At this stage, non standard cosmologies are not explored but the validity of subgrid physical recipes can be much more effectively tested with the detailed structure of such re-simulated galaxies (dynamics of disks, bulges, chemical composition, etc). I intend to explore the yet smaller scale lensing signal one can predict with these zoom, especially for galaxy-galaxy lensing and the strong lensing regimes.

As stated, we may have to wait a long time before sufficiently large and resolved hydrodynamical simulations can meet at once all the requirements of the upcoming surveys. In this context, I would like to explore simpler simulations containing accurate predictions for the galaxy-host halo relations. Such small systems could be somehow randomised into larger volumes, where large scale properties can easily be derived (from pure N-body,or generation of halo catalogues in the halo-model formalism...). This could be seen as an extension of existing semi-analytical models. However, "reshuffling" more advanced simulation outputs, may require using modern deep learning techniques that I am keen to explore in the future.

As a final word, I would say that this thesis work allowed me to acquire a broad range of numerical and statistical skills, develop by myself a variety of HPC tools and acquire a substantial knowledge of astronomical data, not directly by analysing current observational data but rather by simulating them while aiming to bring simulations as close as possible to observations. I truly believe that this kind of work is essential to really understand limitating issues in the data or their processing and to make the most of cosmological data sets. I found it extremely simulating as it allows to grasp a wide range of expertise. I intend to push this effort further in the coming years.

Appendix A

Complements to chapter 1

A.1 Additional cosmological definitions

Following the formalism described in section 1.1, some useful variables should be introduced in addition.

A.1.1 Redshift

Because the light rays are progating through an expanding Universe, the relative dilatation of the light's wavelength due to the expansion can be related to the scale factor as:

$$z = \frac{\lambda_{\rm obs} - \lambda_{\rm emit}}{\lambda_{\rm emit}} \qquad 1 + z = \frac{a(t_{\rm obs})}{a(t_{\rm emit})}\,. \tag{A.1}$$

This definition can be described in detail, by considering light rays as following null geodesic in the FLRW metric, *i.e.* $ds = 0$. For small distance, Hubble found a linear relation between the redshift and the distance of galaxies, the so-called Hubble law: such as $c\,z = H_0\,d$. The discovery of the shift of galaxy spectrum as depending of their distance, by Hubble in 1933, has the first evidence of a expanding Universe. Notice that this relation does not take the pecular velocities of galaxies into account, but only the apparent velocity induced by the expansion of the spacetime.

A.1.2 Distances

The notion of distance in cosmology is more complex as we have to consider the expansion and the curvature of the Universe. We can first define physical and comoving distance, as the spatial measure by considering (or not) the expansion respectively, *i.e.* they can be related as:

$$D_{\rm phy} = a(t) D_c\,. \tag{A.2}$$

The comoving distance $D_c = f_K(\omega)$ is a function of the curvature K, as defined by the FLRW metric such as:

$$f_K(\omega) \begin{cases} 1/\sqrt{K}\sin(\sqrt{K}\omega) & K > 0 \\ \omega & K = 0 \\ 1/\sqrt{-K}\sinh(\sqrt{-K}\omega) & K < 0 \end{cases} \tag{A.3}$$

One can also define the angular diameter distance to an object at a redshift z, such that:

$$d_A(z) \propto \int_0^z \frac{dz'}{H(z')}\,. \tag{A.4}$$

A.2 The spherical collapse for an Einstein-de-Sitter Universe

The initial conditions of the spherical density fluctuation R_i, δ_i can be related by:

$$\delta_i + 1 = \frac{3M}{4\pi R_i^3 \rho_0} = \frac{\rho}{\rho_0} \,. \tag{A.5}$$

According to an EdS Universe ($\Omega_m = 1$ and $\Omega_\Lambda = 0$), the solution of the spherical collapse is known, as explained in Peebles (1980). Remembering that in this case $a(t) = (3/2H_0 t)^{2/3}$, thus two solution can be found depending of the sign of the initial overdensity as:

- initial over-dense fluctuation $\delta_i > 0$:

$$\delta_i \frac{a(t)}{a(t_i)} = \frac{3}{5}\left(\frac{3}{4}(\theta - \sin\theta)\right) \,, \qquad \delta + 1 = \frac{9}{2}\frac{(\theta - \sin\theta)^2}{(1-\cos\theta)^3} \,. \tag{A.6}$$

- initial under-dense fluctuation $\delta_i < 0$:

$$\delta_i \frac{a(t)}{a(t_i)} = -\frac{3}{5}\left(\frac{3}{4}(\theta - \sin\theta)\right) \,, \qquad \delta + 1 = \frac{9}{2}\frac{(\sinh\theta - \theta)^2}{(\cosh\theta - 1)^3} \,. \tag{A.7}$$

Thus, for an Einstein-de-Sitter model, the probability of forming a halo depends only of the initial overdensity and the scale factor. We observe that for $\delta_i > 0$, the over-dense regions tend to become denser as time goes. The density perturbation δ diverges when collapse occurs (or virialisation) for a certain θ and time.

A.3 Numerical simulation - The smoothing scheme

By considering a simulation grid with a cell size Δx, one can use different interpolation scheme to deposit the mass particle onto the cells:

- The Nearest-grid-point (NGP), as the particle is associated to the closest cell only:

$$W(x) = \frac{1}{\Delta x}\delta_{\mathrm{D}}\left(\frac{x}{\Delta x}\right) \,. \tag{A.8}$$

- The cloud-in-cell (CIC), which spreads the particle mass over $2^3 = 8$ cells (for 3D) as:

$$W(x) = \frac{1}{\Delta x}\begin{cases} 1, \text{for } |x| < 1/2\Delta x \,, \\ 0, \text{otherwise} \,. \end{cases} \tag{A.9}$$

- The triangular shape cloud (TSC), which spreads the particle mass on $3^3 = 27$ cells (for 3D) as:

$$W(x) = \frac{1}{\Delta x}\begin{cases} 1 - |x|/\Delta x, \text{for } |x| < \Delta x \,, \\ 0, \text{otherwise} \,, \end{cases} \tag{A.10}$$

- A Gaussian kernel with a fixed width σ as:

$$W(x) = \frac{1}{\sqrt{2\pi}\sigma}\mathrm{e}^{-\frac{x^2}{2\sigma^2}} \,. \tag{A.11}$$

Appendix B

On the projected mass distribution around galaxy clusters : a Lagrangian theory of harmonic power spectra (article)

Overview

The statistics of multipolar moments Q_m, described in the chapter 3, are also predicted in the paper below in the Gaussian random field approximation which should represent well the early universe on large scales. By comparing the statistics of Q_m between numerical simulation and prediction from linear theory, we could highlight the impact of the non-linear evolution of the density field on the multipolar power spectrum.

In this study, clusters are identified as peaks of density in the initial Gaussian field, and are characterised by their peak height ν. The statistics of multipolar moments Q_m are quantified with/without the condition of being centred on a peak. In comparison, the peak condition induces:

- a significant boost at the monopole ($m = 0$),
- a depletion at the dipole (due to the centred) ($m = 1$),
- a slightly suppression of the power at the quadrupole ($m = 2$),
- and finally leaves all other multipoles $m > 2$ unchanged.

Using the perturbative Gram-Charlier expansion, the weakly non-linear regime is also investigated. We find that gravitational evolution induces a non-linear bias of the multipolar moments proportional to the height and the variance of the field. Taking the non-linear evolution of the density field around clusters into account, we predict a boost the excess of multipolar power at all orders m. Indeed, the ratio between the multipolar moments with/without the centred peak predicted by the perturbative theory are consistent with the results presented in the chapter 3, found using an N-body simulation (Gouin et al. 2017).

Astronomy & Astrophysics manuscript no. mpoles˙constrainedGRF˙aa˙v4
June 2, 2017

On the projected mass distribution around galaxy clusters : a Lagrangian theory of harmonic power spectra

Sandrine Codis[1]⋆, Raphaël Gavazzi[2], Christophe Pichon[2,3], and Céline Gouin[2]

[1] Canadian Institute for Theoretical Astrophysics, University of Toronto, 60 St. George Street, Toronto, ON M5S 3H8, Canada
[2] Institut d'Astrophysique de Paris, UMR7095 CNRS & Université Pierre et Marie Curie, 98bis Bd Arago, F-75014, Paris, France
[3] Korea Institute of Advanced Studies (KIAS) 85 Hoegiro, Dongdaemun-gu, Seoul, 02455, Republic of Korea

June 2, 2017

Abstract

Aims. Gravitational lensing allows to quantify the angular distribution of the convergence field around clusters of galaxies to constrain their connectivity to the cosmic web. We describe in this paper the corresponding theory in Lagrangian space where analytical results can be obtained by identifying clusters to peaks in the initial field.
Methods. We derive the three-point Gaussian statistics of a two-dimensional field and its first and second derivatives. The formalism allows us to study the statistics of the field in a shell around a central peak, in particular its multipolar decomposition.
Results. The peak condition is shown to significantly remove power from the dipolar contribution and to modify the monopole and quadrupole. As expected, higher order multipoles are not significantly modified by the constraint. Analytical predictions are successfully checked against measurements in Gaussian random fields. The effect of substructures and radial weighting is shown to be small and does not change the qualitative picture. The non-linear evolution is shown to induce a non-linear bias of all multipoles proportional to the cluster mass.
Conclusions. We predict the Gaussian and weakly non-Gaussian statistics of multipolar moments of a two-dimensional field around a peak as a proxy for the azimuthal distribution of the convergence field around a cluster of galaxies. A quantitative estimate of this multipolar decomposition of the convergence field around clusters in numerical simulations of structure formation and in observations will be presented in two forthcoming papers.

Key words. Galaxies: clusters: general – large-scale structure of Universe – Gravitational lensing: weak – Methods: analytical – Methods: statistical

1. Introduction

Galaxies are not islands uniformly distributed in the Universe. Over the last decades and with the increasing precision of both observations and simulations, they have been shown to reside in a complex network made of large filaments surrounded by walls and voids and intersecting at the overdense nodes of this so-called cosmic web (Klypin & Shandarin 1993; Bond et al. 1996). From the pioneering works of Zeldovich in the seventies to the peak-patch picture of Bond & Myers (1996), the anisotropic nature of the gravitational collapse have been used to explain the birth and growth of the cosmic web. The origin of filaments and nodes lies in the asymmetries of the initial Gaussian random field describing the primordial universe and amplified by gravitational collapse. The above-mentioned works pointed out the importance of non-local tidal effects in weaving the cosmic web. The high-density peaks define the nodes of the evolving cosmic web and completely determine the filamentary pattern in between. In particular, one can appreciate the crucial role played by the study of constrained random fields in understanding the geometry of the large-scale matter distribution.

Galaxy clusters sitting at these nodes are continuously fed by their connected filaments (e.g. Aubert et al. 2004, and reference therein; see also Pogosyan et al, in prep. for a study of the connectivity of the cosmic web). The key role played by this anisotropic environment in galaxy formation is increasingly underlined. For instance, it has been observed that the properties of galaxies –morphology, colours, luminosities, spins among others – are correlated to their large-scale environment (see Oemler 1974; Guzzo et al. 1997; Tempel & Libeskind 2013; Kovač et al. 2014, among many others).

Numerical simulations allow us to study the details of this large-scale structure of the Universe together with its impact on the formation and evolution of galaxies. Using N-body simulations, Hahn et al. (2007); Gay et al. (2010); Metuki et al. (2015) found that the properties of dark matter halos such as their morphology, luminosity, colour and spin parameter depend on their environment as traced by the local density, velocity and tidal field. In addition to scalar quantities, it also appears that their shape and spin are correlated to the directions of the surrounding filaments and walls both in dark matter (see for instance Aubert et al. 2004; Bailin & Steinmetz 2005; Brunino et al. 2007; Aragón-Calvo et al. 2007; Sousbie et al. 2008; Paz et al. 2008; Codis et al. 2012; Aragon-Calvo & Yang 2014) and hydrodynamical simulations (Navarro et al. 2004; Hahn et al. 2010; Dubois et al. 2014).

Analytical works provide important insights to understand the results of those simulations in the quasi-linear regime. As already pointed out, the theory of constrained random fields is an important tool that allows analytical calculations in the linear or weakly non-linear regime which is effective at large scales or early times in the Universe. Virialised halos are the highly non-linear result of gravitational dynamics. They tend to form in

⋆ E-mail: codis@cita.utoronto.ca

the high-density peaks of the density field by gravitational instability and as such represent a biased tracer of the density field (Kaiser 1984; Bardeen et al. 1986). Peak statistics has focused a lot of attention in the recent years as it provides a unique way to analytically study the statistics of halos from their spatial distribution to their mass function (Paranjape & Sheth 2012) or their spin (Codis et al. 2015), at least for rare enough objects (Ludlow & Porciani 2011).

Despite clear evidence from numerical simulations, the detection of filaments and cold flows is still a debated but crucial issue as filamentary flows are often depicted as the solution to the missing baryons problem (Persic & Salucci 1992; Fukugita et al. 1998; Davé et al. 2001; Shull et al. 2012). In particular, gravitational lensing has emerged as a potential powerful probe of the filamentary cosmic web despite being challenging because of the systematics and the weakness of the signal (Dietrich et al. 2005; Mead et al. 2010; Martinet et al. 2016).

Gravitational lensing is related to the projected density integrated along the line of sight from distant source to the observer. The so-called convergence κ is proportional to the projection of the density contrast δ, and, as such, it inherits its statistical properties. In particular, projection will tend to wash the non gaussianities of the δ field out. One would therefore try and enhance the importance of the filamentary structure by looking at the statistical properties of the convergence field at the vicinity of the rarest, most singular, events, which are the clusters at the nodes of the web. In this work, we quantify the amount of symmetry of the matter distribution around clusters of galaxies by means of the aperture multipolar moments of the convergence field (Schneider & Bartelmann 1997) and their power spectrum. In particular, this tool should allow us to detect the signature of filaments feeding galaxy clusters in weak lensing surveys. This paper aims to do the theory of this observable in the Gaussian regime while a companion paper (Gouin et al. 2017) explores the fully non-linear regime by analyzing clusters of galaxies within cosmological N-Body simulations.

This works complements in two dimensions the 3D harmonic analysis of infall at the Virial radius presented in Aubert & Pichon (2007). The paper is organized as follows. Section 2 describes the mathematical formalism from the general definition of multipolar moments to the statistical description of peaks in Gaussian random fields (GRF hereafter) and their impact on the statistics of the multipolar moments. Section 3 then compares the predictions to measurements in Gaussian random fields. Section 4 studies the effect of substructures and Section 5 adds a generic radial weight function. We describe the weakly non-linear evolution of the multipolar moment in Sect. 6. Finally, we give preliminary conclusions of this work in Sect. 7 and propose possible follow-up developments. A statistical characterisation of the geometry of peaks for 2D Gaussian random fields is given in App. A.

2. Formalism

2.1. Aperture multipolar moments

The focus of this paper lies in the azimuthal mass distribution at various scales around massive galaxy clusters. For a thin gravitational lens plane, the convergence κ at a given position $\mathbf{r}$ in the sky corresponds to the projected excess surface density expressed in units of the so-called critical density $\Sigma_{\rm crit}$

$$\kappa(\mathbf{r}) = \frac{1}{\Sigma_{\rm crit}} \int \mathrm{d}z \, (\rho(\mathbf{r}, z) - \overline{\rho}) \, , \tag{1}$$

with the convention that the line-of-sight corresponds to the z-axis and the plane of the sky $\mathbf{r}$ vector can be defined by polar coordinates (r, φ). The critical density involves distance ratios between a fiducial source at an angular diameter distance $D_{\rm s}$, the distance to the lensing mass $D_{\rm l}$ and the distance between the lens and the source $D_{\rm ls}$

$$\Sigma_{\rm crit} = \frac{c^2}{4\pi G} \frac{D_{\rm s}}{D_{\rm l} D_{\rm ls}} \, . \tag{2}$$

On cosmological scales, the thin lens approximation is generally not valid and the integrated deflections experienced by light rays as they travel from the source to the observer requires numerical treatment but for most cosmological applications the integration of the deflections along the unperturbed light rays (so-called Born approximation, see eg Bartelmann & Schneider 2001) yields a linear integral relation between the convergence κ and the density contrast δ. For a known time-varying[1] three-dimensional power spectrum $P_\delta(\mathbf{k}, \chi)$, and for a given source plane redshift $z_{\rm s}$, one can thus write the convergence power spectrum $P_\kappa(\ell, z_{\rm s})$ by means of the Limber approximation (Blandford et al. 1991; Miralda-Escudé 1991; Kaiser 1992; Bartelmann & Schneider 2001; Simon 2007)

$$P_\kappa(\ell, z_s) = \frac{9}{4} \Omega_m^2 \left(\frac{H_0}{c} \right)^4 \int_0^{\chi_s} \mathrm{d}\chi \frac{(\chi_s - \chi)^2}{\chi_s^2} \frac{P_\delta(\ell/\chi, \chi)}{a^2(\chi)} \, . \tag{3}$$

Following early works by Schneider & Bartelmann (1997), we define the aperture multipolar moments of the convergence (projected surface mass density) field κ as

$$Q_m = \int_0^\infty \mathrm{d}r \, r^{1+m} w_m(r) \int_0^{2\pi} \mathrm{d}\varphi \, \mathrm{e}^{im\varphi} \kappa(r, \varphi) \, , \tag{4}$$

with a radial weight function $w_m(r)$ commonly defined on a compact support. Those multipoles aim to quantify possible asymmetries in the mass distribution as probed by gravitational lensing.

The covariance between multipolar moments can straightforwardly be written as

$$\langle Q_n Q_m^* \rangle = 2\pi \, i^{n-m} \int k \mathrm{d}k \, U_n(k) U_m(k) \, P(k) \, . \tag{5}$$

where $U_n(\ell)$ is the Hankel transform of the radial weight function

$$U_m(\ell) = \int r \mathrm{d}r \, r^m w_m(r) J_m(\ell r) \, , \tag{6}$$

$J_m(x)$ are the first kind Bessel functions and $P(k)$ is the power spectrum of the two-dimensional random field κ.

In a suite of papers (including Gouin et al. (2017) and Gavazzi et al, in prep.), we propose to use the full statistics of these multipolar moments around clusters of galaxies. The covariance of the aperture multipolar moments in specific locations of space, such as the vicinity of clusters, becomes

$$\langle Q_n Q_m^* | \mathrm{clusters} \rangle = \iint_0^\infty r \mathrm{d}r \, r' \mathrm{d}r' \iint_0^{2\pi} \mathrm{d}\varphi \mathrm{d}\varphi' \; r^n w_n(r) r'^m w_m(r') \times \mathrm{e}^{i(n\varphi - m\varphi')} \langle \kappa(r, \varphi) \kappa(r', \varphi') | \mathrm{clusters} \rangle \, , \tag{7}$$

[1] where time variation is captured by an explicit dependence on comoving distance χ

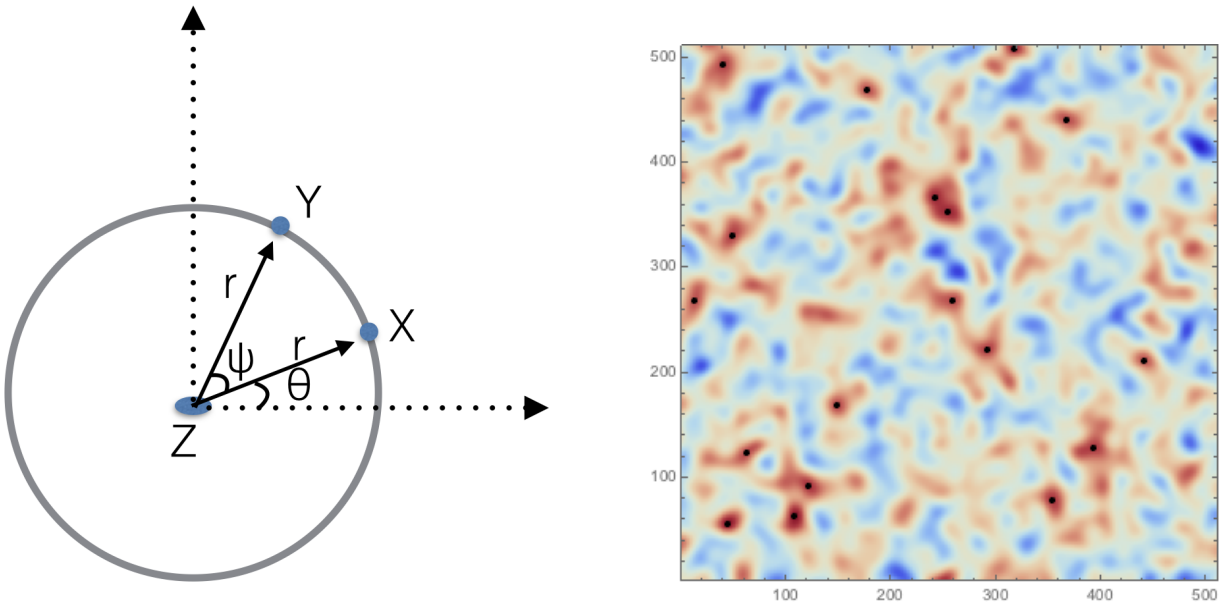

Figure 1. Left-hand panel: This paper aims at describing the angular distribution of a 2D Gaussian field κ around a peak in $\mathbf{r}_z$. We will therefore consider two points on the annulus at a distance r from the central peak. Their respective cartesian coordinates are $\mathbf{r}_x = r(\cos\theta, \sin\theta)$ and $\mathbf{r}_y = r(\cos\theta + \psi, \sin\theta + \psi)$. In particular, we will compute the expectation value of the product of the field in those two locations on the annulus given a central peak. Right-hand panel : example of such a 2D Gaussian random field with a power-law power spectrum with spectral index $n_s = 0$. Peaks of height $\nu = 3 \pm 0.5$ are highlighted with black dots. We hereby investigate the polar distribution of the field around such peaks.

where $\langle\kappa(r,\varphi)\kappa(r',\varphi')|\text{clusters}\rangle$ is a constrained two-point correlation function as we impose a cluster at the origin of the polar coordinate system.

In order to develop a physical intuition of the effect of this cluster constraint on the statistics of the multipolar moments, we propose in this paper to study analytically this observable for a Gaussian random field in which clusters are identified as high peaks. To simplify the problem, we drop the radial weight function and focus on Gaussian random fields smoothed with a Gaussian kernel on a given scale R. In what follows, we will investigate the angular distribution of a Gaussian random field around a peak. We therefore need to study the joint statistics of the field in three locations of space (the location of the peak and two arbitrary points on the circle at a distance r away from the central peak). In addition, according to the peak theory originally developed in Bardeen et al. (1986), we need to consider the field, its first and second derivatives at the location of the peak. In Sect. 2.2, we will first present the result for the joint PDF of those random variables before computing the resulting multipolar decomposition around a central peak in Sect. 2.6.

2.2. Three-point statistics of the field and its derivatives

For a given two-dimensional Gaussian field κ (for example, the projected density contrast), we define the moments

$$\sigma_0{}^2 = \langle\kappa^2\rangle, \qquad \sigma_1{}^2 = \langle(\nabla\kappa)^2\rangle, \qquad \sigma_2{}^2 = \langle(\Delta\kappa)^2\rangle. \quad (8)$$

From these moments, we will use two characteristic lengths $R_0 = \sigma_0/\sigma_1$ and $R_\star = \sigma_1/\sigma_2$, as well as the spectral parameter

$$\gamma = \frac{\sigma_1{}^2}{\sigma_0\sigma_2}. \quad (9)$$

Let us now define the following normalised random variables

$$x = \frac{1}{\sigma_0}\kappa, \qquad x_i = \frac{1}{\sigma_1}\nabla_i\kappa, \qquad x_{ij} = \frac{1}{\sigma_2}\nabla_i\nabla_j\kappa, \quad (10)$$

which have unit variance by construction.

In what follows, $\mathcal{P}(\mathbf{X})$ denotes the one-point probability density (PDF) and $\mathcal{P}(\mathbf{X},\mathbf{Y},\mathbf{Z})$ designates the joint PDF for the normalized field and its derivatives, $\mathbf{X} = \{x\}$, $\mathbf{Y} = \{y\}$ and $\mathbf{Z} = \{z, z_i, z_{ij}\}$, at three prescribed comoving locations ($\mathbf{r}_x$,$\mathbf{r}_y$ and $\mathbf{r}_z$) separated by a distance $r = |\mathbf{r}_x - \mathbf{r}_z| = |\mathbf{r}_y - \mathbf{r}_z|$ so that we are considering the density field in two locations, $\mathbf{r}_x$ and $\mathbf{r}_y$ on a same infinitely thin shell around the central peak in $\mathbf{r}_z$ – see also the left-hand panel of Fig. 1 –. The right-hand panel of Fig. 1 shows a Gaussian random field and the position of its peaks. This paper aims to investigate the angular matter distribution around those peaks.

For a Gaussian field (in particular cosmic fields at early times or large scales), the joint PDF is a multivariate normal distribution

$$\mathcal{N}(\mathbf{X},\mathbf{Y},\mathbf{Z}) = \frac{\exp\left[-\frac{1}{2}\begin{pmatrix}\mathbf{X}\\ \mathbf{Y}\\ \mathbf{Z}\end{pmatrix}^{\mathrm{T}}\cdot\mathbf{C}^{-1}\cdot\begin{pmatrix}\mathbf{X}\\ \mathbf{Y}\\ \mathbf{Z}\end{pmatrix}\right]}{\det|\mathbf{C}|^{1/2}\,(2\pi)^{(6+3\mathrm{d}+\mathrm{d}^2)/4}}, \quad (11)$$

where d is the dimension – $d = 2$ here – and $\mathbf{C}$ is the covariance matrix which depends on the separation vectors only because of homogeneity

$$\mathbf{C} = \begin{pmatrix} 1 & \langle xy\rangle & \mathbf{C_{XZ}} \\ \langle xy\rangle & 1 & \mathbf{C_{YZ}} \\ \mathbf{C}_{\mathbf{XZ}}^{\mathrm{T}} & \mathbf{C}_{\mathbf{YZ}}^{\mathrm{T}} & \mathbf{C_{ZZ}} \end{pmatrix}, \quad (12)$$

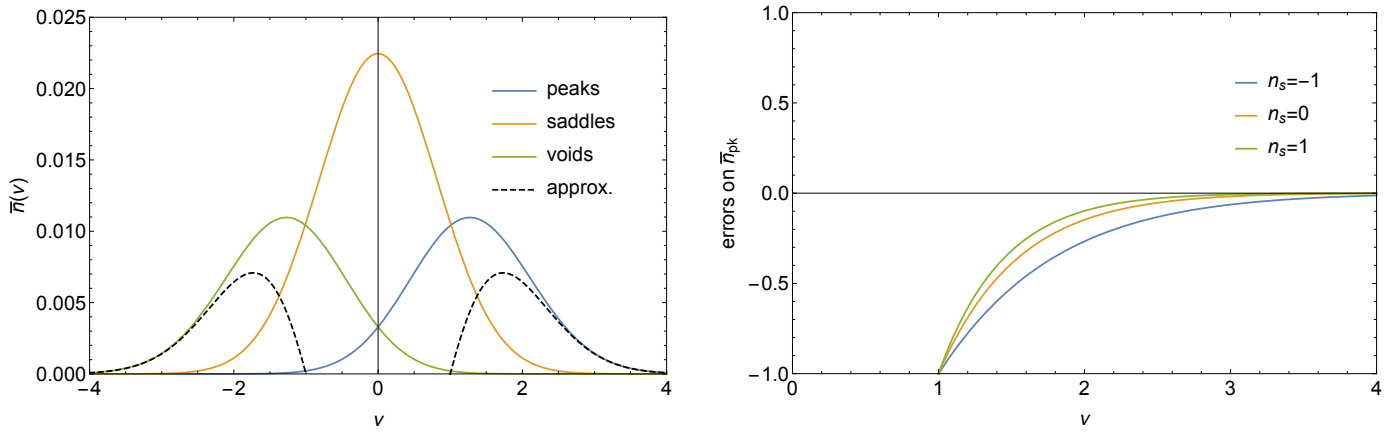

Figure 2. Left-hand panel: Number density of minima, saddle points and peaks compared to the approximation of rare events in units of $R_\star^{-2}$. Right-hand panel : relative error on the number density of peaks of height ν when using the rare event approximation instead of the exact result. Different colours correspond to different spectral indices as labeled.

with

$$\mathbf{C_{XZ}} = (\langle xz\rangle, \langle xz_1\rangle, \langle xz_2\rangle, \langle xz_{11}\rangle, \langle xz_{12}\rangle, \langle xz_{22}\rangle), \tag{13}$$

$$\mathbf{C_{YZ}} = (\langle yz\rangle, \langle yz_1\rangle, \langle yz_2\rangle, \langle yz_{11}\rangle, \langle yz_{12}\rangle, \langle yz_{22}\rangle), \tag{14}$$

$$\mathbf{C_{ZZ}} = \begin{pmatrix} 1 & 0 & 0 & -\gamma/2 & 0 & -\gamma/2 \\ 0 & 1/2 & 0 & 0 & 0 & 0 \\ 0 & 0 & 1/2 & 0 & 0 & 0 \\ -\gamma/2 & 0 & 0 & 3/8 & 0 & 1/8 \\ 0 & 0 & 0 & 0 & 1/8 & 0 \\ -\gamma/2 & 0 & 0 & 1/8 & 0 & 3/8 \end{pmatrix}. \tag{15}$$

For instance, for a 2D power-law power spectrum with spectral index n_s smoothed with a Gaussian filter (r is now the separation in units of the Gaussian smoothing length)

$$\langle xz\rangle = {}_1F_1\left(\frac{n_s}{2}+1;1;-\frac{r^2}{4}\right) \equiv \xi(r), \tag{16}$$

$$\langle xy\rangle = \xi(|\mathbf{r}_x - \mathbf{r}_y| = 2r\sin(\psi/2)), \tag{17}$$

$$\langle x\nabla z\rangle = \frac{\sqrt{n_s+2}}{2\sqrt{2}}\,{}_1F_1\left(\frac{n_s}{2}+2;2;-\frac{r^2}{4}\right)\mathbf{r}, \tag{18}$$

$$\langle xz_{11}\rangle = -\frac{\gamma}{2}\left[2\cos^2(\theta+\psi)\,{}_1F_1\left(\frac{n_s}{2}+2;1;-\frac{r^2}{4}\right)\right. \tag{19}$$

$$\left. -\cos(2(\theta+\psi))\,{}_1F_1\left(\frac{n_s}{2}+2;2;-\frac{r^2}{4}\right)\right], \tag{20}$$

$$\langle xz_{12}\rangle = -\frac{r^2\gamma(n_s+4)}{32}\sin(2(\theta+\psi))\,{}_1F_1\left(\frac{n_s}{2}+3;3;-\frac{r^2}{4}\right), \tag{21}$$

$$\langle xz_{22}\rangle = -\frac{\gamma}{2}\left[2\sin^2(\theta+\psi)\,{}_1F_1\left(\frac{n_s}{2}+2;1;-\frac{r^2}{4}\right)\right. \tag{22}$$

$$\left. +\cos(2(\theta+\psi))\,{}_1F_1\left(\frac{n_s}{2}+2;2;-\frac{r^2}{4}\right)\right]. \tag{23}$$

Here ${}_1F_1(a;b;z)$ is the confluent hypergeometric function, ξ is the two-point correlation function of the field and the spectral parameter reads $\gamma = \sqrt{(n_s+2)/(n_s+4)}$. The correlation matrix $\mathbf{C_{YZ}}$ is obviously the same as $\mathbf{C_{XZ}}$ once ψ has been set to zero.

2.3. The central peak condition

Eq. (11) is sufficient to compute the expectation of any quantity involving the fields and its derivatives up to second order in three different locations. This is the case if one wants to implement a peak condition at the $\mathbf{r}_z$ location. Indeed, following Longuet-Higgins (1957); Adler (1981); Bardeen et al. (1986), this peak constraint reads $|\det z_{ij}|\delta_{\rm D}(z_i)\Theta_H(-\lambda_i)$ where $\delta_D(z_i) \equiv \delta_D(z_1)\delta_D(z_2)$ is a product of Dirac delta functions which imposes the gradient to be zero, $\Theta_H(-\lambda_i) \equiv \Theta_H(-\lambda_1)\Theta_H(-\lambda_2)$ an Heaviside function forcing the curvatures (equivalently the eigenvalues of the Hessian matrix λ_i) to be negative. The factor $|\det z_{ij}| = |z_{11}z_{22} - z_{12}^2|$ encodes the volume associated to each peak, in other words the Jacobian which allows us to go from a smoothed field distribution to the discrete distribution of peaks. The rareness of the peak ν can also be imposed by adding a factor $\delta_{\rm D}(z-\nu)$. We will therefore denote $n_{\rm pk}(\mathbf{Z})$ the localized density of peaks

$$n_{\rm pk}(\mathbf{Z}) = \frac{1}{R_\star^2}|\det z_{ij}|\delta_{\rm D}(z_i)\Theta_H(-\lambda_i)\delta_{\rm D}(z-\nu)\,. \tag{24}$$

The most difficult part in the peak constraint is often to impose the sign of the curvatures and the positivity of the Jacobian which can prevent from getting analytical results as it is the case for 3D differential peak counts (Gay et al. 2012) or peak-peak correlation functions (as described in Baldauf et al. (2016) in one dimension and Regos & Szalay (1995) in three dimensions) which can only be solved numerically. A standard approximation to keep results analytical is to drop this sign constraint and remove the absolute values of the determinant factor for high contrasts as one expects rare enough critical points to be essentially peaks. If this approximation is very accurate for one-point statistics, it may not be the case for $(N > 1)$-point statistics. For instance, peak-peak correlation functions on small scales are not very well reproduced by this approximation even for large contrasts because the contribution from the other critical points actually dominates at small distance (there is at least one saddle point between two peaks!). However, in the context of this work, we impose the peak constraint in one location only and therefore the rare peak approximation is expected to be accurate for $\nu \gtrsim 2$. As an illustration, Fig. 2 displays the Gaussian mean number density of minima, saddle points and peaks (Longuet-Higgins (1957); Adler (1981) and later generalised to weakly

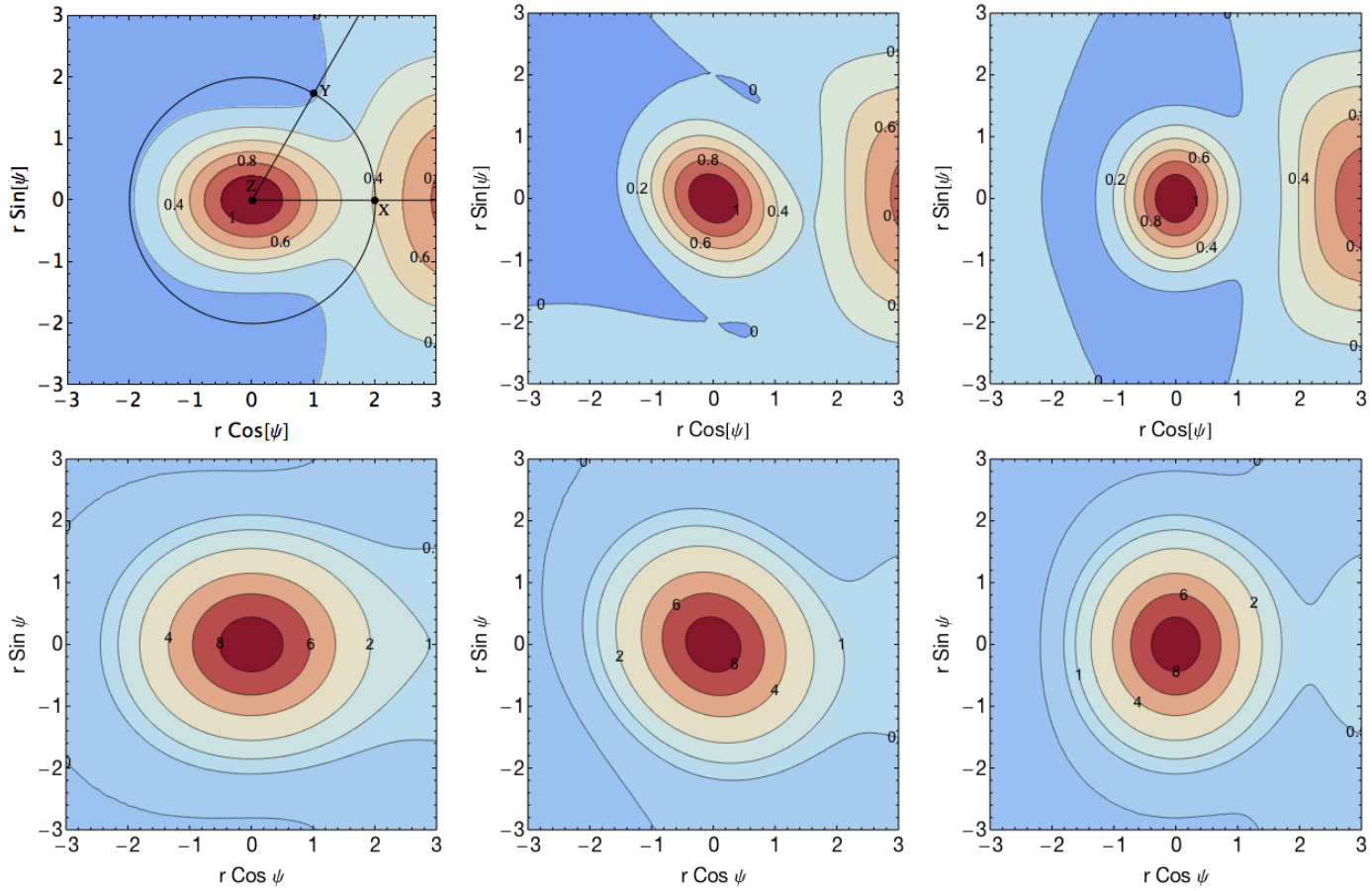

Figure 3. Top panels: expected two-point correlation function $\langle\kappa\kappa'|\mathrm{pk}\rangle$ in units of σ_0^2 for a 2D power spectrum with spectral index $n_s = 0$ and a central peak of height $\nu_\star = \sqrt{7/3}\gamma$ and eigenvalues $\lambda_{1\star} = (-\sqrt{7/3} + \sqrt{1/3})/2$ and $\lambda_{2\star} = (-\sqrt{7/3} - \sqrt{1/3})/2$ in $\mathbf{r}_z$. Different values of θ, the angle between the major axis of the ellipse (i.e smaller curvature) and the first point on the annulus, between 0 and $\pi/2$ are displayed from left to right. ψ is the angle between $\mathbf{r}_x$ and $\mathbf{r}_y$ and r is the separation to the central peak (in units of the smoothing length) so that the displayed value corresponds to the correlation function between this point, $\mathbf{r}_y$, and the one on the positive x-axis at the same radius, $\mathbf{r}_x$. The values we chose here correspond to the most likely height and curvatures of a peak (and do not depend on the spectral index). Bottom panels: same as top panels for $\nu_r = 3$. The corresponding most likely curvatures of the peak are $\lambda_{1r} = -0.94$ and $\lambda_{2r} = -1.6$.

non-Gaussian fields by Pogosyan et al. (2011))

$$\begin{aligned}\bar{n}_{\mathrm{pk/min}}(\nu) &= \frac{\gamma^2\sqrt{2}\exp\left(-\frac{\nu^2}{2}\right)}{16\pi^{3/2}R_\star^2}(\nu^2-1)\left(1\pm\mathrm{erf}\left(\frac{\gamma\nu}{\sqrt{2(1-\gamma^2)}}\right)\right)\\ &+\frac{\sqrt{2}\exp\left(-\frac{3\nu^2}{6-4\gamma^2}\right)}{16\sqrt{3-2\gamma^2}\pi^{3/2}R_\star^2}\left(1\pm\mathrm{erf}\left(\frac{\gamma\nu}{\sqrt{2(1-\gamma^2)(3-2\gamma^2)}}\right)\right)\\ &\pm\frac{\sqrt{1-\gamma^2}}{8\pi^2}\gamma\nu\exp\left(-\frac{\nu^2}{2-2\gamma^2}\right),\\ \bar{n}_{\mathrm{sad}}(\nu) &= \frac{\sqrt{2}\exp\left(-\frac{3\nu^2}{6-4\gamma^2}\right)}{8\sqrt{3-2\gamma^2}\pi^{3/2}R_\star^2},\end{aligned}$$

and compares the latter to the high-ν approximation (related to the genus) $\chi(\nu) = \langle\det z_{ij}\delta_{\mathrm{D}}(z_i)\delta_{\mathrm{D}}(z-\nu)\rangle/R_\star^2$ which can be easily computed

$$\chi(\nu) = \frac{\gamma^2}{4\sqrt{2}\pi^{3/2}R_\star^2}\exp\left(-\frac{\nu^2}{2}\right)(\nu^2-1)\,. \tag{25}$$

The relative error between the number density of peaks and its high-ν approximation is shown on the right-hand panel of Fig. 2.

2.4. Density correlations on the circle surrounding a central peak with given geometry

The expected product of projected density κ in two locations of space $\mathbf{r}_x$ and $\mathbf{r}_y$ such that $\mathbf{r}_x - \mathbf{r}_z = r(\cos\theta, \sin\theta)$ and $\mathbf{r}_y - \mathbf{r}_z = r(\cos(\theta+\psi), \sin(\theta+\psi))$ and given a peak in $\mathbf{r}_z$ of height ν and curvatures $0 > \lambda_1 > \lambda_2$ along the first and second coordinates can be analytically computed. For instance for a power-law power spectrum with $n_s = 0$ (and $\gamma = 1/\sqrt{2}$), we get

$$\begin{aligned}\frac{\langle\kappa(r,\theta)\kappa(r,\theta+\psi)|\mathrm{pk}\rangle}{\sigma_0^2} &= \xi(|\mathbf{r}_x-\mathbf{r}_y|)\\ &+\exp\left(-\frac{r^2}{2}\right)\left[l_0+l_2r^2+l_4r^4\right],\end{aligned} \tag{26}$$

where

$$l_0 = (\nu^2-1), \tag{27}$$

$$l_2 = [\nu^2+\sqrt{2}\nu I_1(1-2e\cos\psi\cos(2\theta+\psi)) - \cos\psi]/2, \tag{28}$$

$$\begin{aligned}l_4 = \Big[&\nu^2 - 2\cos^2\psi + 2\sqrt{2}\nu I_1(1-2e\cos\psi\cos(2\theta+\psi))\\ &+2I_1^2(1-2e\cos(2\theta))(1-2e\cos(2\theta+2\psi))\Big]/16,\end{aligned} \tag{29}$$

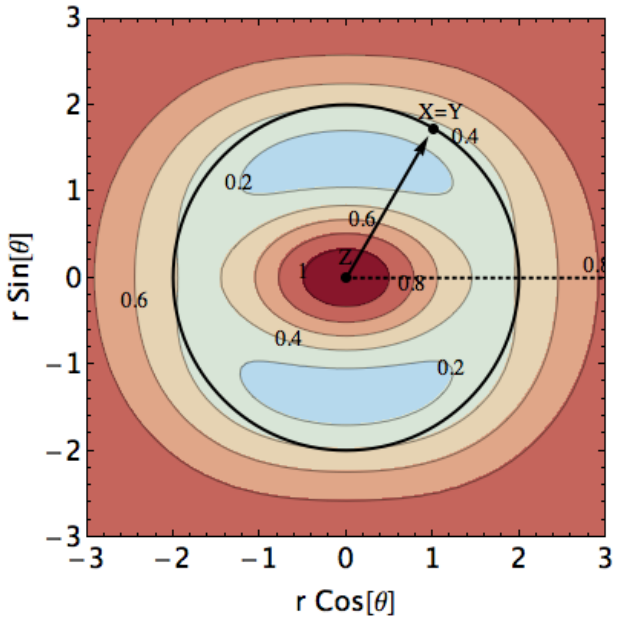

Figure 4. Zero lag annulus correlation function $\left\langle \kappa(r,\theta)^2 | \mathrm{pk}(\nu) \right\rangle$ in units of σ_0^2 for a central peak with height $\nu_\star = \sqrt{7/3}\gamma$ and eigenvalues $\lambda_{1\star} = (-\sqrt{7/3} + \sqrt{1/3})/2$ and $\lambda_{2\star} = (-\sqrt{7/3} - \sqrt{1/3})/2$ in $\mathbf{r}_z$ for a Gaussian random field with power spectrum $P(k) \propto k^0$ smoothed with a Gaussian filter (similar to Fig. 3 when the two points on the annulus are the same). The separation r is given in units of the smoothing length.

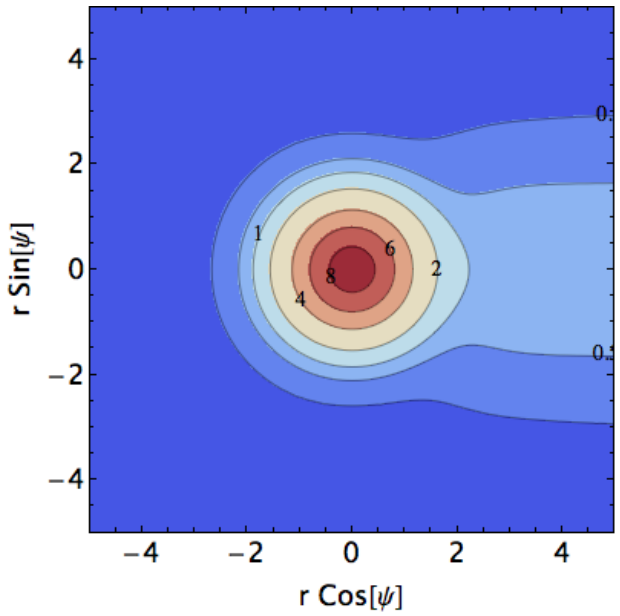

Figure 5. Annulus correlation function $\langle \kappa(r,\theta)\kappa(r,\theta+\psi) | \mathrm{pk}(\nu) \rangle$ in units of σ_0^2 for a central peak with height $\nu = 3$ in a Gaussian random field with power spectrum $P(k) \propto k^0$ smoothed with a Gaussian filter. The separation r is given in units of the smoothing length. The angular anisotropy of the annulus correlation function will be quantified using a multipolar decomposition in Sect. 2.6.

$I_1 = \lambda_1 + \lambda_2$ is the trace of the density Hessian at the location of the peak, $e = (\lambda_2 - \lambda_1)/(2I_1)$ is the ellipticity of the peak and the unconstrained correlation function is

$$\xi(|\mathbf{r}_x - \mathbf{r}_y|) = \exp\left(-\frac{r^2}{2}(1-\cos\psi)\right). \tag{30}$$

To start with, Fig. 4 shows the zero lag contribution to the annulus correlation function (i.e when the two points are at the same location on the annulus, $\psi = 0$) in the frame of the central peak. As expected the amplitude of fluctuations around the peak have an ellipsoidal shape, more elongated along the smallest curvature $\lambda_{1\star}$. Note that this zero-lag annulus correlation is dominated by the square of the mean density profile at small separations and by the fluctuations at larger separations.

Fig. 3 then displays the full constrained correlation function on the annulus. We use different orientations of the pair $(\mathbf{r}_x, \mathbf{r}_y)$ with regard to the axis of smaller curvature (corresponding to λ_1) of the central peak. The orientation of $\mathbf{r}_x$ is described by the angle θ which is taken to be $0, \pi/4$ and $\pi/2$ from the left-hand to the right-hand panel. On each plot, the angle between $\mathbf{r}_x$ and $\mathbf{r}_y$, namely ψ, vary between 0 and 2π and the separation to the central peak is described by the value r. We show the result for two different peak heights, the most likely value $\nu_\star = \gamma\sqrt{7/3}$ (top panels) and a rarer case $\nu_r = 3$ (bottom panels) more relevant to our study. In each case respectively, we fix the peak curvatures to their most likely values $\lambda_{1\star} = (-\sqrt{7/3} + \sqrt{1/3})/2, \lambda_{2\star} = (-\sqrt{7/3} - \sqrt{1/3})/2$ and $\lambda_{1r} = -0.94, \lambda_{2r} = -1.6$ (we refer the reader to App. A for a description of the most likely geometry of a peak). As expected, the product of density is larger when the separation vectors are close one to the other and aligned with the major axis of the peak. For the case of a rare peak (bottom panels), the prominence of the peak is obviously larger (increased magnitude and spatial extend of the peak). Conversely, the common peak, $\nu_\star$ occupies a smaller volume and is surrounded by two closer voids and peaks. In what follows, we do not fix the shape of the peak and therefore we marginalise over λ_1 and λ_2.

2.5. Density correlations around a peak of specified height ν

If one wants to marginalise over the shape of the peak (which means integrating over the eigenvalues λ_1 and λ_2 in the range $\lambda_2 < \lambda_1 < 0$), then the expected product of projected densities on the annulus (the annulus two-point correlation function) becomes

$$\frac{\langle \kappa(r,\theta)\kappa(r,\theta+\psi)|\mathrm{pk}(\nu)\rangle}{\sigma_0^2} = \frac{\left\langle xy\,\det(z_{ij})\delta_{\mathrm{D}}(z-\nu)\delta_{\mathrm{D}}(z_i)\Theta_H(-\lambda_i)\right\rangle}{\left\langle \det(z_{ij})\delta_{\mathrm{D}}(z_i)\Theta_H(-\lambda_i)\right\rangle},$$

where we marginalize over all variables except ν which is fixed. Unfortunately, this expression cannot be analytically computed. For sufficiently rare peaks (high ν), we drop the constraint on the sign of the eigenvalues (high critical points are most of the time peaks) and an explicit expression for $\langle \kappa(r,\theta)\kappa(r,\theta+\psi)|\mathrm{pk}(\nu)\rangle$ can be obtained

$$\begin{aligned}\frac{\langle \kappa(r,\theta)\kappa(r,\theta+\psi)|\mathrm{pk}(\nu)\rangle}{\sigma_0^2} &= \xi(|\mathbf{r}_x-\mathbf{r}_y|) + \frac{2f_{21}^2}{\nu^2-1} + 4f_{11}f_{21} \\ &+ \frac{\nu^4-6\nu^2+3}{\nu^2-1}f_{11}^2 - \frac{n_s+2}{4}r^2 f_{22}^2\cos\psi - \frac{2\cos(2\psi)}{\nu^2-1}(f_{21}-f_{11})^2, \end{aligned} \tag{31}$$

where f_{ij} and the unconstrained correlation function $\xi(|\mathbf{r}_x - \mathbf{r}_y|)$ are functions of the following Kummer confluent hypergeomet-

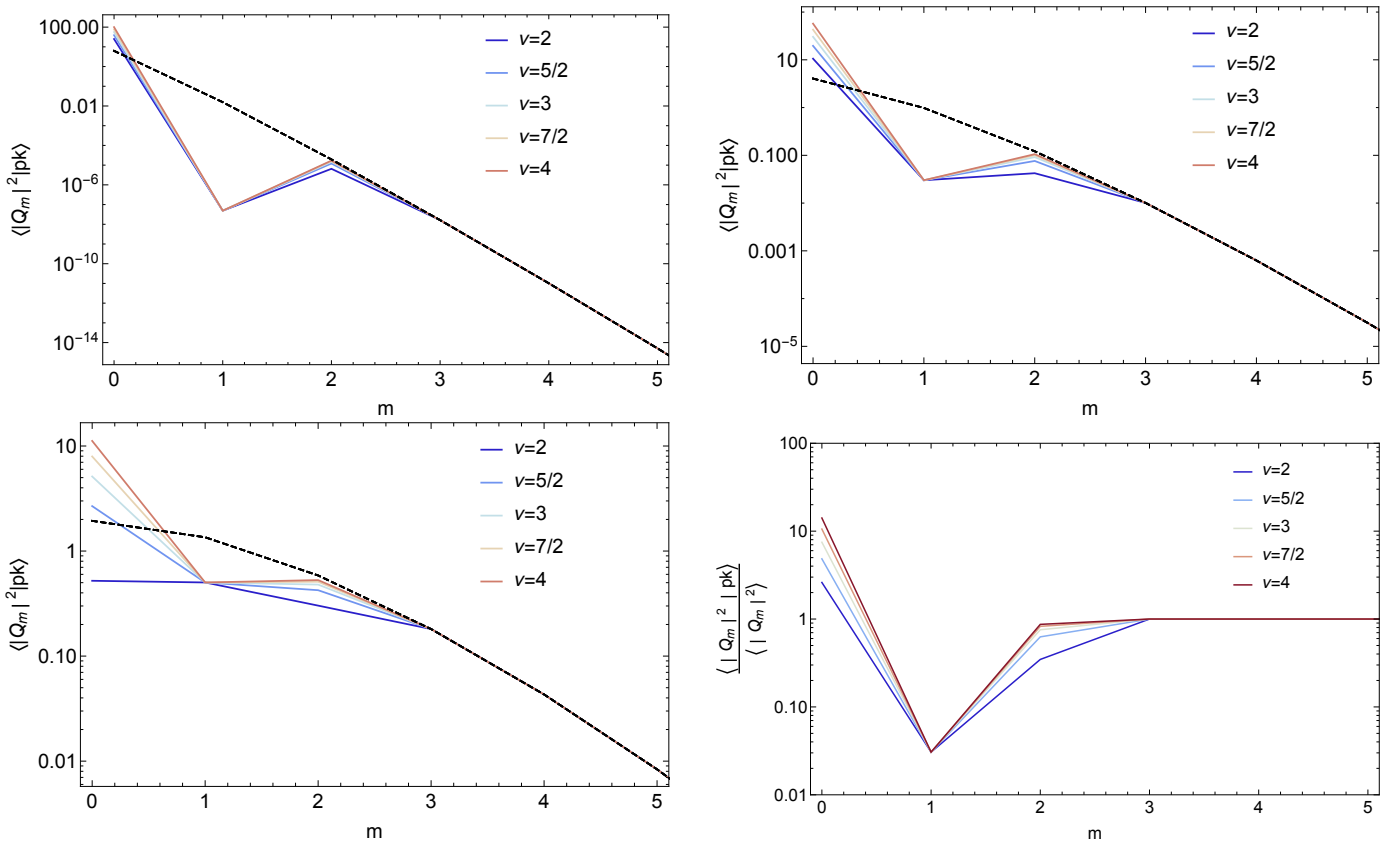

Figure 6. Multipoles $|Q_m|^2|$ for a central peak with height $\nu = 2$ to 4 as labeled in a Gaussian random field with power spectrum $P(k) \propto k^0$ smoothed with a Gaussian filter and on the annulus at a distance $r = 0.1R$ (top left-hand panel), R (top right), $2R$ (bottom left). The dashed line corresponds to the random case (where we do not impose a central peak). The bottom right-hand panel shows the ratio of those multipoles to the random case for $r = R$.

ric functions

$$f_{ij} = {}_1F_1\left(\frac{n_s}{2}+i; j; -\frac{r^2}{4}\right), \tag{32}$$

$$\xi(|\mathbf{r}_x - \mathbf{r}_y|) = {}_1F_1\left(\frac{n_s}{2}+i; j; -\frac{r^2}{2}(1-\cos\psi)\right). \tag{33}$$

As an illustration, for a power spectrum $P(k) \propto k^0$, it becomes

$$\frac{\langle\kappa(r,\theta)\kappa(r,\theta+\psi)|\mathrm{pk}(\nu)\rangle}{\sigma_0^2} = \xi(|\mathbf{r}_x-\mathbf{r}_y|) + \exp\left(-\frac{r^2}{2}\right) \times \frac{8(\nu^2-1)^2 - 8\nu^2r^2 + r^4 - 4\left(\nu^2-1\right)r^2\cos\psi - r^4\cos 2\psi}{8\left(\nu^2-1\right)}, \tag{34}$$

where $\xi(|\mathbf{r}_x - \mathbf{r}_y|) = \exp\left(-\frac{r^2}{2}(1-\cos\psi)\right)$ is the unconstrained correlation function on the annulus. The apparent singularity at $\nu = \pm 1$ is due to our high ν approximation which breaks down in this regime as many $\nu = 1$ critical points are not peaks but saddle points. Fig. 5 illustrates the behaviour of $\langle\kappa(r,\theta)\kappa(r,\theta+\psi)|\mathrm{pk}(\nu)\rangle$ for a central peak with height $\nu = 3$. Similarly to the case where the peak geometry is imposed, here the annulus correlation function is larger when the separation vectors are close one to the other and aligned with the major axis of the peak. The isocontours are close to spherical for small separations but become very anisotropic and elongated along the axis $\psi = 0$ (when the two points overlap) at larger separations.

2.6. Multipoles around a peak of specified height ν

Once the two-point correlation function around a peak – $\langle\kappa(r,\theta)\kappa(r,\theta+\psi)|\mathrm{pk}(\nu)\rangle$ – is known, one can compute the corresponding multipolar moments that we define here as

$$\left\langle|Q_m|^2|\mathrm{pk}\right\rangle(r,\nu) = \int_0^{2\pi}\frac{\mathrm{d}\psi}{2\pi\sigma_0^2}\,\langle\kappa(r,\theta)\kappa(r,\theta+\psi)|\mathrm{pk}\rangle\, e^{im\psi}. \tag{35}$$

The result is again analytical. As expected, only the first three multipoles are modified by the peak condition, the rest being unchanged

$$\left\langle|Q_m|^2|\mathrm{pk}\right\rangle = \left\langle|Q_m|^2\right\rangle \text{ for all } m \geq 3\,. \tag{36}$$

For instance, for $P(k) \propto k^0$ power spectra, those multipoles read

$$\left\langle|Q_0|^2|\,\mathrm{pk}\right\rangle = \left\langle|Q_0|^2\right\rangle + \frac{r^4 - 8\nu^2r^2 + 8(\nu^2-1)^2}{8(\nu^2-1)}\exp\left(-\frac{r^2}{2}\right), \tag{37}$$

$$\left\langle|Q_1|^2|\,\mathrm{pk}\right\rangle = \left\langle|Q_1|^2\right\rangle - \frac{1}{4}r^2\exp\left(-\frac{r^2}{2}\right), \tag{38}$$

$$\left\langle|Q_2|^2|\,\mathrm{pk}\right\rangle = \left\langle|Q_2|^2\right\rangle - \frac{1}{16}\frac{r^4}{\nu^2-1}\exp\left(-\frac{r^2}{2}\right), \tag{39}$$

$$\left\langle|Q_m|^2|\,\mathrm{pk}\right\rangle \overset{m\geq 3}{=} \left\langle|Q_m|^2\right\rangle \equiv \exp\left(-\frac{r^2}{2}\right)I_m\left(\frac{r^2}{2}\right), \tag{40}$$

where I_m are the modified Bessel functions of the first kind. We note in particular that the correction to the monopole (resp.

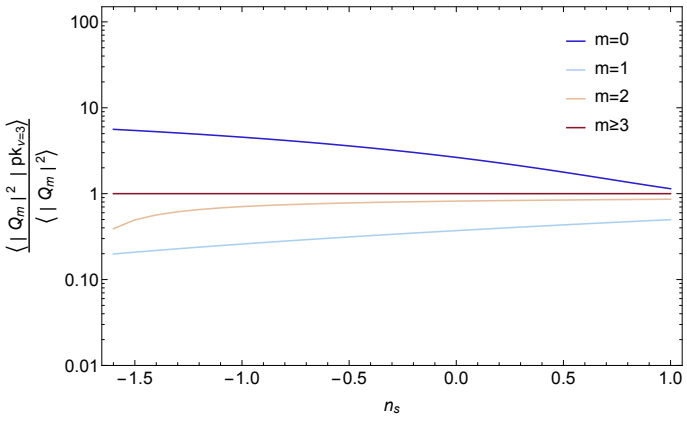

Figure 7. Same as Fig. 6 for central peaks of height $\nu = 3$ and separation $r = 1$ (in units of the smoothing length) as a function of the spectral index n_s.

dipole, quadrupole) is maximal for $r = 0$ (resp. $\sqrt{2}$, 2). It can easily be checked that the condition of zero gradient only affects the dipole, while the constraint on the peak height changes the monopole and the Hessian modifies both the monopole and quadrupole.

Fig. 6 shows the amplitude of the multipoles for various peak heights and separations. There is a significant drop of power in the dipole while the change in the monopole and quadrupole is much less pronounced. The dependance on the peak height is rather small. Those predictions will be checked against GRF realizations in Sect. 3.

2.7. Dependence on the slope of the power spectrum

In this work, we have shown results for a power-law power spectrum ($n_s = 0$) but the qualitative conclusions can be shown to be almost independent from the spectral index. To illustrate this property, we have computed the multipoles for different slopes of the power spectrum from -1.5 (close to the effective spectral index of the convergence field at cluster scale) to 1 as displayed on Fig. 7. The correction to the monopole and dipole are quasi-linearly suppressed when n_s increases while the quadruple is constant for a wide range of slopes $n_s \lesssim 1$ and shows only a decrease at very low spectral indices. Overall, it shows that the qualitative picture described in this paper does not depend significantly on the slope of the power spectrum. Investigating the effect of the running is left for future works as no analytical results can be obtained in this case. The study of a more realistic ΛCDM power spectrum in the non-linear regime will be presented elsewhere.

3. Comparison with direct measurements in GRF

Let us generate ten maps of a 2048^2 GRF with power spectrum $P(k) \propto k^0$. Each map is then smoothed with a Gaussian kernel on $R = 8$ pixels. A portion of such a map is displayed in the right-hand panel of Fig. 1.

Peaks are then found using the code `map2ext` (Colombi et al. 2000; Pogosyan et al. 2011): for every pixel a segment of quadratic surface is fit in the tangent plane based on the field values at the pixel of origin and its neighbours. The position of the extremum of this quadratic surface, its height and its Hessian are computed. The extremum is counted into the tally of the type determined by its Hessian (two negative eigenvalues for peaks) if its position falls within the original pixel. Several additional checks are performed to preclude registering extrema in the neighbouring pixels and minimize missing extrema due to jumps in the fit parameters as region shifts to the next pixel. This procedure performs with better than 1% accuracy when the map is smoothed with a Gaussian filter whose full width at half maximum exceeds 6 pixels.

The field is then interpolated at 100 equally spaced points on the circle located at $r = R$ around each peak and Fourier transformed. Only the square modulus of the Fourier coefficients are stored. For comparison, a similar procedure is followed to estimate the multipolar decomposition around the same number of random points in the field.

The resulting multipolar decomposition measured in GRF is displayed on Fig. 8 for various peak heights and separations. Those measurements are in very good agreement with the theoretical predictions described in Sect. 2.6. The high-ν approximation used to derive the prediction is therefore shown to be very accurate in the regime $\nu \geq 2.5$. Below this threshold, some departures – in particular in the quadrupole – are seen and would require a numerical integration of the equation with the correct peak curvature constraints.

4. Effect of substructures

In practice, measurements in simulations and observations of the angular distribution of the convergence field around clusters naturally involve two separate scales : the (relatively large) scale of the cluster and the (smaller) scale of the convergence field (or the dark matter density field in a N-body simulation) around it. Even if those scales are not identical, they are necessarily highly correlated and the effect described in this paper should persist. To study the effect of substructures, let us redo the analysis but introducing two different smoothing lengths, one R_1 for the field z at the location of the peak and one R_2 at the location of the annulus. In this section only, we will denote $R = R_2/R_1 \leq 1$ the corresponding (dimensionless) ratio. The same formalism as described above applies but all the coefficients of the covariance matrix are changed. Let us first redefine the random variables as

$$z = \frac{1}{\sigma_0}\kappa(\mathbf{r}_z), \quad z_i = \frac{1}{\sigma_1}\nabla_i\kappa(\mathbf{r}_z), \quad z_{ij} = \frac{1}{\sigma_2}\nabla_i\nabla_j\kappa(\mathbf{r}_z), \tag{41}$$

$$x = \frac{1}{\sigma_0}\kappa(\mathbf{r}_x), \quad y = \frac{1}{\sigma_0}\kappa(\mathbf{r}_y), \tag{42}$$

where the factors σ_i are the respective variances of the field, gradient and Laplacian smoothed on scale R_1. With this definition, one can easily recompute the coefficients of the covariance matrix. For instance,

$$\langle xz\rangle = \langle yz\rangle = \beta^{-n_s-2}\,{}_1F_1\left(\frac{n_s}{2}+1;1;-\frac{r^2}{4\beta^2}\right), \tag{43}$$

$$\langle xy\rangle = R^{-\frac{n_s+2}{2}}\,{}_1F_1\left(\frac{n_s}{2}+1;1;-\frac{r^2}{2R^2}(1-\cos\psi)\right), \tag{44}$$

$$\langle xz_{22}\rangle = -\frac{\gamma}{2}\beta^{-n_s-4}\left[2\sin^2(\theta+\psi)\,{}_1F_1\left(\frac{n_s}{2}+2;1;-\frac{r^2}{4\beta^2}\right) + \cos(2(\theta+\psi))\,{}_1F_1\left(\frac{n_s}{2}+2;2;-\frac{r^2}{4\beta^2}\right)\right], \tag{45}$$

where the separation r is again a dimensionless quantity (expressed in units of R_1) and β is the dimensionless quadratic mean

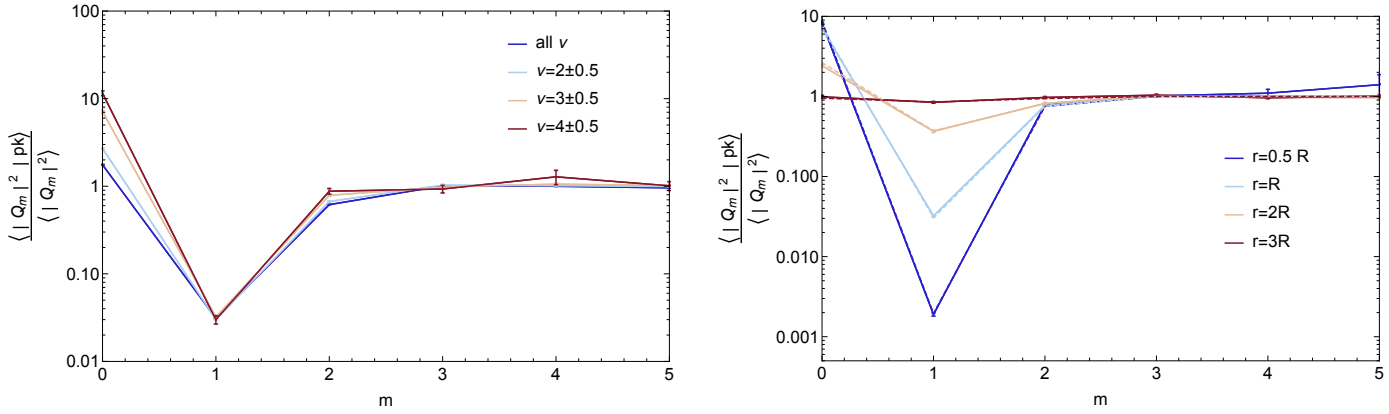

Figure 8. Left-hand panel: Same as the bottom right-hand panel of Fig. 6 for measurements in ten realizations of a 2048^2 2D GRF smoothed with a Gaussian filter on 8 pixels. The height of the peaks are binned as labelled and the separation considered here is $r = R = 8$ pixels. Right-hand panel: Same as left-hand panel when we vary the separation r instead of the peak height which is set to $\nu = 3$ here. We overplotted the theoretical predictions with dashed lines that are almost indistinguishable from the measurements.

of the two smoothing lengths

$$\beta = \sqrt{(1+R^2)/2}, \tag{46}$$

which ranges from $1/\sqrt{2}$ (when R_2 goes to zero) to 1 (when the two smoothing scales are equal $R_2 = R_1$).

An analytical solution for the mean amplitude of the multipoles of the field around a central peak can again be computed. For the same example of a power-law power spectrum $P(k) \propto k^0$, those multipoles read

$$\left\langle |Q_0|^2|\mathrm{pk}\right\rangle = \left\langle |Q_0|^2\right\rangle + \frac{a_0^{\mathrm{pk}}}{8\beta^{12}(\nu^2-1)}\exp\left(-\frac{r^2}{4\beta^2}\right), \tag{47}$$

$$\left\langle |Q_1|^2|\mathrm{pk}\right\rangle = \left\langle |Q_1|^2\right\rangle - \frac{r^2}{4\beta^8}\exp\left(-\frac{r^2}{4\beta^2}\right), \tag{48}$$

$$\left\langle |Q_2|^2|\mathrm{pk}\right\rangle = \left\langle |Q_2|^2\right\rangle - \frac{r^4}{16(\nu^2-1)\beta^{12}}\exp\left(-\frac{r^2}{4\beta^2}\right), \tag{49}$$

$$\left\langle |Q_m|^2|\mathrm{pk}\right\rangle \overset{m\geq 3}{=} \left\langle |Q_m|^2\right\rangle \equiv \frac{1}{R^2}\exp\left(-\frac{r^2}{2R^2}\right) I_m\left(\frac{r^2}{2R^2}\right). \tag{50}$$

where I_m are the modified Bessel functions of the first kind and

$$a_0^{\mathrm{pk}} = r^4 - 8\beta^2\left[1+\beta^2(\nu^2-1)\right]r^2 + 8\beta^4\left[2+4\beta^2(\nu^2-1)+\beta^4(\nu^4-6\nu^2+3)\right].$$

The limit $R = \beta = 1$ trivially reduces to the former Eqs. (37-40).

Those small-scale multipoles are displayed in Fig. 9 for $R = 1/100$ to $R = 1$. The multi-scale approach described in this section does not modify the $m > 2$ multipoles. As expected, the correction due to the peak decreases when R goes to 0 as the scales decorrelate. In addition, we expect that non-linearities and corrections beyond the Hessian will change the power of higher order multipoles.

5. Beyond the thin shell approximation

The effect of the radial weight function in Eq. (7) can be studied by relaxing the assumption that $\mathbf{r}_x$ and $\mathbf{r}_y$ are on a same infinitely thin shell around the central peak in $\mathbf{r}_z$. Let us therefore consider the general setting for which $\mathbf{r}_x$ is at a distance r from the central peak and $\mathbf{r}_y$ at a distance r'. In this case, the constrained two-point correlation function reads

$$\frac{\langle\kappa(r,\theta)\kappa(r,\theta+\psi)|\mathrm{pk}(\nu)\rangle}{\sigma_0^2} = \xi(|\mathbf{r}_x-\mathbf{r}_y|) + \frac{2f_{21}f'_{21}}{\nu^2-1} + 2(f'_{11}f_{21}+f_{11}f'_{21}) + \frac{\nu^4-6\nu^2+3}{\nu^2-1}f_{11}f'_{11} - \frac{n_s+2}{4}r^2\cos\psi f_{22}f'_{22} - \frac{2\cos(2\psi)}{\nu^2-1}(f_{21}-f_{11})(f'_{21}-f'_{11}), \tag{51}$$

where f, f' and the unconstrained correlation function $\xi(|\mathbf{r}_x-\mathbf{r}_y|)$ are functions of the following Kummer confluent hypergeometric functions

$$f_{ij} = {}_1F_1\left(\frac{n_s}{2}+i; j; -\frac{r^2}{4}\right), \tag{52}$$

$$f'_{ij} = {}_1F_1\left(\frac{n_s}{2}+i; j; -\frac{r'^2}{4}\right), \tag{53}$$

$$\xi(|\mathbf{r}_x-\mathbf{r}_y|) = {}_1F_1\left(\frac{n_s}{2}+i; j; -\frac{r^2+r'^2-2rr'\cos\psi}{4}\right). \tag{54}$$

It can easily be checked that Eq. (51) trivially reduces to Eq. (31) when $r' = r$. As an illustration, for a power-law power spectrum $P(k) \propto k^0$, the correction to the unconstrained correlation function $\xi(|\mathbf{r}_x-\mathbf{r}_y|)$ reads

$$\frac{\langle\kappa(r,\theta)\kappa(r',\theta+\psi)|\mathrm{pk}\rangle}{\sigma_0^2} - \xi(|\mathbf{r}_x-\mathbf{r}_y|) = \exp\left(-\frac{r^2+r'^2}{4}\right)\delta\xi, \tag{55}$$

with

$$\delta\xi = \frac{8(\nu^2-1)^2 - 4\nu^2(r^2+r'^2) + r^2r'^2(1-\cos 2\psi) - 4\left(\nu^2-1\right)rr'\cos\psi}{8\left(\nu^2-1\right)}.$$

From Eq. (51), one can now easily compute the statistics of the multipoles including the radial weight function $w_n(r)$ that appears in Eq. (7). We find again that only the amplitude of the

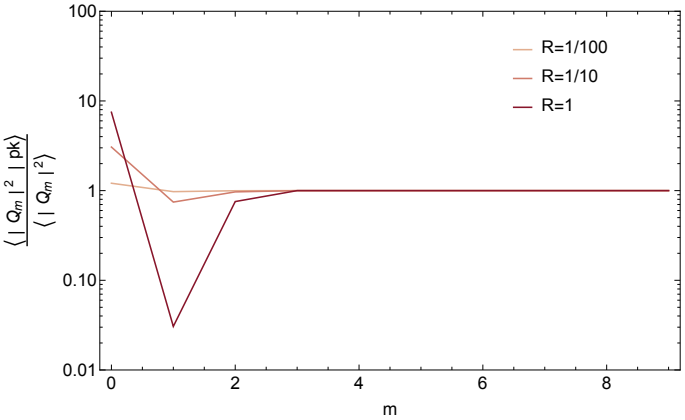

Figure 9. Same as the bottom right-hand panel of Fig. 6 when the field is smoothed at two different scales whose ratio R goes from 1/100 to 1.

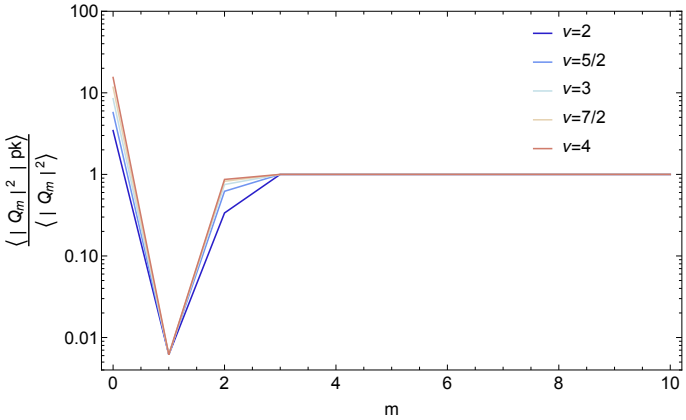

Figure 10. Same as the bottom right-hand panel of Fig. 6 when we apply a radial weight function defined by Eq. (61) with $R_{\rm max}$ equals the smoothing length and $\alpha = 0.5$ (which means that the minimum radius considered is half the smoothing length).

first three multipoles are affected by the peak constraint

$$\left\langle |Q_0|^2|{\rm pk}\right\rangle = \left\langle |Q_0|^2\right\rangle + \int_{\mathcal{S}_0} \frac{r^4-8\nu^2r^2+8(\nu^2-1)^2}{8(\nu^2-1)} \exp\left(-\frac{r^2}{2}\right), \quad (56)$$

$$\left\langle |Q_1|^2|{\rm pk}\right\rangle = \left\langle |Q_1|^2\right\rangle - \int_{\mathcal{S}_1} \frac{r^2}{4} \exp\left(-\frac{r^2}{2}\right), \quad (57)$$

$$\left\langle |Q_2|^2|{\rm pk}\right\rangle = \left\langle |Q_2|^2\right\rangle - \int_{\mathcal{S}_2} \frac{1}{16}\frac{r^4}{\nu^2-1} \exp\left(-\frac{r^2}{2}\right), \quad (58)$$

$$\left\langle |Q_m|^2|{\rm pk}\right\rangle \overset{m\geq 3}{=} \left\langle |Q_m|^2\right\rangle, \quad (59)$$

where $\int_{\mathcal{S}_m}$ stands for the following 2D radial integral

$$\int_{\mathcal{S}_m} f(r,r') = (2\pi)^2\sigma_0^2 \int r{\rm d}r\, r'{\rm d}r'\, r^n w_n(r) r'^m w_m(r'). \quad (60)$$

Fig. 10 shows the resulting multipoles for a radial weight function defined following Schneider & Bartelmann (1997) as

$$R_{\rm max}^{1+m}\, w_m(r) = \frac{1}{x^{1+m}+\alpha^{1+m}} - \frac{1}{1+\alpha^{1+m}} + \frac{(1+m)(x-1)}{(1+\alpha^{1+m})^2} \quad (61)$$

over the range $x = r/R_{\rm max} \in [\alpha, 1]$ and zero elsewhere (which was found to be optimal for an isothermal mass distribution). The qualitative picture does not change : the most affected multipole is the dipole whose power is significantly reduced by the peak constraint, the monopole and quadrupole are slightly affected in a ν-dependant way and all other coefficients are unaffected.

6. A non-linear theory of harmonic power spectra

In this section, we study the weakly non-linear evolution of the multipolar moments. We therefore no longer assume that the PDF is Gaussian $\mathcal{P}(x,y,z) = G(x,y,z)$. Instead, we expand the PDF around a Gaussian by means of the so-called Gram-Charlier expansion (Cramér 1946; Pogosyan et al. 2009a). For simplicity, we will restrict ourselves to the case where we only impose the height of the cluster but not the rest of the peak condition (no zero gradient or constraint on the eigenvalues of the Hessian). We will show that this effect dominates the high multipoles.

6.1. The Gram Charlier expansion

The Gaussian PDF has zero means and covariance matrix

$$\mathbf{C} = \begin{pmatrix} 1 & b & a \\ b & 1 & a \\ a & a & 1 \end{pmatrix}, \quad (62)$$

with $a = \xi(r)$ and $b = \xi(2r\sin(\psi/2))$.

We first diagonalise this matrix and use a new set of variables (u,v,z) where

$$w = \frac{y-az}{\sqrt{1-a^2}} \quad (63)$$

$$u = \frac{x(1-a^2)+y(a^2-b)+za(b-1)}{\sqrt{(1-b)(1-2a^2+b)(1-a^2)}} \quad (64)$$

so that

$$\mathcal{P}(u,w,z) = N(u)N(w)N(z) \quad (65)$$

with N a normal distribution of zero mean and unit variance.

Following Gay et al. (2012); Codis et al. (2013), we then use a Gram-Charlier expansion of the PDF

$$\mathcal{P}(u,w,z) = G(u,w,z)\left[1 + \sum_{i+j+k=3}^{\infty} \frac{H_i(u)H_j(w)H_k(z)}{i!\,j!\,k!} \left\langle u^i w^j z^k\right\rangle_{\rm GC}\right]$$

where H_i represent probabilistic Hermite polynomials and the Gram-Charlier coefficients are given by

$$\left\langle u^i w^j z^k\right\rangle_{\rm GC} = \left\langle H_i(u)H_j(w)H_k(z)\right\rangle. \quad (66)$$

Once the joint PDF is known, we can compute the annulus two-point correlation function $\langle xy|z=\nu\rangle$ as

$$\langle xy|z=\nu\rangle = \frac{\int {\rm d}x\,{\rm d}y\,\mathcal{P}(u(x,y,z),w(y,z),\nu)xy}{\mathcal{P}(z=\nu)}, \quad (67)$$

which can be rewritten

$$\langle xy|z=\nu\rangle = \frac{\int {\rm d}u\,{\rm d}w\,\mathcal{P}(u,w,\nu)x(u,w,\nu)y(u,w,\nu)}{\mathcal{P}(z=\nu)}, \quad (68)$$

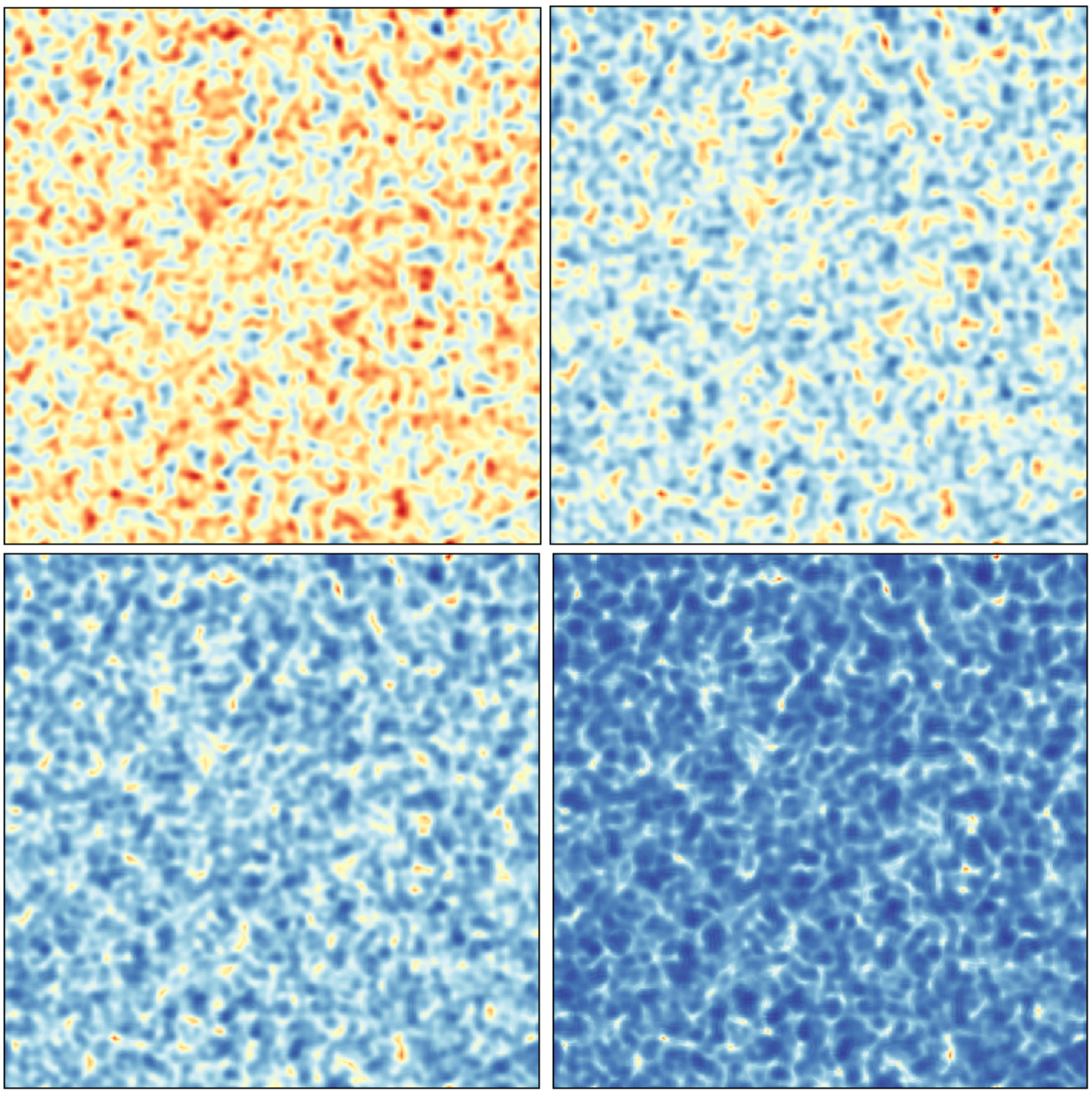

Figure 11. A slice through the fields $n_{\rm step}$ =0,1,2 and 3 obtained by a Zeldovich displacement of an initial GRF. We measure the multipolar moments around all points of height $\nu > 2$ in those maps.

where xy is a polynomial of u and w

$$xy = a^2z^2 + uza\sqrt{\frac{(1-b)(1-2a^2+b)}{1-a^2}} + wza\frac{1+b-2a^2}{\sqrt{1-a^2}} + uw\sqrt{(1-b)(1-2a^2+b)} + (b-a^2)w^2 \quad (69)$$

which is the sum of four terms proportional respectively to $H_0(u)H_0(w)$, $H_1(u)H_0(w)$, $H_0(u)H_1(w)$, $H_1(u)H_1(w)$ and $H_0(u)(H_2(w) + H_0(w))$ as $H_0(x) = 1$, $H_1(x) = x$ and $H_2(x) = x^2 - 1$. Using the property of orthogonality of Hermite polynomials, it is then easy to compute Eq. 68 so that eventually

$$\langle xy|z=\nu\rangle = b + a^2(\nu^2-1) + \Delta_{\rm NL}\,, \quad (70)$$

where the non-linear contribution reads

$$\Delta_{\rm NL}= \frac{\sum_{k=1}^{\infty}\frac{H_k(\nu)}{k!}\left\langle H_k(z)\left[2a\nu(x-az)+xy-b-2azx+a^2z^2+a^2\right]\right\rangle}{1+\sum_{k=3}^{\infty}\frac{H_k(\nu)}{k!}\langle z^k\rangle_{\rm GC}},$$

which, at first order in σ_0 – the amplitude of fluctuations –, is given by[2]

$$\Delta^{(1)}_{\rm NL}= a^2(2\nu-\nu^3)\left\langle z^3\right\rangle + a(\nu^3-3\nu)\left\langle xz^2\right\rangle + \nu\langle xyz\rangle\,.$$

In terms of multipoles, it means that for $m > 0$, we get a non-linear bias given by

$$\frac{\left\langle|Q_m|^2|\nu\right\rangle}{\langle|Q_m|^2\rangle} = 1 + \nu\frac{\langle xyz\rangle_m}{b_m} + O(\sigma_0^2)\,, \quad (71)$$

where the subscript m refers to the associated multipole of order m. The multipoles near a high density cluster is therefore biased compared to random locations, this bias being proportional to the height ν with a proportionality coefficient related to the ratio between the isosceles three-point function $\langle xyz\rangle$ and the two-point correlation function of its base $b = \langle xy\rangle = \xi(2r\sin(\psi/2))$. Note that the all-order expression is also easily obtained once it

[2] An easy way to get this expression is to only keep Gram-Charlier coefficients $\left\langle u^i w^j z^k\right\rangle_{\rm GC}$ for which $i + j + k = 3$ which were shown to be equivalent to cumulants and correspond exactly to the first-order correction, proportional to σ_0 (Gay et al. 2012).

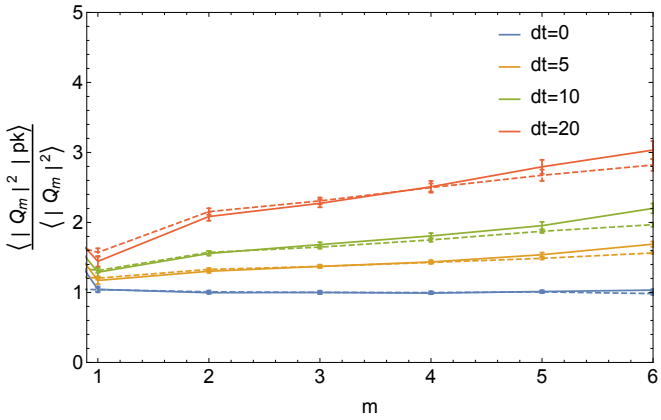

Figure 12. Ratio between the multipolar moments at a distance $r = 8$ pixels from a field point of height $\nu > 2$ compared to random locations, for a GRF displaced following the Zeldovich approximation for different time steps between 0 and 20 as labeled and smoothed over 3 pixels. The solid line is the measurements and the dashed line is the prediction for $m > 0$ given by Eq. 71.

is realised that the only terms which depend on the angle ψ are b and the cumulants involving the product xy

$$\frac{\left\langle |Q_m|^2|\nu\right\rangle}{\langle |Q_m|^2\rangle} = 1 + \frac{\sum_{k=1}^{\infty}\frac{H_k(\nu)}{k!}\langle H_k(z)(xy-b)\rangle_m}{b_m\left(1+\sum_{k=3}^{\infty}\frac{H_k(\nu)}{k!}\langle z^k\rangle_{\rm GC}\right)}. \quad (72)$$

The monopole is also easy to compute

$$\frac{\left\langle |Q_0|^2|\nu\right\rangle}{\langle |Q_0|^2\rangle} = 1 + \frac{a^2(\nu^2-1)}{b_0} + \delta q_0^{\rm NL}, \quad (73)$$

where the first order non-linear correction reads

$$\delta q_0^{\rm NL} = +\nu\frac{a^2(2-\nu^2)\left\langle z^3\right\rangle + a(\nu^2-3)\left\langle xz^2\right\rangle + \langle xyz\rangle_0}{b_0} + O(\sigma_0^2).$$

6.2. Comparison with simulations

To test the $m > 0$ prediction, we have generated various GRF and displaced the density field following a Zeldovich displacement with different time steps denoted $n_{\rm step}$ =0,1,2 and 3 (from Gaussian to more evolved fields). In practice, we compute the displacement field as the gradient of the gravitational potential by FFT and we multiply by a constant times $n_{\rm step}$. We then move the mass in each pixel according to this displacement and distribute it to the eight closest pixels. Those fields are illustrated on Fig. 11. We measure the multipoles around field point of height $\nu > 2$ together with the mean height of those peaks (resp. $\bar{\nu} = 2.36, 2.52, 2.63, 2.86$) and the multipolar decomposition of the bispectrum $\langle xyz\rangle_m$. The result is displayed on Fig. 12 and shows a fair agreement of the $m > 0$ multipoles with the prediction given in Eq. 71.

7. Conclusions

We have computed the statistics of the multipolar moments around a peak for a generic two-dimensional Gaussian field as a proxy for the azimuthal distribution of matter around clusters seen by weak gravitational lensing experiments. For rare enough peaks ($\nu \gtrsim 2.5$), all results are completely analytical. It is shown that only the monopole, dipole and quadrupole are affected by the central peak while higher order multipoles are essentially left unchanged by the peak constraint. Overall, the dominant effect we find is a significant drop in the dipole coefficient as expected from the zero gradient condition. Substructures in the Gaussian field and the addition of a radial weighting function do not change this qualitative picture.

This feature in the dipole can also be detected in numerical simulations of structure formation as will be shown in a forthcoming paper (Gouin et al. 2017). We anticipate that higher order corrections will also emerge from the non-linear evolution of the density field in the vicinity of peaks beyond the Gaussian picture described here but also from possible departure from the peak model itself which, as we showed in this paper, boils down to modifying the power in the monopole, dipole and quadrupole only. As an illustration, we have computed the non-linear bias of the multipolar moments due to the height of the cluster. This bias is proportional to the height ν and to the variance of the field σ by means of the rescaled bispectrum. This approach based on the statistics of multipolar moments in the convergence field around clusters will soon be applied to data (Gavazzi et al, in prep.).

Extensions of this analytical work in the future might include i) an investigation of the accuracy of the large ν approximation and a precise numerical integration in the regime of intermediate contrasts where this approximation breaks down, ii) a study of the effect of the scale-dependence of the power spectrum.

Acknowledgements. This work is partially supported by the grants ANR-13-BS05-0005 of the French Agence Nationale de la Recherche. This work has made use of the Horizon cluster on which the GRF maps were generated, hosted by the Institut d'Astrophysique de Paris. We warmly thank D. Pogosyan for insightful discussions, his careful reading of the manuscript and for providing us with his code `map2ext` to detect extrema in 2D maps. We also thank S. Rouberol for running the Horizon cluster for us and D. Munro for freely distributing his Yorick programming language and opengl interface (available at `yorick.sourceforge.net`).

References

Adler, R. J. 1981, The Geometry of Random Fields (Chichester: Wiley)
Aragón-Calvo, M. A., van de Weygaert, R., Jones, B. J. T., & van der Hulst, J. M. 2007, *ApJ Let.*, 655, L5
Aragon-Calvo, M. A. & Yang, L. F. 2014, *MNRAS*, 440, L46
Aubert, D. & Pichon, C. 2007, *MNRAS*, 374, 877
Aubert, D., Pichon, C., & Colombi, S. 2004, *MNRAS*, 352, 376
Bailin, J. & Steinmetz, M. 2005, *ApJ*, 627, 647
Baldauf, T., Codis, S., Desjacques, V., & Pichon, C. 2016, *MNRAS*, 456, 3985
Bardeen, J. M., Bond, J. R., Kaiser, N., & Szalay, A. S. 1986, *ApJ*, 304, 15
Bartelmann, M. & Schneider, P. 2001, *Phys. Rep.*, 340, 291
Blandford, R. D., Saust, A. B., Brainerd, T. G., & Villumsen, J. V. 1991, *MNRAS*, 251, 600
Bond, J. R., Kofman, L., & Pogosyan, D. 1996, *Nature*, 380, 603
Bond, J. R. & Myers, S. T. 1996, *ApJ Sup.*, 103, 1
Brunino, R., Trujillo, I., Pearce, F. R., & Thomas, P. A. 2007, *MNRAS*, 375, 184
Codis, S., Pichon, C., Devriendt, J., et al. 2012, *MNRAS*, 427, 3320
Codis, S., Pichon, C., & Pogosyan, D. 2015, *MNRAS*, 452, 3369
Codis, S., Pichon, C., Pogosyan, D., Bernardeau, F., & Matsubara, T. 2013, *MNRAS*, 435, 531
Colombi, S., Pogosyan, D., & Souradeep, T. 2000, Physical Review Letters, 85, 5515
Cramér, H. 1946, Mathematical Methods of Statistics (Princeton Univ. Press)
Davé, R., Cen, R., Ostriker, J. P., et al. 2001, *ApJ*, 552, 473
Dietrich, J. P., Schneider, P., Clowe, D., Romano-Díaz, E., & Kerp, J. 2005, *A&A*, 440, 453
Doroshkevich, A. G. 1970, Astrophysics, 6, 320
Dubois, Y., Pichon, C., Welker, C., et al. 2014, *MNRAS*, 444, 1453
Fukugita, M., Hogan, C. J., & Peebles, P. J. E. 1998, *ApJ*, 503, 518
Gay, C., Pichon, C., Le Borgne, D., et al. 2010, *MNRAS*, 404, 1801
Gay, C., Pichon, C., & Pogosyan, D. 2012, *Phys. Rev. D*, 85, 023011
Gouin, C., Gavazzi, R., Codis, S., et al. 2017, ArXiv e-prints
Guzzo, L., Strauss, M. A., Fisher, K. B., Giovanelli, R., & Haynes, M. P. 1997, *ApJ*, 489, 37

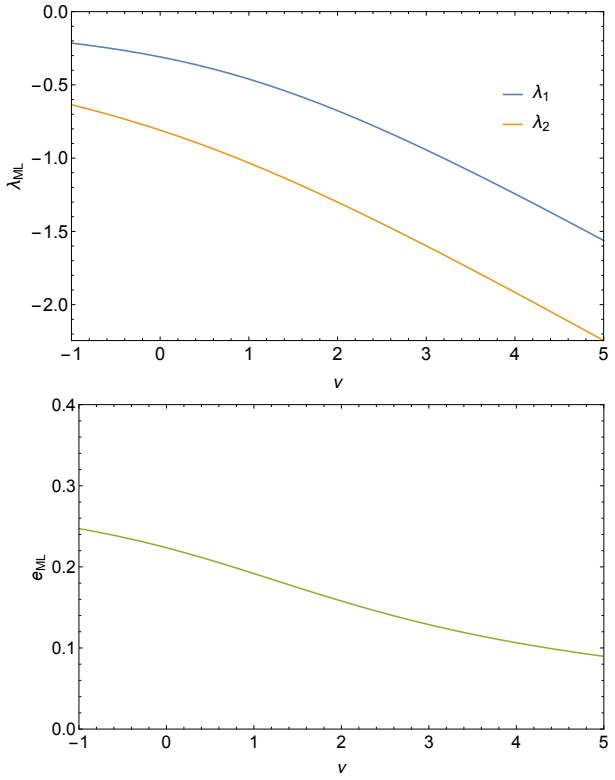

Figure A.1. Most likely peak curvatures as a function of the peak height ν (top panel) and the corresponding most likely peak ellipticity (bottom panel). Those results do not depend on the spectral index.

Hahn, O., Porciani, C., Carollo, C. M., & Dekel, A. 2007, *MNRAS*, 375, 489
Hahn, O., Teyssier, R., & Carollo, C. M. 2010, *MNRAS*, 405, 274
Kaiser, N. 1984, *ApJ Let.*, 284, L9
Kaiser, N. 1992, *ApJ*, 388, 272
Klypin, A. & Shandarin, S. F. 1993, *ApJ*, 413, 48
Kovač, K., Lilly, S. J., Knobel, C., et al. 2014, *MNRAS*, 438, 717
Longuet-Higgins, M. S. 1957, Philosophical Transactions of the Royal Society of London Series A, 249, 321
Ludlow, A. D. & Porciani, C. 2011, *MNRAS*, 413, 1961
Martinet, N., Clowe, D., Durret, F., et al. 2016, *A&A*, 590, A69
Mead, J. M. G., King, L. J., & McCarthy, I. G. 2010, *MNRAS*, 401, 2257
Metuki, O., Libeskind, N. I., Hoffman, Y., Crain, R. A., & Theuns, T. 2015, *MNRAS*, 446, 1458
Miralda-Escudé, J. 1991, *ApJ*, 380, 1
Navarro, J. F., Abadi, M. G., & Steinmetz, M. 2004, *ApJ Let.*, 613, L41
Oemler, Jr., A. 1974, *ApJ*, 194, 1
Paranjape, A. & Sheth, R. K. 2012, *MNRAS*, 426, 2789
Paz, D. J., Stasyszyn, F., & Padilla, N. D. 2008, *MNRAS*, 389, 1127
Persic, M. & Salucci, P. 1992, *MNRAS*, 258, 14P
Pogosyan, D., Gay, C., & Pichon, C. 2009a, *Phys. Rev. D*, 80, 081301
Pogosyan, D., Pichon, C., & Gay, C. 2011, *Phys. Rev. D*, 84, 083510
Pogosyan, D., Pichon, C., Gay, C., et al. 2009b, *MNRAS*, 396, 635
Regos, E. & Szalay, A. S. 1995, *MNRAS*, 272, 447
Schneider, P. & Bartelmann, M. 1997, *MNRAS*, 286, 696
Shull, J. M., Smith, B. D., & Danforth, C. W. 2012, *ApJ*, 759, 23
Simon, P. 2007, *A&A*, 473, 711
Sousbie, T., Pichon, C., Colombi, S., & Pogosyan, D. 2008, *MNRAS*, 383, 1655
Tempel, E. & Libeskind, N. I. 2013, *ApJ Let.*, 775, L42

Appendix A: Typical peak geometry

The typical geometry of a Gaussian peak in two dimensions can easily be computed. Starting from the Gaussian joint PDF of the field value ν and local curvatures $\lambda_1 > \lambda_2$ (Doroshkevich 1970; Pogosyan et al. 2009b)

$$\mathcal{P}(\nu,\lambda_1,\lambda_2)=\frac{2\sqrt{J_2}}{\pi\sqrt{1-\gamma^2}}\exp\left(-\frac{1}{2}\left(\frac{\nu+\gamma I_1}{\sqrt{1-\gamma^2}}\right)^2-\frac{1}{2}I_1^2-J_2\right), \quad (A.1)$$

where $I_1 = \lambda_1 + \lambda_2$ and $J_2 = (\lambda_1 - \lambda_2)^2$, one can show that the PDF for a peak to have height ν and geometry $0 > \lambda_1 > \lambda_2$ reads (Bardeen et al. 1986; Codis et al. 2015)

$$\mathcal{P}(\nu,\lambda_1,\lambda_2|\mathrm{pk}) = \frac{8\sqrt{3}(\lambda_1-\lambda_2)\lambda_1\lambda_2}{\pi\sqrt{1-\gamma^2}}\times$$
$$\exp\left(-\frac{1}{2}\left(\frac{\nu+\gamma(\lambda_1+\lambda_2)}{\sqrt{1-\gamma^2}}\right)^2-\frac{1}{2}(\lambda_1+\lambda_2)^2-(\lambda_1-\lambda_2)^2\right). \quad (A.2)$$

It has to be emphasized that here we do impose exactly the peak constraint given by Eq. (24). The most likely value of the peak height and curvatures is therefore given by $\nu_\star = \sqrt{7/3}\,\gamma$, $\lambda_{1,2\star} = (-\sqrt{7/3} \pm \sqrt{1/3})/2$ which corresponds to an ellipticity $e_\star = 1/(2\sqrt{7})$.

If ν is fixed e.g to a rare value $\nu_r = 3$, the maximum of the PDF given by Eq. (A.2) is changed to $\lambda_{1r} = -0.94$ and $\lambda_{2r} = -1.6$ so that the ellipticity of the peak is given by $e_r = 0.13$, independently from the spectral parameter γ. The evolution of the most likely peak curvatures as a function of height is shown in Fig A.1. In particular, it illustrates the well-known result that high peaks are increasingly spherical.

Bibliography

Abadi, M. G., Moore, B., & Bower, R. G. 1999, MNRAS, 308, 947 21

Abbott, T., Abdalla, F. B., Allam, S., et al. 2016, Phys. Rev. D, 94, 022001 55

Agertz, O., Moore, B., Stadel, J., et al. 2007, MNRAS, 380, 963 39

Agertz, O., Teyssier, R., & Moore, B. 2011, MNRAS, 410, 1391 41

Aihara, H., Arimoto, N., Armstrong, R., et al. 2018a, Publications of the Astronomical Society of Japan, 70, S4 51

Aihara, H., Armstrong, R., Bickerton, S., et al. 2018b, Publications of the Astronomical Society of Japan, 70, S8 51

Akenine-Möller, T., Haines, E., & Hoffman, N. 2008, Real-Time Rendering 3rd Edition (Natick, MA, USA: A. K. Peters, Ltd.), 1045 65

Aldering, S. C. G. et al. 2004 [arXiv:astro-ph/0405232] 29

Allgood, B., Flores, R. A., Primack, J. R., et al. 2006, MNRAS, 367, 1781 15

Alsing, J., Heavens, A., & Jaffe, A. H. 2017, MNRAS, 466, 3272 55

Anderson, L., Aubourg, É., Bailey, S., et al. 2014, MNRAS, 441, 24 28

Angulo, R. E., Chen, R., Hilbert, S., & Abel, T. 2014, MNRAS, 444, 2925 63

Angulo, R. E., Springel, V., White, S. D. M., et al. 2012, MNRAS, 426, 2046 36, 38

Aragón-Calvo, M. A., van de Weygaert, R., & Jones, B. J. T. 2010, MNRAS, 408, 2163 68

Astier, P., Guy, J., Regnault, N., et al. 2005, in American Astronomical Society Meeting Abstracts, Vol. 207, 15.04 29

Aubert, D., Amara, A., & Metcalf, R. B. 2007, MNRAS, 376, 113 63, 65, 92, 93

Aubert, D., Pichon, C., & Colombi, S. 2004, MNRAS, 352, 376 38

Bacon, D. J., Refregier, A. R., & Ellis, R. S. 2000, MNRAS, 318, 625 54

Baldry, I. K., Balogh, M. L., Bower, R. G., et al. 2006, MNRAS, 373, 469 21

Baldry, I. K., Glazebrook, K., Brinkmann, J., et al. 2004, ApJ, 600, 681 18

Balestra, I., Mercurio, A., Sartoris, B., et al. 2016, ApJS, 224, 33 30

Bamba, K., Capozziello, S., Nojiri, S., & Odintsov, S. D. 2012, Ap&SS, 342, 155 6

Bardeen, J. M., Bond, J. R., Kaiser, N., & Szalay, A. S. 1986, ApJ, 304, 15 23

Barnes, J. & Hut, P. 1986, Nature, 324, 446 35

Barreira, A., Llinares, C., Bose, S., & Li, B. 2016, Journal of Cosmology and Astro-Particle Physics, 2016, 001 62

Bartelmann, M. 1995, A&A, 303, 643 52

Bartelmann, M. & Schneider, P. 2001, Phys. Rep., 340, 291 45, 47

Baugh, C. M., Cole, S., & Frenk, C. S. 1996, MNRAS, 283, 1361 18

Becker, M. R. 2013, MNRAS, 435, 115 61

Begeman, K. G., Broeils, A. H., & Sanders, R. H. 1991, MNRAS, 249, 523 30

Behroozi, P. S., Conroy, C., & Wechsler, R. H. 2010a, ApJ, 717, 379 18, 20, 21

Behroozi, P. S., Conroy, C., & Wechsler, R. H. 2010b, ApJ, 717, 379 20

Behroozi, P. S., Wechsler, R. H., & Conroy, C. 2013, ApJ, 770, 57 20

Belokurov, V., Walker, M. G., Evans, N. W., et al. 2010, ApJ, 712, L103 33

Belokurov, V., Walker, M. G., Evans, N. W., et al. 2009, MNRAS, 397, 1748 33

Belokurov, V., Zucker, D. B., Evans, N. W., et al. 2006, ApJ, 647, L111 33

Benson, A. J., Frenk, C. S., Lacey, C. G., Baugh, C. M., & Cole, S. 2002, MNRAS, 333, 177 33

Berlind, A. A. & Weinberg, D. H. 2002, ApJ, 575, 587 20, 24, 38

Bernardeau, F. 1998, ArXiv e-prints, astro 6

Bernardeau, F. 2013, ArXiv e-prints [[arXiv]1311.2724] 11

Bernardeau, F., Colombi, S., Gaztañaga, E., & Scoccimarro, R. 2002, Phys. Rep., 367, 1 11, 22

Bernardeau, F. & Kofman, L. 1995, ApJ, 443, 479 22

Bernardeau, F., Pichon, C., & Codis, S. 2014, Phys. Rev. D, 90, 103519 22

Bernardeau, F. & Valageas, P. 2010, Phys. Rev. D, 81, 043516 9

Bernardeau, F., van Waerbeke, L., & Mellier, Y. 1997, A&A, 322, 1 45

Bertone, G., Hooper, D., & Silk, J. 2005, Phys. Rep., 405, 279 30

Bertschinger, E. 1998, Annual Review of Astronomy and Astrophysics, 36, 599 35

Betoule, M., Kessler, R., Guy, J., et al. 2014, A&A, 568, A22 29

Beutler, F., Blake, C., Colless, M., et al. 2011, MNRAS, 416, 3017 28

Bhattacharya, S., Habib, S., Heitmann, K., & Vikhlinin, A. 2013, ApJ, 766, 32 52

Birnboim, Y. & Dekel, A. 2003, MNRAS, 345, 349 18

Blake, C. & Glazebrook, K. 2003, ApJ, 594, 665 28

Blandford, R. & Narayan, R. 1986, ApJ, 310, 568 49, 61

Blandford, R. D., Saust, A. B., Brainerd, T. G., & Villumsen, J. V. 1991, MNRAS, 251, 600 55

Blas, D., Lesgourgues, J., & Tram, T. 2011, J. Cosmology Astropart. Phys., 7, 034 23, 24, 55, 72

Blot, L., Crocce, M., Sefusatti, E., et al. 2018, ArXiv e-prints, arXiv:1806.09497 119

Bode, P., Ostriker, J. P., & Turok, N. 2001, ApJ, 556, 93 13, 30

Boltzmann, L. 1884, Annalen der Physik, 258, 291 3

Bond, J. R., Cole, S., Efstathiou, G., & Kaiser, N. 1991, ApJ, 379, 440 23

Bond, J. R., Kofman, L., & Pogosyan, D. 1996, Nature, 380, 603 69

Borriello, A. & Salucci, P. 2001, MNRAS, 323, 285 31

Bose, S., Hellwing, W. A., Frenk, C. S., et al. 2016, MNRAS, 455, 318 13, 14

Bower, R. G., Benson, A. J., Malbon, R., et al. 2006, MNRAS, 370, 645 38

Boylan-Kolchin, M., Bullock, J. S., & Kaplinghat, M. 2011, MNRAS, 415, L40 33

Boylan-Kolchin, M., Springel, V., White, S. D. M., Jenkins, A., & Lemson, G. 2009, MNRAS, 398, 1150 36, 37

Bradač, M., Lombardi, M., & Schneider, P. 2004, A&A, 424, 13 63

Bradač, M., Schneider, P., Lombardi, M., & Erben, T. 2005, A&A, 437, 39 52

Brandt, T. D. 2016, ApJ, 824, L31 5

Brown, M. L., Taylor, A. N., Bacon, D. J., et al. 2003, MNRAS, 341, 100 55

Bruzual, G. & Charlot, S. 2003, MNRAS, 344, 1000 108

Bryan, G. L. & Norman, M. L. 1998, ApJ, 495, 80 13

Bryan, G. L., Norman, M. L., O'Shea, B. W., et al. 2014, ApJS, 211, 19 39

Bullock, J. S., Kolatt, T. S., Sigad, Y., et al. 2001, MNRAS, 321, 559 13, 14

Burkert, A. 1995, ApJ, 447, L25 32

Burkert, A. 2000, ApJ, 534, L143 16

Byrd, G. & Valtonen, M. 1990, ApJ, 350, 89 21

Carlberg, R. G., Yee, H. K. C., Ellingson, E., et al. 1996, ApJ, 462, 32 30

Carlson, J. & White, M. 2010, The Astrophysical Journal Supplement Series, 190, 311 59

Carrasco, J. J. M., Hertzberg, M. P., & Senatore, L. 2012, Journal of High Energy Physics, 2012, 82 118

Cen, R., Dong, F., Bode, P., & Ostriker, J. P. 2004, ArXiv Astrophysics e-prints [astro-ph/0403352] 24

Chabrier, G. 2003, Publications of the Astronomical Society of the Pacific, 115, 763 108

Chang, C. & Jain, B. 2014, MNRAS, 443, 102 114

Chang, C., Jarvis, M., Jain, B., et al. 2013, MNRAS, 434, 2121 57

Chang, C., Pujol, A., Gaztañaga, E., et al. 2016, MNRAS, 459, 3203 24

Chen, Y.-C., Ho, S., Blazek, J., et al. 2018, ArXiv e-prints [[arXiv]1805.00159] 114

Chisari, N., Laigle, C., Codis, S., et al. 2016, MNRAS, 461, 2702 113

Chisari, N. E., Koukoufilippas, N., Jindal, A., et al. 2017, MNRAS, 472, 1163 41

Chisari, N. E., Richardson, M. L. A., Devriendt, J., et al. 2018, ArXiv e-prints, arXiv:1801.08559 44

Choudhury, T. R. & Padmanabhan, T. 2005, A&A, 429, 807 29

Clerkin, L., Kirk, D., Lahav, O., Abdalla, F. B., & Gaztañaga, E. 2015, MNRAS, 448, 1389 24

Clowe, D., Bradač, M., Gonzalez, A. H., et al. 2006, ApJ, 648, L109 52, 53

Clowe, D., Gonzalez, A., & Markevitch, M. 2004, ApJ, 604, 596 52

Clowe, D., Luppino, G. A., Kaiser, N., Henry, J. P., & Gioia, I. M. 1998, ApJ, 497, L61 52

Clowe, D. & Schneider, P. 2001, ArXiv e-prints, astro 52

Codis, S., Gavazzi, R., Dubois, Y., et al. 2015a, MNRAS, 448, 3391 41, 113

Codis, S., Gavazzi, R., Pichon, C., & Gouin, C. 2017, A&A, 605, A80 vii, ix, xii, 69, 119

Codis, S., Pichon, C., Devriendt, J., et al. 2012a, MNRAS, 427, 3320 22

Codis, S., Pichon, C., Devriendt, J., et al. 2012b, MNRAS, 427, 3320 41

Codis, S., Pichon, C., & Pogosyan, D. 2015b, MNRAS, 452, 3369 41, 113

Codis, S., Pogosyan, D., & Pichon, C. 2018, ArXiv e-prints [[arXiv]1803.11477] 67, 68, 74

Colavincenzo, M., Sefusatti, E., Monaco, P., et al. 2018, ArXiv e-prints, arXiv:1806.09499 119

Cole, S. & Lacey, C. 1996, MNRAS, 281, 716 13

Cole, S., Lacey, C. G., Baugh, C. M., & Frenk, C. S. 2000, MNRAS, 319, 168 18, 38

Cole, S., Norberg, P., Baugh, C. M., et al. 2001, MNRAS, 326, 255 18

Cole, S., Percival, W. J., Peacock, J. A., et al. 2005, MNRAS, 362, 505 28

Conroy, C., Wechsler, R. H., & Kravtsov, A. V. 2006, ApJ, 647, 201 20

Cooray, A. & Sheth, R. 2002, Phys. Rep., 372, 1 24, 25

Couchman, H. M. P. 1991, ApJ, 368, L23 35

Couchman, H. M. P., Barber, A. J., & Thomas, P. A. 1999, MNRAS, 308, 180 62

Coupon, J., Arnouts, S., van Waerbeke, L., et al. 2015, MNRAS, 449, 1352 20, 38, 54

Croft, R. A. C., Romeo, A., & Metcalf, R. B. 2018, MNRAS, 477, 1814 115

Croton, D. J., Gao, L., & White, S. D. M. 2007, MNRAS, 374, 1303 15, 24

Croton, D. J., Springel, V., White, S. D. M., et al. 2006a, MNRAS, 365, 11 20

Croton, D. J., Springel, V., White, S. D. M., et al. 2006b, MNRAS, 365, 11 38

Das, S. & Bode, P. 2008, ApJ, 682, 1 61

Davidzon, I., Ilbert, O., Laigle, C., et al. 2017, A&A, 605, A70 114

de Blok, W. J. G. & Bosma, A. 2002, A&A, 385, 816 31

de Blok, W. J. G., McGaugh, S. S., & Rubin, V. C. 2001, AJ, 122, 2396 31

de Blok, W. J. G., Walter, F., Brinks, E., et al. 2008, AJ, 136, 2648 32

de Jong, J. T. A., Kuijken, K., Applegate, D., et al. 2013, The Messenger, 154, 44 53

de Lapparent, V., Geller, M. J., & Huchra, J. P. 1986, ApJ, 302, L1 26

De Lucia, G., Springel, V., White, S. D. M., Croton, D., & Kauffmann, G. 2006, MNRAS, 366, 499 18, 38

Dekel, A. & Birnboim, Y. 2006, MNRAS, 368, 2 18

Dekel, A., Birnboim, Y., Engel, G., et al. 2009, Nature, 457, 451 17

Dekel, A. & Silk, J. 1986, ApJ, 303, 39 18

DES Collaboration, Abbott, T. M. C., Abdalla, F. B., et al. 2017, ArXiv e-prints, arXiv:1708.01530 51, 118

Desjacques, V., Crocce, M., Scoccimarro, R., & Sheth, R. K. 2010, Phys. Rev. D, 82, 103529 24

Despali, G., Giocoli, C., & Tormen, G. 2014, MNRAS, 443, 3208 15, 16, 68

Despali, G. & Vegetti, S. 2017, MNRAS, 469, 1997 43, 44

Di Cintio, A., Brook, C. B., Macciò, A. V., et al. 2014, MNRAS, 437, 415 43

Diemand, J., Kuhlen, M., Madau, P., et al. 2008, Nature, 454, 735 15

Diemand, J., Zemp, M., Moore, B., Stadel, J., & Carollo, C. M. 2005, MNRAS, 364, 665 13

Diemer, B. & Kravtsov, A. V. 2014, ApJ, 789, 1 13

Dietrich, J. P., Werner, N., Clowe, D., et al. 2012, Nature, 487, 202 67

Dolag, K., Borgani, S., Murante, G., & Springel, V. 2009, MNRAS, 399, 497 43

Dressler, A. 1980, ApJ, 236, 351 21

Driver, S. P., Hill, D. T., Kelvin, L. S., et al. 2011, MNRAS, 413, 971 53

Drlica-Wagner, A., Bechtol, K., Rykoff, E. S., et al. 2015, ApJ, 813, 109 33

Dubinski, J. & Carlberg, R. G. 1991, ApJ, 378, 496 15

Dubois, Y., Devriendt, J., Slyz, A., & Teyssier, R. 2012, MNRAS, 420, 2662 40

Dubois, Y., Gavazzi, R., Peirani, S., & Silk, J. 2013, MNRAS, 433, 3297 41

Dubois, Y., Peirani, S., Pichon, C., et al. 2016, MNRAS, 463, 3948 41

Dubois, Y., Pichon, C., Welker, C., et al. 2014, MNRAS, 444, 1453 vii, ix, 40, 41, 42, 92, 113

Duffy, A. R., Schaye, J., Kay, S. T., & Dalla Vecchia, C. 2008, MNRAS, 390, L64 13

Duffy, A. R., Schaye, J., Kay, S. T., et al. 2010, MNRAS, 405, 2161 43

Dvornik, A., Cacciato, M., Kuijken, K., et al. 2017, MNRAS, 468, 3251 91

Dyson, F. W., Eddington, A. S., & Davidson, C. 1920, Philosophical Transactions of the Royal Society of London Series A, 220, 291 45

Efstathiou, G., Davis, M., White, S. D. M., & Frenk, C. S. 1985, The Astrophysical Journal Supplement Series, 57, 241 35

Einasto, J. 1965, Trudy Astrofizicheskogo Instituta Alma-Ata, 5, 87 13

Einasto, J., Klypin, A. A., Saar, E., & Shandarin, S. F. 1984, MNRAS, 206, 529 13

Einstein, A. 1905, Annalen der Physik, 322, 891 1

Einstein, A. 1907, Annalen der Physik, 328, 371 3

Einstein, A. 1916, Annalen der Physik, 354, 769 2, 45

Eisenstein, D. J. & Hu, W. 1998, ApJ, 496, 605 23

Eisenstein, D. J. et al. 2005, Astrophys. J., 633, 560 28, 29

Elbert, O. D., Bullock, J. S., Garrison-Kimmel, S., et al. 2015, MNRAS, 453, 29 32

Erben, T. & CFHTLenS Collaboration. 2012, in American Astronomical Society Meeting Abstracts, Vol. 219, American Astronomical Society Meeting Abstracts #219, 130.09 51

Erben, T., Hildebrandt, H., Miller, L., et al. 2013, MNRAS, 433, 2545 51

Etherington, I. M. H. 1933, Philosophical Magazine, 15, 761 49

Evans, C. J., Barbuy, B., Bonifacio, P., Chemla, F., & al. 2012, in Society of Photo-Optical Instrumentation Engineers (SPIE) Conference Series, Vol. 8446, Ground-based and Airborne Instrumentation for Astronomy IV, 84467K 115

Evans, N. W. & Wilkinson, M. I. 2000, MNRAS, 316, 929 30

Evrard, A. E. 1988, MNRAS, 235, 911 39

Evrard, A. E., Metzler, C. A., & Navarro, J. F. 1996, ApJ, 469, 494 30

Faber, S. M., Worthey, G., & Gonzales, J. J. 1992, in IAU Symposium, Vol. 149, The Stellar Populations of Galaxies, ed. B. Barbuy & A. Renzini, 255 18

Fabian, A. C. 2012, Annual Review of Astronomy and Astrophysics, 50, 455 20

Falco, E. E., Gorenstein, M. V., & Shapiro, I. I. 1985, ApJ, 289, L1 49

Fall, S. M. & Efstathiou, G. 1980, MNRAS, 193, 189 17

Faltenbacher, A. & White, S. D. M. 2010, ApJ, 708, 469 15

Ferreras, I., Charlot, S., & Silk, J. 1999, ApJ, 521, 81 18

Fosalba, P., Gaztañaga, E., Castander, F. J., & Crocce, M. 2015, MNRAS, 447, 1319 59, 91

Fosalba, P., Gaztañaga, E., Castander, F. J., & Manera, M. 2008, MNRAS, 391, 435 61

Frenk, C. S., White, S. D. M., Davis, M., & Efstathiou, G. 1988, ApJ, 327, 507 13

Friedmann, A. 1922, Zeitschrift fur Physik, 10, 377 2

Friedmann, A. 1924, Zeitschrift fur Physik, 21, 326 2

Furlong, M., Bower, R. G., Theuns, T., et al. 2015, MNRAS, 450, 4486 41

Ganeshaiah Veena, P., Cautun, M., van de Weygaert, R., et al. 2018, ArXiv e-prints [[arXiv]1805.00033] 113

Gao, L., Frenk, C. S., Boylan-Kolchin, M., et al. 2011, MNRAS, 410, 2309 15

Gao, L., Navarro, J. F., Frenk, C. S., et al. 2012, MNRAS, 425, 2169 36

Gao, L., White, S. D. M., Jenkins, A., Stoehr, F., & Springel, V. 2004, MNRAS, 355, 819 15

Gardiner, T. A. & Stone, J. M. 2005, Journal of Computational Physics, 205, 509 39

Garnavich, P. M., Kirshner, R. P., Challis, P., et al. 1998, ApJ, 493, L53 29

Genel, S., Vogelsberger, M., Springel, V., et al. 2014, MNRAS, 445, 175 41

Gentile, G., Salucci, P., Klein, U., Vergani, D., & Kalberla, P. 2004, MNRAS, 351, 903 32

Ghigna, S., Moore, B., Governato, F., et al. 2000, ApJ, 544, 616 15

Gil-Marín, H., Percival, W. J., Cuesta, A. J., et al. 2016, MNRAS, 460, 4210 28

Giocoli, C., Jullo, E., Metcalf, R. B., et al. 2016a, MNRAS, 461, 209 59

Giocoli, C., Jullo, E., Metcalf, R. B., et al. 2016b, MNRAS, 461, 209 62, 64, 91

Giocoli, C., Tormen, G., & Sheth, R. K. 2012, MNRAS, 422, 185 13

Giocoli, C., Tormen, G., Sheth, R. K., & van den Bosch, F. C. 2010, MNRAS, 404, 502 15

Glazebrook, K. & Blake, C. 2005, ApJ, 631, 1 28

Gnedin, O. Y. & Zhao, H. 2002, MNRAS, 333, 299 32

Gonzalez, A. H., Zaritsky, D., & Zabludoff, A. I. 2007, ApJ, 666, 147 30

Gouin, C., Gavazzi, R., Codis, S., et al. 2017, A&A, 605, A27 vii, ix, xii, 56, 119, 125

Governato, F., Zolotov, A., Pontzen, A., et al. 2012, MNRAS, 422, 1231 33

Graham, A. W., Merritt, D., Moore, B., Diemand, J., & Terzić, B. 2006, AJ, 132, 2701 13

Gunn, J. E. & Gott, J. Richard, I. 1972, ApJ, 176, 1 21

Guo, Q., White, S., Boylan-Kolchin, M., et al. 2011, MNRAS, 413, 101 33, 38

Gurbatov, S. N., Saichev, A. I., & Shandarin, S. F. 1989, MNRAS, 236, 385 9

Gurbatov, S. N., Saichev, A. I., & Shandarin, S. F. 2012, Physics Uspekhi, 55, 223 9

Guzik, J. & Seljak, U. 2001, MNRAS, 321, 439 54

Haardt, F. & Madau, P. 1996, ApJ, 461, 20 39

Hahn, O., Teyssier, R., & Carollo, C. M. 2010, MNRAS, 405, 274 41

Hamana, T. & Mellier, Y. 2001, MNRAS, 327, 169 59

Hamana, T., Yoshida, N., Suto, Y., & Evrard, A. E. 2001, ApJ, 561, L143 24

Hatfield, P. W., Lindsay, S. N., Jarvis, M. J., et al. 2016, MNRAS, 459, 2618 114

Hayashi, E., Navarro, J. F., Power, C., et al. 2004, MNRAS, 355, 794 32

Hayashi, E., Navarro, J. F., & Springel, V. 2007, MNRAS, 377, 50 15

Hayashi, E., Navarro, J. F., Taylor, J. E., Stadel, J., & Quinn, T. 2003, ApJ, 584, 541 15

Hearin, A. P., Zentner, A. R., Berlind, A. A., & Newman, J. A. 2013, MNRAS, 433, 659 38

Heckman, T. M. & Best, P. N. 2014, Annual Review of Astronomy and Astrophysics, 52, 589 20

Hellwing, W. A., Schaller, M., Frenk, C. S., et al. 2016, MNRAS, 461, L11 41

Hennawi, J. F. & Spergel, D. N. 2005, ApJ, 624, 59 59

Henriques, B. M. B., White, S. D. M., Thomas, P. A., et al. 2015, MNRAS, 451, 2663 38

Hernquist, L. 1990, ApJ, 356, 359 13

Heymans, C., Brown, M. L., Barden, M., et al. 2005, MNRAS, 361, 160 55

Heymans, C., Grocutt, E., Heavens, A., et al. 2013, MNRAS, 432, 2433 56

Heymans, C., Rowe, B., Hoekstra, H., et al. 2012a, MNRAS, 421, 381 51

Heymans, C., Van Waerbeke, L., Bacon, D., et al. 2006, MNRAS, 368, 1323 52

Heymans, C., Van Waerbeke, L., Miller, L., et al. 2012b, MNRAS, 427, 146 51

Hicken, M., Wood-Vasey, W. M., Blondin, S., et al. 2009, ApJ, 700, 1097 29

Hilbert, S., Hartlap, J., White, S. D. M., & Schneider, P. 2009, A&A, 499, 31 59, 60, 61, 62, 64, 92

Hilbert, S., White, S. D. M., Hartlap, J., & Schneider, P. 2007, MNRAS, 382, 121 59

Hildebrandt, H., Erben, T., Kuijken, K., et al. 2012, MNRAS, 421, 2355 51

Hildebrandt, H., Viola, M., Heymans, C., et al. 2017, MNRAS, 465, 1454 56

Hockney, R. W. & Eastwood, J. W. 1981, Computer Simulation Using Particles 35

Hoekstra, H., Franx, M., & Kuijken, K. 2000, ApJ, 532, 88 52

Hoekstra, H., Franx, M., Kuijken, K., & Squires, G. 1998, ApJ, 504, 636 52

Hoekstra, H., Hsieh, B. C., Yee, H. K. C., Lin, H., & Gladders, M. D. 2005, ApJ, 635, 73 53

Hoffmann, K., Bel, J., & Gaztañaga, E. 2017, MNRAS, 465, 2225 24

Hogg, D. W., Blanton, M. R., Eisenstein, D. J., et al. 2003, ApJ, 585, L5 21

Hopkins, P. F., Hernquist, L., Cox, T. J., et al. 2006, The Astrophysical Journal Supplement Series, 163, 1 18

Hopkins, P. F., Kereš, D., Oñorbe, J., et al. 2014, MNRAS, 445, 581 41

Hubble, E. 1929, Proceedings of the National Academy of Science, 15, 168 2

Hubble, E. P. 1936, Realm of the Nebulae 17

Hudson, M. J., Gillis, B. R., Coupon, J., et al. 2015, MNRAS, 447, 298 54

Hut, P., Makino, J., & McMillan, S. 1995, ApJ, 443, L93 35

Irwin, M. J., Belokurov, V., Evans, N. W., et al. 2007, ApJ, 656, L13 33

Jain, B. & Seljak, U. 1997a, ApJ, 484, 560 45

Jain, B. & Seljak, U. 1997b, ApJ, 484, 560 60

Jain, B., Seljak, U., & White, S. 2000, ApJ, 530, 547 59, 61

Jee, M. J., Tyson, J. A., Schneider, M. D., et al. 2013, ApJ, 765, 74 56

Jenkins, A., Frenk, C. S., White, S. D. M., et al. 2001, MNRAS, 321, 372 12

Jing, Y. P. & Suto, Y. 2000, ApJ, 529, L69 13

Jing, Y. P. & Suto, Y. 2002, ApJ, 574, 538 13, 15, 68

Johnston, D. E., Sheldon, E. S., Wechsler, R. H., et al. 2007, ArXiv e-prints, arXiv:0709.1159 52

Jose, C., Lacey, C. G., & Baugh, C. M. 2016, MNRAS, 463, 270 24

Jungman, G., Kamionkowski, M., & Griest, K. 1996, Phys. Rep., 267, 195 30

Kaiser, N. 1984, ApJ, 284, L9 23, 24

Kaiser, N. 1992, ApJ, 388, 272 55

Kaiser, N. & Squires, G. 1993, ApJ, 404, 441 48, 52

Kaiser, N., Squires, G., & Broadhurst, T. 1995, ApJ, 449, 460 52

Kauffmann, G. & White, S. D. M. 1993, MNRAS, 261 13

Kaviraj, S., Laigle, C., Kimm, T., et al. 2017, MNRAS, 467, 4739 41, 43, 94, 108, 109, 110

Kennicutt, Jr., R. C. 1998, ApJ, 498, 541 18, 40

Kereš, D., Katz, N., Weinberg, D. H., & Davé, R. 2005, MNRAS, 363, 2 17

Khandai, N., Di Matteo, T., Croft, R., et al. 2015, MNRAS, 450, 1349 40

Kilbinger, M. 2015, Reports on Progress in Physics, 78, 086901 45

Kilbinger, M., Fu, L., Heymans, C., et al. 2013, MNRAS, 430, 2200 56, 57

Kilbinger, M., Heymans, C., Asgari, M., et al. 2017, MNRAS, 472, 2126 61

Kim, J., Park, C., Rossi, G., Lee, S. M., & Gott, J. Richard, I. 2011, Journal of Korean Astronomical Society, 44, 217 36

Kim, S. Y., Peter, A. H. G., & Hargis, J. R. 2017, ArXiv e-prints, arXiv:1711.06267 33

Kitching, T. D., Heavens, A. F., Alsing, J., et al. 2014, MNRAS, 442, 1326 55

Kitching, T. D., Heavens, A. F., Taylor, A. N., et al. 2007, MNRAS, 376, 771 55

Kleinheinrich, M., Schneider, P., Rix, H. W., et al. 2006, A&A, 455, 441 53

Klypin, A., Kravtsov, A. V., Valenzuela, O., & Prada, F. 1999, ApJ, 522, 82 15, 33, 34

Klypin, A., Yepes, G., Gottlöber, S., Prada, F., & Heß, S. 2016, MNRAS, 457, 4340 13, 36

Klypin, A., Zhao, H., & Somerville, R. S. 2002, ApJ, 573, 597 30, 31

Klypin, A. A., Trujillo-Gomez, S., & Primack, J. 2011, ApJ, 740, 102 15

Knebe, A., Knollmann, S. R., Muldrew, S. I., et al. 2011, MNRAS, 415, 2293 38

Kofman, L., Pogosyan, D., Shandarin, S. F., & Melott, A. L. 1992, ApJ, 393, 437 9

Köhlinger, F., Viola, M., Joachimi, B., et al. 2017, MNRAS, 471, 4412 55

Köhlinger, F., Viola, M., Valkenburg, W., et al. 2016, MNRAS, 456, 1508 55

Komissarov, S. S. 1999, MNRAS, 303, 343 39

Koposov, S., Belokurov, V., Evans, N. W., et al. 2008, ApJ, 686, 279 33

Koposov, S. E., Belokurov, V., Torrealba, G., & Evans, N. W. 2015, ApJ, 805, 130 33

Kormendy, J. & Ho, L. C. 2013, Annual Review of Astronomy and Astrophysics, 51, 511 20

Kraljic, K., Arnouts, S., Pichon, C., et al. 2018a, MNRAS, 474, 547 22

Kraljic, K., Pichon, C., Dubois, Y., et al. 2018b, MNRAS, 3061 22

Kravtsov, A. V. 2009, Advances in Astronomy, in press [[arXiv]0906.3295] 33

Kravtsov, A. V., Berlind, A. A., Wechsler, R. H., et al. 2004, ApJ, 609, 35 38

Kravtsov, A. V. & Klypin, A. A. 1999, ApJ, 520, 437 24

Kravtsov, A. V., Klypin, A. A., Bullock, J. S., & Primack, J. R. 1998, ApJ, 502, 48 30

Kuhlen, M., Diemand, J., Madau, P., & Zemp, M. 2008, in Journal of Physics Conference Series, Vol. 125, Journal of Physics Conference Series, 012008 36

Kuijken, K., Heymans, C., Hildebrandt, H., et al. 2015, MNRAS, 454, 3500 51

Laigle, C., McCracken, H. J., Ilbert, O., et al. 2016, ApJS, 224, 24 55

Laigle, C., Pichon, C., Arnouts, S., et al. 2018, MNRAS, 474, 5437 22

Laigle, C., Pichon, C., Codis, S., et al. 2015, MNRAS, 446, 2744 113

Larson, R. B. 1974, MNRAS, 169, 229 18

Laureijs, R., Amiaux, J., Arduini, S., et al. 2011, ArXiv e-prints [[arXiv]1110.3193] 43, 57, 58, 69, 118

Laureijs, R., Gondoin, P., Duvet, L., et al. 2012, in Society of Photo-Optical Instrumentation Engineers (SPIE) Conference Series, Vol. 8442, Society of Photo-Optical Instrumentation Engineers (SPIE) Conference Series 45

Leauthaud, A., Saito, S., Hilbert, S., et al. 2017, MNRAS, 467, 3024 vii, x, 92

Leauthaud, A., Tinker, J., Behroozi, P. S., Busha, M. T., & Wechsler, R. H. 2011, ApJ, 738, 45 20

Leauthaud, A., Tinker, J., Bundy, K., et al. 2012, ApJ, 744, 159 20, 54

Lee, J., Kim, S., Jeong, H., et al. 2018, ApJ, 864, 69 113

Lee, K.-G., Hennawi, J. F., Stark, C., & Prochaska, e. a. 2014, ApJ, 795, L12 115

Leitherer, C., Schaerer, D., Goldader, J. D., et al. 1999, The Astrophysical Journal Supplement Series, 123, 3 40

Lemaître, A. G. 1931, Monthly Notices of the Royal Astronomical Society, 91, 483 2

Lesgourgues, J. 2011, ArXiv e-prints [[arXiv]1104.2932] 23, 55, 72

Li, C., Kauffmann, G., Jing, Y. P., et al. 2006a, MNRAS, 368, 21 24

Li, G.-L., Mao, S., Jing, Y. P., Kang, X., & Bartelmann, M. 2006b, ApJ, 652, 43 63

Limber, D. N. 1953, ApJ, 117, 134 55

Lin, H., Dodelson, S., Seo, H.-J., et al. 2012, ApJ, 761, 15 55

Linde, A. 2014, ArXiv e-prints [[arXiv]1402.0526] 6

Lippich, M., Sánchez, A. G., Colavincenzo, M., et al. 2018, ArXiv e-prints, arXiv:1806.09477 119

Lombardi, M. & Bertin, G. 1998, A&A, 335, 1 52

Lovell, M. R., Frenk, C. S., Eke, V. R., et al. 2014, MNRAS, 439, 300 16

Ludlow, A. D., Bose, S., Angulo, R. E., et al. 2016, MNRAS, 460, 1214 13

Ludlow, A. D., Navarro, J. F., Angulo, R. E., et al. 2014, MNRAS, 441, 378 36

Ludlow, A. D., Navarro, J. F., Boylan-Kolchin, M., et al. 2013, MNRAS, 432, 1103 13

Luppino, G. A. & Kaiser, N. 1997, ApJ, 475, 20 52

Macciò, A. V., Kang, X., Fontanot, F., et al. 2010, MNRAS, 402, 1995 33

MacCrann, N., Zuntz, J., Bridle, S., Jain, B., & Becker, M. R. 2015, MNRAS, 451, 2877 57

Madau, P., Shen, S., & Governato, F. 2014, ApJ, 789, L17 33

Madgwick, D. S., Hawkins, E., Lahav, O., et al. 2003, MNRAS, 344, 847 24

Maiolino, R., Nagao, T., Grazian, A., et al. 2008, A&A, 488, 463 108

Mandelbaum, R., Seljak, U., Cool, R. J., et al. 2006a, MNRAS, 372, 758 30, 52, 54

Mandelbaum, R., Seljak, U., & Hirata, C. M. 2008, Journal of Cosmology and Astro-Particle Physics, 2008, 006 53

Mandelbaum, R., Seljak, U., Kauffmann, G., Hirata, C. M., & Brinkmann, J. 2006b, MNRAS, 368, 715 54

Mannucci, F., Cresci, G., Maiolino, R., Marconi, A., & Gnerucci, A. 2010, MNRAS, 408, 2115 108

Marinoni, C., Le Fèvre, O., Meneux, B., et al. 2005, A&A, 442, 801 24

Markevitch, M. 2006, in ESA Special Publication, Vol. 604, The X-ray Universe 2005, ed. A. Wilson, 723 53

Markevitch, M., Gonzalez, A. H., Clowe, D., et al. 2004, ApJ, 606, 819 52

Mashchenko, S., Couchman, H. M. P., & Wadsley, J. 2006, Nature, 442, 539 33

Matsubara, T. 1999, ApJ, 525, 543 24

Maturi, M. & Merten, J. 2013, A&A, 559, A112 67

Merritt, D., Graham, A. W., Moore, B., Diemand, J., & Terzić, B. 2006, AJ, 132, 2685 13

Merten, J., Coe, D., Dupke, R., et al. 2011, MNRAS, 417, 333 52

Metcalf, R. B. & Petkova, M. 2014, MNRAS, 445, 1942 64

Mihos, J. C. & Hernquist, L. 1996, ApJ, 464, 641 18

Mikkola, S. & Aarseth, S. 2002, Celestial Mechanics and Dynamical Astronomy, 84, 343 35

Miller, L. & CFHTLenS Collaboration. 2012, in American Astronomical Society Meeting Abstracts, Vol. 219, American Astronomical Society Meeting Abstracts #219, 130.03 51

Miralda-Escude, J. 1991, ApJ, 380, 1 55, 56

Mo, H. J., Mao, S., & White, S. D. M. 1998, MNRAS, 295, 319 17

Mo, H. J. & White, S. D. M. 1996, MNRAS, 282, 347 24

Mo, H. J. & White, S. D. M. 2002, MNRAS, 336, 112 11

Mohr, J. J., Mathiesen, B., & Evrard, A. E. 1999, ApJ, 517, 627 30

Monaghan, J. J. 1992, ARA&A, 30, 543 39

Moore, B. 1994, Nature, 370, 629 32, 34

Moore, B. 1999, Royal Society of London Philosophical Transactions Series A, 357, 3259 13

Moore, B., Ghigna, S., Governato, F., et al. 1999a, ApJ, 524, L19 15, 33

Moore, B., Katz, N., Lake, G., Dressler, A., & Oemler, A. 1996, Nature, 379, 613 21

Moore, B., Quinn, T., Governato, F., Stadel, J., & Lake, G. 1999b, MNRAS, 310, 1147 30

More, S., Kravtsov, A. V., Dalal, N., & Gottlöber, S. 2011, ApJS, 195, 4 36, 38

Moster, B. P., Macciò, A. V., Somerville, R. S., Johansson, P. H., & Naab, T. 2010a, MNRAS, 403, 1009 18

Moster, B. P., Naab, T., & White, S. D. M. 2013, MNRAS, 428, 3121 20

Moster, B. P., Naab, T., & White, S. D. M. 2018, MNRAS, 477, 1822 20

Moster, B. P., Somerville, R. S., Maulbetsch, C., et al. 2010b, ApJ, 710, 903 18, 20, 36

Muñoz, J. A., Madau, P., Loeb, A., & Diemand, J. 2009, MNRAS, 400, 1593 33

Muldrew, S. I., Pearce, F. R., & Power, C. 2011, MNRAS, 410, 2617 38

Navarro, J. F., Eke, V. R., & Frenk, C. S. 1996a, MNRAS, 283, L72 32

Navarro, J. F., Frenk, C. S., & White, S. D. M. 1996b, ApJ, 462, 563 12

Navarro, J. F., Frenk, C. S., & White, S. D. M. 1997, ApJ, 490, 493 12

Navarro, J. F., Hayashi, E., Power, C., et al. 2004, MNRAS, 349, 1039 13, 41

Neto, A. F., Gao, L., Bett, P., et al. 2007, MNRAS, 381, 1450 13, 14

Newman, A. B., Ellis, R. S., & Treu, T. 2015, ApJ, 814, 26 94

Newman, A. B., Treu, T., Ellis, R. S., & Sand, D. J. 2013, ApJ, 765, 25 94

Nunes, R. C., Pan, S., & Saridakis, E. N. 2016, Phys. Rev. D, 94, 023508 28

Oñorbe, J., Boylan-Kolchin, M., Bullock, J. S., et al. 2015, MNRAS, 454, 2092 43

Oemler, Augustus, J. 1974, ApJ, 194, 1 21

Oh, S.-H., de Blok, W. J. G., Brinks, E., Walter, F., & Kennicutt, Jr., R. C. 2011, AJ, 141, 193 32

Okabe, N., Takada, M., Umetsu, K., Futamase, T., & Smith, G. P. 2010, Publications of the Astronomical Society of Japan, 62, 811 52

Oman, K. A., Navarro, J. F., Fattahi, A., et al. 2015, MNRAS, 452, 3650 32

Omma, H., Binney, J., Bryan, G., & Slyz, A. 2004, MNRAS, 348, 1105 40

Ostriker, J. P. & Mark, J. W. K. 1968, ApJ, 151, 1075 30

Pace, F., Maturi, M., Meneghetti, M., et al. 2007, A&A, 471, 731 63

Palunas, P. & Williams, T. B. 2000, AJ, 120, 2884 32

Parker, L. C., Hoekstra, H., Hudson, M. J., van Waerbeke, L., & Mellier, Y. 2007, ApJ, 669, 21 53, 54

Parker, L. C., Hudson, M. J., Carlberg, R. G., & Hoekstra, H. 2005, ApJ, 634, 806 30, 52

Peacock, J. A., Cole, S., Norberg, P., et al. 2001, Nature, 410, 169 26

Peacock, J. A. & Smith, R. E. 2000, MNRAS, 318, 1144 24

Peebles, P. J. E. 1970, AJ, 75, 13 30

Peebles, P. J. E. 1980, The large-scale structure of the universe 7, 124

Peirani, S., Dubois, Y., Volonteri, M., et al. 2017, MNRAS, 472, 2153 43

Peirani, S., Sonnenfeld, A., Gavazzi, R., et al. 2018, ArXiv e-prints, arXiv:1801.09754 94

Peng, Y.-j., Lilly, S. J., Kovač, K., et al. 2010, ApJ, 721, 193 21

Perlmutter, S., Aldering, G., Goldhaber, G., et al. 1999, ApJ, 517, 565 29

Peter, A. H. G., Rocha, M., Bullock, J. S., & Kaplinghat, M. 2013, MNRAS, 430, 105 15

Peterson, J. R. & Fabian, A. C. 2006, Phys. Rep., 427, 1 21

Petkova, M., Metcalf, R. B., & Giocoli, C. 2014, MNRAS, 445, 1954 64

Pichon, C., Gay, C., Pogosyan, D., et al. 2010, in American Institute of Physics Conference Series, Vol. 1241, American Institute of Physics Conference Series, ed. J.-M. Alimi & A. Fuözfa, 1108–1117 68, 69

Pichon, C., Vergely, J. L., Rollinde, E., Colombi, S., & Petitjean, P. 2001, MNRAS, 326, 597 115

Pires, S., Starck, J. L., Amara, A., et al. 2009, MNRAS, 395, 1265 52

Planck Collaboration, Aghanim, N., Arnaud, M., et al. 2016a, A&A, 594, A11 26

Planck Collaboration, Aghanim, N., Arnaud, M., et al. 2016b, A&A, 594, A11 27, 32

Pogosyan, D., Pichon, C., Gay, C., et al. 2009, MNRAS, 396, 635 69

Pontzen, A. & Governato, F. 2012, MNRAS, 421, 3464 43

Pope, A. C., Matsubara, T., Szalay, A. S., et al. 2004, ApJ, 607, 655 28

Potter, D., Stadel, J., & Teyssier, R. 2017, Computational Astrophysics and Cosmology, 4, 2 36

Prada, F., Klypin, A. A., Cuesta, A. J., Betancort-Rijo, J. E., & Primack, J. 2012, MNRAS, 423, 3018 36

Press, W. H. & Schechter, P. 1974, ApJ, 187, 425 10

Randall, S. W., Markevitch, M., Clowe, D., Gonzalez, A. H., & Bradač, M. 2008, ApJ, 679, 1173 5, 52

Rau, S., Vegetti, S., & White, S. D. M. 2013, MNRAS, 430, 2232 63

Read, J. I. & Gilmore, G. 2005, MNRAS, 356, 107 32

Rhee, G., Valenzuela, O., Klypin, A., Holtzman, J., & Moorthy, B. 2004, ApJ, 617, 1059 32

Ricotti, M. 2003, MNRAS, 344, 1237 13

Riess, A. G., Filippenko, A. V., Challis, P., et al. 1998, AJ, 116, 1009 29

Riess, A. G., Macri, L., Casertano, S., et al. 2009, ApJ, 699, 539 29

Robertson, H. P. 1935, ApJ, 82, 284 2

Rocha, M., Peter, A. H. G., Bullock, J. S., et al. 2013, MNRAS, 430, 81 16, 32

Rood, H. J., Page, T. L., Kintner, E. C., & King, I. R. 1972, ApJ, 175, 627 30

Rosdahl, J., Katz, H., Blaizot, J., et al. 2018, MNRAS, 479, 994 114

Roszkowski, L., Sessolo, E. M., & Trojanowski, S. 2018, Reports on Progress in Physics, 81, 066201 5

Rubin, V. C., Burstein, D., Ford, W. K., J., & Thonnard, N. 1985, ApJ, 289, 81 30

Rubin, V. C., Ford, W. K., J., & Thonnard, N. 1980, ApJ, 238, 471 30

Rudd, D. H., Zentner, A. R., & Kravtsov, A. V. 2008, ApJ, 672, 19 41

Salpeter, E. E. 1955, ApJ, 121, 161 108

Salucci, P. & Burkert, A. 2000, ApJ, 537, L9 30

Salucci, P., Lapi, A., Tonini, C., et al. 2007, MNRAS, 378, 41 30

Sánchez-Conde, M. A. & Prada, F. 2014, MNRAS, 442, 2271 36

Sartoris, B., Biviano, A., Fedeli, C., et al. 2016, MNRAS, 459, 1764 58, 59, 66, 69

Sato, M., Hamana, T., Takahashi, R., et al. 2009, ApJ, 701, 945 59

Schaller, M., Frenk, C. S., Bower, R. G., et al. 2015, MNRAS, 451, 1247 43

Schawinski, K., Urry, C. M., Simmons, B. D., et al. 2014, MNRAS, 440, 889 18, 19

Schaye, J., Crain, R. A., Bower, R. G., et al. 2015, MNRAS, 446, 521 40

Schmidt, M. 1959, ApJ, 129, 243 18

Schneider, A. & Teyssier, R. 2015, Journal of Cosmology and Astro-Particle Physics, 2015, 049 119

Schneider, M. D., Frenk, C. S., & Cole, S. 2012, J. Cosmology Astropart. Phys., 5, 030 15

Schneider, P. & Bartelmann, M. 1997, MNRAS, 286, 696 67, 68

Schneider, P., Ehlers, J., & Falco, E. E. 1992, Gravitational Lenses 45, 53, 61

Schneider, P. & Seitz, C. 1995, A&A, 294, 411 50

Schneider, P. & Sluse, D. 2013, A&A, 559, A37 49

Schneider, P., van Waerbeke, L., Kilbinger, M., & Mellier, Y. 2002, A&A, 396, 1 56

Scoccimarro, R. & Frieman, J. 1996, The Astrophysical Journal Supplement Series, 105, 37 22

Scoccimarro, R., Sheth, R. K., Hui, L., & Jain, B. 2001, ApJ, 546, 20 24

Seitz, C. & Schneider, P. 1995, A&A, 297, 287 50, 52

Seitz, C. & Schneider, P. 1997, A&A, 318, 687 50

Seljak, U. 2000, MNRAS, 318, 203 24

Seljak, U. & Zaldarriaga, M. 1996, Astrophys. J., 469, 437 23

Semboloni, E., Hoekstra, H., Schaye, J., van Daalen, M. P., & McCarthy, I. G. 2011, MNRAS, 417, 2020 59, 91, 119

Shandarin, S. F. & Zeldovich, Y. B. 1989, Rev. Mod. Phys., 61, 185 8

Shankar, F., Mei, S., Huertas-Company, M., et al. 2014, MNRAS, 439, 3189 38

Sheldon, E. S., Johnston, D. E., Frieman, J. A., et al. 2004, AJ, 127, 2544 54

Sheth, R. K. & Tormen, G. 1999, MNRAS, 308, 119 24

Sheth, R. K. & Tormen, G. 2002, MNRAS, 329, 61 11

Sijacki, D., Vogelsberger, M., Genel, S., et al. 2015, MNRAS, 452, 575 41

Silk, J. & Mamon, G. A. 2012, Research in Astronomy and Astrophysics, 12, 917 20

Silk, J. & Rees, M. J. 1998, A&A, 331, L1 20

Smith, A., Cole, S., Baugh, C., et al. 2017, MNRAS, 470, 4646 38

Smith, R. E., Peacock, J. A., Jenkins, A., et al. 2003, MNRAS, 341, 1311 23, 25

Smith, R. E., Scoccimarro, R., & Sheth, R. K. 2007, Phys. Rev. D, 75, 063512 24

Smoot, G. F., Bennett, C. L., Kogut, A., et al. 1992, ApJ, 396, L1 1, 26

Sofue, Y. & Rubin, V. 2001, Annual Review of Astronomy and Astrophysics, 39, 137 30

Somerville, R. S. 2002, ApJ, 572, L23 33

Sonnenfeld, A., Treu, T., Gavazzi, R., et al. 2013, ApJ, 777, 98 94

Soucail, G., Fort, B., Mellier, Y., & Picat, J. P. 1987, A&A, 172, L14 45

Spergel, D., Gehrels, N., Baltay, C., et al. 2015, ArXiv e-prints [[arXiv]1503.03757] 45, 57

Spergel, D. N. & Steinhardt, P. J. 2000a, Phys. Rev. Lett., 84, 3760 5, 30

Spergel, D. N. & Steinhardt, P. J. 2000b, Physical Review Letters, 84, 3760 13

Spergel, D. N., Verde, L., Peiris, H. V., et al. 2003, The Astrophysical Journal Supplement Series, 148, 175 26

Springel, V. 2005, MNRAS, 364, 1105 35, 36, 39

Springel, V. 2010, MNRAS, 401, 791 39

Springel, V., Frenk, C. S., & White, S. D. M. 2006, Nature, 440, 1137 28

Springel, V., Pakmor, R., Pillepich, A., et al. 2018, MNRAS, 475, 676 40, 41

Springel, V., Wang, J., Vogelsberger, M., et al. 2008a, MNRAS, 391, 1685 15

Springel, V., Wang, J., Vogelsberger, M., et al. 2008b, MNRAS, 391, 1685 36

Stadel, J., Potter, D., Moore, B., et al. 2009, MNRAS, 398, L21 36

Starck, J. L., Pires, S., & Réfrégier, A. 2006, A&A, 451, 1139 52

Starkenburg, E., Helmi, A., De Lucia, G., et al. 2013, MNRAS, 429, 725 33

Stoehr, F., White, S. D. M., Tormen, G., & Springel, V. 2002, MNRAS, 335, L84 15

Sutherland, R. S. & Dopita, M. A. 1993, ApJS, 88, 253 39

Suto, D., Peirani, S., Dubois, Y., et al. 2017, PASJ, 69, 14 43, 44

Suzuki, N., Rubin, D., Lidman, C., et al. 2012, ApJ, 746, 85 29

Swaters, R. A., Madore, B. F., van den Bosch, F. C., & Balcells, M. 2003, ApJ, 583, 732 32

Takada, M., Ellis, R. S., Chiba, M., & Greene, J. E. e. a. 2014, PASJ, 66, R1 115

Takahashi, R., Hamana, T., Shirasaki, M., et al. 2017a, ApJ, 850, 24 59

Takahashi, R., Hamana, T., Shirasaki, M., et al. 2017b, ApJ, 850, 24 61, 91

Takahashi, R., Sato, M., Nishimichi, T., Taruya, A., & Oguri, M. 2012, ApJ, 761, 152 23, 25

Taylor, A. N. & Watts, P. I. R. 2000, MNRAS, 314, 92 22

Tegmark, M., Blanton, M. R., Strauss, M. A., et al. 2004, ApJ, 606, 702 26, 29

Tegmark, M., Eisenstein, D. J., Strauss, M. A., et al. 2006, Phys. Rev. D, 74, 123507 28

Tempel, E., Stoica, R. S., & Saar, E. 2013, MNRAS, 428, 1827 114

Tenneti, A., Mandelbaum, R., Di Matteo, T., Feng, Y., & Khandai, N. 2014, MNRAS, 441, 470 41

Teyssier, R. 2002, A&A, 385, 337 39

Teyssier, R., Pires, S., Prunet, S., et al. 2009, A&A, 497, 335 36, 61

Teyssier, R., Pontzen, A., Dubois, Y., & Read, J. I. 2013, MNRAS, 429, 3068 33, 43

The Dark Energy Survey Collaboration. 2005, ArXiv e-prints, astro 51

Tinker, J. L., Robertson, B. E., Kravtsov, A. V., et al. 2010, ApJ, 724, 878 24

Tollerud, E. J., Bullock, J. S., Strigari, L. E., & Willman, B. 2008, ApJ, 688, 277 33

Tomczak, A. R., Lemaux, B. C., Lubin, L. M., et al. 2017, MNRAS, 472, 3512 21

Toomre, A. 1977, in Evolution of Galaxies and Stellar Populations, ed. B. M. Tinsley & D. C. Larson, Richard B. Gehret, 401 18

Tormen, G., Diaferio, A., & Syer, D. 1998, MNRAS, 299, 728 15

Treu, T., Schmidt, K. B., Brammer, G. B., et al. 2015, ApJ, 812, 114 114

Troxel, M. A., MacCrann, N., Zuntz, J., et al. 2017, ArXiv e-prints [[arXiv]1708.01538] 56

Ueda, S., Kitayama, T., Oguri, M., et al. 2018, ApJ, 866, 48 5

Vale, C. & White, M. 2003, ApJ, 592, 699 59, 63

van Daalen, M. P., Schaye, J., Booth, C. M., & Dalla Vecchia, C. 2011, MNRAS, 415, 3649 41

van den Bosch, F. C., Ogiya, G., Hahn, O., & Burkert, A. 2018, MNRAS, 474, 3043 16

van den Bosch, F. C., Robertson, B. E., Dalcanton, J. J., & de Blok, W. J. G. 2000, AJ, 119, 1579 32

van Uitert, E., Joachimi, B., Joudaki, S., et al. 2018, MNRAS, 476, 4662 53, 118

van Waerbeke, L. 2000, MNRAS, 313, 524 52

Van Waerbeke, L., Mellier, Y., Erben, T., et al. 2000a, A&A, 358, 30 45

Van Waerbeke, L., Mellier, Y., Erben, T., et al. 2000b, A&A, 358, 30 54

Velander, M., van Uitert, E., Hoekstra, H., et al. 2014, MNRAS, 437, 2111 54

Velliscig, M., Cacciato, M., Hoekstra, H., et al. 2017, MNRAS, 471, 2856 53, 91

Villumsen, J. V. 1989, The Astrophysical Journal Supplement Series, 71, 407 35

Viola, M., Cacciato, M., Brouwer, M., et al. 2015, MNRAS, 452, 3529 53

Vogelsberger, M., Genel, S., Springel, V., et al. 2014, Nature, 509, 177 41

Vogelsberger, M., Zavala, J., & Loeb, A. 2012, MNRAS, 423, 3740 15, 16, 17, 32

Wadsley, J. W., Stadel, J., & Quinn, T. 2004, New A, 9, 137 39

Walker, A. G. 1937, Proceedings of the London Mathematical Society, (Series 2) volume 42, p. 90-127, 42, 90 2

Walker, M. G. & Peñarrubia, J. 2011, ApJ, 742, 20 32

Walsh, D., Carswell, R. F., & Weymann, R. J. 1979, Nature, 279, 381 45

Wambsganss, J., Cen, R., & Ostriker, J. P. 1998, ApJ, 494, 29 63

Warren, M. S., Quinn, P. J., Salmon, J. K., & Zurek, W. H. 1992, ApJ, 399, 405 15, 68

Watson, W. A., Iliev, I. T., D'Aloisio, A., et al. 2013, MNRAS, 433, 1230 36

Weinberg, D. H., Bullock, J. S., Governato, F., Kuzio de Naray, R., & Peter, A. H. G. 2015, Proceedings of the National Academy of Science, 112, 12249 32

Weinberg, S. 1972, Gravitation and Cosmology: Principles and Applications of the General Theory of Relativity 2

Welker, C., Devriendt, J., Dubois, Y., Pichon, C., & Peirani, S. 2014, MNRAS, 445, L46 113

Welker, C., Dubois, Y., Pichon, C., Devriendt, J., & Chisari, N. E. 2018, A&A, 613, A4 113

White, M. & Vale, C. 2004, Astroparticle Physics, 22, 19 63

White, S. D. M. & Frenk, C. S. 1991, ApJ, 379, 52 18, 38

White, S. D. M. & Rees, M. J. 1978, MNRAS, 183, 341 17

Wittman, D. M., Tyson, J. A., Kirkman, D., Dell'Antonio, I., & Bernstein, G. 2000, Nature, 405, 143 45, 54

Yang, X., Kratochvil, J. M., Huffenberger, K., Haiman, Z., & May, M. 2013, Phys. Rev. D, 87, 023511 59, 91

Yang, X., Mo, H. J., & van den Bosch, F. C. 2003, MNRAS, 339, 1057 18

York, D. G., Adelman, J., Anderson, John E., J., et al. 2000, AJ, 120, 1579 26

Yoshida, N., Springel, V., White, S. D. M., & Tormen, G. 2000, ApJ, 544, L87 15

Zackrisson, E. 2011, ArXiv e-prints [[arXiv]1101.4033] 114

Zavala, J., Vogelsberger, M., & Walker, M. G. 2013, MNRAS, 431, L20 32, 33

Zehavi, I., Zheng, Z., Weinberg, D. H., et al. 2011, ApJ, 736, 59 24

Zehavi, I., Zheng, Z., Weinberg, D. H., et al. 2005, ApJ, 630, 1 24

Zentner, A. R., Berlind, A. A., Bullock, J. S., Kravtsov, A. V., & Wechsler, R. H. 2005, ApJ, 624, 505 15

Zhang, Y., Yang, X., Wang, H., et al. 2013, ApJ, 779, 160 114

Zheng, Z., Berlind, A. A., Weinberg, D. H., et al. 2005, ApJ, 633, 791 20

Zwicky, F. 1933, Helvetica Physica Acta, 6, 110 30